ISSN 1451 - 9372(Print)
ISSN 2217 - 7434(Online)
JANUARY-MARCH 2021
Vol.27, Number 1, 1-106

Chemical Industry & Chemical Engineering Quarterly

The AChE Journal for Chemical Engineering,
Biochemical Engineering, Chemical Technology,
New Materials, Renewable Energy and Chemistry

www.ache.org.rs/ciceq

Journal of the
Association of Chemical Engineers of
Serbia, Belgrade, Serbia

Chemical Industry &
Chemical Engineering
CI&CE Quarterly

EDITOR-In-Chief
Vlada B. Veljković
Faculty of Technology, University of Niš, Leskovac, Serbia
E-mail: veljkovicvb@yahoo.com

ASSOCIATE EDITORS

Jonjaua Ranogajec
Faculty of Technology, University of Novi Sad, Novi Sad, Serbia

Srđan Pejanović
Department of Chemical Engineering, Faculty of Technology and Metallurgy, University of Belgrade, Belgrade, Serbia

Milan Jakšić
ICEHT/FORTH, University of Patras, Patras, Greece

EDITORIAL BOARD (Serbia)
Đorđe Janaćković, Sanja Podunavac-Kuzmanović, Viktor Nedović, Sandra Konstantinović, Ivanka Popović
Siniša Dodić, Zoran Todorović, Olivera Stamenković, Marija Tasić, Jelena Avramović, Goran Nikolić, Dunja Sokolović

ADVISORY BOARD (International)

Dragomir Bukur
Texas A&M University,
College Station, TX, USA

Milorad Dudukovic
Washington University,
St. Luis, MO, USA

Jiri Hanika
Institute of Chemical Process Fundamentals, Academy of Sciences
of the Czech Republic, Prague, Czech Republic

Maria Jose Cocero
University of Valladolid,
Valladolid, Spain

Tajalli Keshavarz
University of Westminster,
London, UK

Zeljko Knez
University of Maribor,
Maribor, Slovenia

Igor Lacik
Polymer Institute of the Slovak Academy of Sciences,
Bratislava, Slovakia

Denis Poncelet
ENITIAA, Nantes, France

Ljubisa Radovic
Pen State University,
PA, USA

Peter Raspor
University of Ljubljana,
Ljubljana, Slovenia

Constantinos Vayenas
University of Patras,
Patras, Greece

Xenophon Verykios
University of Patras,
Patras, Greece

Ronnie Willaert
Vrije Universiteit,
Brussel, Belgium

Gordana Vunjak Novakovic
Columbia University,
New York, USA

Dimitrios P. Tassios
National Technical University of Athens,
Athens, Greece

Hui Liu
China University of Geosciences, Wuhan, China

FORMER EDITOR (2005-2007)
Professor Dejan Skala
University of Belgrade, Faculty of Technology and Metallurgy, Belgrade, Serbia

Journal of the
Association of Chemical Engineers of
Serbia, Belgrade, Serbia

Chemical Industry & Chemical Engineering CI&CE Quarterly

Vol. 27 Belgrade, January-March 2021 No. 1

Chemical Industry & Chemical Engineering Quarterly (ISSN 1451-9372) is published quarterly by the Association of Chemical Engineers of Serbia, Kneza Miloša 9/I, 11000 Belgrade, Serbia

Editor:
Vlada B. Veljković
veljkovic@yahoo.com

Editorial Office:
Kneza Miloša 9/I, 11000 Belgrade, Serbia
Phone/Fax: +381 (0)11 3240 018
E-mail: shi@yubc.net
www.ache.org.rs

For publisher:
Tatijana Duduković

Secretary of the Editorial Office:
Slavica Desnica

Marketing and advertising:
AChE Marketing Office
Kneza Miloša 9/I, 11000 Belgrade, Serbia
Phone/Fax: +381 (0)11 3240 018

Publication of this Journal is supported by the Ministry of Education, Science and Technological Development of the Republic of Serbia

Subscription and advertisements make payable to the account of the Association of Chemical Engineers of Serbia, Belgrade, No. 205-2172-71, Komercijalna banka a.d., Beograd

Computer typeface and paging:
Vladimir Panić

Printed by:
Faculty of Technology and Metallurgy, Research and Development Centre of Printing Technology, Karnegijeva 4, P.O. Box 3503, 11120 Belgrade, Serbia

Abstracting/Indexing:
Articles published in this Journal are indexed in *Thompson Reuters* products: *Science Citation Index - Expanded*™ - access *via Web of Science*®, part of *ISI Web of Knowledge*℠

CONTENTS

Activities of the Association of Chemical Engineers of Serbia are supported by:

- Ministry of Education, Science and Technological Development, Republic of Serbia
- Hemofarm Koncern AD, Vršac, Serbia
- Faculty of Technology and Metallurgy, University of Belgrade, Belgrade, Serbia
- Faculty of Technology, University of Novi Sad, Novi Sad, Serbia
- Faculty of Technology, University of Niš, Leskovac, Serbia
- Institute of Chemistry, Technology and Metallurgy, University of Belgrade, Belgrade, Serbia

CI&CEQ
Chemical Industry & Chemical Engineering Quarterly

Available on line at
Association of the Chemical Engineers of Serbia *AChE*
www.ache.org.rs/CICEQ

Chem. Ind. Chem. Eng. Q. 27 (1) 1–13 (2021) CI&CEQ

CLEAN PRINTING PROCESS OF COTTON WITH NATURAL DYES: EFFECT OF PASTE FORMULATION COMPONENTS ON PRINTING PERFORMANCES

AMAL BEN FADHEL[1]
WAFA MILED[2,3]
WAFA HADDAR[1,3]
NIZAR MEKSI[1,4]

[1]University of Monastir, Faculty of Sciences of Monastir, Research Unit of Applied Chemistry and Environment, Monastir, Tunisia
[2]University of Monastir, Textile Engineering Laboratory, Higher Institute of Technological Studies of Ksar Hellal, Ksar Hellal, Tunisia
[3]Department of Early Childhood, University College Taraba, Taif University, Saudi Arabia
[4]University of Monastir, National Engineering School of Monastir, Textile Engineering Department, Monastir, Tunisia

SCIENTIFIC PAPER

UDC 677.21:667.027.4

Article Highlights

- *Corchorus olitorius* L. was tested in printing paste formulation as natural dye
- The printing pastes were applied on cotton fabric using screen printing process
- The resulting color shades varied from green to brown
- The effects of various print formulation components on printing quality were investigated

Abstract

A novel natural dye Corchorus olitorius L. was investigated in the preparation of printing pastes for screen printing of cotton fabric. To ensure ecological printing, greener thickeners were used such as: sodium alginate, carboxymethyl cellulose and Ceratonia siliqua L. flour. The nature and concentration of thickener, dyestuff and urea concentrations, mordant type and fixation method were explored. Printed cotton fabric qualities were evaluated by determining different parameters: color strength, penetration percentage, printing fastnesses and mechanical properties, whereas print paste quality was evaluated by measuring its apparent viscosity. The higher dye concentration used in the printing paste led to better apparent viscosity and color strength levels. The increase of urea concentration improved the color strength, but reduced the apparent viscosity of printing paste. Best results of viscosity and color strength parameters were obtained using ferrous sulfate as a mordant and sodium alginate as a thickener, the results being 1346.67 mPa s^{-1} *and 4.90, respectively. The resulting color shades varied from green to brown and very good color fastnesses was achieved, but depended mainly on the used experimental conditions.*

Keywords: natural dyes, cleaner printing process, cotton fabrics, past formulation components, components effect, printing qualities.

Textile screen printing is a stencil technique of printmaking, in which a design is imposed on a polyester or polyamide screen of fine mesh, with blank areas coated with an impermeable substance. The printing paste is forced into the mesh openings by the pushing operation of a squeegee to reach finally the textile surface [1,2]. For the textile printing industry, the most used dyes include acid, direct, vat, reactive, pigment and disperse dyes [1,2]. These dyes ensure generally acceptable to very good fastness properties but may have hazardous effects on consumers, workers and the environment [3-5]. Such crucial disadvantage is noticeable even at very low concentrations. To deal with the ecological problems associated with coloration processes using synthetic dyes as well as their undesirable auxiliaries, several studies have been directed. Studies proposed the minimization and the optimization of classic auxiliaries and dye consumptions [6,7], the substitution by other less toxic compounds [8,9], the development of novel generations of eco-friendly dyes and auxiliaries [10-15], the use of new greener and recyclable solvents instead of

---

Correspondence: A.B. Fadhel, Research Unity of Applied Chemistry and Environment, Faculty of Sciences of Monastir, 5000 Monastir, Tunisia.
E-mail: benfadhelamal19891@gmail.com
Paper received: 4 October, 2019
Paper revised: 27 May, 2020
Paper accepted: 4 June, 2020

https://doi.org/10.2298/CICEQ191004019B

water [16-18], and the creation of innovated processes [19,20].

Many environmental programs have been also established [20-24]. In this context, the application of bio-sourced compounds such as natural dyes in textile coloration processes have been increasingly attracting more attention [25]. The use of natural dyes in the dyeing process was established to be very promising. Many successful applications of bio-sourced pigments and dyes were proposed in the dyeing field [26-32]. Several industrial applications were also noted. However, until now, only few studies have reported the application of natural dyes in printing processes. In fact, compared to the dyeing field, the literature described that only some dyes extracted from known plants, such as madder, curcuma, rhubarb, pomegranate, orange tree leaves, alkanet roots, etc., have been tested for printing processes of natural and synthetic fibers, in the presence of metallic mordants [33-39], chitosan [40-42] and bio-mordants [33,34,37--39,43-44].

In this study, *Corchorus olitorius* L. presented in Figure 1 was chosen as a natural source to develop printing experiments on bleached cotton fabrics. Currently, *C. olitorius* L. belongs to the Tiliaceae family and originates from India and Africa, but nowadays, it is found especially throughout the tropics. It was cultivated to provide bark for the production of fibers (jute) and its mucilaginous leaves are used as a vegetable [45]. The leaves of *C. olitorius* L. are very rich in many components such as vitamins (vitamin A, ascorbic acid, etc.), proteins, lipids, fibers, etc. [46]. In addition, these leaves contain secondary metabolites such as polyphenols, flavonoids, tannins, steroids, etc. [47]. The leaves of this plant were not used previously either in dyeing or printing of textile materials. The color and the mucilaginous characteristic of *C. olitorius* L. leaves inspired us to explore this plant as a green dye in textile printing processes. The presence of the mucilage is the first parameter that allows us to use this dye. This metabolite in some way ensures the viscosity of the printing paste. So, this natural dye was applied for the first time in this study on bleached cotton fabric by the screen printing process at semi-industrial scale. Two fixation methods were employed, steaming and thermofixation.

Figure 1. Corchorus olitorius L.

The effects of the thickener type, the dyestuff and urea concentrations according to thickener concentration, and the mordant type were investigated. The apparent viscosity of printing paste, the color, fastness and mechanical properties of printed fabric were analyzed and discussed.

EXPERIMENTAL

Textile material and chemicals used

Commercially bleached cotton fabric was supplied from (Ayed Company of Textile Trade, Tunisia). Technical features of the selected fabric were: twill weave; warp count, 16 ends per cm; weft count, 32 picks per cm; area density, 385.2 g m^{-1}; tensile strength through warp direction, 494.09 N m^{-2}; tensile strength through weft direction, 213.06 N m^{-2}.

Commercial grade *Corchorus olitorius* L. powder was used in this work as a natural dye for cotton printing. It was purchased from a local market in Tunisia.

Alum ([$KAl(SO_4)_2$], Fluka), ferrous sulfate ($FeSO_4 \cdot 7H_2O$, Fluka), urea (CH_4N_2O, MOPCO, Egypt) and sodium bicarbonate ($NaHCO_3$, Fluka) were laboratory grade reagents and were used as received.

Sodium alginate (Bezema, Switzerland), carboxymethyl cellulose (CMC) (Jeniuschem, Italy) and commercial local *Ceratonia siliqua* L. flour were used as green thickeners. Tubicide TDM (Bezema, Switzerland) was used as an antifungal agent free of formaldehyde for printing pastes.

Preparation of printing paste

The stock paste of each thickener was prepared by slow sprinkling of 7% of natural thickener powder with distilled water under continuous stirring during 2 h in order to prevent lump formation.

For the preparation of the printing paste, 357.1 g of the thickening paste prepared previously was taken to add 20 g of the natural dye, 30 g of the mordant, 50 g of urea and 25 g of sodium bicarbonate with 4 g of the antifungal agent. Distilled water was added to this mixture until a total amount of 1 kg was reached. The preparation of the paste was carried out by an electric stirrer in a uniform manner. The paste was kept next to it and was ready for printing.

Apparent viscosity measurements

Apparent viscosity measurements of the printing pastes were carried out at 25 °C using a rheometer

(Rheotec RC30, France) equipped with the coaxial cylinder system CC14 DIN. This parameter is one of the key factors that can extremely affect the printing quality. Each experiment was performed in triplicate and results were given in terms of the mean value.

Cotton printing process

The prepared printing paste was applied to cotton fabric by using a semi-industrial scale table for screen printing processes (SILKB 480 Mathis AG, Switzerland). Then, after drying, two fixation methods were tested. In fact, the printed samples were treated either at 130 °C for 5 min by thermofixation method or at 102 °C for 30 min by steaming method. Next, the printed samples were washed with cold water at 40 °C for 10 min and then hot water at 60 °C for 5 min in order to remove the residual unfixed paste. Finally, they were rinsed well and air-dried at room temperature.

Color evaluation

Color evaluations of printed samples were based on the following colorimetric parameters: color strength (*K*/*S*), parameter *Integ*(*K*/*S*) and the penetration percentage *PP* (%).

Color measurements of printed samples were carried out by a SpectraFlash SF300 colorimeter equipped with a DataMaster 2.3 software (Datacolor International, USA), using D65 light source and a viewing angle of 10°.

The color strength (*K*/*S*) values were calculated using the Kubelka-Munk equation [48,49]:

$$K/S = \frac{(1-R)^2}{2R} \tag{1}$$

where: R is decimal fraction of a reflectance of printed fabric; K is absorption coefficient; S is scattering coefficient.

Integ(*K*/*S*) can provide an efficient colorimetric evaluation when the shades of printed fabrics vary according to experimental parameters. *Integ*(*K*/*S*) is given by the following equation [50]:

$$Integ(K/S) = \sum E_\lambda \left(\frac{K}{S}\right)_\lambda \left(\overline{x_\lambda} + \overline{y_\lambda} + \overline{z_\lambda}\right) \tag{2}$$

where E_λ is the spectral energy distribution of the light source (D65/10°); $(K/S)_\lambda$ is the color strength of the printed fabric; $\overline{x_\lambda}, \overline{y_\lambda}, \overline{z_\lambda}$ are the CIE standard observer color matching functions.

The penetration percentage *PP* (%) was used to evaluate the depth of the dye across the textile surface. The penetration percentage value *PP* (%) of the printing paste was determined by using the following equation [51-53]:

$$PP(\%) = 100\frac{Integ(K/S)_b}{0.5(Integ(K/S)_f + Integ(K/S)_b)} \tag{3}$$

Where $(K/S)_f$ and $(K/S)_b$ are the color strength values of the front and back side of the printed fabric, respectively.

For all color measurements, each experiment was performed in triplicate and results were given in terms of the mean value.

Fastness testing

Fastness properties of printed fabrics were controlled with ISO standard methods. The specific tests concern colorfastness to washing (ISO 105-C02, 2010), colorfastness to light (ISO 105-B01, 2015) and colorfastness to rubbing (ISO 105-X12, 2016). In order to verify the reproducibility of results, each experiment related to fastnesses testing was performed in triplicate.

For washing fastness, the results were evaluated using the relation between the CIELAB color difference ΔE^*_{ab} and the gray scale fastness grade GS_C (Table 1), reported in ISO 105-A05 (1996) [54]. ΔE^*_{ab} was calculated between the washed and unwashed samples using the following CIELAB color difference equation [55]:

$$\Delta E^*_{ab} = \sqrt{\Delta L^{*2} + \Delta a^{*2} + \Delta b^{*2}} \tag{4}$$

Table 1. Relation between CIELAB color difference ΔE^*_{ab} and the grey scale fastness grade GS_C (ISO105-A05 (1996))

CIELAB color difference ΔE^*_{ab}	Grey scale fastness grade GS_C
$\Delta E^*_{ab} < 0.40$	5
$0.40 \le \Delta E^*_{ab} < 1.25$	4.5
$1.25 \le \Delta E^*_{ab} < 2.10$	4
$2.10 \le \Delta E^*_{ab} < 2.95$	3.5
$2.95 \le \Delta E^*_{ab} < 4.10$	3
$4.10 \le \Delta E^*_{ab} < 5.80$	2.5
$5.80 \le \Delta E^*_{ab} < 8.20$	2
$8.20 \le \Delta E^*_{ab} < 11.60$	1.5
$\Delta E^*_{ab} \ge 11.60$	1

Mechanical properties evaluation

Mechanical properties of printed cotton fabrics were appreciated through the determination of the maximum force using the grab method. Before proceeding to mechanical evaluation, samples were stored under standard relative atmospheric conditions T = 20±2 °C, Hr = 65±4% for 24 h after washing.

Thus, the tensile strength levels of printed samples were measured according to ISO 13934-2, 1999(F), using tensile testing machine (LR5K, USA), with a crosshead speed of 100 mm min^{-1} and a load of 2.00 N. All experiments were performed in triplicate. The presented results were the mean values of the three experiments for each weft and warp direction.

RESULTS AND DISCUSSION

The nature and concentration of thickener, dyestuff and urea concentrations, the mordant type as well as the type of fixation method are the main operating conditions influencing the screen printing process. First, the effects of these parameters were studied on the print paste quality by measuring its apparent viscosity, then on the printed cotton fabrics performances by evaluating their color, fastness and mechanical properties.

Effect of the nature of thickener on printing quality

Effect on the apparent viscosity of print pastes

The main purpose of the thickener is to increase the viscosity of the printing paste. Consequently, the printing paste could be applied on the textile surface without bleeding or spreading and be capable of maintaining the design outlines. In this work, sodium alginate, carboxymethyl cellulose and *Ceratonia siliqua* L. flour were mixed with *Corchorus olitorius* L. powder as a natural dye, in the presence of alum or ferrous sulfate as mordants. First, the apparent viscosity of the printing pastes was measured. Results are mentioned in Figure 2.

In Figure 2, it was found that sodium alginate is the thickener that offers the most important values of apparent viscosity. In addition, apparent viscosity becomes more important, especially in the case of ferrous sulfate as a mordant (1346.67 mPa s^{-1}). However, *C. siliqua* L. flour gave poor values of apparent viscosity for both cases of mordant. In terms of thickening quality, the studied thickeners could be classified in the following order: sodium alginate > carboxymethyl cellulose > *C. siliqua* L. flour.

The obtained result can be explained by the important ability of sodium alginate to absorb a great amount of water and swell significantly in comparison to other thickening agents. However, *Ceratonia siliqua* L. flour is the thickener that presents the lowest swelling capacity.

Effect on the color and fastness properties of printed fabrics

In the screen printing process, the thickener may also improve the color strength and fastness properties of printed fabrics. So, the effect of thickener type on color properties and printing fastnesses were also investigated in this work. Likewise, using natural dyes, the mordant often fixes the dye and prevents discoloration of the surface of the textile material. In fact, mordant has the power to improve the fastness properties of printed samples. Besides, using different kinds of mordants with natural dyes, a variety of colors can be obtained [35]. In this study, color properties were appreciated by determining both the color strength and penetration percentage, whereas printing fastnesses were measured according to washing, rubbing and light. All the obtained results are summarized in Table 2 for both the steaming and thermofixation methods.

Table 2 shows that the color strength values obtained with sodium alginate are clearly higher for the two fixation methods. Moreover, the combination of sodium alginate with ferrous sulfate gave the highest color strength value compared to other results

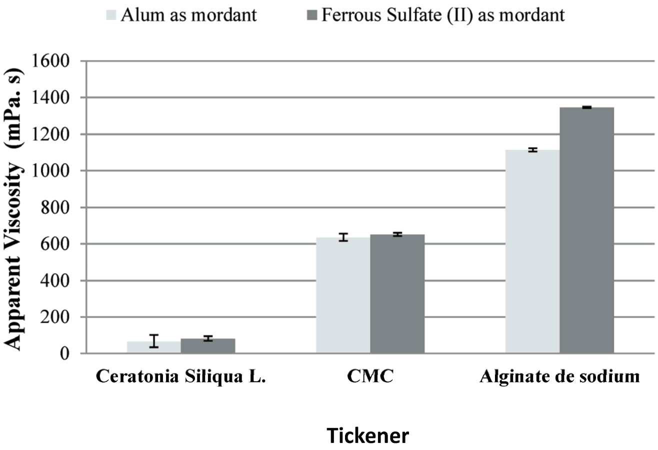

Figure 2. Effect of the type of thickener on apparent viscosity.

Table 2. Effect of thickener type on Integ color strength, penetration percentage and fastness properties of printed cotton fabrics

Fixation method	Thickener	Mordant type	Integ. color strength	Penetration %	Washing fastness (ISO 105-C02)	Rubbing fastness (ISO 105-X12) Dry	Rubbing fastness (ISO 105-X12) Wet	Light fastness (ISO 105-B01)
Steaming	CMC	Without mordant	0.43±0.07	14.61±0.083	1.5	2-3	2	4
		Alum	0.89 ±0.065	28±0.8	2.5	4-5	4-5	5
		Ferrous sulfate (II)	4.08±0.167	13±0.4	3.5	4-5	4	7
	Sodium alginate	Without Mordant	0.29 ±0.064	39.93±0.34	1	2-3	2	4
		Alum	0.97±0.045	27±0.3	1.5	4-5	3-4	3
		Ferrous sulfate (II)	4.90±0.104	11±0.07	1	4-5	3	6
	Ceratonia siliqua L.	Without mordant	0.59 ±0.059	21.64±0.09	1.5	3	2	2
		Alum	0.81±0.030	36±0.5	1	4-5	3-4	2
		Ferrous sulfate (II)	1.79±0.025	23±0.1	2.5	4-5	4	5
Thermofixation	CMC	Without mordant	0.20±0.11	34.94±0.37	1	2	2	3
		Alum	0.87±0.031	20±0.2	2	4-5	4	4
		Ferrous sulfate (II)	3.78±0.118	11±0.2	2	3-4	3	6
	Sodium alginate	Without mordant	0.26 ±0.037	67.83±0.134	1	2	1-2	3
		Alum	0.64±0.043	29±0.7	1	4	3-4	3
		Ferrous sulfate (II)	4.37±0.126	10±0.2	2	3-4	2-3	5
	Ceratonia siliqua L.	Without mordant	0.62±0.04	24.87±0.34	1	2-3	2	2
		Alum	0.81±0.030	35±0.6	1	4	3	4
		Ferrous sulfate (II)	2.27±0.203	15±1.2	1.5	4	3-4	6

obtained with alum. All samples treated with alum underlined color strength values less than 1. It causes this mordant to be poorly suited using *C. olitorius* L., whatever the thickener studied.

Color strength also shows a big dependency on the used fixation method. Printed fabrics fixed by steaming showed a slight improvement of color strength. Indeed, steaming of natural dye prints is a process involving dyestuff penetration [56]. The condensed water vapor accelerates the penetration of the dye molecules into the textile surface, from where an increase in the color strength of the printed fabrics fixed by the steaming is observed, compared to those fixed by the thermofixation method [33]. As can be shown in Figure 3, the steaming process introduces hot vapor to the cellulosic micro-vacuums leading to a swelling phenomenon. Swelled cellulose allows better interactions with the paste. By swelling, the cellulose conformation becomes more regular and leading to a better deposition of the paste. In this study, the penetration percentage evolution in function of thickener type or mordant type shows a reversed behavior since this parameter decreases for higher color strength.

Besides, results indicate that washing fastness depends directly on the type of thickener and mordant, but the influence of the fixation method is more remarkable. In fact, washing fastness results are closely related to the interactions that could be created after printing. These interactions are ensured by mordant which may act as mediator between natural dye and hydroxyl groups of the cellulosic material. The selected fixation method is also crucial in this case. For all experiments, the fixation by steaming showed better washing fastness results. As presented in Figure 3, this may be attributed to the easier penetration of natural dyestuff into cotton vacuums, which became more accessible after swelling by steaming treatment [33].

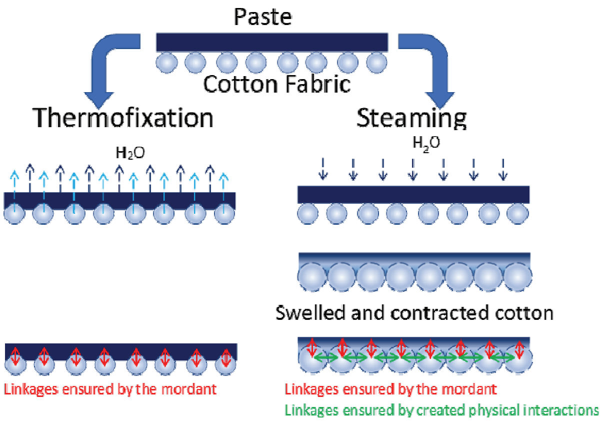

Figure 3. Influence of the fixation process (steaming or thermofixation) on the behavior of paste fixation.

Carboxymethyl cellulose demonstrated the highest washing fastness compared to the other two thickeners studied. These results are acceptable. Likewise, the sample treated with ferrous sulfate and steaming possessed the most interesting washing fastness which is of the order of 3.5. From these results, it can be concluded that the selection of suitable thickener depends on the type of mordant used in the printing paste and the selected fixation method.

Although sodium alginate is widely used in the industry, results obtained with carboxymethyl cellulose as thickener allow a slight improvement in rubbing and light fastness as presented in Table 2. Results indicate also that dry rubbing fastness could be as high as grade 4, while wet rubbing fastness is in the range of 3 to 4-5 for alum regardless of method of fixation used. For ferrous sulfate experiments, the results show that dry rubbing fastness could be as high as grade 3-4, while wet rubbing fastness is in the range of grade 2-3 to 4. This implies that the type of thickener and mordant have a slight effect on rubbing fastness. For light fastness, the obtained grades are given in Table 2 which should be considered with great importance because natural dyes are well known by their insufficient light fastness levels [57]. This presents one of the most important limitations of natural dyes in dyeing processes. Surprisingly, in our case, printing with *C. olitorius* L. gives good results. This may be attributed to the synergistic effect of paste components. In fact, the interactions between the components of the printing paste and the interactions between these components and cotton cellulose may create a printed surface which is more stable towards light than the natural dye when the latter is applied alone on textile fabric.

Taking into account the evolution of the color strength and the fastness properties, the results presented in Table 2 show that the depth of the printing paste on the textile material is related to the type of the thickening agent in terms of chemical composition, rheological properties and molecular weight [58]. It can also be noted that fastness results could be considered as sufficient if only washing and rubbing fastness values are higher than 3-4. For light fastness, the value should be higher than 5. All these interpretations were deduced from printing factories and they are appropriate only for the clothing sector.

Effect on the tensile strength of printed fabrics

Following the determination of color strength and fastness properties, the tensile strength through the weft and warp directions of printed cotton fabrics was also studied. The obtained values are reported in Figure 4a and b, respectively.

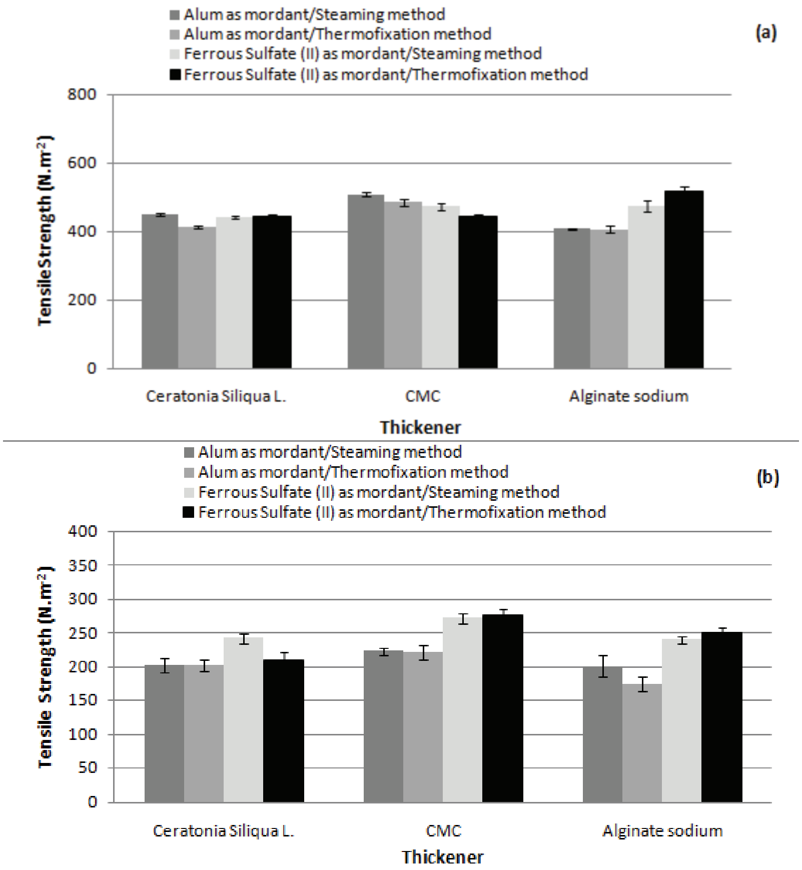

Figure 4. Effect of the type of thickener on fabric tensile strength: a) warp direction; b) weft direction.

From these figures, it can be observed that printed fabrics with sodium alginate and CMC emphasize generally remarkable tensile strength values compared to those of *C. siliqua* L. flour. Taking into account that the initial tensile strength through the warp direction is equal to 494.09 N m^{-2} and the initial tensile strength through the weft direction is equal to 213.6 N m^{-2}, the tensile strength decreases generally for many fabrics printed with *C. olitorius* L. according to the tensile strength of unprinted fabric. For example, in the warp direction, and in the presence of alum, sodium alginate showed a decrease of about 17% for both fixation methods. Similarly, for the weft direction, sodium alginate (alum, thermofixation method) and CMC (alum, steaming method) caused fabric degradations of 17 and 16%, respectively.

However, an increase of the tensile strength is observed in some cases, especially with sodium alginate, irrespective of the fixation method (ferrous sulfate, weft direction).

Related to all printing qualities investigated until now, results with CMC and ferrous sulfate were the most encouraging which will be considered for the next printing experiments.

Effect of dye concentration on printing quality

The amount of natural dye was varied from 0, 5, 10, 20, 30 and 40 g Kg^{-1} in the tested printing pastes. The apparent viscosity, color strength, penetration factor, fastness properties and mechanical properties (tensile strength) were the evaluation parameters of printing quality.

Effect on the apparent viscosity of print pastes

The results of apparent viscosity are plotted in Figure 5. This figure shows that as the dye amount increases, the apparent viscosity decreases for all tested mordants. This result seems obvious since the amount of dye was varied according to the amount of thickener, *i.e.*, when the amount of dye increases, the amount of thickener decreases. Consequently, the apparent viscosity decreases too. On the other hand, the values of the apparent viscosity of the printing pastes containing ferrous sulfate are slightly higher than those of alum. The results described elsewhere, showed also that the use of ferrous sulfate allows more stable conditions [59].

Effect on the color and fastness properties of printed fabrics

Table 3 shows the effect of dye concentration on the color strength, penetration percentage and fastness properties of printed cotton fabrics for both steaming and thermofixation methods. The *Integ*(*K*/*S*) values presented in Table 3 note that as the dye concentration increases in the printing paste, the amount of dye entering into the fiber increases and consequently, the color strength increases too. Generally, the increase of dye concentration is related to the increase of the availability of dye molecules in the printing paste. Thus, the fixed dye on the surface of textile support rises and the color strength becomes more important [60]. The *Integ*(*K*/*S*) values increase rapidly as the concentration of natural dyestuff increases from 0 to 20 g kg^{-1} of the weight of printing paste regardless of the type of mordant or the fixation method. For dye concentrations higher than 20 g kg^{-1}, the *Integ*(*K*/*S*) values decrease, because there was an significant loss of dye during washing of the printed samples.

Results of washing fastness are also given in Table 3 which show that generally higher dye concentrations made washing fastness lower. This is probably because of the lack of accessible sites on the surface of textile support. In addition, and as found before, the steaming fixation method allowed better fastness results. The same observation is noted for rubbing fastness. However, light fastness results

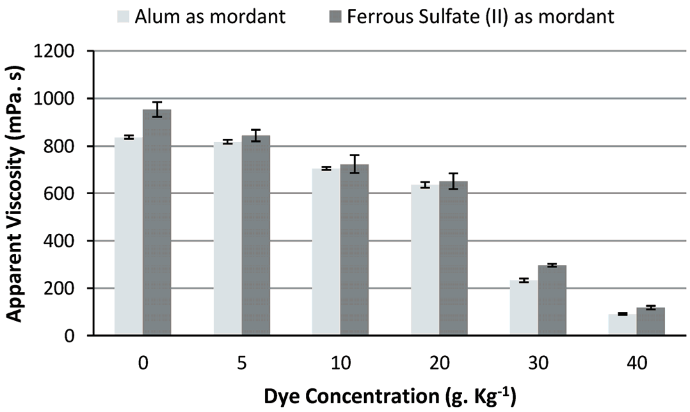

Figure 5. Effect of the dye concentration on apparent viscosity.

Table 3. Effect of dye concentration on Integ color strength, penetration percentage and fastness properties of printed cotton fabrics

Fixation method	Dye concentration g kg^{-1}	Mordant type	Integ. color strength	Penetration %	Washing fastness (ISO 105-C02)	Rubbing fastness (ISO 105-X12)		Light fastness (ISO 105-B01)
						Dry	Wet	
Steaming	0	Alum	0.51±0.049	31±3.9	4.5	4-5	4	2
		Ferrous sulfate (II)	2.35±0.282	26±3.7	3	4-5	4	3
	5	Alum	0.54±0.053	30±2.9	2.5	4-5	4-5	3
		Ferrous sulfate (II)	2.64±0.109	18±0.8	3	4-5	4	6
	10	Alum	0.57± 0.069	28±2.9	2	5	5	3
		Ferrous sulfate (II)	3.66±0.243	17±0.3	2.5	4-5	4	4
	20	Alum	0.89±0.065	28±0.8	2.5	4-5	4-5	5
		Ferrous sulfate (II)	4.08± 0.167	13±0.4	3.5	4-5	4	7
	30	Alum	0.84±0.049	25±2.6	2	4-5	4	5
		Ferrous sulfate (II)	3.98±0.129	13±0.4	3.5	4	3	7
	40	Alum	0.65±0.076	28±3.1	1.5	4	3	2
		Ferrous sulfate (II)	3.12±0.279	14±1.3	3.5	3-4	3	6
Thermofixation	0	Alum	0.21±0.043	60±8.9	1.5	5	5	2
		Ferrous sulfate (II)	1.19±0.123	28±2.5	1	4	3	3
	5	Alum	0.23±0.017	50±3	1.5	4-5	4	2
		Ferrous sulfate (II)	1.65±0.055	25±1.3	2.5	4	3-4	5
	10	Alum	0.46±0.041	33 ±3	2	4-5	4	2
		Ferrous sulfate (II)	3.18±0.266	15±1.3	2	4-5	4	3
	20	Alum	0.87± 0.031	20±0.2	2	4-5	4	4
		Ferrous sulfate (II)	3.78± 0.118	11±0.2	2	3-4	3	6
	30	Alum	0.81±0.039	23±1.4	2	4-5	4	3
		Ferrous sulfate (II)	3.50±0.095	13±0.6	2	4	3	6
	40	Alum	0.53±0.019	38±3.2	1	4	3	3
		Ferrous sulfate (II)	2.73±0.118	13±0.5	1.5	3	2-3	5

reach 7 for high dye concentrations (20 and 30 g kg^{-1}) and with ferrous sulfate. As noted above, the samples printed in the presence of ferrous sulfate, showed significant fastness properties compared to those printed with alum. This may be explained by iron, which is able to form a rigid complex with both cellulose cotton fiber and natural dye. It seems that this complex is more stable towards light than that of aluminum.

Effect on the tensile strength of printed fabrics

Otherwise, the tensile strength of printed samples was performed in order to evaluate the effect of variation of dye amount through the thermofixation and steaming methods on the fabric structure. The results obtained for this parameter are presented in Figure 6.

From Figure 6, it can be seen that the tensile strength values of different printing samples are around 409 and 511 N m^{-2} in the warp direction, whatever the fixation method used. In this direction, the dye amount of 40 g kg^{-1} presents the most important fabric degradation in the case of alum and with the thermofixation method. This fabric degradation is of the order of 17%. Likewise, the tensile strength studied in the weft direction showed slight decrease, with the exception of the dye amounts of 20 and 40 g kg^{-1}. In fact, the fabric degradation is of the order of 16% for 20 g kg^{-1} for alum using the thermofixation method. The amount of dye of 40 g kg^{-1} underlines fabric degradations of the order of 23% in the steaming method and a second one of the order of 36% in the heat setting.

Effect of the urea amount on printing quality

Urea is an essential auxiliary in the printing paste formulations. It can increase the dye solubility in water and so enhance the color brightness and color intensity [34]. Indeed, the fibers will swell, thanks to the action of this auxiliary, making easier the capillarity penetration of pastes [34]. For these reasons, the effect of the urea amount was also studied by varying its concentration from 0 to 150 g kg^{-1} of the weight of printing paste.

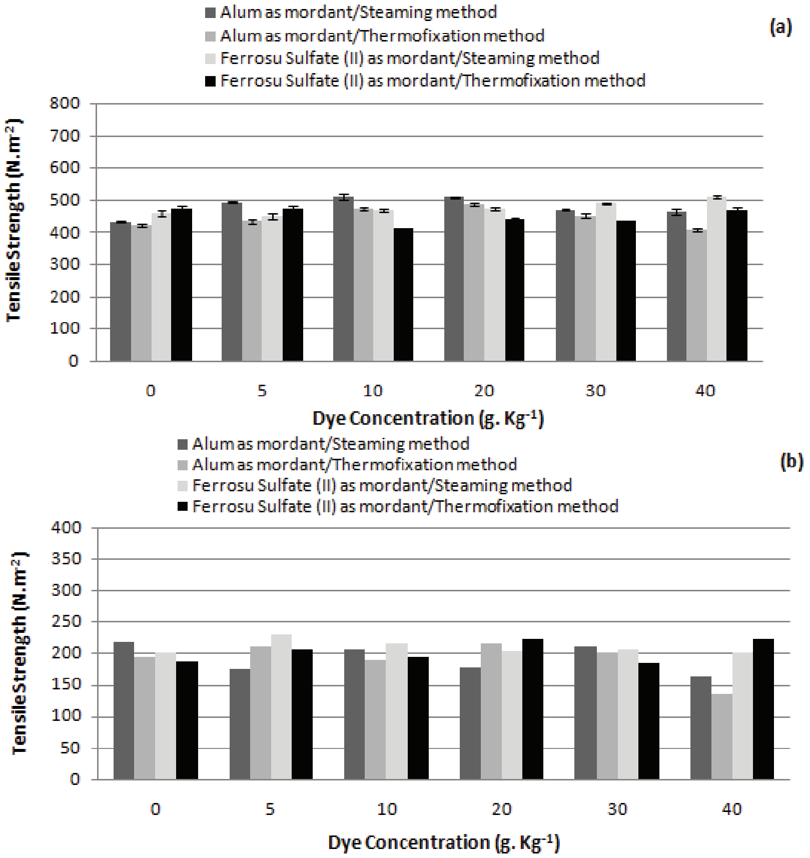

Figure 6. Effect of the dye concentration on fabric tensile strength: (a) warp direction; (b) weft direction.

Effect on the apparent viscosity of print pastes

Figure 7 shows the effect of the urea concentration on apparent viscosity. It was observed that the apparent viscosity values increase rapidly as the urea amount in the printing paste increases from 0 to 150 g kg^{-1} of the weight of printing paste. This result is also expected since the amount of urea was varied according to the amount of water.

Effect on the color and fastness properties of printed fabrics

From Table 4, it can be seen that for both mordants, ferrous sulfate and alum, when the urea amount increases from 0 to 50 g kg^{-1}, the color strength and wash fastness increase, but the penetration percentage decreases. This behavior becomes much more important in the case of experiments done with ferrous sulfate and fixed by steaming. This result may be attributed to the role of urea, which is a

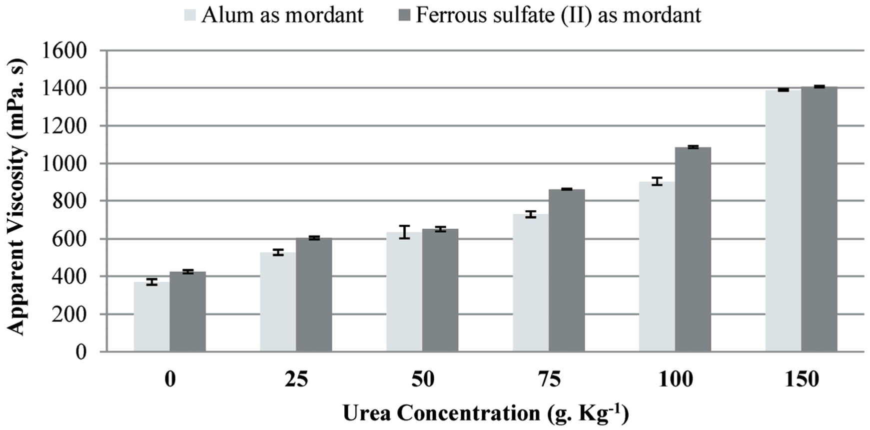

Figure 7. Effect of the urea concentration on apparent viscosity.

Table 4. Effect of urea concentration on Integ color strength, penetration percentage and fastness properties of printed cotton fabrics

Fixation method	Urea concentration g kg^{-1}	Mordant type	Integ. color strength	Penetration %	Washing fastness (ISO 105-C02)	Rubbing fastness (ISO 105-X12)		Light fastness (ISO 105-B01)
						Dry	Wet	
Steaming	0	Alum	0.44±0.041	43±1.9	2	4	3-4	3
		Ferrous sulfate (II)	0.98±0.040	21±0.7	3	4	3-4	5
	25	Alum	0.76±0.037	28±5.6	1	4	4	2
		Ferrous sulfate (II)	1.493±0.144	13±1.3	2.5	4-5	4	6
	50	Alum	0.89±0.065	28.5±0.8	2.5	4-5	4-5	5
		Ferrous sulfate (II)	4.08± 0.167	13±0.4	3.5	4-5	4	7
	75	Alum	0.99±0.065	15±0.5	3	4	4	2
		Ferrous sulfate (II)	1.74±0.055	19±0.6	3	4-5	3-4	7
	100	Alum	0.80±0.039	19±0.8	1.5	4	4	3
		Ferrous sulfate (II)	0.71±0.051	23±2.2	2	4-5	4	7
	150	Alum	0.70±0.034	21±1.1	1.5	4	3-4	4
		Ferrous sulfate (II)	0.67±0.065	22±1.9	2	4	3	6
Thermofixation	0	Alum	0.44±0.010	43±2	1	3-4	3	2
		Ferrous sulfate (II)	0.84±0.051	43±1.4	2.5	4	3	4
	25	Alum	0.62±0.013	14±2	1.5	4-5	4-5	2
		Ferrous sulfate (II)	1.42±0.082	34±0.7	1.5	4	3	5
	50	Alum	0.87± 0.031	0.20±0.002	2	4-5	4	4
		Ferrous sulfate (II)	3.78± 0.118	11± 0.2	2	3-4	3	6
	75	Alum	0.62±0.060	12±2	2.5	4	4	3
		Ferrous sulfate (II)	1.50±0.035	23±0.3	2.5	4	3-4	5
	100	Alum	0.44 ±0.050	27±3	1	4-5	3	2
		Ferrous sulfate (II)	0.59±0.050	31±2	1.5	4	3-4	6
	150	Alum	0.31±0.021	35±2.3	1.5	3-4	3	2
		Ferrous sulfate (II)	0.39±0.035	42±3.2	2	3-4	3-4	5

humectant agent. Indeed, urea can create a eutectic mixture with water. The increase of the urea amount enhanced the swelling of cotton fibers, especially during steaming fixation and so increased the dye solubility. Moreover, using a urea concentration between 50 and 75 g kg^{-1}, the highest color strength and consequently the lowest penetration percentage values are reached with both ferrous sulfate and alum, for the two methods of fixation. After that, a decline of color yield can be observed for higher urea concentrations. This can be attributed to the difficult spreading of paste due to the hygroscopic behavior of urea, making slower the solubility of the whole paste. So, this may make the diffusion of dye molecules more difficult.

Best washing fastness results (Table 4) are also noted for this interval of urea concentration regardless of the fixation process or the mordant type used. However, the influence of these parameters on rubbing fastness is not clear. For light fastness results, an significant influence of mordants can be noticed. With ferrous sulfate, light fastness reached higher performances.

Effect on the tensile strength of printed fabrics

A comparison of the tensile strength values of fabrics printed with *C. olitorius* L. in both warp and weft directions according to the variation of the urea amount is shown in Figure 8. The fabric degradation through the warp direction is not important, except for the urea quantity of 150 g kg^{-1}. This urea amount underlines fabric degradation in the case of alum with a percentage of 17% for the steaming method and 24% for the thermofixation method. However, the fabric degradation through the weft direction is extremely important. For 75 g kg^{-1} of urea, the tensile strength of cotton fabric printed with ferrous sulfate and using the steaming method decreased by a percentage of 35%. Using an amount of urea equal to 100 g kg^{-1} and in the presence of alum as a mordant, the fabric degradation reached 38 and 22% for the steaming and thermofixation methods, respectively. It also reached 17% for ferrous sulfate in the case of the thermofixation method.

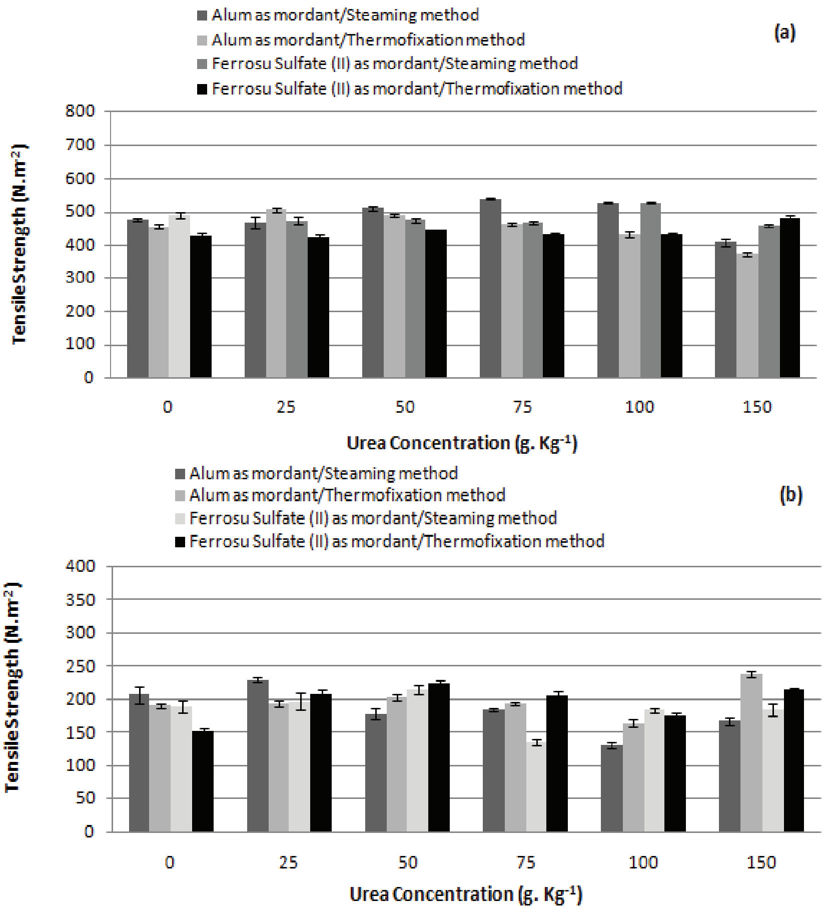

Figure 8. Effect of the urea concentration on fabric tensile strength: (a) warp direction; (b) weft direction.

CONCLUSION

In this study, the potential application of a new natural dye *Corchorus olitorius* L. leaves in the screen printing process of cotton fabrics was investigated in order to solve ecological and toxicological problems related to some of synthetic dyestuffs. For this aim, thickener type, dye and urea concentration, mordant type and fixation method were varied and studied.

Printing results showed a big dependency on the thickener type, the dye and urea concentrations. Among all the tested greener thickeners, carboxymethyl cellulose exhibited generally better results in terms of color strength, penetration percentage, fastness properties and mechanical properties.

The most stable prepared printing paste leading to the best apparent viscosity was obtained with sodium alginate. According to the obtained color strength values, 20 g kg^{-1} of dye and 50 g kg^{-1} of urea was selected as the optimum concentration of printing paste.

Results also showed that the samples printed and fixed by steaming method gave higher color strength. Fastness properties of samples printed have been good. A remarkable light fastness can reach the order of 7 for some conditions, especially with ferrous sulfate.

All theses discussed, using the new proposed natural dye, were confirmed on a semi-industrial scale.

REFERENCES

[1] A.D. Broadbent, Basic principles of textile coloration, Society of dyers and colorists, Bradford, 2001, pp. 493-526

[2] L.W.C. Miles, Textile printing, Society of dyers and colorists, Bradford, 2003

[3] K.T. Chung, S.E. Stevens, Jr., Environ. Toxicol. Chem. 12 (1993) 2121-2132

[4] A.K. Yadav, C.K. Jain, D.S. Malik, Sustain. Environ. Res. 3 (2014) 95-102

[5] W. Miled, S. Roudesli, A. Haj Said, J. Text. Apparel. Technol. Manage. 6 (2010)1-6

[6] F.M.D. Chequer, G.A. Rodrigues de Oliveira, E.R.A. Ferraz, J.C. Cardoso, M.V.B. Zanoni, D. Palma de Oliveira, In Eco-friendly textile dyeing and finishing, M.Gunay (Ed.), Intech Open, London, 2013, pp.151-176

[7] E. Ozturk, H. Koseoglu, M. Karaboyacı, N.O. Yigit, U. Yetis, M. Kitis, J. Clean. Prod. 130 (2016) 92-102

[8] E. Ozturk, U. Yetis, F.B. Dilek, G.N. Demirer, J. Clean. Prod. 17 (2009) 239-247

[9] F. Ferrero, M. Periolatto, G. Rovero, M. Giansetti, J. Clean. Prod.19 (2011) 1377-1384

[10] N. Meksi, M. Ben Ticha, M. Kechida, M.F. Mhenni, J. Clean. Prod. 24 (2012)149-158

[11] M. Ben Ticha, N. Meksi, N. Drira, M. F. Mhenni, Chem. Ind. Chem. Eng. Q. 20 (2014) 463-470

[12] M. Ben Ticha, N. Meksi, N. Drira, M. F.Mhenni, Res. J. Text. Apparel 19 (2015)16-25

[13] M. Ben Ticha, W. Haddar, N. Meksi, A. Guesmi, M.F. Mhenni, Carbohydr. Polym. 154 (2016) 287-295

[14] F. Bouatay, N. Meksi, F. Slah, M.F. Mhenni, J. Text. Sci. Eng. 4 (2014)

[15] F. Bouatay, N. Meksi, S. Adeel, F. Salah, F. Mhenni, J. Nat. Fibers 13 (2016) 423-436

[16] D. Grandjean, S. Karelle, BE Pat. 1011895 A3 (2000)

[17] G.A. Montero, C.B. Smith, W.A. Hendrix, D.L. Butcher, Ind. Eng. Chem. Res. 39 (2000) 4806-4812

[18] N. Meksi, A. Moussa, J. Clean. Prod.161 (2017) 105-126

[19] V. Tiwari, P.S. Vankar, Colourage. 48 (2001) 25-28

[20] T. Bechtold, A. Turcanu, J. Clean. Prod. 17 (2009) 1669-1679

[21] T. Bechtold, A. Turcanu, E. Ganglberger, S. Geissler, J. Clean. Prod.11 (2003) 499-509

[22] J.J. Long, H.M. Xu, C.L. Cui, X.C. Wei, F. Chen, A.K. Cheng, J. Clean. Prod. 65 (2014) 574-582

[23] Centexbel, Textile dyeing in ionic liquids, Textile dyeing in ionic liquids, http://www.centexbel.be/projects/textile-dyeing-in-ionic-liquids. 2012 (accessed 7 June 2012)

[24] T. Agnhage, A. Perwuelz, N. Behary, J. Clean. Prod. 70 (2017) 61-67

[25] M. Shahid, S. Ul-Islam, F. Mohammad, J. Clean. Prod. 53 (2013) 310-331

[26] M. Kamel, R.M. El-Shishtawy, B.M. Youssef, H. Mashaly, Dyes Pigm. 73 (2005) 103-110

[27] M. Montazer, M. Parvinzadeh, Fiber. Polym. 8 (2007) 181-185

[28] P.S. Vankar, S. Rakhi, W. Samudrika, Pigm. Resin. Technol. 38 (2009) 242-247

[29] H. Gouila, N. Meksi, W. Haddar, M.F. Mhenni, H.B. Jannet, Ind. Crop. Prod. 35 (2012) 31-36

[30] W. Haddar, N. Baaka, N. Meksi, M. Ben Ticha, A. Guesmi, M.F. Mhenni, Fiber. Polym. 16 (2015) 1506-1511

[31] W. Haddar, M. Ben Ticha, N. Meksi, A. Guesmi, Nat. Prod. Res. 32 (2018) 141-148

[32] M. Ben Ticha, N. Meksi, H.E. Attia, W. Haddar, A. Guesmi, H. Ben Jannet, M. F. Mhenni, Dyes. Pigm. 141 (2017) 103-111

[33] M. Rekaby, A.A. Salem, S.H. Nassar, J. Text. Inst. 100 (2009) 486-495

[34] D. Maamoun, H. Osman, S.H. Naasar, J. Int. Environ. App. Sci. 9 (2014) 90-99

[35] A.T. Özguney, P. Seçim, A. Demir, T. Gulumser, E.Özdogan, Text. Confect. 25 (2015) 166-171

[36] S. Babel, R. Gupta, J. Textile. Sci. Eng. 6 (2016) 230

[37] A. Ragheb, S. Tawfik, J.I. Abd -El Thalouth, M.M. Mosaad, Int. J. Phar. Sci. Res. 919 (2017) 611-620

[38] J.I. Abd -El Thalouth. J. Am. Sci. 7 (2011) 623-640

[39] S.N. Chattopadhayay, N.C. Pan, J. Nat. Fibers 16 (2019) 1077-1088

[40] O.A. Hakeim, A. Abou-Okeil, L.A.W. Abdob, A. Waly, J. App. Polym. Sci. 97 (2005) 559-563

[41] M.D. Teli, J. Sheikh, P. Shastrakar, J. Text. 2013, Article ID 320510

[42] A.A. Hebeish, A.A. Shahin, M. Rekaby, A.A. Ragheb, Egypt. J. Chem. 58 (2015) 659-670

[43] A.A. Hebeish, A.A. Ragheb, S.H. Nassar, E.E. Allam, J.I. A. El Thalouth, J. App. Polym. Sci. 102 (2006) 338-347

[44] H.M. El-Hennawy, K.A. Ahmed, I. Abd-El Thalouth, Ind. J. Fibre Text. 37 (2012) 145-249

[45] S. İlhan, F. Savaroglu, F. Çolak, J. Ethnopharmacol. 89 (2007) 55-59

[46] M. Loumerem, A. Alercia, Genet. Resour. Crop. Evol. 63 (2016) 1103-1111

[47] K. Mibei, N.K. Ojijon, S.M. Karanja, J.K. Kinyua, Annals: Food. Sci. Tech. 1 (2012) 37-42

[48] P. Kubelka, J. Opt. Soc. Am. 38 (1948) 448-457

[49] P. Kubelka, J. Opt. Soc. Am. 44 (1954) 330-334

[50] A.N. Derbyshire, W.N. Marshall, J. Soc. Dyers. Col. 96 (1980) 166-167

[51] E.P.A. Kumbasar, M. Bide, Dyes. Pigm. 47 (2000)189--199

[52] D.O. Çatal, A.T. Özguney, E.P.A. Kumbasar, Text. Confect. 22 (2012) 309-316

[53] L. Wang, F. Zhu, J. Shao, Q. Yang, D. Lu, Cellulose 20 (2013) 2125-2135

[54] A.D. Broadbent, Basic principles of textile coloration, Society of dyers and colorists, Bradford, 2001, pp. 533--536

[55] A.D. Broadbent, Basic principles of textile coloration, Society of dyers and colorists, Bradford, 2001, pp. 565--568

[56] S. E. A. Nahed, Y.A. Youssef, R.M. El-Shishtawy, A.A. Mousa, Color. Technol. 122 (2006) 324-32

[57] E.K. Hwang, Y.H. Lee, H.D. Kim, Fiber. Polym. 9 (2008) 334-340

[58] E.M.R. El-Zairy, Autex Res. J. 11 (2011) 66-70

[59] M.G. Uddin, J. Text. 10 (2014) 1-8

[60] C.W.M. Yuen, S.K.A. Ku, P.S. Choi, C.W. Kan, Fiber. Polym. 5 (2004) 117-121.

AMAL BEN FADHEL[1]
WAFA MILED[2,3]
WAFA HADDAR[1,3]
NIZAR MEKSI[1,4]

[1]University of Monastir, Faculty of Sciences of Monastir, Research Unit of Applied Chemistry and Environment, Monastir, Tunisia
[2]University of Monastir, Textile Engineering Laboratory, Higher Institute of Technological Studies of Ksar Hellal, Ksar Hellal, Tunisia
[3]University of Taif, University college of Turabah, Fashion design and textile department, Taif, Saudi Arabia
[4]University of Monastir, National Engineering School of Monastir, Textile Engineering Department, Monastir, Tunisia

NAUČNI RAD

ČIST PROCES ŠTAMPANJA PAMUKA PRIRODNIM BOJIMA: UTICAJ KOMPONENTA PASTE NA PERFORMANSE ŠTAMPE

Nova prirodna boja dobijena iz Corchorus olitorius L. korišćena je u pripremi štamparskih pasta za sitoštampu pamučnih tkanina. Da bi se obezbedilo ekološko štampanje, korišćena su" zelenija" sredstva za zgušnjavanje, kao što su: natrijum-alginat, karboksimetil celuloza i brašno Ceratonia silikua L. Istražena je priroda i koncentracija zgušnjivača, koncentracije bojila i uree, tip močila i način fiksiranja. Kvalitet štampanog pamučnog platna ocenjen je određivanjem različitih parametara: jačine boje, procenta prodiranja, brzine štampe i mehaničkih svojstava, dok je kvalitet paste za štampu ocenjen merenjem njene prividne viskoznosti. Veća koncentracija boje koja se koristi u štamparskoj pasti dovela je do bolje prividne viskoznosti i jačine boje. Povećanje koncentracije uree poboljšalo je jačinu boje, ali smanjilo prividnu viskoznost štamparske paste. Najbolji rezultati viskoznosti (1347 mPa s) i čvrstoće boje (4,90) dobijeni su upotrebom gvožđe(II)-sulfata kao močila i natrijum-alginata kao zgušnjivača. Dobijene nijanse boja varirale su od zelene do smeđe. Postignuta je dobra postojanost boja, ali je to zavisilo od primenjenih eksperimentalnih uslova.

Ključne reči: prirodne boje, čistiji postupak štampe, pamučne tkanine, komponente paste, efekat komponenata, kvalitet štampe.

CI&CEQ
Chemical Industry & Chemical Engineering Quarterly
Available on line at
Association of the Chemical Engineers of Serbia *AChE*
www.ache.org.rs/CICEQ
Chem. Ind. Chem. Eng. Q. 27 (1) 15–20 (2021) CI&CEQ

EXPERIMENTAL HEAT TRANSFER STUDIES ON COPPER NANOFLUIDS IN A PLATE HEAT EXCHANGER

SRINIVASAN PERIASAMY MANIKANDAN[1]
RAJOO BASKAR[2]

[1]Department of Chemical Engineering, Kongu Engineering College, Erode, India
[2]Department of Food Technology, Kongu Engineering College, Erode, India

SCIENTIFIC PAPER

UDC 536.2:546.56:544:66

Article Highlights

- Copper/ethylene glycol/propylene glycol/water mixed nanofluids were prepared
- The heat transfer performance of the copper suspended base fluid was studied
- Obtained Nusselt number was compared with base fluids at different temperatures
- Effect of copper nanoparticle concentration on the heat transfer coefficient was also studied

Abstract

The objective of the present work is to study the influence of copper nanoparticle concentration on heat transfer performance of a mixed base fluid. In the present study, the performance of copper nanoparticles in ethylene glycol (eg) + propylene glycol (pg) + water (W) base fluid was analyzed in the chevron-type plate heat exchanger. The sol-gel method was used to prepare copper nanoparticles (100 nm), dispersed in two different mixed base fluids of volume fractions 5%EG + 5%PG + 90%W and 15%EG + 5%PG + 80%W. Experiments were performed by varying the nanoparticle concentration from 0.2 to 1.0 vol.%. Three different hot fluid inlet temperatures were used (55, 65 and 75 °C). It is revealed from the study that the rate of heat transfer increased significantly with the mixed base fluid. Result shows that at 75 °C, 9 and 14.9% enhancement in the Nusselt number is obtained for 5%EG + 5%PG + 90%W and 15%EG + 5%PG + 80%W base fluid, respectively, for the nanoparticle concentration of 1%.

Keywords: heat transfer, nanofluid, plate heat exchanger.

Improvement in the rate of heat transfer in industrial processes may save energy consumption and utilization significantly. From the energy point of view, it is important to reduce the energy consumption by modifying the production method or upgrading the equipment used for the above purpose. The development of miniaturized technology, mini- and micro-components, has been introduced as one of the heat transfer enhancement techniques. Shell and tube heat exchangers are used in many process industries. The plate heat exchanger is an alternative heat exchanger for shell and tube exchangers and is used even at a moderate temperature and pressure. Plate heat exchangers are used in the diary, food and process industries. The advantages of plate heat exchangers include their higher efficiency, compactness and lower weight when compared to conventional heat exchangers of the same capacity.

Over the years, several studies focusing on heat transfer enhancements using nanoparticles have been published. For instance, Lee *et al.* [1] and Das *et al.* [2] measured thermal conductivity of Al_2O_3 and CuO nanoparticles suspended in ethylene glycol and water (EG/W) using a transient hot wire method. They found that a 4% volume concentration of CuO nanoparticles increased the thermal conductivity by 20%. They determined that thermal conductivity increased linearly with volume concentration.

Similar studies conducted by Eastman *et al.* [3] show the enhancement of thermal conductivity up to 41% with copper nanoparticles. The experiments performed with less than 100 nm of copper nanoparticles by Li and Xuan [4,5] gave a larger heat transfer coef-

---

Correspondence: S.P. Manikandan, Department of Chemical Engineering, Kongu Engineering College, Erode-638 060, India.
E-mail: sriperiasamy@gmail.com
Paper received: 20 December, 2019
Paper revised: 31 May, 2020
Paper accepted: 5 June, 2020

https://doi.org/10.2298/CICEQ191220020P

ficient than that calculated from the experimental data. Garg *et al.* [6] reported that thermal conductivity of larger size copper nanoparticle dispersed nanofluids showed moderate increase in thermal conductivity with increasing of the copper nanoparticle concentration. They have used 200 nm copper nanoparticles. Li *et al.* [7] investigated convective heat transfer and flow characteristics of copper-water nanofluid and observed considerable improvement in rate of heat transfer. In the last few decades, large number of investigations were reported which mainly focused on the preparation, characterization and measurement of thermo-physical properties of nanofluids and were summarized by Ghadimi *et al.* [8]. Researchers widely employed EG and its aqueous mixtures as base fluids for nanofluids and research showed that the heat transfer performances of these nanofluids are significantly higher than those of base EG and EG/W [9-12]. Only a few heat transfer studies have been reported on EG based CuO nanofluids, even though copper has higher thermal conductivity. Also, the works with respect to mixed base fluids is lacking in the literature.

The main objective of this present study is to investigate the heat transfer performance in the plate heat exchanger by suspending copper nanoparticles in the two different mixed base fluids of volume fractions with 5%EG + 5%PG + 90%W and 15%EG + 5%PG + 80%W. The result obtained from the experimental studies is compared with the McCabe and Kim model selected from literature.

MATERIALS AND METHODS

Experimental setup

The plate heat exchanger consists of corrugated plates assembled into a frame. The hot fluid flows in one direction in alternating chambers while the cold fluid flows in true counter-current flow in the other alternating chambers [13].

The schematic diagram and photographic view of the experimental setup (plate heat exchanger) of the present study is shown in Figure 1.

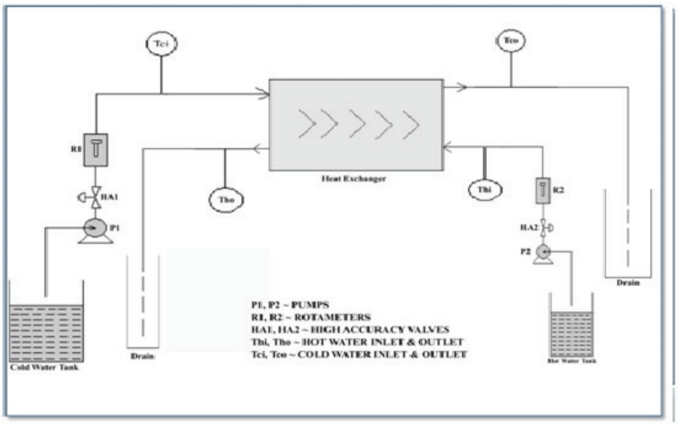

(a) Schematic diagram

(b) Photographic view

Figure 1. Schematic diagram and photographic view of the experimental setup.

The experimental setup consists of a cold fluid container with a temperature controller, a hot fluid container with a temperature controller, two flow meters for controlling hot and cold fluid flows, two pumps along with the corrugated plate heat exchanger. The cold fluid was pumped into the chevron PHE, passing through a rotameter, and returned to the reservoir. Hot water used as a hot fluid passes through a control valve and a rotameter and then enters the PHE in a counter flow direction. The flow rate was monitored and controlled by the flow meters [14,15]. The inlet and outlet temperatures of the fluid were measured by four K-type thermocouples inserted additionally within the PHE. The PHE provided by Alfa Laval consists of 13 stainless-steel corrugated plates, creating 7 flow channels for the hot fluid and 6 flow channels for the cold fluid. The corrugation angle is 60°, which is the angle between the corrugation and the axis parallel to the plate length. The plate length is 0.154 m and the thickness of the plate is 0.25 mm.

Nanofluid preparation

Nanofluid is prepared by two step sol-gel method [16]. First the copper nanoparticle is prepared then dissolved in two different mixed base fluids of volume fractions of 15%EG + 5%PG + 80%W, and 5%EG + 5%PG + 90%W and used in the PHE as cold fluid. The SEM image of prepared copper nanoparticle is shown in Figure 2.

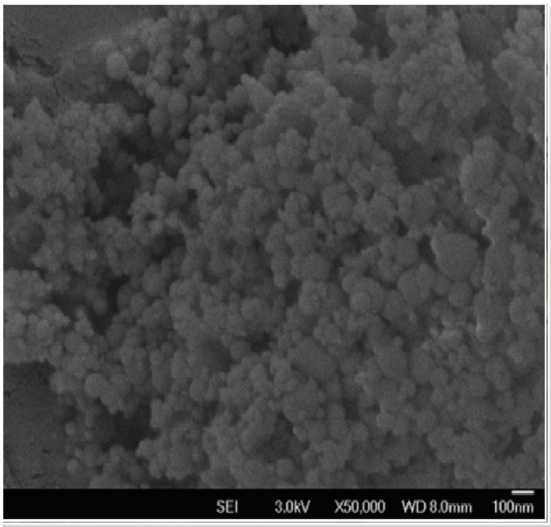

Figure 2. SEM image of copper nanoparticles.

Formulas used in heat transfer studies

Determination of experimental Nusselt number. Eqs. (1)-(6) are used to evaluate the Nusselt number of the nanofluid experimentally:

$$\frac{1}{U}=\frac{1}{h_{hot}}+\frac{\Delta x}{k_m}+\frac{1}{h_{nano}} \tag{1}$$

$$U=\frac{Q}{A\Delta TLMTD} \tag{2}$$

$$Q=mc_{pnf}(T_{c,out}-T_{c,in}) \tag{3}$$

$$A=NLW \tag{4}$$

$$\Delta TLMTD=\frac{\left(T_{hot,in}-T_{cold,in}\right)-\left(T_{hot,out}-T_{cold,out}\right))}{\ln(\frac{T_{hot,in}-T_{cold,in}}{T_{hot,out}-T_{cold,out}})} \tag{5}$$

$$Nu=\frac{h_{nano}D_H}{K_{nano}} \tag{6}$$

For all the calculations, the fluid properties such as thermal conductivity, viscosity, density, specific heat capacity, as well as the Reynolds number and Prandtl number, are evaluated at bulk mean temperatures of hot and cold fluids [17-20].

Determination of Nusselt number using models. Eqs. (7) and (8) are used to evaluate the Nusselt number of the nanofluid using the McCabe model [13] and the Kim model [21], respectively.

$$Nu=0.37\left(N\mathrm{Re}\right)^{0.67}\left(N\mathrm{Pr}\right)^{0.33} \tag{7}$$

$$Nu=0.295\left(N\mathrm{Re}\right)^{0.64}\left(N\mathrm{Pr}\right)^{0.32\left(\left(\frac{\Pi}{2}-\beta\right)\right)} \tag{8}$$

RESULTS AND DISCUSSION

Effect of copper nanoparticle concentration on Nusselt number of mixed base fluid of 5% EG + 5% PG + 90%W at different hot fluid temperatures

The Nusselt number is the significant factor in evaluating heat transfer performance of nanofluids. In order to study the heat transfer performance of the copper nanoparticle, the Nusselt number was determined by observing the effect of nanoparticle volume fraction (0.2, 0.4, 0.6, 0.8 and 1.0%), hot fluid inlet temperature (55, 65 and 75 °C) for the proposed base fluid concentrations and the results are presented in Figures 3-5. The obtained experimental Nusselt number enhancement results were validated with theoretical models proposed by Mc Cabe *et al.* and Kim *et al.* The experiments were repeated by arbitrarily selecting nanoparticle concentration to ensure reproducibility of the results and observed that the deviation is negligible.

From Figure 3, it is observed that the Nusselt number increases significantly at a hot fluid inlet temperature of 55 °C, with the increase in nanoparticle concentration. The percentage increases of the Nusselt number are 4, 5.2, 6, 6.5 and 7 for the hot fluid inlet temperatures of 55 °C at the nanofluid concentrations of 0.2, 0.4, 0.6, 0.8 and 1.0 vol.%, respectively. This may be due to the thermal conductivity enhancement with increasing volume concentration [22,23].

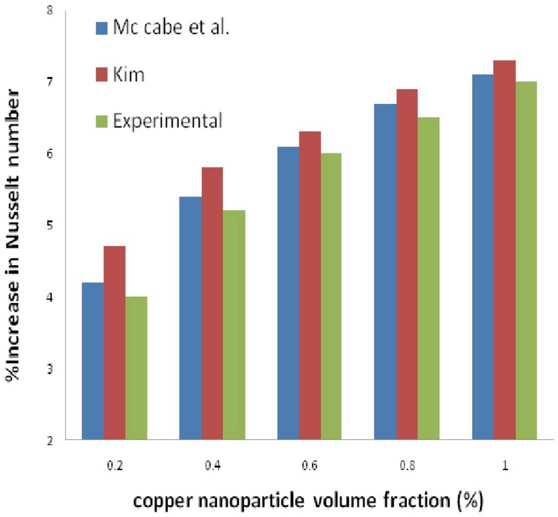

Figure 3. Effect of copper nanoparticle concentration on Nusselt number enhancement for a mixed base fluid of 5% EG + 5% PG + 90% W at a hot fluid inlet temperature of 55 °C.

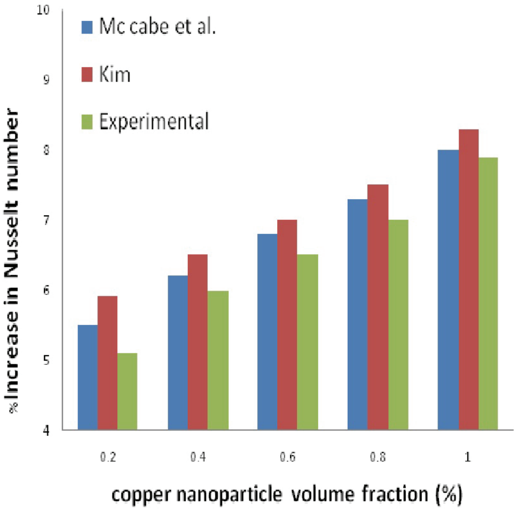

Figure 4. Effect of copper nanoparticle concentration on Nusselt number enhancement for a mixed base fluid of 5% EG + 5% PG + 90% W at a hot fluid inlet temperature of 65 °C.

It is evidenced from Figure 4 that, at the variation of hot fluid inlet temperature at 65 °C, the base fluid exhibits linear increase in the Nusselt number with increasing concentration and temperature.

The effect of copper nanoparticle addition on further increase in the hot fluid inlet temperature to 75 °C is reported in Figure 5. It was noted that the Nusselt number increases further with increasing temperature and nanoparticle concentration and maximum Nusselt number enhancement of 9.0% was observed at 1.0 vol.% of nanoparticle concentration. Enhancement in the Nusselt number is due to the inclusion of high thermal conductivity copper nanoparticle.

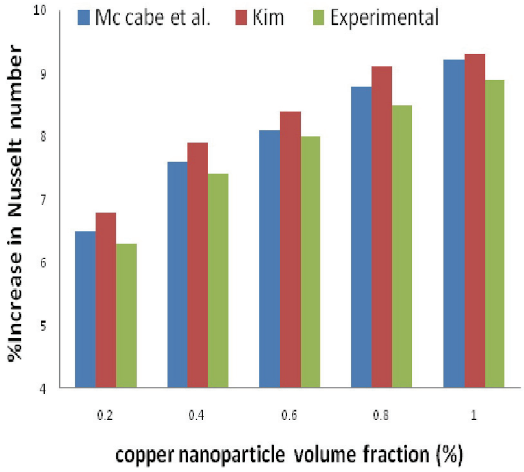

Figure 5. Effect of copper nanoparticle concentration on Nusselt number enhancement for a mixed base fluid of 5% EG + 5% PG + 90% W at a hot fluid inlet temperature of 75 °C.

Effect of copper nanoparticle concentration on the Nusselt number of mixed base fluid of 15% EG + 5% PG + 80%W at different hot fluid temperatures

Figures 6-8 show the effect of copper nanoparticle on the Nusselt number for a base fluid of 15%EG + 5%PG + 80%W at a hot fluid inlet temperature of 55, 65 and 75 °C, respectively.

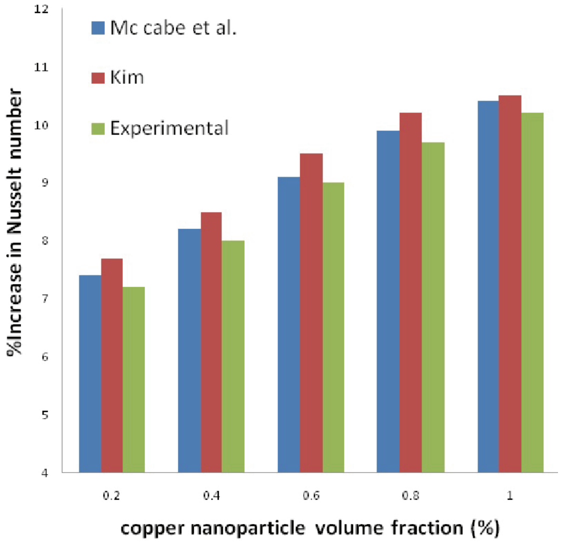

Figure 6. Effect of copper nanoparticle concentration on Nusselt number enhancement for a mixed base fluid of 15% EG + 5% PG + 80% W at a hot fluid inlet temperature of 55 °C.

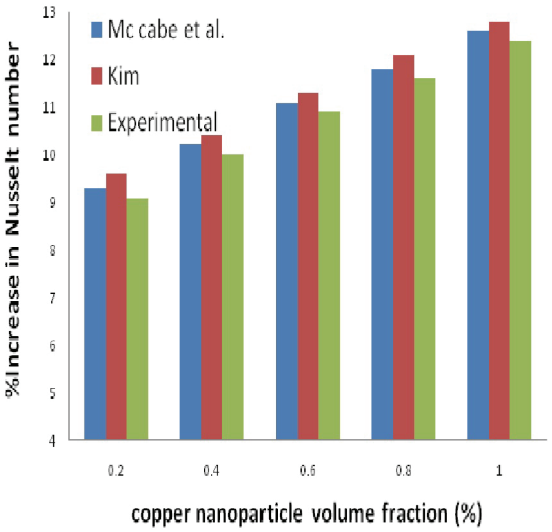

Figure 7. Effect of copper nanoparticle concentration on Nusselt number enhancement for a mixed base fluid of 15% EG + 5% PG + 80% W at a hot fluid inlet temperature of 65 °C.

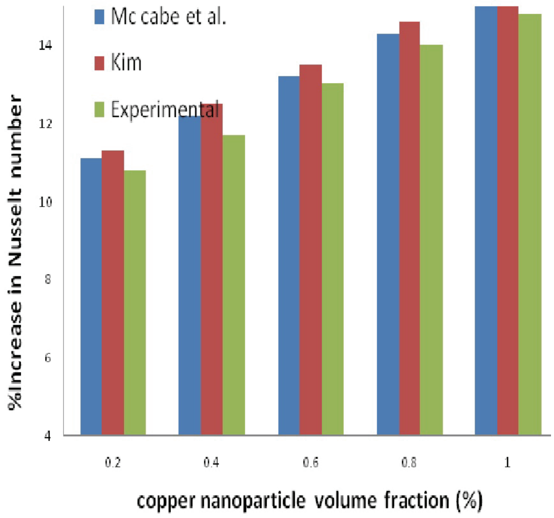

Figure 8. Effect of copper nanoparticle concentration on Nusselt number enhancement for a mixed base fluid of 15% EG + 5% PG + 80% W at a hot fluid inlet temperature of 75 °C.

From Figures 6-8, the similar trend of effect is observed, *i.e.*, increasing the nanoparticle concentration increases the Nusselt number and a 10.2, 12.4 and 14.9% increase in the Nusselt number for the nanoparticle concentration of 1.0 vol.% and hot fluid inlet temperatures of 55, 65 and 75 °C, respectively, is observed. There is good agreement between the results calculated from these experimental values and the correlation. It was noticed that the calculated Nusselt number falls within ±6% deviation with experimental results for 5%EG + 5%PG + 90%W nanofluids and ±8% deviation for 15%EG + 5%PG + 80%W nanofluids. Hence, there exists better agreement between the correlation results and experimental results, which shows the accuracy of the results of the experiment.

CONCLUSION

The present study focused on the benefits of using copper nanoparticles in a plate heat exchanger. The following were the conclusions that were drawn from heat transfer studies of a mixed base fluid by adding copper nanoparticle:

i. 1.0 vol.% of copper nanoparticle has increased the Nusselt number by 9% and 14.9% for the base fluid 5%EG + 5%PG + 90%W and 15%EG + 5%PG + 80%W, respectively.

ii. Among the three operating temperatures selected, the Nusselt number enhancement was high at a hot fluid inlet temperature of 75 °C.

iii. The experimental result of the Nusselt number was validated with McCabe *et al.* and Kim *et al.* models. A good agreement between the measured values with selected models at all mixed base fluid concentrations was obtained.

iv. The employed mixed base fluid could be easily recovered and reused for the process. Hence, the mixed base fluid can be used as an energy efficient heat transfer fluid.

Nomenclature

U	Overall heat transfer coefficient, W/m^{2}K
h	Convective heat transfer coefficient, W/m^{2}K
Cp	Specific heat capacity, J/(kg K)
Q	Heat flux, W/m^2
A	Heat transfer area, m^2
$LMTD$	Logarithmic Mean Temperature Difference
m	Mass of fluid, kg
T	Temperature, K
N	Number of channels, dimensionless
L	Plate width, m
Re	Reynolds number, dimensionless
Pr	Prandtl number, dimensionless
D_H	Hydraulic radius, m

Greek symbols

κ	Thermal conductivity, W/(m K)
μ	Viscosity, Pa s
ρ	Density, kg/m^3
β	Corrugation angle

Subscripts

nano	Nanofluid
p	Particle
in	Inlet
out	Outlet
cold	Cold fluid

hot	Hot fluid

Acknowledgment

The authors thank the management of Kongu Engineering College for utilizing and carrying out the research work in the laboratory.

REFERENCES

[1] S.U.S. Choi, S. Lee, S. Li, J.A. Eastman, J. Heat Transfer 121 (1999) 280-289

[2] S.K. Das, N. Putra, P. Thiesen, W. Roetzel, J. Heat Transfer 125 (2003) 567-574

[3] J.A. Eastman, S.U.S. Choi, S. Li, W. Yu, L.J. Thompson, App. Phys. Lett. 78 (2001) 718-720

[4] Y. Xuan, Q. Li, Int. J. Heat Fluid Flow 21 (2000) 58-64

[5] Y. Xuan, Q. Li, J. Heat Transfer 125 (2003) 151-155

[6] J. Garg, B. Poudel, M. Chiemsa, J.B. Gordan, J.J. Ma, J.B. Wang, J. App. Phys. 103 (2008) 074301-074306

[7] Q. Li, Y. Xuan, Sci. China, Ser. E: Technol. Sci. 45 (2002) 408-416

[8] A. Ghadimi, R. Saidur, H.S.C Metselaar, Int. J. Heat Mass Transfer 54 (2011) 4051-4068

[9] S.M. Sohel Murshed, C.A. Nieto de Castro, Appl. Energy 184 (2016) 681-695

[10] R. Barzegarian, M.K. Moraveji, A. Aloueyan, Exp. Therm. Fluid Sci. 74 (2016) 11-18

[11] D. Huang, Z. Wu, B. Sunden, Exp. Therm. Fluid Sci. 72 (2016) 190-196

[12] J.R. Satti, D.K. Das, D. Ray, Int. J. Heat Mass Transfer 107 (2016) 871- 881

[13] W.L. McCabe, J.C. Smith, P. Harriot, Unit Operations in Chemical Engineering, 7th ed., McGraw-Hill International Edition, New York, 2006

[14] S.P. Manikandan, R. Baskar, Period. Polytech. Chem. Eng. 62 (2018) 317-322

[15] S.P. Manikandan, R. Baskar, Chem. Ind. Chem. Eng. Q. 24 (2018) 309-318

[16] M.S. Liu, M.C. Lin, C.Y. Tsai, C.C. Wang, Int. J. Heat Mass Transfer 49 (2006) 3028-3033

[17] Y. Xuan, W. Roetzel, Int. J. Heat Mass Transfer 43 (2000) 3701-3707

[18] R.S. Vajjha, D.K. Das, B.M. Mahagaonkar, Petrol. Sci. Technol. 27 (2009) 612-624

[19] J. Koo, C. Kleinstreuer, J. Nanoparticle Res. 6 (2004) 577-588

[20] B.C. Sahoo, R.S. Vajjha, R. Ganguli, G.A. Chukwu, D.K. Das, Petrol. Sci. Technol. 27 (2009) 1757-1770

[21] D. Kim, Y.H. Kwon, C.G. Li, J.K. Lee, D.S. Hong, J.G. Lee, S.H. Kim, J. Nanosci. Nanotechnol. 11 (2011) 5769--5774

[22] H.E. Patel, T. Sundararajan, S.K. Das, J. Nanopart. Res. 12 (2010) 1015-1031

[23] W. Yu, H. Xie, I. Chen, Y. Li, Powder Technol. 197 (2010) 218-221.

SRINIVASAN PERIASAMY MANIKANDAN[1]
RAJOO BASKAR[2]

[1]Department of Chemical Engineering, Kongu Engineering College, Erode, India
[2]Department of Food Technology, Kongu Engineering College, Erode, India

NAUČNI RAD

EKSPERIMENTALNO PROUČAVANJE PRENOSA TOPLOTE U NANOFLUIDIMA NA BAZI BAKRA U PLOČASTOM RAZMENJIVAČU TOPLOTE

Cilj ovog rada je proučavanje uticaja koncentracije nanočestica bakra na performanse prenosa toplote u smešama osnovnih tečnosti: etilen glikol (EG), propilen glikol (PG) + voda (V), u pločastom razmenjivaču toplote tipa ševron. Za pripremu nanočestica (100 nm) korišćena je sol-gel metoda; one su dispergovane u dve različite mešavine osnovnih tečnosti (vol. %): a) 5% EG + 5% PG + 90% V i b) 15% EG + 5% PG + 80% V. Eksperimenti su izvedeni promenom koncentracije nanočestica u opsegu 0,2-1,0 vol.%. Korišćene su tri različite ulazne temperature tečnosti (55, 65 i 75 °C). Utvrđeno je da se brzina prenosa toplote u smeši osnovnih tečnosti znatno povećava. Rezultat pokazuje da se na 75 °C postiže 9%, odnosno 14,9% poboljšanje Nuseltovog broja za smešu 5% EG, 5% PG i 90% V, odnosno 15% EG, 5% PG i 80% V, pri koncentraciji nanočestica od 1%.

Ključne reči: prenos toplote, nanofluid, pločasti razmenjivač toplote.

CI&CEQ
Chemical Industry & Chemical Engineering Quarterly

Available on line at
Association of the Chemical Engineers of Serbia *AChE*
www.ache.org.rs/CICEQ

Chem. Ind. Chem. Eng. Q. 27 (1) 21–34 (2021) CI&CEQ

DRAGANA BOŽIĆ[1]
MILAN GORGIEVSKI[2]
VELIZAR STANKOVIĆ[2]
MILORAD CAKIĆ[3]
SILVANA DIMITRIJEVIĆ[1]
VESNA CONIĆ[1]

[1]Mining and Metallurgy Institute Bor, Bor, Serbia
[2]University of Belgrade, Technical Faculty in Bor, Bor, Serbia
[3]University of Niš, Faculty of Technology in Leskovac, Leskovac, Serbia

SCIENTIFIC PAPER

UDC 66.081.3:544.723:546.815

BIOSORPTION OF LEAD IONS FROM AQUEOUS SOLUTIONS BY BEECH SAWDUST AND WHEAT STRAW

Article Highlights

- Beech sawdust and wheat straw can be successfully used for the sorption of lead ions
- During the sorption process the pH changes with time
- Kinetics of metal ions sorption is reasonably fast
- The Temkin isotherm model has shown the best fit with the experimental data
- Maximum sorption capacity for lead ions on the used adsorbents was almost 10 mg g^{-1}

Abstract

This paper presents the results of the Pb^{2+} *adsorption from synthetic* $Pb(NO_3)_2$ *solutions, using the beech sawdust and wheat straw as adsorbents. Physicochemical characterization of the adsorbents included the specific surface area,* pH_{pzc}*, SEM-EDS and FTIR analysis. Adsorption kinetics and isotherms, as well as changes in the pH solution during the process, were monitored and analyzed. The results showed that the adsorption is well explained by the pseudo-second order kinetic model for both adsorbents. Adsorption of the* Pb^{2+} *on sawdust and straw is well described by the Temkin isotherm, which is confirmed by the high values of the regression coefficient* R^2*. The maximum adsorption capacity of lead ions on the beech sawdust and wheat straw was 9.9 and 9.7 mg* g^{-1}*, respectively. The obtained results have indicated that the beech sawdust and wheat straw are suitable adsorbents for the adsorption of lead ions from dilute aqueous solutions.*

Keywords: biosorption, Pb^{2+}*, beech sawdust, wheat straw, adsorption isotherms.*

Discharging the industrial, mining and metallurgical effluents, containing various heavy metal ions into the surface water streams, represents a significant concern for the society and a great threat to the environment due to their toxicity, which could cause severe problems to the organisms living in the waters. As a result of uncontrolled wastewater discharge, the pollution level of the environment has particularly increased during the first half of the 20th century. In order to respond to the pollution of surface and groundwater, the scientists and industry have faced a great challenge to try to improve or even completely replace the industrial processes with new cleaner technologies that have to reduce or completely eliminate the harmful effects of industrial or mining operations on the environment. This particularly took place during the last three decades of the past century and continues until today [1,2]. There are still the industrial and mining areas affecting the environment, less in developed, but much more in developing countries. The main causes of the water pollution by heavy metals are wastewaters from urban areas; water originating from active or abandoned mines; effluents from ferrous and non-ferrous metallurgy [3,4]; waters from the textile and leather processing industry; from electronics; and, especially, from agricultural activities using various phytochemicals, which partly penetrate into the ground by rain, or otherwise fall and remain there for a long time, affecting ground pollution and the underground waters, or rivers and creeks flowing through the agricultural areas [1,5,6].

Heavy metal ions are as a rule toxic and some of them make organo-metallic cancerous substances,

---

Correspondence: D. Božić, Mining and Metallurgy Institute Bor, Zeleni bulevar 35, 19210 Bor, Serbia.
E-mail: dragana.bozic@irmbor.co.rs
Paper received: 13 November, 2019
Paper revised: 21 May, 2020
Paper accepted: 16 June, 2020

https://doi.org/10.2298/CICEQ191113021B

which enter living organisms through the food chain [2]. In this view, the lead ions and their various compounds are particularly harmful in general for the living world. The increased lead level, for example, accumulated in a human body, can cause severe renal and other impairments, such as: hepatitis, anemia, infertility in women, as well as nerve diseases. According to the physico-chemical properties of lead, Pb^{2+} can easily replace Ca^{2+} in calcified tissues (bones and teeth), but can also form a variety of soluble complexes with bioligands in biological fluids and tissues. Plants can also adsorb and accumulate lead, either from ground or water containing lead compounds, into their roots, stalks, fruits or leaves, depending on the plant species [4,8]. Wastewater from the smelters and foundries of lead, glass and ceramic production, lead battery industry, weapon and ammunition industry contain a substantial amount of lead, approximately around 100 ppm or less [3]. In mine waters the lead concentration is usually less than 1 ppm. Elimination of lead from such wastewater prior to its discharge into the environment is a great challenge for researchers working in various disciplines, due to its extremely harmful effect on organisms.

Various methods for heavy metals removal from industrial effluents can be successfully applied today for this purpose. One of the new approaches that can be efficient in the removal of lead ions from wastewater is adsorption - a technique that can eliminate metal ions to very low concentrations [7]. Biosorption is a new direction within adsorption, in which, instead of classical adsorbents, different living materials are used.

Biosorption

The adsorption process of metal ions can take place on various plant materials, and such a phenomenon is named in the relevant literature as biosorption, while the plant material itself is called biosorbent [9,10]. Biosorption is a process for heavy metal ions removal from the wastewater that has induced a great interest of researchers all over the world. Intensive investigations have been carried out using various combinations of biosorbents and heavy metal ions, for now, at a laboratory scale, in order to form a new technological process, integrating the adsorption of metal ions on biomass with its combustion after loading for the green energy production [11,12]. The basic advantage of biosorption, over other methods of wastewater treatment, is that the biosorbents can efficiently purify those industrial solutions having lower concentration of pollutants, reaching the close output concentration, or even lower than the MAC is, for a considered ion [10].

Extensive research has shown that many agricultural by-products, as well as the other waste materials from food or wood industries, can be used as biosorbents for the adsorption of heavy metal ions from wastewater [13,40,41]. Materials that were tested as potentially possible low-cost sorbents were: walnut and nut shell, spent grain, olive stones, peanut skins, onion and orange peels, rice husks, leaves, coffee and tea waste, tree fern and other similar plant waste materials [7].

Special attention has been focused on the lingocellulose biosorbents, such as bark, leaves, or the wooden mass of various trees. Sawdust, which has exhibited a significant potential as biosorbent, has particularly attracted the attention of researchers working in the wastewater purification area [9,10].

Besides sawdust of various sorts of trees, the straw of different crops has also been proved as a potentially effective biosorbent for the adsorption of metal ions from aqueous solutions [14,10]. Straw and sawdust are mainly composed of cellulose, hemicelluloses, lignin, saccharine and other compounds. Straw contains different functional groups, such as hydroxyl-, carboxyl-, sulfhydryl-, amino- and amide--groups, which can be potentially active sites for attracting and bonding of metal ions [15]. Wheat-, rise-, oats- or barley-straw is particularly convenient to be used in such research due to their widespread presence and easy accessibility, as well as for a massive worldwide production.

The main objective of this work is to designate the adsorption ability of beech sawdust and wheat straw towards lead ions, as well as to determine the effect of various parameters on the adsorption process and to get an insight on the adsorption kinetics and mechanism of lead ions attracting to the used biosorbents. The process equilibrium *via* adsorption isotherms will also be considered. Synthetic solutions of different concentration of lead ions will serve as a model system in this study.

EXPERIMENTAL

Materials

Synthetic salt solutions of $Pb(NO_3)_2$ (MERCK), were used for the adsorption of lead ions. The parent solution with a concentration of 0.2 g dm^{-3} having the initial pH value of 5.65.

Wheat straw was collected from the local fields in the vicinity of Bor (Eastern Serbia), while beech sawdust was taken from a local saw mill. A monosized sieve fraction (-1 + 0.4) mm of both biosorbents was used in the adsorption experiments.

Methods

Characterization of the biosorbents

Specific surface area. The specific surface area of beech sawdust and wheat straw of the chosen sieve fraction (-1 + 0.4) mm, was determined by the adsorption method using a solution of methylene blue, as follows in the reference [16]. UV-Vis spectrophotometer (PU 8620 UV/Vis) was used to determine methylene blue concentration.

Point of zero charge (pH_{pzc}). The point of zero charge (pH_{pzc}) is the pH value of solution, where the surface charge density is equal to zero, *i.e.,* at that point the number of positively charged sites is equal to the number of negatively charged sites [17]

SEM and EDS measurements

Morphology of beech sawdust and wheat straw was analyzed, before and after the adsorption of Pb^{2+}, using a scanning electron microscope (JSM IT 300LV JEOL) with an integrated energy-dispersive X-ray detector (X-max SDD 170 mm^2, Oxford Instruments). Both samples of biosorbents before scanning were steamed with a thin layer of gold in a sputter coater (JOEL JFC-1300) making them conductive. The prepared samples were then transferred into a microscope chamber and micro photos were taken at voltage of 20 kV. The EDS analysis was done by recording several points on the surface of samples in order to better detect a heterogeneous distribution of elements.

FTIR

Infrared spectra of the investigated samples were recorded using a Bomem MB-100 (Hartmann & Braun, Canada) FTIR spectrometer, in a range of 4000–400 cm^{-1}, at the resolution of 2 cm^{-1} and with 16 scans. Prior the analysis, the samples were compressed in potassium bromide (KBr) to form tablets. The obtained FTIR spectra were then analyzed using Win Bomem Easy software.

Adsorption of lead ions on the beech sawdust and wheat straw

The adsorption experiments were carried out in laboratory beakers, each equipped with a magnetic stirrer, in order to keep the biosorbent in suspension. Stirring rate was kept constant in all experiments, and was 300 min^{-1}. Prior the adsorption experiments, the biosorbents were washed with 200 cm^3 of distilled water and afterwards dried. Two series of adsorption experiments were carried out to study the adsorption kinetics and adsorption equilibrium.

Synthetic solution of Pb^{2+}, concentration of 0.2 g dm^{-3}, was used as an aqueous phase for the kinetic experiments. Mass of 1 g of previously washed and dried biosorbent (beech sawdust or wheat straw) was brought into contact with 50 cm^3 of synthetic $Pb(NO_3)_2$ solution flora for different contact time. After a certain time, the suspension was filtered and the filtrate was analyzed on the Pb^{2+} content. In parallel with this, the concentration of alkali and alkaline earth metal ions was determined with the aim of trying to describe the mechanism of the adsorption process, as well as to determine the cation exchange capacity.

Concentrations of lead ions, as well as alkali and alkaline earth metal ions, were determined using the atomic absorption spectrophotometer (Perkin--Elmer 403 AAS).

The adsorption capacity of biosorbent q_t is defined as a mass of ions adsorbed on the unit mass of biosorbent, at constant temperature [18,19]. The adsorption capacity, as well as its change with the adsorption time, was determined from the mass balance, according to the following equation:

$$q_t = \frac{c_i - c_t}{m} V \tag{1}$$

where: q_t is the mass of adsorbed metal per unit mass of adsorbent (mg g^{-1}) at time t; c_i and c_t are the initial and actual concentrations of metal ions at time t (mg dm^{-3}); V - volume of treated solution (dm^3); m - mass of adsorbent (g). The adsorption degree (*AD)* is defined as the percentage of adsorbed metal ions, described by the following relationship:

$$AD = 100(1 - c_t / c_i) \tag{2}$$

It represents an ability of how many metal ions can be removed from a solution by a particular biosorbent. *AD* is also an indicator of the adsorbent saturation, as well as the solution depletion, *i.e.*, of the process completion.

During the adsorption, a change of the solution pH value was also monitored with time. All experiments were carried out at the ambient temperature.

A series of experiments was carried out contacting a constant mass of adsorbent (1 g) with the equal volume of solution (0.05 dm^3), which contained different initial concentrations of metal ions in a range from 0.005 to 0.2 g dm^{-3}. The phases were kept in suspension with a magnetic stirrer for a period of 60 min, considering that this contact is long enough to achieve equilibrium between phases [7,20]. Afterwards, the suspension was filtered, and filtrate analyzed for the residual content of lead ions.

Pseudo-first- and pseudo-second order reaction kinetic models

For modeling the adsorption process rate, two kinetic models were tested, *i.e.*, the pseudo-first- and pseudo-second order kinetic model, and compared with the experimental data. The pseudo-first order kinetic model can be expressed by the following differential equation [31]:

$$\frac{\mathrm{d}q_t}{\mathrm{d}t} = k_1\left(q_e - q_t\right) \tag{3}$$

or, in its integral form, as a linear equation in a system with semi-logarithmic coordinates:

$$\log(q_e - q_t) = \log q_e - \frac{k_1}{2.303}t \tag{4}$$

where: q_e - is the adsorption capacity at equilibrium (mg g^{-1}); q_t - is the adsorption capacity at the process time t (mg g^{-1}); k_1 - is the constant rate of the pseudo-first reaction order (min^{-1}); and t - is the process time (min).

The differential equation, describing the pseudo-second reaction order kinetics may be presented as:

$$\frac{\mathrm{d}q_t}{\mathrm{d}t} = k_2\left(q_e - q_t\right)^2 \tag{5}$$

The integral form of Eq. (5) will be:

$$\frac{1}{\left(q_e - q_t\right)} = \frac{1}{q_e} + k_2 t \tag{6}$$

Rearranging Eq. (6) to get it in a linear form, leads to the following equation:

$$\frac{t}{q_t} = \frac{1}{k_2 q_e^{\,2}} + \frac{t}{q_e} \tag{7}$$

where k_2 is the adsorption rate constant for the pseudo-second reaction order (g mg^{-1} min^{-1}).

RESULTS AND DISCUSSION

Physical, chemical and physicochemical characteristics of the biosorbents

The beech sawdust moisture was 8.5%, while the wheat straw was 7.23%, both calculated on the initial biosorbent weight. It can be said that there is no significant moisture difference between the used biosorbents due to their similar way of storage, *i.e.*, both were packed in paper bags and stored in a laboratory chamber under the same humidity.

The fraction of sawdust ash was 2.06%, based on the initial weight of dried sawdust, while the ash fraction from straw was almost three times higher and amounted to 6.2%, calculated on dry straw. Chemical composition of both ashes is shown in Table 1.

Obviously, with the exception of MgO, SiO_2 and MnO content, which are almost equal in both ashes, there is a strong difference in the chemical composition between ashes of these two biosorbents. It can be seen, from Table 1, that the beech sawdust ash has a dominant CaO content, which is approximately three times higher than the one in the wheat straw ash. Unlike the beech sawdust, the wheat straw contained much more alkali metals than the beech sawdust. So, the K_2O content in the wheat straw ash was more than 6 times higher than in the sawdust ash, while Na_2O was about 2.5-3 times higher. Special attention was paid here to the content of alkali and alkaline earth metals in the straw and sawdust, due to their impact, particularly calcium and potassium, on the adsorption process, which will be considered through further text. Physical and physicochemical properties of the considered biosorbents are summarized and presented in Table 2.

Table 2. Physical and physicochemical properties of the biosorbents

Biosorbent property	Beech sawdust	Wheat straw
Specific surface area, m^2 g^{-1}	1.08 [3,7,17]	1.54 [3,7,17]
Moisture, %	8.5	7.23
COD, mg O_2 dm^{-3}	0.8	18
CEC / mmol Me^{z+} g^{-1}	1.45	1.86
Point of the zero charge, pH$_{pzc}$	7.4 [3,7,17]	6.7 [3,7,17]

The content of organic substances in water from straw washing, expressed as a chemical oxygen demand (COD), is about 22.5 times higher than the content of organic substances in water from sawdust washing [17]. It means that the content of soluble organic substances, which could be transferred from the biosorbents into the aqueous phase, is much higher in the case of wheat straw than in the case of

Table 1. Chemical composition (mass%) of beech sawdust and wheat straw ash

Material	Na_2O	K_2O	MgO	CaO	Fe_2O_3	SiO_2	SO_3	Al_2O_3	P_2O_5	TiO_2	MnO	Others
Sawdust	1.51	4.56	3.32	22.39	3.00	34.08	24.7	4.73	1.17	0.18	0.13	0.17
Straw	4.14	28.62	3.25	6.83	0.55	36.36	16.12	0.29	3.0	0.017	0.11	0.173

beech sawdust. This issue must be taken into consideration, in particular how to treat water from washing the wheat straw before its discharging, or to use it as a fertilizer for watering a plantation, for example.

Based on the results shown in Table 2, the total cation exchange capacity (*CEC*), expressed as a sum of alkali and alkaline earth ions, transferred from the solid to the aqueous phase, is slightly higher for the wheat straw.

As shown in Table 2, the corresponding pH_{pzc} values for the wheat straw and beech sawdust are close to each other, and were 6.7 and 7.4, respectively. It means that at pH <6.7 for wheat straw, or <7.4 for beech sawdust, the surface area of the corresponding adsorbent is positively charged, while at pH >6.7 for straw, or >7.4 for sawdust, the surface area of the adsorbent will be negatively charged.

Rinsing of the biosorbents

Rinsing of both sawdust and straw was carried out from two reasons:

- in order to remove physically entrained organic and inorganic dirtiness, as fine particles of the biosorbents and earth;
- in order to get an insight on the amount of alkali and alkaline earth metals that will be leached out from the biosorbents at rinsing, as well as to see whether and how the rinsing itself affects the adsorption capacity of the used biosorbents;

The procedure of the rinsing experiments was described in detail elsewhere [12]. After each portion of distilled water passing through a filter, the filtrate was sampled and analyzed on the content of Na^+, K^+, Ca^{2+} and Mg^{2+}. Prior the analysis, the pH and conductivity values of filtrate were both measured as well.

Adsorption

Change of alkali and alkaline earth metals concentration at rinsing the biosorbents and after the completion adsorption of Pb^{2+}

Contact between a biosorbent and water solution containing adsorbate, has a twofold effect. Alkali and alkaline earth metals from biosorbents will partly be leached out by water, while a portion of them (mainly calcium and magnesium) will take part in the ion exchange process with heavy metal ions present in the solution [10]. To get evidence on the amount of these metals, which will be rinsed from biosorbents and how much will be replaced by heavy metal ions from water solution, a series of experiments was carried out, as described earlier.

Table 3 presents the concentrations of alkali and alkaline earth metal ions in filtrate, measured after rinsing the biosorbents with water and after the adsorption of Pb^{2+}.

After rinsing the sawdust and wheat straw (Table 3), the potassium ions have been leached for the most part of the molecular structure of adsorbents. Also, it can be seen that after the adsorption of Pb^{2+} on the sawdust and straw, the Ca^{2+} have been leached for the most part where it is assumed that these ions are largely involved in the process of ion exchange.

Change of the solution pH value with time, during the adsorption of Pb^{2+}

It was remarked in our earlier works [7,9,17] that the pH of solution changes sharply with the adsorption time, particularly in the first few minutes of the process, indicating an interaction between the solid and aqueous phase. In some cases, this change was significant, as it was during the adsorption of Pb^{2+} on the sawdust and straw, which is illustrated in Figure 1.

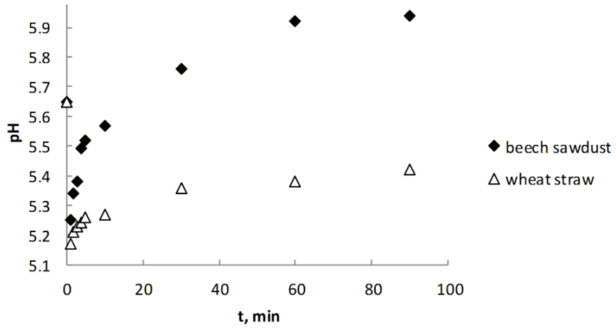

Figure 1. Change of the pH value with time at the adsorption of Pb^{2+} on beech sawdust and wheat straw.

Monitoring the pH value change, in the first few minutes of adsorption (see Figure 1), a sudden drop was observed in the pH at very beginning of the

Table 3. Concentration of alkali and alkaline earth metal ions in the filtrate (mmol g^{-1}), measured upon the rinsing with distilled water and after adsorption of Pb^{2+}

Procedure	Na^+	K^+	Ca^{2+}	Mg^{2+}
Rinsing of sawdust with distilled water	0.0056	0.0177	0.011	0.003
Rinsing of wheat straw with distilled water	0.0026	0.061	0.011	0.005
Adsorption of Pb^{2+}onto sawdust	0.0018	0.0017	0.00625	0.002
Adsorption of Pb^{2+} onto wheat straw	0.002	0.0058	0.0073	0.005

process, and then an increase during the rest of process, reaching approximately the constant pH value at the end of the experiment. Here, a significant difference in pH behavior was found between the biosorbents. Wheat straw could not achieve the starting pH value of 5.65, approaching steadily to a value of 5.45, while, in case of the sawdust, the pH value reached the initial value within the first 20 min, tending to reach even pH ≈ 6 at the end of the process. All these pH changes were taking place during the first 60 min from the start of the process. A dramatic drop, followed with a sudden increase in the pH change, corresponds to the first 20 min of the adsorption process, when the fastest adsorption rate takes place, which is presented in Figure 1. It was assumed that a sudden decrease in the pH value, during the initial stage of the process, is a consequence of a rapid replacement between the Pb^{2+} and hydrogen atoms from the functional groups contained in a molecular structure of biosorbents. Further adsorption is carried out by a substitution of calcium atoms from biosorbent structure with Pb^{2+} and, in parallel with the ion exchange reactions between the Pb^{2+} and H^+ from hydroxylic and phenolic functional groups from the cellulose structure [17], leading to a further increase in the pH of the aqueous phase for almost 0.7 in the case of sawdust, while in the case of wheat straw, a smaller increment of the pH appeared of approximately 0.3.

SEM-EDS analysis of beech sawdust and wheat straw

Based on the SEM analysis, the structure of the adsorbents' surface was visually examined. A certain difference in the structure between the untreated beech sawdust and wheat straw were observed, and the corresponding ones after the adsorption of lead ions. The SEM images of the surface morphology of the beech sawdust and wheat straw, before and after the adsorption of lead ions are shown in Figure 2a-d.

Figure 2a and c presents the micrographs of the surface of untreated beech sawdust and wheat straw. The macro-pores and cavities of larger dimensions inside the particles can be seen. The presence of macro-pores and cavities facilitates an easier movement of the aqueous phase through the structure of adsorbents, causing an easy transfer of metal ions through the internal particles structure and reaching the active sites at the internal surface to be adsorbed on [21,22].

After the adsorption of lead ions onto beech sawdust and wheat straw, the SEM images have also been taken - Figure 2b and d, in which a modified surface morphology of the adsorbents, compared to the untreated one, can be observed. A relatively compact and uniformly ordered lamellar structure of the particles is observed after the adsorption of lead ions

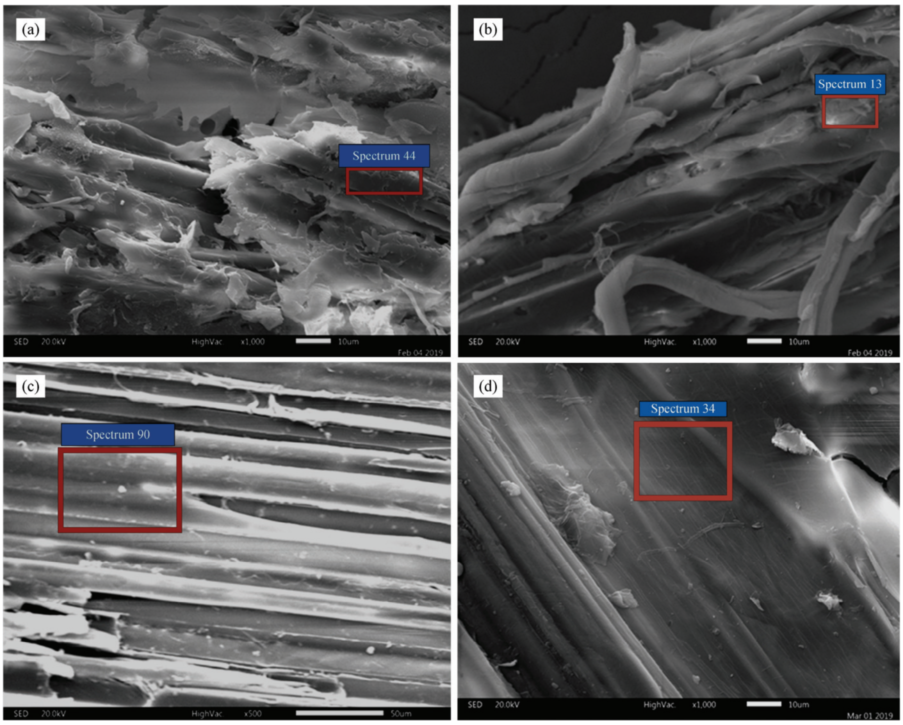

Figure 2. SEM images of beech sawdust and wheat straw: a) beech sawdust after rinsing with distilled water (1000x magnification); b) beech sawdust after adsorption of lead ions (1000x magnification); c) wheat straw after rinsing with distilled water (500x magnification); d) wheat straw after adsorption of lead ions (1000x magnification).

on them. In relation to the morphology of untreated adsorbents, Figure 2a and c, a change in the morphology is evident in Figure 2b and d, which is manifested by a compact cellulose structure, as a result of incorporation of the lead ions into the molecular structure. These changes in the morphology suggest that the biosorption of lead ions is associated with the chemical changes in the surface of adsorbents, what was confirmed by the FTIR analysis and will be discussed through the next subtitle.

The EDS analysis of beech sawdust and wheat straw was done by selection several points on the surface of samples to detect a heterogeneous distribution of elements. The peaks for C, O and Ca can be observed in Figure 3a, spectrum 44, for the untreated beech sawdust. After adsorption of lead ions (Figure 3b, spectrum 13), the peaks for Ca disappeared while the peaks for Pb occur. This indicates that calcium was replaced by lead in the ion exchange process.

The peaks for C, O, Si, Ca, K and Mg can be observed on the EDS spectrum of untreated wheat straw, (Figure 3c, spectrum 90). After adsorption of lead ions (Figure 3d, spectrum 34), the peaks for Si, Ca, K and Mg disappeared, while several peaks for Pb occurred, which clearly indicates that besides Ca, K and Mg also take part in the ion exchange process with lead ions.

FTIR analysis of beech sawdust and wheat straw

The lignocelluloses materials have a complex chemical composition. Therefore, the FTIR spectroscopy is mainly used to compare the FTIR spectra of biosorbents before and after the adsorption process, in order to identify the functional groups responsible for the adsorption of metal ions. The adsorption bands in the range from 1300 to 1000 cm^{-1} correspond to —OH, C—OH, and —O—C—O vibrations of the glycoside cellulose groups. The adsorption bands corresponding to a deformation of CH— groups appear in the range from 1000 to 700 cm^{-1} [23-26].

Bands from 1730 to 1260 cm^{-1} originate from the —C—OH, CH—, —CH$_2$ and C=O vibrations, and are typical for hemicelluloses. Bands from 1600 to 1260 cm^{-1} correspond to the C=C and —OCH$_3$ vibrations, typical for lignin. At the low-frequency area of the spectra, from 600 to 400 cm^{-1}, the bands from valent —O—M vibrations are expected, indicating a metal interaction with biosorbent. At the high frequency area of the spectra, around 3400 cm^{-1}, bands of the valent —OH (alcohols and phenols), as well as the =NH vibrations are expected [27]. Figures 4 and 5 present a set of the FTIR spectra of rinsed adsorbents and those after the adsorption of Pb^{2+}.

An adsorption band around 1735 cm^{-1} can be observed on both spectra. It corresponds to a C=O group of aldehydes and ketones, the position of which is shifted to the lower frequencies, and whose intensity is decreased significantly after the adsorption process, indicating that this functional group is involved in the capturing of lead ions. Bands in the area under 600 cm^{-1} (marked by the arrows on both

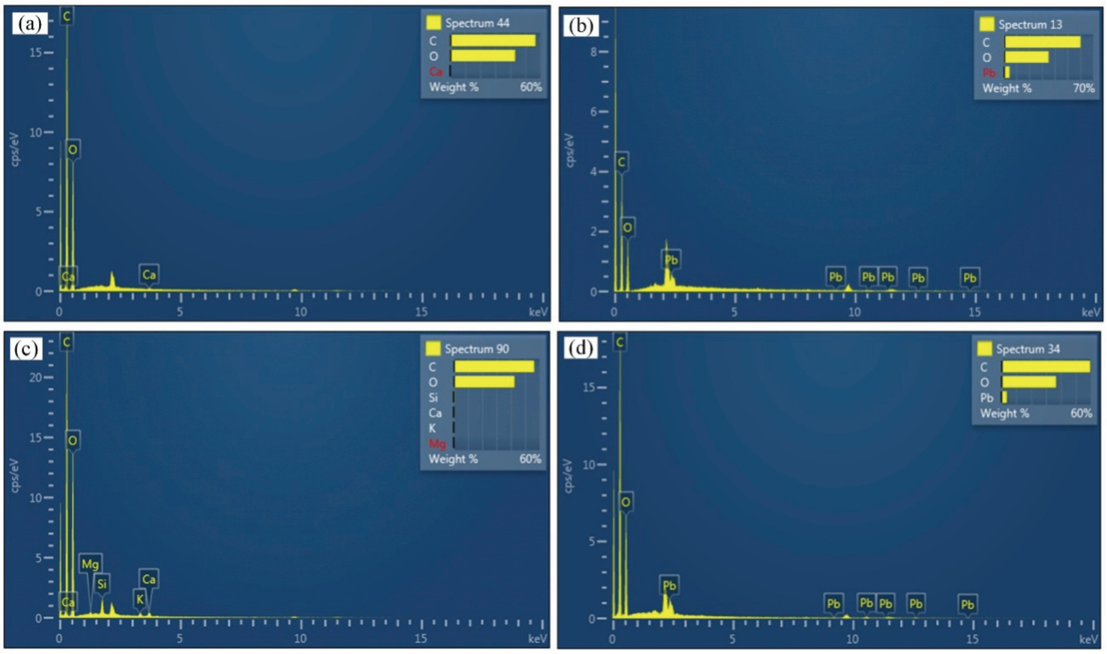

Figure 3. EDS spectra of beech sawdust and wheat straw: a) raw beech sawdust; b) beech sawdust after adsorption of lead ions; c) raw wheat straw; d) wheat straw after adsorption of lead ions.

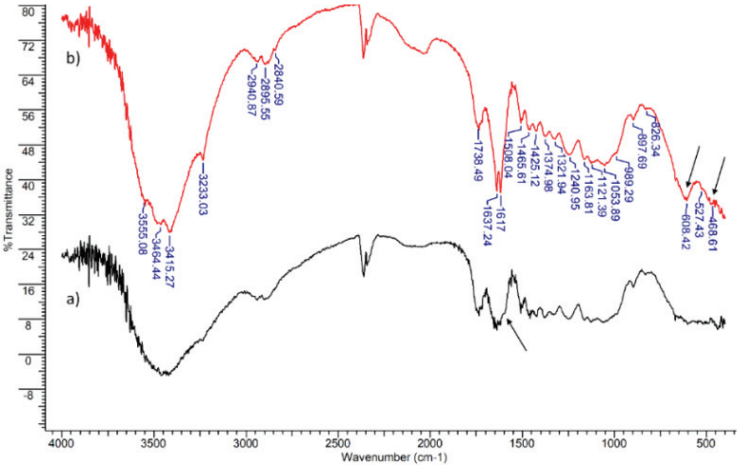

Figure 4. FTIR spectra of beech sawdust: a) after rinsing with distilled water; b) after adsorption of Pb^{2+}.

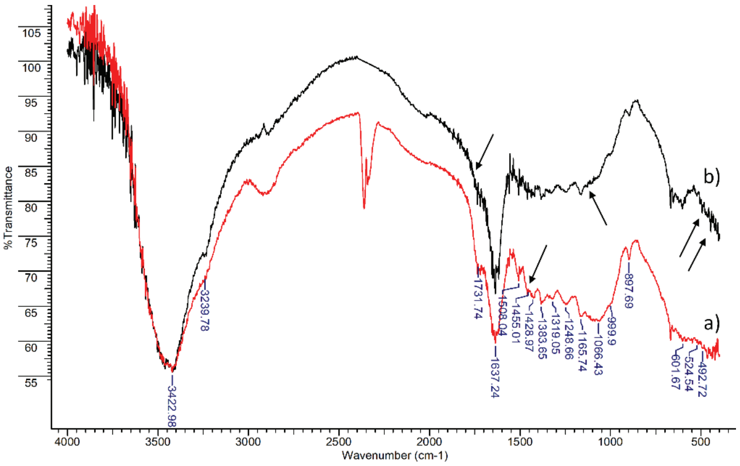

Figure 5. FTIR spectra of wheat straw: a) after rinsing with distilled water; b) after adsorption of Pb^{2+}.

spectra) correspond to the valent O—Pb vibrations. It was observed that the number of bands decreases for beech sawdust in a domain of valent vibrations of the unsaturated groups of aromatic type (1650 cm^{-1}), while the frequency gets slightly lower after the adsorption of Pb^{2+}. Changes in the valent —OH groups are observed, indicating that in addition to the C=O group, the —OH and aromatic groups are also responsible for the adsorption of Pb^{2+} [28].

Rate of the Pb^{2+} adsorption

Kinetics of the Pb^{2+} adsorption was investigated with the aim of obtaining an insight in the overall adsorption rate and adsorption reaction order, as well as to derive the reaction rate constants for the used biosorbents, also, to get data on the amount of adsorbed metal ion exchange with time, as well as the process time required to achieve the adsorption equilibrium between the aqueous and solid phase for given experimental conditions. The process time was kept constant and was 90 min in all experiments. The process time is an important parameter affecting the adsorption process rate [29], which changes gradually in such a way that the rate is high at the process beginning and then decreases, approaching almost a zero value at equilibrium. Here, the adsorption capacity change with time is presented in Figure 6.

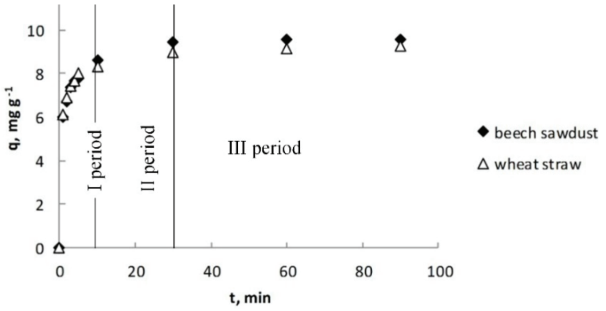

Figure 6. Change in the adsorption capacity of the Pb^{2+} with time: on beech sawdust and wheat straw.

Looking at the curves shape, three periods of the process rate are easily recognizable. In the I period, the adsorption capacity of Pb^{2+} rises rapidly up within the first 10-15 min, meaning a fast occupation of free sites on the easily accessible surface by the Pb^{2+} and their adsorption on them. After the fast I period, the process entered in the II period, when Pb^{2+} must penetrate into the internal structure of biosorbent particles to find vacant active sites to be adsorbed on. It is assumed that, during the II period, with a slower adsorption rate, the adsorption is limited by a diffusion transport of Pb^{2+} through the adsorbent internal structure, consisting from the macro- and micro--pores and counter-current flux of the exchanged ions outwards [7,30]. The rate of q rises more slowly with time, approaching an equilibrium value, which was achieved after 30 min of the process, when an increment in the adsorption capacity against time became almost negligible (III period of the process). In the III period of the adsorption, one may consider that almost all active sites were occupied by the Pb^{2+}, and the process equilibrium is achieved at given experimental conditions. During study of the adsorption kinetics, the maximum achieved adsorption capacity of Pb^{2+} on beech sawdust was 9.6 mg g^{-1}, while it was 9.3 mg g^{-1} for wheat straw. It could be assumed that the adsorption capacities are rather modest than high, and are close to those values obtained for the same or similar biosorbents [9]. The important fact is that the achieved adsorption capacities are almost equal within an interval of ±3%. An engineering significance is that both biosorbents could be used with the same efficiency, either in mixture or replacing one with another. By then, the achieved *AD*, for wheat straw was 96.4%, while for sawdust it has reached almost 99.5%. Both values are encouraging in consideration of the biosorbents use for their potential implementation at the industrial scale. Knowing either maximum achieved adsorption capacity q, or *AD* at a given process time, a compromise has to be made between these properties and the process time, allowing us to determine a residence time in the adsorber, operating in a batch mode.

Testing of the kinetic models

From Eq. (4), it is possible to evaluate the values of k_1 from the corresponding graph slopes, while q_e can be calculated from the corresponding intercepts of the graphs log $(q_e - q_t)$ *vs.* t, as it is presented in Figure 7, in which the linearized form of the experimental results from Figure 6 are plotted.

The obtained experimental values of q_e and those calculated using Eq. (4), as well as the obtained values of the correlation coefficient (R^2), are summarized and presented in Table 4. It can be seen that the pseudo-first order kinetic model does not describe fairly well the adsorption process. Significant discrepancy, particularly between the computed and experimental q_e values, as well as not so high R^2 values, eliminates the pseudo-first reaction order model from further consideration.

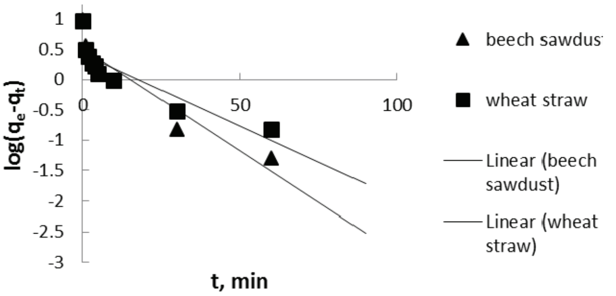

Figure 7. Pseudo-first reaction order model for the lead ions adsorption: on beech sawdust and wheat straw.

A non-linear shape of the curves presented in Figure 6, strongly indicates the biosorption process nature, which follows the pseudo-second reaction order kinetic model, which was pointed out through our earlier works and confirmed by other scientists, working on the metal ions biosorption on various biosorbents [9,10].

A linearized form, given by Eq. (7), is presented in Figure 8, expressed as $t/q_{(t)}$ against the process time t. Obviously, a linear dependence is obtained in

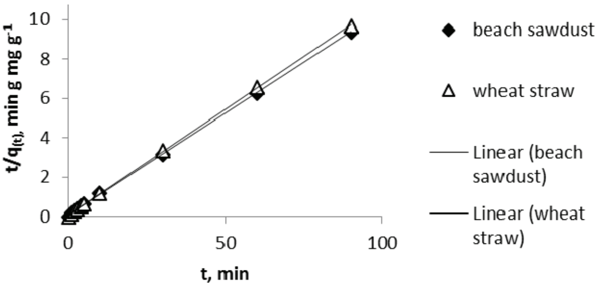

Figure 8. Linearized form of the pseudo-second order reaction for the Pb^{2+} adsorption: on beech sawdust and wheat straw.

Table 4. Kinetic parameters of the Pb^{2+} adsorption on beech sawdust and wheat straw

Adsorbent	Pseudo-first-order kinetic model				Pseudo-second-order kinetic model			
	k_1 / min^{-1}	$q_{e,exp}$ / mg g^{-1}	$q_{e,cal}$ / mg g^{-1}	R^2	k_2 / g $mg^{-1}min^{-1}$	$q_{e,exp}$ / mg g^{-1}	$q_{e,cal}$ / mg g^{-1}	R^2
Beech sawdust	0.076	9.6	3.258	0.892	0.125	9.6	12.82	0.999
Wheat straw	0.053	9.3	2.63	0.781	0.152	9.3	11.90	0.999

both considered cases and the experimental data fits well with Eq. (7). Based on the linear dependence, the reciprocal values of q_e were evaluated from the corresponding slopes, while the rate constants k_2 were calculated from the corresponding intercepts for both biosorbents. The obtained experimental values for q_e and those calculated from Eq. (5), as well as the corresponding rate constants and correlation coefficients (R^2) are summarized in Table 4.

Kinetic parameters, obtained using the linear regression analysis for the tested models, as well as the corresponding correlation coefficients R^2, have shown better fitting with the pseudo-second reaction order kinetic model than with the pseudo-first one for both considered biosorbents. Namely, the adsorption capacity values, calculated using Eq. (4), significantly differ from those experimentally obtained. Experimental values of the adsorption capacity showed a good agreement with those ones calculated using Eq. (6). The obtained correlation coefficients R^2 are also very high in case of the pseudo-second order reaction model in comparison with the pseudo-first one. It means that the adsorption kinetics can be fairly modeled with the pseudo-second reaction order model. The same findings were already reported by us, as well as by other scientists, for some other metal ions and other biosorbents [7,17].

Adsorption isotherms

An adsorption isotherm is a relationship between the concentrations of adsorbed species on the adsorbent surface, q_e, in contact with the same species in the aqueous phase, C_e, at equilibrium at given temperature. Three frequently used relationships of adsorption isotherms are the Langmuir, Freundlich and Temkin isotherm model [15], which were tested with the experimental results obtained in this study in a way described in the experimental part. Experimental data for q_e plotted against the corresponding C_e, for beech sawdust and wheat straw are presented in Figure 9.

Each of the mentioned isotherm model will be tested with the experimental data in order to determine how they fit to each other.

Langmuir isotherm

This model of isotherm could be described by Eq. (8) [32]:

$$q_e = \frac{q_m K_L C_e}{1 + K_L C_e} \tag{8}$$

where: C_e - equilibrium concentration of metal ions (mg dm^{-3}); q_e - mass of adsorbed Pb^{2+} per unit of the biosorbent mass at equilibrium (mg g^{-1}); q_m - maximum adsorption capacity (mg g^{-1}); K_L - the Langmuir constant (dm^3 mg^{-1}).

Linearization of Eq. (8) leads to the following relationship:

$$\frac{C_e}{q_e} = \frac{1}{K_L q_m} + \frac{1}{q_m} C_e \tag{9}$$

Figure 10 presents the linearized form of the Langmuir isotherm given by Eq. (9) for beech sawdust (Figure 10a) and wheat straw (Figure 10b) and compared with the experimental data derived from Figure 9. The ratio of C_e/q_e as a function of C_e is a straight line with a slope of $1/q_m$, while the intercept is $1/q_m K_L$. The parameters q_m, K_L and regression coefficient R^2 are summarized in Table 5.

Evidently, there is a significant discrepancy between the experimental data and theoretical lines, so that the Langmuir model cannot be applied for describing the adsorption equilibrium of the considered systems.

Freundlich isotherm

The Freundlich isotherm is used as an empirical model describing the adsorption from the solution over the surface heterogeneity and exponential distribution the active sorbent sites of the sorption material [33]. The Freundlich isotherm is expressed

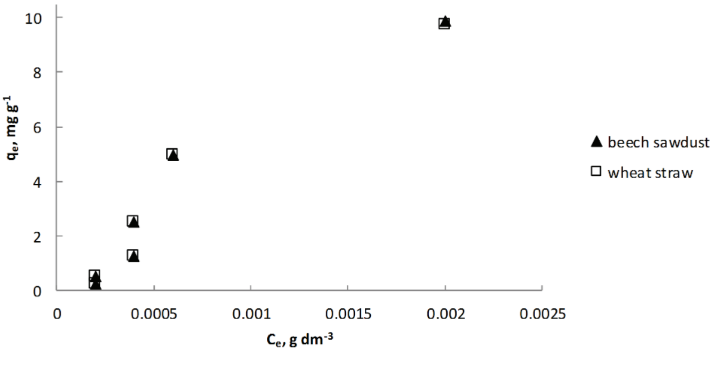

Figure 9. Adsorption isotherms for beech sawdust and wheat straw.

Table 5. Equilibrium parameters of the adsorption isotherm

Adsorbent	Model									
	Langmuir				Freundlich			Temkin		
	K_L / dm^3 mg^{-1}	q_m / mg g^{-1}	q_{exp} / mg g^{-1}	R^2	K_F / dm^3 g^{-1}	n	R^2	K_T	B / dm^3 m^{-1}	R^2
Sawdust	0.66	16.95	9.9	0.84	190546	0.66	0.847	24.9	2.832	0.97
Wheat straw	128.35	25.97	9.7	0.82	1600	1.12	0.689	24.47	2.77	0.97

by the following equation [2]:

$$q_e = K_F C_e^{\frac{1}{n}} \tag{10}$$

Linearization of the relationship (10), leads to the following expression:

$$\log q_e = \log K_F + \frac{1}{n}\log C_e \tag{11}$$

where: K_F - Freundlich constant related to the adsorption capacity (dm^{3}g^{-1}); n - adsorption intensity.

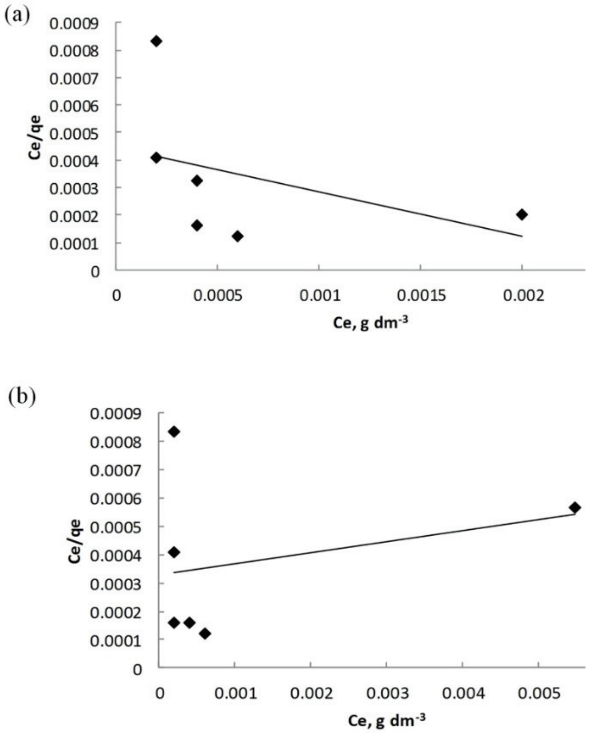

Figure 10. Linearized form of the Langmuir isotherm for beech sawdust (a) and wheat straw (b).

Figure 11 presents the linearized form of the Freundlich isotherm in the log-log coordinate system, together with the corresponding experimental data for sawdust (Figure 11a) and straw (Figure 11b). Log q_e *vs.* a function of log C_e should give a straight line with a slope of 1/n and intercept log K_F. Parameter 1/n relates to the adsorption intensity and varies with material heterogeneity [32]. Parameters n, K_F and R^2 are also given in Table 5, together with the ones evaluated for the Langmuir adsorption isotherm model.

Here, there is a certain matching between the theory and experimental data for both biosorbents.

Temkin isotherm

The Temkin adsorption isotherm model assumes a uniform distribution of the binding energy to a maximum energy, wherein the interaction between adsorbent-adsorbate, the heat of adsorption of all adsorbates decreases linearly with a degree of surface coverage [8]. The Temkin model is developed to be valid on the whole external and internal surface, including pore walls [34].

The Temkin isotherm is given by the following expression:

$$q_e = B\ln\left(K_T C_e\right) \tag{12}$$

It can be developed to the linear form giving the following relationship:

$$q_e = B\ln K_T + B\ln C_e \tag{13}$$

where: B - constant, relating to the adsorption heat ($B = RT/b$) (dm^3 m^{-1}); b - variable adsorption energy, J mol^{-1}; K_T - the Temkin isotherm constant (dm^3 mg^{-1}).

Figure 12 presents the Temkin isotherm in a semi-logarithmic coordinate system, according to Eq. (12), for beech sawdust (Figure 12a) and wheat straw (Figure 12b). Linear dependence of q_e and ln C_e allows determining values of the constant B, from the corresponding slopes, as well as values of the constant K_T from the corresponding intercepts. Constant K_T corresponds to the maximum energy of binding, while constant B relates to the heat of adsorption. The Temkin isotherm constants B and K_T, as well as the correlation coefficients (R^2), are also given in Table 5.

The adsorption equilibrium of Pb^{2+} on biosorbents is well represented by the Temkin adsorption isotherm model in relation to the Langmuir and Freundlich model, having the highest value of R^2 for both biosorbents (0.971 for beech sawdust and 0.969 for wheat straw), as shown in Figure 12 and Table 5. Similar results were published by other researchers, using the same kind of biosorbents and ions [35-39].

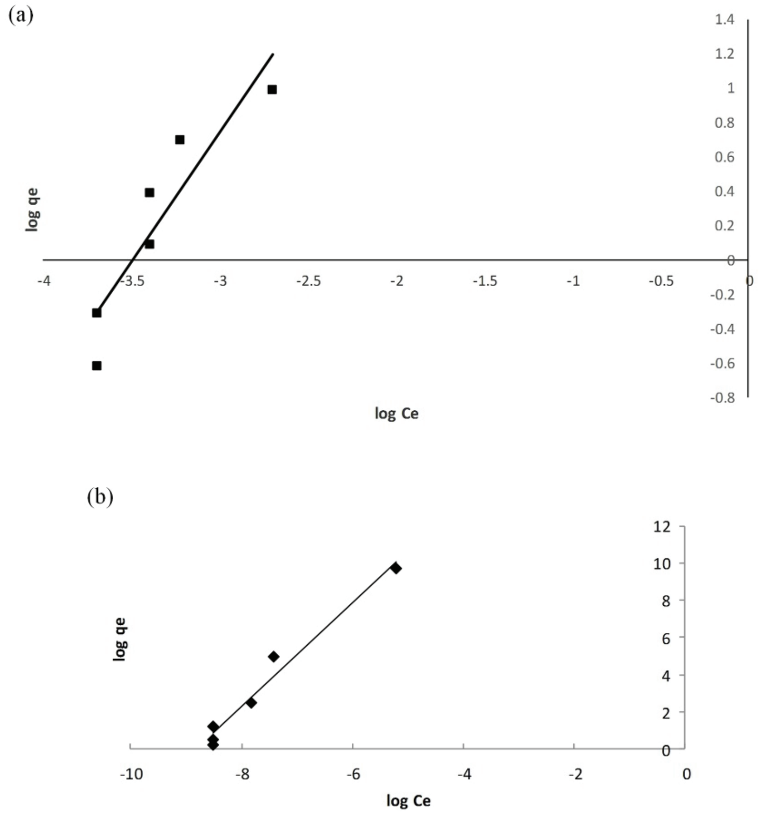

Figure 11. Linearized form of the Freundlich isotherms for beech sawdust (a) and wheat straw (b).

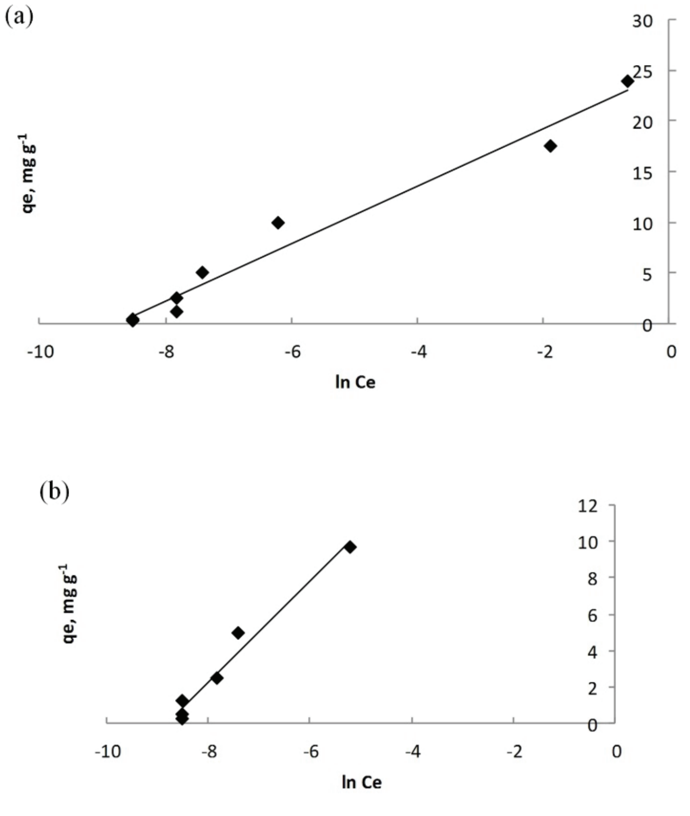

Figure 12. Linearized form of the Temkin isotherms for beech sawdust (a) and wheat straw (b).

CONCLUSION

Based on the analysis of the obtained results, the following conclusions can be derived.

On the SEM micrographs of beech sawdust and wheat straw macro-pores and cavities of larger dimensions can be seen. It is assumed that the lead ions easily penetrate through these pores and cavities into the adsorbents' structure to be adsorbed at the internal active sites. The EDS analysis of used adsorbents was done by recording several points on the surface of samples to detect a heterogeneous distribution of elements. For beech sawdust, calcium could be exchanged with lead during the adsorption process, while for wheat straw Ca, K and Mg were exchanged with lead during the adsorption process.

Based on the FTIR analysis, the C=O group of aldehydes and ketones, —OH and aromatic groups may be responsible for the adsorption of Pb^{2+}.

The adsorption kinetics is well described by the pseudo-second-order kinetic model, whereby the chemisorption is a possible way of adsorbate bonding on the surface of the biosorbents.

The Temkin isotherm model has shown the best fit with the experimental data. Maximum achieved adsorption capacity for the adsorption of lead ions was 9.9 mg g^{-1} for beech sawdust, while it was 9.7 mg g^{-1} for wheat straw.

Acknowledgements

This work was financially supported by the Ministry of Education, Science and Technological Development of the Republic of Serbia, Grant No. 451-03-9/2021-14/ 200052 and the scientific research work at the University of Belgrade, Technical Faculty in Bor, according to the contract with registration number 451-03-9/2021-14/ 200131.

REFERENCES

[1] S.S. Ahluwalia, D. Goyal, Bioresour. Technol. 98 (2007) 2243-2257

[2] M. Yurtsever, A. Şengil, J. Hazard. Mater. 163(2009) 58-64

[3] M.N.M. Ibrahim, W.S.W. Ngah, M.S. Norliyana, W.R.W. Daud, M. Rafatullah, O. Sulaiman, R. Hashim, J. Hazard. Mater. 182 (2010)377-385

[4] N.H. Bhatti, S. Ghufrana, A.H.E. Muhammad, J. Chin. Chem. Soc. 55 (2008) 1235-1242

[5] O.S. Lawal, A.R.S. Ajayi, O.O. Rabiu, J. Hazard. Mater. 177 (2010) 829-835

[6] A. Sönmezay, M. Salim, N. Bektaş, Trans. Nonferrous Met. Soc. China 22 (2012)3131-3139

[7] D. Božić, V. Stanković, M. Gorgievski, G. Bogdanović, R. Kovačević, J.Hazard. Mater. 171 (2009) 684-692

[8] S.P. Kumar, C. Vincent, K. Kirthika, K.S. Kumar, Braz. J. Chem. Eng. 27 (2010)339-346

[9] D. Božić, M. Gorgievski, V. Stanković, N. Štrbac, S. Šerbula, N. Petrović, Ecol. Eng. 58 (2013) 202-206

[10] M. Gorgievski, D. Božić, V. Stanković, V. Trujić, Proceedings of the Faculty of Technology in Leskovac, 20 (2011) 35-43 (In Serbian)

[11] V. Stanković, D. Božić, M. Gorgievski, G. Bogdanović, Chem. Ind. Chem. Eng. Q. 15 (2009) 237−249

[12] V. Stanković, M. Gorgievski, D. Božić, Biomass Bioenergy 88 (2016) 17-23

[13] M. Petrović, T. Šoštarić, M. Stevanović, J. Petrović, M. Mihajlović, A. Ćosović, S. Stanković, Ecol. Eng. 99 (2017) 83-90

[14] R. Zhang, J. Zhang, X. Zhang, C. Dou, R. Han, J. Taiwan Inst. Chem. Eng. 45 (2014) 2578-2583

[15] U. Farooq, J.A. Kozinski, M.A. Khan, M. Athar,, Biotechnol. J. 101 (2010) 5043-5053

[16] M.R. Unnitham, T.S. Anirudham, Ind. Eng. Chem. Res.. 40 (2001) 2693-2701

[17] M. Gorgievski, D. Božić, V. Stanković, N. Štrbac, S. Šerbula, Ecol. Eng. 58 (2013) 113-122

[18] V.D. Stanković, Fenomeni prenosa i operacije u metalurgiji-2 Prenos toplote I mase; Univerzitet u Beogradu, Tehnički fakultet, Bor, Srbija (1998) (In Serbian)

[19] A. Witek-Krowiak, R.G. Szafran, S. Modelski, Desalination 265 (2011) 126-134

[20] M.A.K.M. Hanafiah, W.S.W. Ngah, S.H. Zolkafly, L.C. Teong, Z.A.A. Majid, J. Environ. Sci. 24 (2012) 261-268

[21] V. Murphy, S. Tofail, H. Hughes, P. Mcloughlin, Chem. Eng. J. 148 (2009) 425-433

[22] A. Girao, G. Caputo, M.C. Ferro, Compr. Anal. Chem. 75 (2017) 154-166

[23] D. Marković-Nikolić, A. Bojić, S. Savić, S. Petrović, D. Cvetković, M. Cakić, G. Nikolić, J. Spectrosc. (2018) 1-16

[24] D. Marković-Nikolić, A. Bojić, D. Bojić, M. Cakić, D. Cvetković, G. Nikolić, Chem. Ind. Chem. Eng. Q. 24 (2018) 319-332

[25] S. Glišić, M. Cakić, G. Nikolić, B. Danilović, J. Mol. Struct. 1084 (2015) 345-351

[26] G.O. El-Sayed, H.A. Dessouki, S.S. Ibrahim, Chem. Sci. J. 1 (2010) 1-11

[27] R. Gill, Q. Nadeem, R. Nadeem, R. Nazir, S. Navaz, J. Basic Environ. Sci. 5 (2014) 306-317

[28] T.K. Naiya, B. Singha, S.K. Das, Proc. Int. Conf. Chem. Chem Process (2011)

[29] M. Zhang, Chem. Eng. Technol. 172 (2011) 361-368

[30] K.K. Singh, U. Singh, A. Yadav, J. Chem. Pharm. Res. 3 (2011) 338-348

[31] Y. Ho, G. Mckay, Process Biochem. 34 (1999)451-465

[32] K.K. Singh, U. Singh, A. Yadav, J. Chem. Pharm. Res. 3 (2011) 338-348

[33] O.A. Adelaja, I.A. Amoo, A.D. Aderibigbe, Arch. Appl. Sci. Res. 3 (2011) 50-60

[34] S.R. Shukla, S.P. Roshan, J. Chem. Technol. Biotechnol. 80 (2005) 176-183

[35] M. Sassi, B. Bestani, A.H. Said, N. Benderdouche, E. Guibal, Desalination 262 (2010) 243-250

[36] V.B. Dang, H.D. Doan, Bioresource Technol. 100 (2009) 211-219

[37] D. Diriba, A. Hussen, V. Rao, Bull. Environ. Contam. Toxicol. 93 (2014) 126-131

[38] L. Chun, C. Hongzhang, Process Biochem. 39 (2004) 541-545

[39] A. Gao, K. Xie, X. Song, K. Zhang, A. Hou, Ecol. Eng. 99 (2017) 343-348

[40] N. Abdel-Ghani, G. El-Chaghaby, F. Helal, Desalin. Water Treat. 51 (2013) 3558-3575

[41] J. Al-Abdullah, A. G. Al Lafi, T. Alnama, W. Al Masri, Y. Amin, M. N. Alkfri, Iran. J. Chem. Chem. Eng. 37 (2018) 131-144.

DRAGANA BOŽIĆ[1]
MILAN GORGIEVSKI[2]
VELIZAR STANKOVIĆ[2]
MILORAD CAKIĆ[3]
SILVANA DIMITRIJEVIĆ[1]
VESNA CONIĆ[1]

[1]Institut za rudarstvo i metalurgiju Bor, Bor, Srbija
[2]Univerzitet u Beogradu, Tehnički fakultet u Boru, Bor, Srbija
[3]Univerzitet u Nišu, Tehnološki fakultet u Leskovcu, Leskovac, Srbija

NAUČNI RAD

BIOSORPCIJA JONA OLOVA IZ VODENIH RASTVORA PILJEVINOM BUKVE I PŠENIČNE SLAME

Ovaj rad predstavlja rezultate adsorpcije jona Pb^{2+} *iz sintetičkih rastvora* $Pb(NO_3)_2$*, koristeći piljevinu bukve i pšeničnu slamu kao adsorbense. Fizičko-hemijska karakterizacija adsorbensa obuhvatala je specifičnu površinu, pHpzc, SEM-EDS i FTIR analizu. Kinetika i izoterme adsorpcije, kao i promene pH rastvora tokom procesa, su praćene i analizirane. Rezultati su pokazali da je adsorpcija dobro objašnjena kinetičkim modelom pseudo-drugog reda za oba adsorbensa. Adsorpciju jona* Pb^{2+} *na piljevini i slami dobro opisuje izoterma Temkin, što potvrđuju visoke vrednosti koeficijenta regresije* R^2*. Maksimalni adsorpcioni kapacitet jona olova na piljevini bukve i pšeničnoj slami bio je 9,9, odnosno 9,7 mg* g^{-1}*. Dobijeni rezultati su pokazali da su piljevina bukve i pšenična slama pogodni adsorbenti za adsorpciju jona olova iz razblaženih vodenih rastvora.*

Ključne reči: biosorpcija Pb^{2+}*, piljevina bukve, pšenična slama, adsorpcione izoterme.*

CI&CEQ
Chemical Industry & Chemical Engineering Quarterly

Available on line at
Association of the Chemical Engineers of Serbia *AChE*
www.ache.org.rs/CICEQ

Chem. Ind. Chem. Eng. Q. 27 (1) 35–44 (2021) CI&CEQ

MAJED M. ALGHAMDI[1]
ADEL A. EL-ZAHHAR[1,2]

[1]Environmental Monitoring, Assessment & Treatment (EMAT) Research Group, Department of Chemistry, College of Science, King Khalid University, Abha, Saudi Arabia
[2]Nuclear Chem. Dept. AEA, Cairo, Egypt

SCIENTIFIC PAPER

UDC 546.26-162-31:544:66:678

CELLULOSE ACETATE BUTYRATE GRAPHENE OXIDE NANOCOMPOSITE MEMBRANE: FABRICATION, CHARACTERIZATION AND PERFORMANCE

Article Highlights

- CAB/GO membrane exhibited improved properties and performance
- The results revealed an improvement of 450% in water flux
- Improved rejection of 144 and 93% for NaCl and Na_2SO_4, respectively
- Higher performance stability, thermal and antifouling properties

Abstract

In this study, the effects of graphene oxide (GO) nanosheets on the physicochemical properties and performances of cellulose acetate butyrate (CAB) membranes were investigated. Nanocomposite membranes were fabricated using CAB and a small amount of GO in the range of 0 to 0.07 wt.%, using a conventional phase-inversion method. Membranes were characterized by different methods and their performances were tested using a dead-end filtration system. Compared with pristine CAB membrane, experimental results demonstrated an improvement in features such as hydrophilicity, permeability, salt rejection, antifouling, and stability. The results proved an increase in the porosity and pore sizes of membranes with GO addition. Furthermore, the membrane containing 0.07 wt.% of GO exhibited a low contact angle of 37° and a dramatic improvement in water flux of about 450% (from 2 to 11 L/(m^2 h)). Moreover, it demonstrated a salt rejection of 39% for NaCl and 87% for Na_2SO_4, corresponding to improvements of about 144 and 93%, respectively. Furthermore, the results revealed a higher antifouling property with an 86% improvement in flux recovery and higher stability in terms of performance and thermal properties compared to CAB.

Keywords: cellulose acetate butyrate, graphene oxide, nanocomposite, membrane, salt rejection.

Although synthetic polymer-based membranes are broadly used and have a huge market, complications associated with highly hydrophobic polymer backbones make them vulnerable to fouling [1]. In order to overcome this disadvantage, several methods have been employed to enhance fouling resistance, mostly by increasing the hydrophilicity [2--5]. Among these methods is the incorporation of different types of nanoparticles into membranes [6-10]. From this point of view, materials such as cellulose esters are known for their outstanding hydrophilicity and low fouling tendency in addition to their significant roles in industry and pharmaceutical technologies [11,12]. Consequently, they can be considered as promising in membrane technology. They also offer the benefit of biocompatibility and have a relatively low cost. However, the lack of reactive functional groups on the polymer chains limits their applications.

In order to enhance their properties, hydroxyl groups of cellulose can be chemically modified to form materials of different physical and chemical properties that could be appropriate for diverse applications [13]. To further enhance membrane performance, polymer blending is also one of the effective

---

Correspondence: M.M. Alghamdi, King Khalid University, College of Science, Department of Chemistry, P.O. Box 9004, Abha 61413, Saudi Arabia.
E-mail: mmalghamdi@kku.edu.sa
Paper received: 28 January, 2020
Paper revised: 28 May, 2020
Paper accepted: 19 June, 2020

https://doi.org/10.2298/CICEQ200128022A

methods that has provided a desirable way to fulfill the expectation of new polymeric materials properties. For example, the cellulose acetate (CA) membrane has often been modified by blending with other materials, such as hydrous manganese dioxide nanoparticles, GO and molybdenum disulfide to gain improved performance, such as higher flux and better selectivity [14,15]. Likewise, the blending of carboxymethyl cellulose acetate and CA also resulted in membranes with enhanced contact angles, morphology, permeability, and antifouling properties [16].

Nowadays, among the nanomaterials that have been incorporated into membranes is graphene oxide (GO). Due to its rich oxygen-containing hydrophilic functional groups, unique two-dimensional structure, large specific surface area, and good mechanical properties [17,18], this material has attracted considerable interest and has been exploited for various membrane applications. In fact, the incorporation of GO has proven to enhance membrane performance in terms of permeate flux, salt rejection, fouling properties, hydrophilicity and surface charges of membranes [19-23]. For example, improved hydrophilicity, permeability, and antifouling performances were observed by incorporating GO and PVDF [24]. Moreover, the work of Zinadini *et al.* also revealed a significant improvement in PES membrane fouling resistance and surface hydrophilicity by blending with GO [25]. Likewise, incorporation of GO has also resulted in improved PSF membrane performance [26]. In particular, the incorporation of GO within CA has been widely investigated and demonstrated outstanding properties. For example, incorporating GO and CA has been investigated recently and it has resulted in increased salt rejection, improved mechanical strength and thermal stability [27,28].

Nevertheless, there have been few reports on cellulose acetate butyrate (CAB)-based membrane applications. This might be due to CAB's low permeability and the fact that it is more hydrophobic than CA. In fact, CAB has a composition of butyryl and acetyl functional groups that can effectively develop the properties of the cellulose [29-32]. In addition, CAB matches the CA membrane in many characteristics but has additional features such as being tougher than CA, having great film formation, and demonstrating good solubility in organic solvents. However, in order to compete with other membranes, further modification of the CAB-based membrane is still required.

Based on these considerations and in addition to the fact that the CAB/GO composite membrane has not been investigated previously, this study was carried out to examine the influence of GO nanosheets on the CAB membrane's characteristics and performance and to address the feasibility of the nanocomposite membrane for application in salt separation. It is proposed that the use of GO could further facilitate interactions with polymers and salts and hence increase membrane stability and salt rejection during filtration [33]. Also, the use of GO could provide diffusion pathways for water transportation and thereby increase the overall flux rate during filtration; this is in addition to its effects on membrane reinforcement, fouling resistance, and antibacterial activity [34].

EXPERIMENTAL

Materials

Cellulose acetate butyrate (CAB), with an average molecular weight of 30000 Da and 49% butyryl, was obtained from Sigma-Aldrich and used as received without further purification. Polyvinylpyrrolidone (PVP) powder (*MW* = 25,000 g/mol), NaCl and Na_2SO_4 were purchased from Sigma-Aldrich. *N*,*N*-dimethylformamide (DMF) with 99.5% purity was supplied by Acros Organics. Graphene oxide (GO) nanosheets (flakes) with carbon content of 42-52% were purchased from Sigma-Aldrich and employed as inorganic nano-modifiers.

Fabrication of nanocomposite membrane

The nanocomposite membranes were fabricated by the casting-solution and the phase-inversion methods. The preparation was performed in a glass reactor by dissolving a fixed amount of CAB (20 wt.%) and PVP (1 wt.%) in DMF and stirring the polymeric solution for more than 1 h *via* a mechanical stirrer until complete dissolution (solution A). GO/formamide solution was prepared by dispersion of GO powders in formamide (30 wt.%) with different concentrations, and the solutions were sonicated for 1 h until forming homogeneous GO/formamide suspensions (solution B). The membrane casting-solutions with varied GO concentrations were prepared by mixing solution A with solution B as presented in Table 1. For better dispersion of GO, the casting-solutions were sonicated for 30 min *via* an ultrasonic bath. Next, the prepared homogeneous casting-solutions were casted onto glass plates by means of a casting knife with a constant thickness of 0.3 mm. Subsequently, the membranes were immersed into deionized water immediately without prior evaporation time. After the exchanging process of solvent and non-solvent, the membranes were reserved in a container filled with deionized water for 24 h to remove any soluble components in the membrane structure. Afterward, the membranes were dried between two filter paper sheets at room temperature (25±2 °C) for 24 h.

Table 1. Composition of the prepared casting-solutions used for membranes fabrication; CAB wt.%: 20.00, PVP wt.%: 1.00

Membrane	GO wt. %	DMF wt. %
1	0	79.00
2	0.01	78.99
3	0.04	78.96
4	0.07	78.93

Membrane characterization

The hydrophilicity of membranes was studied via the water contact angle analysis using deionized water. Field emission scanning electron microscopy (SEM) was used for analyzing the surface morphology. Images were obtained using a Jeol Model 6360 LV SEM (USA). Fourier transform infrared (FTIR) spectra for the prepared membranes were obtained using Nicolet 6700 FT-IR from Thermo Scientific. The spectra of the samples were analyzed in the infrared (IR) region between 4000 and 400 cm^{-1}.

Membrane porosity was measured using the volume fraction process. In this process, the prepared membranes were soaked in deionized water for at least 24 h. The wet membranes were then taken out and the excess water was softly removed from the membranes' surfaces by the aid of tissue paper. After that, the wet membranes were weighed and then dried in a vacuum oven at 70 °C for 24 h and weighed again after drying. The porosity percentage of the membranes (ε) and the water uptake were determined by employing Eqs. (1) and (2), respectively [35]:

$$\varepsilon = 100\frac{W_s - W_d}{\rho_{water} A l} \tag{1}$$

$$\text{Water uptake, \%} = 100\frac{W_s - W_d}{W_d} \tag{2}$$

In these equations, W_s and W_d (g) are the weights of the swollen and dry membranes, respectively; ρ_{water} (g/cm^3) is the water density; A (cm^2) is the membrane area; and l (cm) is the membrane thickness. The membrane surface pore diameter (a) could be calculated using Eq. (3) [36]:

$$a = \sqrt{\frac{8(2.9 - 1.75\varepsilon)\mu l Q_w}{\varepsilon A \Delta P}} \tag{3}$$

where a (m) is the mean pore diameter; Q_w (m^3/s) is the volume of permeated water per unit time; A (m^2) is the membrane effective area; and l (m) is the membrane thickness. μ (Pa s) is the water viscosity at 25 °C; ΔP (Pa) is the trans-membrane pressure; and ε is the porosity percentage.

Membrane performance

The performance of the prepared membranes was investigated using a laboratory designed dead-end filtration system. The salt solutions were prepared separately by dissolving the required amount of salts (Na_2SO_4 and NaCl) in deionized water. Various concentrations of salts in the range of 1 to 2 g/L were prepared. The water flux (J_w) was acquired by determining the amount of water that passed through the membranes in terms of L/m^2 h at a fixed pressure of 1.4 bar (20 psi) and calculated using Eq. (4) [37]:

$$J_w = \frac{Q}{A\Delta t} \tag{4}$$

In Eq. (4), Q (L), A (m^2), and Δt (h) are expressed as the volume of permeated water, the membrane area, and the sampling time, respectively. For salt rejection percentage calculations, Eq. (5) was employed [37]:

$$\text{Rejection ,\%} = 100\left(1 - \frac{C_p}{C_f}\right) \tag{5}$$

where C_p and C_f are salt concentrations in permeate and feed, respectively, which were measured by a conductivity meter.

With regard to the antifouling study, the membranes were first tested using a pure water flux ($J_{w,1}$). The membranes then were subjected to the sodium alginate (SA) solution as a model of an organic fouling material. SA solution with a concentration of 20 mg/L was applied as feed solution until obtaining a stable flux. After the SA permeation experiment, the membranes were washed with deionized water and the second pure water flux ($J_{w,2}$) was then determined. The flux recovery ratio (*FR%*) was calculated using Eq. (6), where the higher value of FR% reflects good antifouling behavior for the membranes:

$$FR\ \% = 100\left(\frac{J_{w,2}}{J_{w,1}}\right) \tag{6}$$

RESULTS AND DISCUSSION

Membrane characterization

The FTIR spectra of the CAB, GO and CAB/GO are presented in Figure 1. The spectrum of GO shows peaks at 1620, 1738 and 3420 cm^{-1} that could be assigned to C=C, C=O and OH bonds, respectively. The peak at 1050 cm^{-1} may be assigned to the epoxy group. The spectra were consistent with the literature

[38,39]. Moreover, the presence of the carboxylic acid OH can be confirmed by the broad band between 2500 and 3300 cm^{-1}.

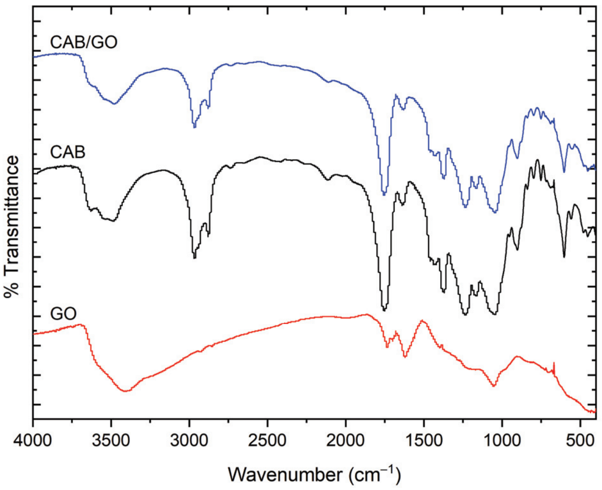

Figure 1. FTIR spectra of GO, CAB, and CAB/GO nanocomposite.

In comparison, the FTIR spectrum of CAB showed a band at 1750 cm^{-1} due to the carbonyl ester group. The peak at 1246 cm^{-1} could be assigned to the asymmetric stretching of C-C-O of the ester group; the band appeared at 1049 cm^{-1} as the result of asymmetric O-C-C stretching attached to the carbonyl carbon. The peak at 1375 cm^{-1} was due to methyl groups in acetate moiety. The absence of vibrations peaks of GO could be an indication of its complete incorporation in the polymer matrix due to its very low content [40]. Also, the overlapping of the peaks at 3630 and 3410 cm^{-1} may suggest the likely formation of hydroxyl hydrogen bonding.

With regard to thermal stability, the prepared CAB and CAB/0.07% GO composite membranes were studied by analyzing the thermal degradation of the samples. The results in Figure 2 showed that the thermal degradation of CAB occurred in three steps. The first step started between 90 and 200 °C with a weight loss of 31%, which involves the evaporation of bound water and the starting of cellulose degradation, yielding aliphatic char and volatile. The remaining two steps appeared between 240 and 450 °C with a total weight loss of 69%. These steps involve the conversion of some aliphatic char to aromatic and gaseous components [41]. The thermogram of CAB/0.07% GO shows one major step between 250 to 450 °C with a total weight loss of 94.5%. This step includes the evaporation of bonding water and thermal degradation of the cellulose skeleton. The presence of GO appeared to enhance thermal property of the CAB and delayed the thermal degradation of the cellulosic materials. This finding could be due to the increased surface area in the presence of GO, which decreased the heat release rate and mass loss rate as well. Also, the GO accumulated on the surface or within the melt polymer layer, acting as a thermal insulation layer and delaying the cellulose degradation.

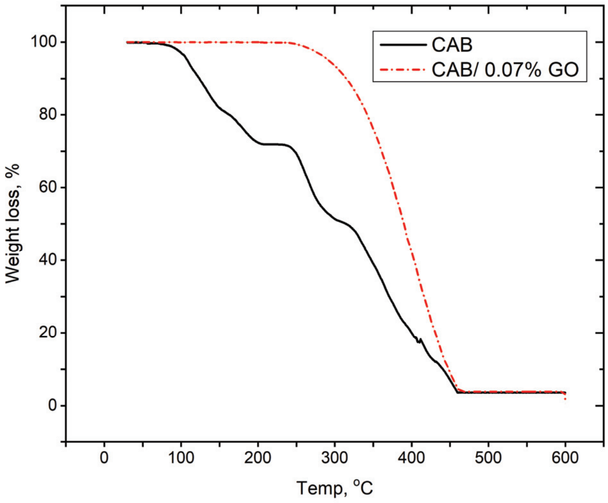

Figure 2. TGA thermograms of CAB and the prepared CAB/0.07 wt.% GO composite, under N_2 atmosphere (10 mL/min) at a heating rate of 10 °C/min.

Furthermore, the effect of GO nanosheets on the morphological surface characteristics of the membrane samples was studied using SEM (Figure 3). The SEM micrographs revealed a porous surface layer with a more sponge-like appearance than those on the CAB membrane [42]. The SEM results clearly showed that GO has a significant effect on the membrane. This could be attributed to the influence that GO, as a hydrophilic material, has on the dynamic stability of the casting solution and hence the phase-inversion process [43]. The addition of GO caused a fast phase separation during the phase-inversion process, which can also lead to higher porosity and the formation of larger pores in the membrane's surface. This outcome might be related to GO functional groups, small amount, and the carbon-based structure of the CAB polymer and GO. In addition, no agglomeration of GO nanomaterials was observed. This could be the result of better dispersion of GO particles due to their functionality, small amount, and a result of the sonication process that was used, which was set at 30 min for verifying optimal dispersion.

The membrane sample's hydrophilicity was measured by determining the contact angle using water drops on the membrane surfaces. The results in Table 2 show variations of membrane-water contact angles at different concentrations of GO. The membrane water contact angle for CAB was found to be around 79°, which is consistent with the literature [44]. Furthermore, it was found that the contact angle significantly decreased with increasing GO concentrations, *i.e.*, the contact angle decreased from 79 to 37°. These results reflect a significant effect of GO on the hydrophilicity of membrane surfaces, even with a very small amount, improving the membranes' hydrophilicity with the GO incorporation within the range of 0 to 0.07 wt.%. This finding may be attributed to the hydrophilic nature of GO and the formation of bigger pores as well.

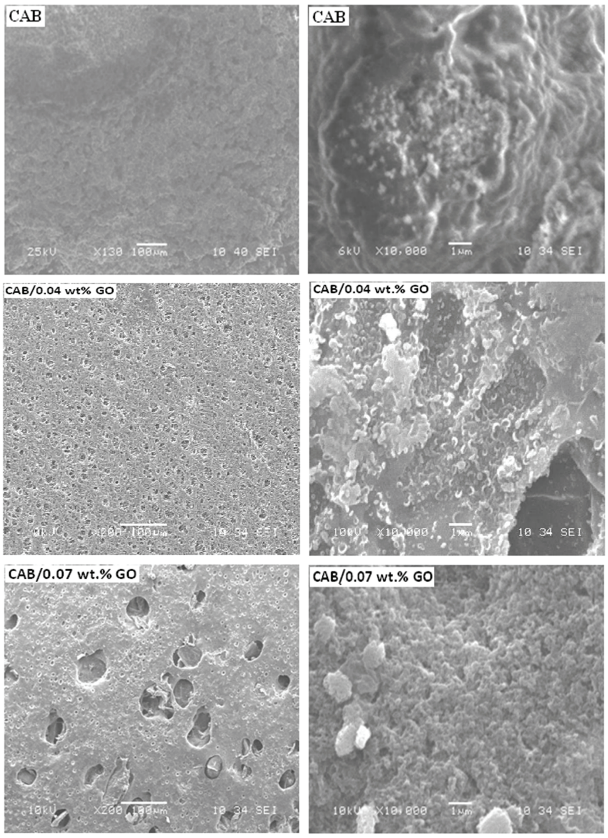

Figure 3. SEM images of: A) the pristine CAB; B) CAB/0.07 wt.% GO composite.

Table 2. CAB/GO nanocomposite membranes characterizeations; membrane thickness: 0.3 mm

GO wt.%	Contact angle °	Porosity %	Mean pore diameter nm	Water uptake %
0	79	54.3	13.4	11.2
0.01	60	65.6	25.2	15.6
0.04	53	76.7	28.3	18.5
0.07	37	84.6	32.1	22.6
0.10	47	71.7	23.12	16.7

In terms of the membranes' porosity and mean pore sizes, it is clear from the results presented in Table 2 that the porosity and mean pore diameter effectively increased with increasing GO content ratios. A small addition of 0.07 wt.% of GO resulted in a considerable increase of around 55 and 140% in porosity and mean pore diameter, respectively. For water uptake percentage, the results also displayed a significant increase in water uptake with an increasing GO content ratio. This may be attributed to the GO inclusion into the membrane surface and within the membrane body that could lead to an increase in both the -OH and -COOH hydrogen bonds, effectively enhancing the hydrophilic property of the membrane and increasing the water absorption, in agreement with the contact angle results. To the contrary, the membrane sample with 0.1 wt.% showed no significant increase in the porosity.

Though the presence of well-dispersed GO could obviously improve the morphology, porous structure and pore size, using larger amounts of GO could negatively affect the nature and type of the pores that are formed [43]. With a higher amount of GO nanomaterials (>0.07 wt.%), the membrane properties exhibited contradictory effects [26]. This might be attributed to GO's ability to migrate through the membrane layer toward the surface when the phase-inversion process take place. This could cause significant changes in the membrane's surface pores and hydrophilicity, decreasing water passage and adsorption of water on the membrane's surface [45].

Membrane performance

Water flux

The pure water flux of the prepared nanocomposite membranes was investigated. The results are shown in Figure 4. The results demonstrated an obvious increase in water flux with GO content, up to 0.07 wt.%. The membrane containing 0.07 wt.% of GO exhibited a water flux of 7.9 L/(m^2 h bar), corresponding to an improvement of about 450% in water flux. This result is comparable to what was obtained for the carbon nanotube membrane/GO [46] and the result is higher than what was found for other GO-incorporated, polymer-based membranes, as shown in Table 3. This finding could be related to the increase in membrane hydrophilicity, which is known to enhance the water flux [47], and which is in agreement with contact angle measurements. Furthermore, the increase of the water flux is consistent with SEM images and the obtained increase in porosity and pore size measurements. This enabled migration of more water molecules through the membrane layer and it improved the water flux [48,49]. It has been reported that improvements in hydrophilicity significantly enhance membrane flux as a result of the adsorption of water molecules on the membrane's surface through hydrogen bonding and/or electrostatic interactions [50]. The addition effects of GO on porosity and pore size could further influence membrane permeability. Nevertheless, any further increase in GO content could have decreased the water flux, as the high concentration of nanoparticles could have caused pore blocking, which would have hindered the water transfer [51,52]. On the other hand, bad nanoparticle dispersion or a nanoparticle agglomeration in the membrane interlayer could also have reduced water flux, which would have resulted in poor membrane performance [53].

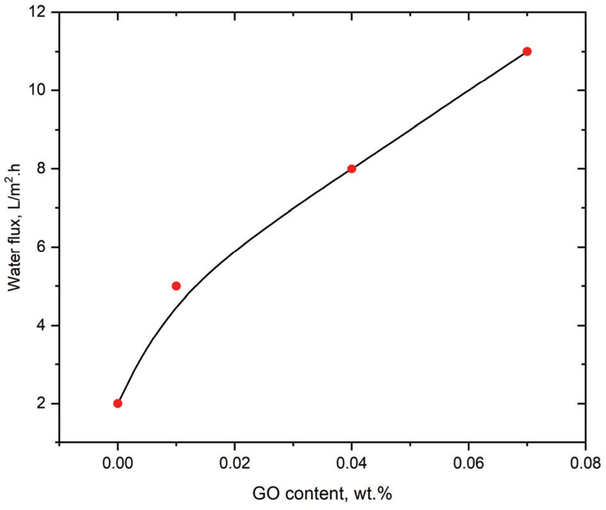

Figure 4. Effect of GO content on the water flux, carried out at a pressure of 1.4 bar.

Salt rejection

The salt rejection efficiency of the prepared membranes was investigated using NaCl and Na_2SO_4 solutions. The results (shown in Figure 5) illustrated an obvious increase in salts rejection with increasing GO content. The results demonstrated a salt rejection of 39% for NaCl and 87% for Na_2SO_4 obtained with 0.07 wt.% of GO, which corresponded to improvements of about 144 and 93% in salt rejection, respectively. Comparisons of performance with other similar GO membranes are shown in Table 3. The nanocomposite membranes of CAB/0.07 wt.% GO illustrated comparable ionic rejection results for NaCl and better results for Na_2SO_4. These results may be explained on the basis of the adsorption properties of the GO nanomaterials, which enhanced the interactions between ions and the membrane matrix, both on the surface and within the pores. Also, such behavior might be related to the possible produced surface charges, which could promote the cation exchange processes. Although this would appear to oppose the trade-off effect that existed between the flux and rejection, a similar observation was reported and proved by Ganesh *et al.* [54].

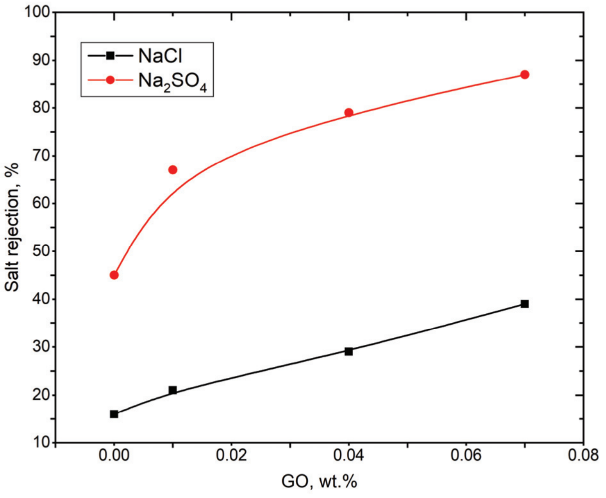

Figure 5. Effect of GO content on the salt rejection efficiency, carried out at a pressure of 1.4 bar.

Effect of permeate volume on the salt rejection

The salt rejection efficiency was also studied against the permeation volume; results are shown in Figure 6. The results clarified that the composite

Table 3. Comparison of flux and salt rejection of different GO-incorporated membranes

Membrane	Water flux, L/(m^2 h bar)	Salt rejection (1000 ppm)		Ref.
		NaCl	Na_2SO_4	
GO	4.76	59%	95.1%	[46]
Carbon nanotube / GO (1:8 mass ratio)	8.02	51.4%	80.0%	[46]
PSF / (1000ppm GO)	2.5	~ 43%	~ 65%	[54]
PSF / (2000ppm GO)	2.5	~ 58%	72%	[54]
CA / (0.005wt.%GO)	0.5	80% (2000ppm)	-	[43]
PES / (0.1wt.%GO)	3.3	-	-	[25]
CAB / (0.07wt.%GO)	7.9	39%	87%	Present work

membranes containing GO showed a higher stable salt rejection with permeate volume, reflecting a higher stability of nanocomposite membrane than the pure CAB membrane. This was observed for both NaCl and Na_2SO_4 solutions. Moreover, the results showed a slight effect on the stability of the nanocomposite membrane with 0.07 wt.% of GO than that of 0.04 wt.% GO. This observation leads to the expectation that increasing GO concentrations of more than 0.07% could provide bad dispersion within the polymeric moiety and lead to lowering the membrane stability. The results obtained regarding this concern showed that the optimal GO concentration to be used in the nanocomposite membrane is 0.07 wt.%.

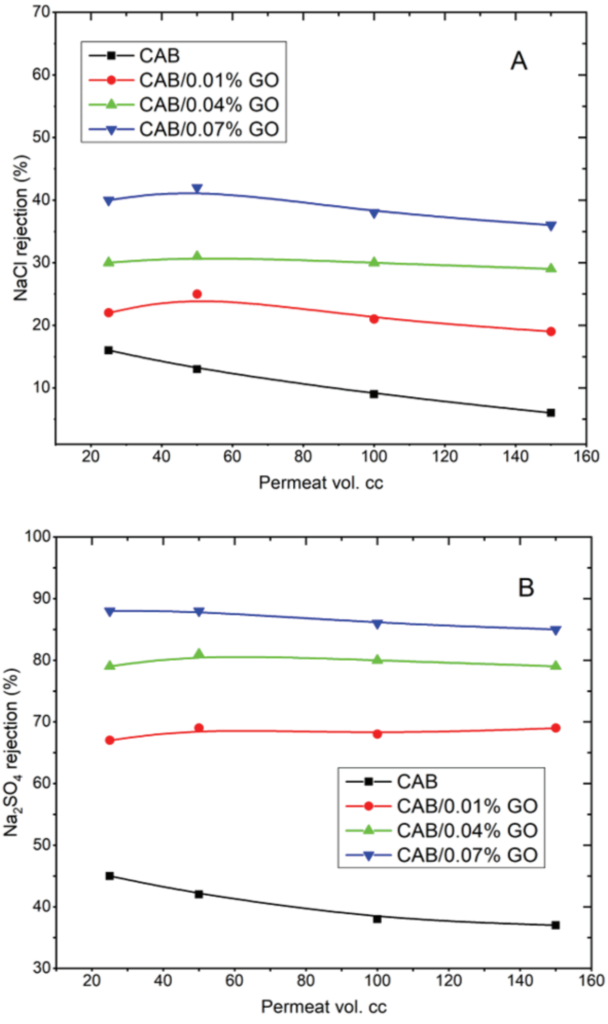

Figure 6. Effect of permeation volume on the salt rejection efficiency: A) for NaCl; B) for Na_2SO_4, using a feed concentration of 1 g/L.

Effect of feed solution concentration on membrane performance

The salt rejection and permeation flux levels of the prepared nanocomposite membranes were also studied at a range of feed concentrations up to 2 g/L. As shown in Figure 7, the results revealed that Na_2SO_4 and NaCl concentrations had a clear effect on membrane performance. A decrease in both salt rejection and permeation flux was noted as feed concentration increased. In terms of salt rejection performance (Figure 7A), a decrease in salt rejection efficiency of about 14% for Na_2SO_4 and 20% for NaCl was attained. This could be attributed to the effect of the Donnan exclusion of co-ions, which could influence the diffusion transport of ions through the membrane [55]. In addition, the effect of high concentrations on the polarization and possible weakening of electrostatic interaction between the ions in the aqueous solution and the charges on the membrane's surface may consequently lead to an increase in ions permeation and therefore decrease rejection efficiency [56].

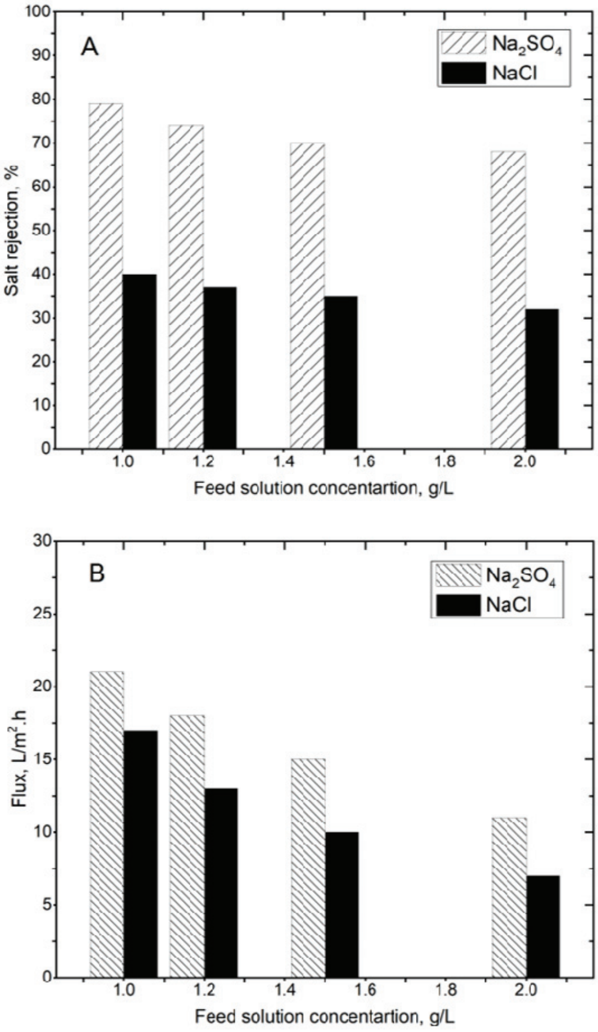

Figure 7. ffect of feed solution concentration of NaCl and Na_2SO_4 on: A) salt rejection efficiency; B) permeation flux rate employing 0.04 wt.% GO nanocomposite membrane at 2.8 bar.

Feed concentration had a more significant effect on permeation flux, with flux reduction of around 49 and 58% for Na_2SO_4 and NaCl solutions, respectively. These results could be explained as follows: as salt concentration increases, there are more ions competing to be adsorbed onto the membrane surfaces; the presence of more ions could decrease pore size and therefore decrease permeation. This finding could also be attributed to concentration polarization, where a denser boundary layer may lead to a decrease in water flux. In addition to the polarization effect, in a high electrolytic solution, the membrane material could shrink and pore size could decrease, causing flux to decrease when feed concentration is higher [57,58].

Antifouling study

The fouling could be considered as the formation of a gel-like layer on the membrane surface as a result of adsorption or the deposition of organic matter within the pores or the surface of the membrane. The improvement of antifouling behavior of the membrane depends on the membrane's hydrophilicity, which could be enhanced by inclusion of hydrophilic groups like -OH and/or -COOH on the membrane surface [59,60]. The CAB/GO composite membranes were highly hydrophilic when compared with pure CAB membranes due to the enhanced water affinity by the presence of GO. The increased water affinity decreased hydrophobic adsorption/deposition of SA on the nanocomposite membrane surface or within the pores. The results presented in Figure 8 represent the water flux of CAB and CAB/GO composite membranes with different GO content ratios. These results show a clear improvement in flux recovery ratio with increasing GO content ratio. This improvement could be attributed to the enhanced hydrophilicity, supported by the change in water contact angle (Table 2). In addition, the presence of GO within the membrane material could create strong electrostatic forces, creating an energetic barrier for the adsorption of SA [61]. Also, the hydroxyl/carboxyl groups of GO could interact with water molecules via Van der Waals forces and hydrogen bonding and forming a molecular layer of water on the membrane surface, which prevents the deposition and/or adsorption of SA [62]. It could be concluded that the presence of GO has an important role in improving antifouling performance of the composite membrane with content up to 0.07 wt.%.

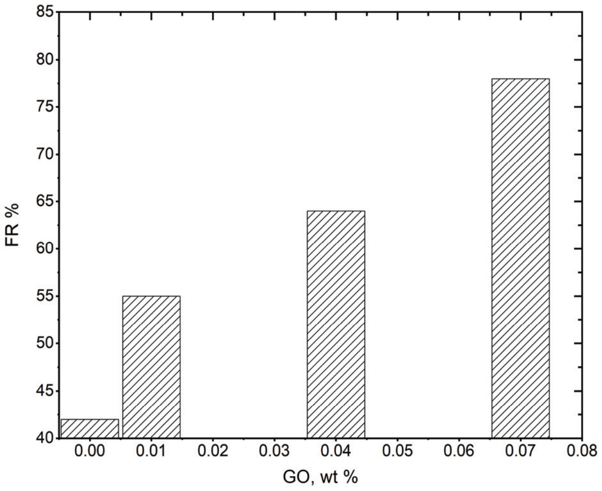

Figure 8. Effect of GO content on the flux recovery ratio of the nanocomposite membranes.

CONCLUSIONS

The results of this work demonstrated characterization and application of a new synthesized membrane nanocomposite of CAB/GO. Based on the results, the nanocomposite membrane proved its significance in terms of improvements in flux, salt rejection, fouling resistance, and stability. As compared to pristine CAB, an increase in the porosity and the pore sizes of membranes with GO content ratios were demonstrated. This resulted in a dramatic improvement in water flux of about 450%, along with 144 and 93% for NaCl and Na_2SO_4 rejection, respectively. Furthermore, the results showed high stability of the nanocomposite membrane toward feed concentration with the separation and flux rate, in addition to higher antifouling and thermal stability properties.

Nomenclature

Symbols

ε	Membrane porosity
W_s	Weight for swollen membrane
W_d	Weight for dry membrane
ρ_w	Density of water
r	Radius of membrane
Q	Volume of permeated water
l	Thickness of membrane
a	Mean pore diameter
μ	Viscosity of water
Q_w	Volume of permeated water per unit time
A	Filtration area
ΔP	Transmembrane pressure
V	Volume of permeate
t	Time interval
C_f	Concentration of the feed
C_p	Concentration of the permeate
$FR\%$	Flux recovery ratio
J_w	Pure water flux
$J_{w,1}$	Pure water flux before fouling

$J_{w,2}$ Pure water flux after fouling

Acknowledgments

The authors extend their appreciation to the Deanship of Scientific Research at King Khalid University for funding this work through the General Research Project under grant number (G.R.P-18-40)".

REFERENCES

[1] C. Güell, R.H. Davis, J. Membr. Sci. 119 (1996) 269-284

[2] A. Akthakul, R.F. Salinaro, A.M. Mayes, Macromolecules 37 (2004) 7663-7668

[3] P. Wang, K.L. Tan, E.T. Kang, K.G. Neoh, J. Adhes. Sci. Technol. 16 (2002) 111-127

[4] F. Liu, C.H. Du, B.K. Zhu, Y.Y. Xu, Polymer 48 (2007) 2910-2918

[5] A.A. El-Zahhar, M.M. Alghamdi, B.M. Asiri, Desalin. Water Treat. 155 (2019) 381-389

[6] H. Rabiee, V. Vatanpour, M.H.D.A. Farahani, H. Zarrabi, Sep. Purif. Technol. 156 (2015) 299-310

[7] V. Vatanpour, M. Esmaeili, M.H.D.A. Farahani, J. Membr. Sci. 466 (2014) 70-81

[8] V. Vatanpour, S.S. Madaeni, A.R. Khataee, E. Salehi, S. Zinadini, H.A. Monfared, Desalination 292 (2012) 19-29

[9] M.M. Alghamdi, A.A. El-Zahhar, B.M. Asiri, Desalin. Water Treat. 165 (2019) 54-62

[10] M.S. Sri Abirami Saraswathi, A. Nagendran, D. Rana, J. Mater. Chem., A 7 (2019) 8723-8745

[11] T. Shibutani, T. Kitaura, Y. Ohmukai, T. Maruyama, S. Nakatsuka, T. Watabe, H. Matsuyama, J. Membr. Sci. 376 (2011) 102-109

[12] X.Y. Qiu, S.W. Hu, Materials 6 (2013) 738-781

[13] A. Shanbhag, B. Barclay, J. Koziara, P. Shivanand, Cellulose 14 (2007) 65-71

[14] S. Vetrivel, D. Rana, M.S. Sri Abirami Saraswathi, K. Divya, N.J. Kaleekkal, A. Nagendran, Polym. Adv. Technol. 30 (2019) 1943-1950

[15] S. Vetrivel, M.S.A. Saraswathi, D. Rana, A. Nagendran, Int. J. Biol. Macromol. 107 (2018) 1607-1612

[16] B.X. Han, D.L. Zhang, Z.Q. Shao, L.L. Kong, S.Y. Lv, Desalination 311 (2013) 80-89

[17] R.K. Joshi, S. Alwarappan, M. Yoshimura, V. Sahajwalla, Y. Nishina, Appl. Mater. Today 1 (2015) 1-12

[18] R. Van Noorden, Nature 442 (2006) 228-229

[19] Y. Wei, Y. Zhang, X. Gao, Z. Ma, X. Wang, C. Gao, Carbon 139 (2018) 964-981

[20] A. Nicolaï, B.G. Sumpter, V. Meunier, Phys. Chem. Chem. Phys. 16 (2014) 8646-8654

[21] Q. Xu, H. Xu, J. Chen, Y. Lv, C. Dong, T.S. Sreeprasad, Inorg. Chem. Front. 2 (2015) 417-424

[22] J. Zhang, Z. Xu, M. Shan, B. Zhou, Y. Li, B. Li, J. Niu, X. Qian, J. Membr. Sci. 448 (2013) 81-92

[23] G.S. Lai, W.J. Lau, P.S. Goh, A.F. Ismail, N. Yusof, Y.H. Tan, Desalination 387 (2016) 14-24

[24] J. Zhang, Z. Xu, W. Mai, C. Min, B. Zhou, M. Shan, Y. Li, C. Yang, Z. Wang, X. Qian, J. Mater. Chem., A 1 (2013) 3101-3111

[25] S. Zinadini, A.A. Zinatizadeh, M. Rahimi, V. Vatanpour, H. Zangeneh, J. Membr. Sci. 453 (2014) 292-301

[26] L.M. Camacho, T.A. Pinion, S.O. Olatunji, Sep. Purif. Technol. 240 (2020) 116645

[27] S.M. Ghaseminezhad, M. Barikani, M. Salehirad, Composites, B 161 (2019) 320-327

[28] Y. Jahani, Desalin. Water Treat. 164 (2019) 62-74

[29] R.J. Lee, Z.A. Jawad, A.L. Ahmad, H.B. Chua, Process Saf. Environ. Prot. 117 (2018) 159-167

[30] P. Kunthadong, R. Molloy, P. Worajittiphon, T. Leejarkpai, N. Kaabbuathong, W. Punyodom, J. Polym. Environ. 23 (2015) 107-113

[31] A.D. Sabde, M.K. Trivedi, V. Ramachandhran, M.S. Hanra, B.M. Misra, Desalination 114 (1997) 223-232

[32] R.J. Lee, Z.A. Jawad, A.L. Ahmad, J.Q. Ngo, H.B. Chua, Improvement of CO2/N-2 separation performance by polymer matrix cellulose acetate butyrate, in: A. Saptoro, W.S. Khur, L.S. Wei, W.P.Q. Ng, M. Anwar, C. Yeo, K.E. Huey (Eds.), 29th Symposium of Malaysian Chemical Engineers, 2017

[33] P. Sun, M. Zhu, K. Wang, M. Zhong, J. Wei, D. Wu, Z. Xu, H. Zhu, ACS Nano 7 (2013) 428-437

[34] S. Liu, T.H. Zeng, M. Hofmann, E. Burcombe, J. Wei, R. Jiang, J. Kong, Y. Chen, ACS Nano 5 (2011) 6971-6980

[35] J.-F. Li, Z.-L. Xu, H. Yang, L.-Y. Yu, M. Liu, Appl. Surf. Sci. 255 (2009) 4725-4732

[36] V. Vatanpour, S.S. Madaeni, R. Moradian, S. Zinadini, B. Astinchap, Sep. Purif. Technol. 90 (2012) 69-82

[37] R. Han, S. Zhang, C. Liu, Y. Wang, X. Jian, J. Membr. Sci. 345 (2009) 5-12

[38] S. Bose, T. Kuila, M.E. Uddin, N.H. Kim, A.K.T. Lau, J.H. Lee, Polymer 51 (2010) 5921-5928

[39] X. Chang, Z. Wang, S. Quan, Y. Xu, Z. Jiang, L. Shao, Appl. Surf. Sci. 316 (2014) 537-548

[40] P. Shanmugaraj, A. Swaminathan, R.K. Ravi, M. Dasaiah, P. Senthil Kumar, A. Sakunthala, J. Mater. Sci.-Mater. Electron. 30 (2019) 20079-20087

[41] J. Alongi, G. Malucelli, Thermal Degradation of Cellulose and Cellulosic Substrates, in: Reactions and Mechanisms in Thermal Analysis of Advanced Materials, A. Tiwari, B. Raj (Eds.), Beverly, Hoboken, NJ, 2015, pp. 301-332

[42] N. Ghaemi, S.S. Madaeni, A. Alizadeh, P. Daraei, A.A. Zinatizadeh, F. Rahimpour, Sep. Purif. Technol. 85 (2012) 147-156

[43] Y. Shi, C. Li, D. He, L. Shen, N. Bao, J. Mater. Sci. 52 (2017) 13296-13306

[44] X. Fu, T. Maruyama, T. Sotani, H. Matsuyama, J. Membr. Sci. 320 (2008) 483-491

[45] P. Daraei, S.S. Madaeni, N. Ghaemi, E. Salehi, M.A. Khadivi, R. Moradian, B. Astinchap, J. Membr. Sci. 415-–416 (2012) 250-259

[46] Y. Han, Y. Jiang, C. Gao, ACS Appl. Mater. Interfaces 7 (2015) 8147-8155

[47] J.-n. Shen, H.-m. Ruan, L.-g. Wu, C.-j. Gao, Chem. Eng. J. 168 (2011) 1272-1278

[48] S. Ansari, A.R. Moghadassi, S.M. Hosseini, Desalination 357 (2015) 189-196

[49] A. Gholami, A.R. Moghadassi, S.M. Hosseini, S. Shabani, F. Gholami, J. Ind. Eng. Chem. 20 (2014) 1517-1522

[50] B.S. Lalia, V. Kochkodan, R. Hashaikeh, N. Hilal, Desalination 326 (2013) 77-95

[51] C.A. Smolders, A.J. Reuvers, R.M. Boom, I.M. Wienk, J. Membr. Sci. 73 (1992) 259-275

[52] X. Chang-Fa, L. Zhao-Feng, J. Appl. Polym. Sci. 41 (1990) 439-444

[53] P. Daraei, S.S. Madaeni, N. Ghaemi, H. Ahmadi Monfared, M.A. Khadivi, Sep. Purif. Technol. 104 (2013) 32-44

[54] B.M. Ganesh, A.M. Isloor, A.F. Ismail, Desalination 313 (2013) 199-207

[55] S.L. Ong, W.W. Zhou, L.F. Song, W.J. Ng, Environ. Eng. Sci. 19 (2002) 429-439

[56] Y. He, G.-M. Li, H. Wang, Z.-W. Jiang, J.-F. Zhao, H.-X. Su, Q.-Y. Huang, J. Taiwan Inst. Chem. Eng. 40 (2009) 289-295

[57] L. Jin, W. Shi, S. Yu, X. Yi, N. Sun, C. Ma, Y. Liu, Desalination 298 (2012) 34-41

[58] L.M. Jin, S.L. Yu, W.X. Shi, X.S. Yi, N. Sun, Y.L. Ge, C. Ma, Polymer 53 (2012) 5295-5303

[59] S.S. Madaeni, N. Ghaemi, J. Membr. Sci. 303 (2007) 221-233

[60] S.S. Madaeni, S. Zinadini, V. Vatanpour, J. Membr. Sci. 380 (2011) 155-162

[61] K. Nakamura, K. Matsumoto, J. Membr. Sci. 280 (2006) 363-374

[62] V. Vatanpour, S.S. Madaeni, R. Moradian, S. Zinadini, B. Astinchap, J. Membr. Sci. 375 (2011) 284-294.

MAJED M. ALGHAMDI[1]
ADEL A. EL-ZAHHAR[1,2]

[1]Environmental Monitoring, Assessment & Treatment (EMAT) Research Group, Department of Chemistry, College of Science, King Khalid University, Abha, Saudi Arabia
[2]Nuclear Chem. Dept. AEA, Cairo, Egypt

NAUČNI RAD

NANOKOMPOZITNA MEMBRANA NA BAZI CELULOZNOG ACETO-BUTIRATA I GRAFEN-OKSIDA: IZRADA, KARAKTERIZACIJA I PERFORMANSE

U ovoj radu, istraživani su efekti nanopropusnih listova grafen oksida (GO) na fizičko-hemijska svojstva i performanse membrana na bazi celuloznog aceto-butirata (CAB). Nanokompozitne membrane su proizvedene korišćenjem CAB i male količine GO u opsegu 0-0,07% primenom konvencionalne metode fazne inverzije. Membrane su okarakterisane različitim metodama, a njihove performanse su testirane pomoću sistema za filtraciju sa proticanjem normalno na membranu. U poređenju sa tradicionalnom CAB membranom, eksperimentalni rezultati su pokazali poboljšanje karakteristika, kao što su hidrofilnost, propustljivost, izdvajanje soli, protiv-obrastanje i stabilnost. Rezultati su dokazali povećanje poroznosti i veličine pora membrana uz dodatak GO. Dalje, membrana koja sadrži 0,07% GO pokazala je nizak kontaktni ugao od 37° i dramatično poboljšanje vodenog fluksa od oko 450% (od 2 do 11 L/(m^2/h)). Štaviše, pokazalo je izbacivanje soli od 39% za NaCl i 87% za Na_2SO_4, što odgovara poboljšanjima od oko 144, odnosno 93%. Dalje, rezultati su pokazali veće svojstvo protiv-obrastanja sa 86% poboljšanjem fluksa i većom stabilnošću u pogledu performansi i termičkih svojstava u poređenju sa CAB.

Ključne reči: celulozni acetate-butirat, grafen-oksid, nanokompozit, membrana, izdvajanje soli.

Chemical Industry & Chemical Engineering Quarterly

Available on line at
Association of the Chemical Engineers of Serbia *AChE*
www.ache.org.rs/CICEQ

Chem. Ind. Chem. Eng. Q. 27 (1) 45–55 (2021) CI&CEQ

LIS DA SILVA OSTIGARD
SILVANA MATTEDI

Federal University of Bahia, Polytechnic School, Chemical Engineering Department, Graduate Program in Chemical Engineering, Salvador, BA, Brazil

SCIENTIFIC PAPER

UDC 536.24:665.6:54:66:004

THERMAL PERFORMANCE EVALUATION OF HOT OILS AND NANOFLUIDS BY SIMULATION OF AN INDIRECT HEATING PLANT

Article Highlights

- Performance evaluation of heat transfer fluids by steady-state simulation of a hot oil system
- Thermal performance comparison between two nanofluids and a paraffinic oil
- A hot oil system in a real industrial plant was considered in the study performed
- Paraffinic oil showed better adjustment to heat duty required by the system
- Paraffinic oil presented operational clearance when compared with the current heat transfer fluid

Abstract

This paper aims to analyze the thermal performance of four different heat transfer fluids in a hot oil system located in a paraffin hydrotreatment and fractionation plant of a petroleum refinery. The software Petro-SIM® (KBC--Yokogawa) was employed to elaborate steady-state simulations intended to compare the heat transfer fluid currently used (eutectic of biphenyl and diphenyl oxide) and three fluids proposed as substitutes: paraffin oil (namely n-C_{13}^{+}*) produced in the same industrial unit, a nanofluid of eutectic of biphenyl and diphenyl oxide and copper at a 6% volume fraction, and a CuO/polydimethylsiloxane nanofluid at a 6% volume fraction. The results showed that n-*C_{13}^{+}* was the only heat transfer fluid that could replace the eutectic diphenyl oxide/biphenyl in the system under analysis since it absorbed the heat duty of 13.79 Gcal/h, which exceeded the thermal energy of 10.57 Gcal/h absorbed by the heat transfer fluid currently used at the same operating parameters. The Cu/eutectic of biphenyl and diphenyl oxide and CuO/polydimethylsiloxane nanofluids presented lower heat duty than the energy needed for the operation of the hot oil system, which was 8.31 and 8.51 Gcal/h, respectively.*

Keywords: heat transfer, heat transfer fluid, hot oil, nanofluids, simulation.

Heat transfer fluids, also known as hot oils, are used for heating or cooling in industrial and household applications. They are of great importance to the world's energy demand as more than 70% of all energy consumed is *produced* by heat transfer [1].

In industrial processes, heat transfer fluids are employed as either vapor or liquid or phase equilibrium of both. Besides water and steam, other substances such as mercury, sodium, potassium, molten salts, and synthetic oils are used for both heating and cooling, each one possessing suitable characteristics for the different application fields according to the desired temperature range [2]. Figure 1 presents the categories discussed by Álvarez [1] as the most commonly used heat transfer fluids in industrial processes.

The oils mentioned in this work belong to the categories of thermal oils and nanofluids. These heat transfer fluids are represented in the figure below as

---

Correspondence: S. Mattedi, Federal University of Bahia (UF-Ba), Polytechnic School, Chemical Engineering Graduate Program, Aristides Novis Street, No. 2, Zip code 40210-630, Salvador, BA, Brazil.
E-mail: silvana@ufba.br
Paper received: 11 October, 2019
Paper revised: 20 May, 2020
Paper accepted: 8 July, 2020

https://doi.org/10.2298/CICEQ191011023O

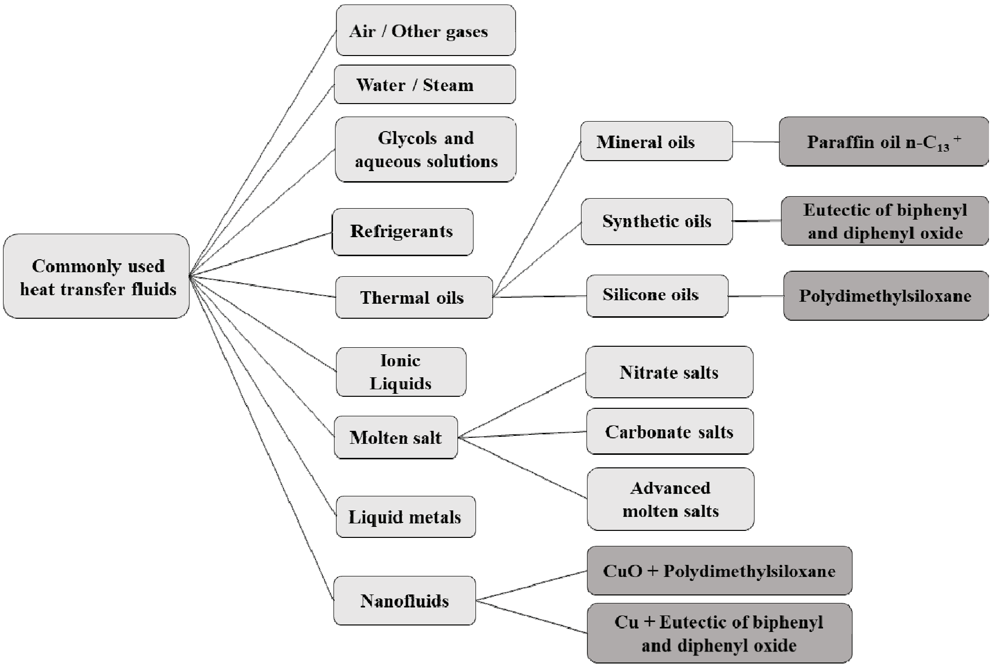

Figure 1. Most commonly used heat transfer fluids. Adapted from Alvarez [1].

the mineral paraffin oil *n*-C_{13}^{+}, the synthetic oil eutectic of biphenyl and diphenyl oxide, the silicon oil polydimethylsiloxane, the nanofluid of copper/eutectic of biphenyl and diphenyl oxide, and the nanofluid of polydimethylsiloxane with copper oxide particles.

Synthetic oils such as Malotherm® TH, Syltherm® 800, Therminol® VP-1, Dowtherm® A and Sandotherm® 59 are commonly used in closed indirect heating systems of industrial processes in general [3]. Besides their application in petroleum plants, petrochemical plants, and refineries, these thermal oils are currently employed in solar power plants, which are considered promising sources of alternative and renewable energy. The fluid acts as a medium for transferring and storing the heat captured by the solar parabolic trough collectors for later conversion into electrical energy [4].

The selection of the most suitable type of hot oil is of great importance to minimize costs and obtain the maximum performance from industrial facilities [1]. Requirements include low reactivity, long-term stability, and low freezing point. Proper characterization of the physical-chemical properties of the fluid is paramount for the design and monitoring of the operation of the industrial unit. The most significant parameters in the evaluation of heat transfer are density, heat capacity, viscosity, and thermal conductivity [5].

The heat transfer fluids currently used have maximum working temperatures of about 400 °C [3]. Molten salts can be used in applications where the temperature can reach 500 °C. However, corrosion and erosion of piping and equipment should be previously evaluated [6]. Liquid metals, such as pure, binary, and eutectic mixtures are suitable for high-temperature operation, above 1000 °C, because their boiling temperature can reach 1300 °C, approximately [6].

An alternative way to increase the allowable operating range for these heat transfer fluids is the addition of nanoparticles of up to 100 nm, which turns them into nanofluids [7].

Research related to nanofluids began in the 1990s, when this nomenclature was used by Choi and Eastman [8] to categorize heat transfer fluids containing nanoparticles in suspension in order to increase their thermal conductivity.

Solid nanoparticles incorporated at low concentrations into conventional heat transfer fluids are generally metals, metal oxides, and carbon-based structures (including nanotubes). This modification of the base substance results in better heat and mass transfer performance by changing the physical-chemical properties of the fluid [9].

Studies in this field of application have been developed looking for novel heat transfer fluids that could provide higher thermal conductivity and thermal stability, which could result in a better thermal performance of the nanofluids. Some of these studies are discussed below.

Kumar *et al.* [7] performed an experimental study with aluminum oxide nanofluids at 0.02, 0.04, 0.06 and 0.08% volume fractions using water, ethylene-glycol and paraffin oil as base fluids. Improvement in the convection heat transfer coefficient was observed in all nanofluids evaluated, influenced by the nanoparticle concentration and higher turbulence.

Using the eutectic mixture of biphenyl and diphenyl oxide as base fluid, Navas *et al.* [10] obtained an 11% increase in the convection heat transfer coefficient by adding copper nanoparticles at a concentration of 5 ppm. Yasinskiy *et al.* [4] documented a 35.4% improvement for the same coefficient in a nanofluid containing 2.44 vol.% of titanium oxide.

Mwesigye *et al.* [11] evaluated the thermal and thermodynamic performance of Cu-Therminol® VP-1 at a high concentration ratio parabolic solar trough collector by means of a numerical study. The authors were able to enhance the heat transfer by 32% with the nanoparticle volume fraction of 6% in the nanofluid.

Bellos and Tzivanidis [12] analyzed different fluids aiming to optimize a solar-driven trigeneration system that featured the organic Rankine cycle (ORC), an absorption heat pump and parabolic trough solar collectors operating with nanofluids. The study investigated nanofluids of polydimethylsiloxane added with CuO and Al_2O_3 in the solar field loop of the trigeneration system. The optimum combination found was with the use of toluene in the ORC and CuO nanofluid at 4.35% in the parabolic trough collectors, which led to the maximum energy efficiency of 24.66%.

Sarafraz *et al.* [13] experimentally evaluated the flow boiling heat transfer coefficient, pressure drop, and fouling resistance of an MgO/Therminol® 66 nanofluid. The authors observed that the nanofluid, at 0.1, 0.2 and 0.3% mass fractions, caused an improvement of the characteristics under evaluation compared to pure Therminol® 66. The lowest concentration nanofluid led to the highest enhancement (about 23.7%) of the heat transfer coefficient.

Sarafraz and Arjomandi [14] experimentally examined the use of gallium and aluminum oxide nano-suspensions to replace water as the heat transfer fluid of a microchannel solar thermal receiver. The nanofluids were prepared at 5, 10 and 15% mass fractions and the authors observed that the nano-suspension at 10% mass fraction presented the best thermal performance to that application. Sarafraz *et al.* [15] experimentally studied gallium and copper oxide nano-suspensions using the same methodology as Sarafraz and Arjomandi [14] and found that the CuO nanofluid at 10% mass fraction had the best performance in heat transfer. Sarafraz and Arjomandi [16] experimentally assessed the thermal performance, pressure drop, and friction factor of a CuO/In nanofluid in microchannel heat exchanging systems as a plausible coolant to be used in solar thermal receivers. The authors' investigation showed that the studied nanofluid had great potential for applications in the temperature range from 170 to 300 °C.

Jalali *et al.* [17] numerically examined the laminar heat transfer of oil and multi-wall carbon nanotubes (MWCNT) nanofluids varying from 0 to 4% volume fractions to be used as cooling fluid jet. The authors observed that the enhancement in the conductivity provided by the increase in the nanoparticle concentration had positive effects in the heat transfer and promoted a better performance of the cooling fluid jet.

In this paper, a closed indirect heating system is analyzed, similar to that shown in Figure 2, concerning the thermal performance of hot oils and nanofluids. The objective is to verify if the oils under investigation can replace Dowtherm® A (fluid currently used), considering the operating conditions of the industrial unit, ensuring that the temperatures required by the four heat exchangers of the system are met.

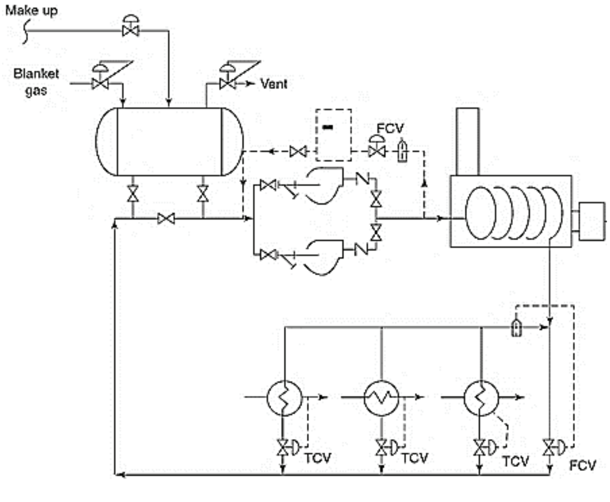

Figure 2. Typical hot oil system. Adapted from Bahadori [2].

In order to check how well the hot oils and nanofluids studied in this work suit the application of interest concerning heat transfer performance, the Petro-SIM® process simulator version 6.2 (KBC-Yokogawa) was employed. This tool has the key feature of providing thermodynamic packages to characterize hydrocarbons and substances present in petroleum refining processes in general. This allows the prediction of the properties of these compounds under different pressure, temperature, and concentration conditions through robust and reliable calculations [18].

Petro-SIM® provides information to determine whether the proposed heat transfer fluid suits the process by using operating and design data of the industrial plant analyzed in this study.

The fluids evaluated in this work are the eutectic mixture of biphenyl and diphenyl oxide (commercially known as Dowtherm® A or Therminol VP-1) [19,20], the paraffin fluid n-C_{13}^{+}, the nanofluids made of Dowtherm® A and copper particles, and Syltherm® 800 (polydimethylsiloxane) [21] containing copper oxide particles.

METHODOLOGY

Designing the simulations

The hot oil system studied in this paper was designed to use a eutectic mixture of diphenyl and biphenyl oxide as an indirect heat transfer medium into four heat exchangers, namely HT-01, HT-02, HT-03 and HT-04. The system provides thermal energy to a paraffin hydrotreatment and fractionation plant in a range from C_8 to C_{18}. Exchangers HT-01 and HT-02 preheat the process streams that feed a reactor, whereas HT-03, HT-04 are distillation column reboilers.

The heating process occurs as discussed by Bahadori [2] and Couto [22]. The oil is pumped and heated in a furnace (or some other heat source that forms the very process, such as steam exhausted from a turbine, for instance). The temperature of the heat transfer fluid typically rises from 11 to 55 °C at the furnace outlet and is distributed to the heat exchangers to meet the heat transfer requirements of the process. After that, the oil returns to an expansion vessel from where it is pumped again, restarting the cycle.

The first piece of information to be provided to Petro-SIM® in assembling simulation is the thermodynamic model that will represent the substances involved. The method for calculating the density of liquid substances should also be chosen in this step of the simulation setting.

The Peng-Robinson equation of state (1976), presented in Eq. (1), was chosen because it is a system primarily composed of nonpolar organic molecules, especially hydrocarbons in the liquid and gas phase at low-pressure conditions:

$$P=\frac{RT}{(v-b)}-\frac{a}{v(v+b)+b(v-b)} \tag{1}$$

The density of the liquid substances was calculated by the software according to Eqs. (2)-(5), which represent the correspondent state correlation (COSTALD), published in 1979 by Hankinson and Thompson, and which exhibits good reliability for gases in general as well as saturated and subcooled liquids [23]:

$$\frac{1}{\rho_s}=\frac{V_{sm}V_{rm}\left[1-\omega f\left(T_{rm}\right)\right]}{M_m} \tag{2}$$

$$V_{rm}=1+\sum_{k=1}^{4}\left(\alpha_k\theta^k\right) \tag{3}$$

$$\theta=\left(1-T_{rm}\right)^{1/3} \tag{4}$$

$$f\left(T_{rm}\right)=\sum_{k=1}^{4}\left(\frac{b_kT_{rm}^{\ (k-1)}}{T_{rm}-1}\right) \tag{5}$$

In the hydrotreatment and fractionation process, the paraffin heated by the hot oil consist of mixtures whose compositions are complex and variable within ranges considered suitable as specifications. Therefore, some simplifications were made to design the simulations. Table 1 shows which compounds and substances were considered cold fluids in each of the heat exchangers of the hot oil system.

Table 1. Cold fluid of each heat exchanger in the hot oil system

Heat exchanger	Cold fluid
HT-01	n-C_8 to n-C_{18}
HT-02	Hydrogen
HT-03	n-C_9 to n-C_{18}
HT-04	n-C_{13} to n-C_{18}

For an easier characterization of the composition of each of the hydrocarbon streams present in the exchangers HT-01, HT-03 and HT-04, only linear paraffins were assumed to be part of their compositions, as these alkanes represent more than 90% in mass of the streams mentioned.

The present work employed a simulation of the paraffin fractionation distillation columns T-01 and T-02, whose reboilers are HT-03 and HT-04, respectively. For this step, shown in Figure 3, it was needed to obtain the composition of these exchangers' paraffin streams as only the linear paraffin feed stream for T-01 is characterized by routine laboratory analyses. Table 2 contains the standardized feed stream composition of T-01 considered in this study.

Figure 3 contains the distillation columns T-01 and T-02 and the process streams, which are called FEED (n-paraffins C_8 to C_{18}), N-C10-, GAS-C10-, N-C10C13, N-C13+. The energy streams to reboiler were labeled E-HT-03 and E-HT-04. The other streams of this kind were represented E-*n*, (where *n* is a two-digit number from 05 to 08).

By analyzing the datasheets and technical documentation of the equipment that makes up this section of the industrial plant, it was possible to obtain

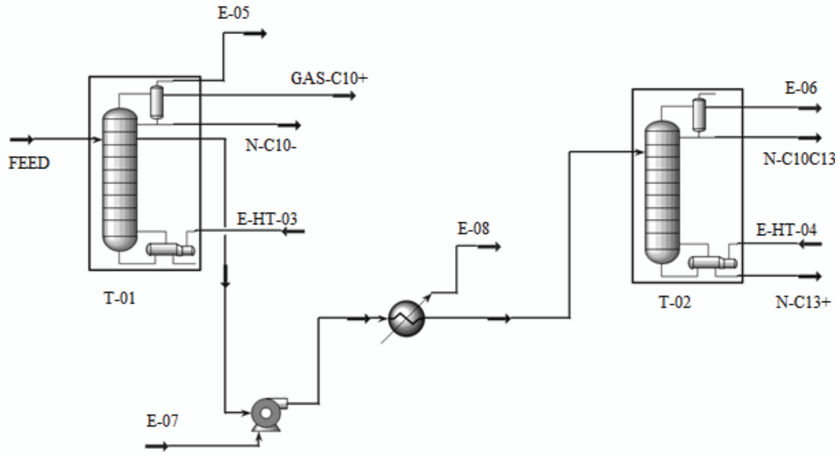

Figure 3. Simulation on Petro-SIM® for fractionation system which contains the reboilers HT-03 and HT-04.

the flow rate, pressure, temperature, pressure drop, and heat transfer area that constitute the design basis of each piece of equipment. Tables 3 and 4 show the data used as inputs to represent these operating conditions in Petro-SIM®.

Table 2. Composition of feed stream to T-01

Component	Feed stream to T-01, mass%
C_8H_{18}	1.65
C_9H_{20}	3.86
$C_{10}H_{22}$	10.98
$C_{11}H_{24}$	21.20
$C_{12}H_{26}$	21.71
$C_{13}H_{28}$	20.54
$C_{14}H_{30}$	14.09
$C_{15}H_{32}$	5.08
$C_{16}H_{34}$	0.79
$C_{17}H_{36}$	0.09
$C_{18}H_{38}$	0.01

Table 3. Input data for pump, furnace, expansion vessel and control valve of the hot oil system

Parameter	P-01	F-01	V-01	PV-01
Flow rate, m³/h	533.0	-	-	-
Inlet pressure, MPa g	1.11	2.30	-	1.52
Outlet pressure, MPa g	2.82	1.57	1.11	1.12
Inlet temperature, °C	350.0	350.0	-	350.0
Outlet temperature, °C	-	385.0	-	-

The simulator calculated the heat exchangers by the steady state rating, which assesses steady-state heat transfer for shell-and-tube-type heat exchangers, considering the stream arrangement, the heat transfer resistance by deposits, and its construction model [24].

The convergence criterion in the exchanger's heat transfer calculation is informed to satisfy the degrees of freedom to the system of equations. The standard configuration of the equipment block in the simulator recommends using the energy balance for hot and cold fluid (Eq. (6)) and the heat transfer equation (Eq. (7)) [24]:

$$\dot{m}_{hot}C_{p\,hot}\Delta T_{hot} - \dot{m}_{cold}C_{p\,cold}\Delta T_{cold} = 0 \qquad (6)$$

$$\dot{Q} = UAf_t\Delta T_{ml} \qquad (7)$$

Based on all the information obtained and assumptions made, the hot oil system was represented in the simulations as shown in Figure 4. Considering the substitute heat transfer fluids proposed in this work, the system was represented in four different operating conditions, where the first one was exactly as foreseen in the design and the others modifying only the heat transfer fluid that circulates through the system.

The devices P-01, F-01, V-01, and the control valve PV-01, were tagged in Figure 4. Heat losses and pressure drops were represented using the terms HLOSS and PDROP, respectively. All the energy

Table 4. Input data for heat exchangers of the hot oil system

Parameter	HT-01		HT-02		HT-03		HT-04	
	Shell	Tubes	Shell	Tubes	Shell	Tubes	Shell	Tubes
Flow rate, m³/h	22.01	46.08	6.66	6.08	77.67	23.78	562.60	237.80
Inlet pressure, MPa g	10.79	1.57	10.79	1.51	0.14	1.52	0.14	1.51
Pressure drop, MPa	0.05	0.02	0.01	0.01	0.00	0.16	0.00	0.18
Inlet temperature, °C	203.0	370.0	38.0	370.0	385.0	255.0	385.0	302.1

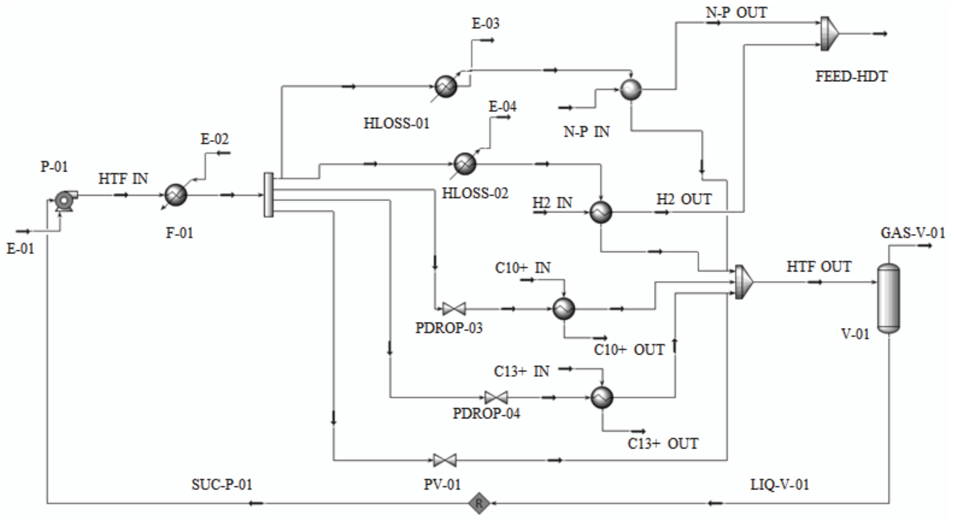

Figure 4. Petro-SIM® simulation for the hot oil system.

streams were labeled E-*n*, (where *n* is a two-digit number from 01 to 04), and the process streams as N-P (for *n*-paraffins), H_2, C10+ and C13+.

The validation of the first simulation was necessary to guarantee that Petro-SIM® reliably represented the cases where the thermal oil is not the eutectic mixture of biphenyl and diphenyl oxide.

The first option was the paraffin oil obtained at the bottom stream of tower T-02. As it is a by-product of the industrial unit where the hot oil system is located, there would be no additional costs for the production of the replacement fluid. In fact, the costs would be reduced since an inventory of synthetic oil from the current heat transfer fluid manufacturer would become unnecessary.

Nanofluid 1 (Cu + eutectic of diphenyl oxide and biphenyl) was selected as a possible substitute as it showed a 12.5% increase in heat transfer efficiency in parabolic solar collectors compared to the base thermal oil reported by Mwesigye *et al.* [11]. This case was simulated to evaluate if the modification of the thermophysical properties of the current working fluid with the addition of copper particles (6 vol.%) could represent a possible increase in productivity gains for the industrial unit due to the more efficient heat transfer.

Nanofluid 2 (composed of CuO + polydimethylsiloxane) was chosen because it achieved a maximum efficiency increase of 24.66% when applied to a trigeneration system as discussed by Bellos and Tzivanidis [12]. Thus, a simulation of the hot oil system was elaborated for this case, aiming to check the performance of this nanofluid at a concentration of 6.0% so as to find positive results, similar to those reported by those authors.

Inclusion of hypothetical components for the evaluation of nanofluids

The addition of nanometer-sized particles in conventional heat transfer fluids causes the enhancement of thermophysical properties, which in turn leads to greater efficiency in heat transfer processes [11].

The nanofluids selected for performance simulations in the studied system were polydimethylsiloxane with CuO (6 vol.%) and a eutectic mixture of biphenyl and diphenyl oxide containing Cu (6 vol.%) developed by Bellos and Tzivanidis [12] and Mwesigye *et al.* [11], respectively.

Since nanofluids are not present in the simulator database, it was necessary to characterize each studied nanofluid as a pure hypothetical component whose density, viscosity, thermal conductivity, and heat capacity properties could be adjusted by data regression so that there was an agreement with the data presented in above cited studies.

Petro-SIM® uses the UNIFAC method to construct the hypothetical component molecule and, based on the contributions of the subgroups added to the structure, calculates the thermodynamic parameters to the new substance [24].

Considering that the base fluids are, respectively, a siloxane-type polymer and a eutectic mixture of aromatic compounds, specific strategies to configure each of them as hypothetical components were needed.

The eutectic mixture of biphenyl and diphenyl oxide was represented by counting the subgroups that constitute both molecules. After this procedure, the proportionality of the mixture was applied according to Table 5 [5], where the sum of the results represents the number of subgroups that were supplied to the simulator for the hypothetical molecule, according to Table 6.

Table 5. Eutectic mixture of biphenyl and diphenyl oxide

Component	Content, mol%
Biphenyl	26.5
Diphenyl oxide	73.5

Table 6. Composition and subgroups for eutectic of biphenyl and diphenyl oxide and hypothetical compound configured on Petro-SIM®

Subgroup	Eutectic mixture		Hypothetical compound
	Biphenyl	Diphenyl oxide	Hypothetical molecule
	Content, mol%		
	26.50	73.50	100.00
ACH	5.00	10.00	10.00
AC	1.00	1.00	1.26
CHO	-	1.00	0.74

The adherence of the proposed component to the characteristics of the actual eutectic mixture was verified by comparing the critical properties and molecular mass calculated by the simulator with the values reported by the manufacturer according to Table 7.

Table 7. Comparison of critical properties and molecular weight for eutectic of biphenyl and diphenyl oxide and hypothetical compound

Property	Eutectic of biphenyl and diphenyl oxide	Hypothetical compound	Error %
Molecular weight, g/mol	166.0	162.0	2.41
Critical temperature, °C	497.0	497.1	0.02
Critical pressure, MPa g	3.13	3.50	11.64
Critical volume, L/mol	0.526	0.449	14.65

In order to construct a representative structure of polydimethylsiloxane (commercially known as Syltherm® 800), the subgroups present in Figure 5 [21] were identified, and their quantity estimated according to Table 8 so that the critical properties were as close as possible to the information in the manufacturer's catalog. Table 9 contains the results obtained with the percentage error associated with each parameter.

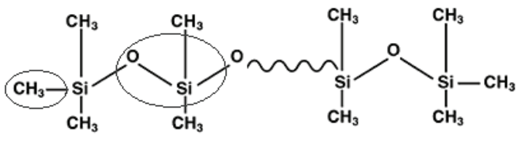

Figure 5. Polydimethylsiloxane polymeric structure. Adapted from Syltherm® 800 Heat Transfer Fluid [21].

Table 8. Representative (hypothetical) structure for polydimethylsiloxane

Subgroup	Structure
SiO	9
CH_3	33

Table 9. Comparison of critical properties and molecular weight for polydimethylsiloxane and hypothetical compound

Property	Polydimethyl-siloxane	Hypothetical compound	Error %
Molecular weight, g/mol	-	980.2	-
Critical temperature, °C	367.0	367.9	0.25
Critical pressure, MPa g	1.09	1.06	3.21
Critical volume, L/mol	3.22	2.93	9.00

Adjustment of the thermophysical properties of the nanofluids

The characterization of the density, viscosity, thermal conductivity, and specific heat of nanofluids is crucial to evaluate their efficiency in the heat transfer phenomena involved in industrial applications [10].

Mwesigye *et al.* [11] calculated the thermophysical properties for the suspension of copper nanoparticles in the eutectic mixture of biphenyl and diphenyl oxide by means of three sets of equations: one for the base fluid, one for the nanoparticles, and another one for the nanofluid.

The polynomials obtained for the base fluid as a function of the temperature (Eqs. (8)-(12)) were derived considering values between 285.15 to 698.15 K based on the data provided by the manufacturer in the product catalog. Eqs. (13)-(15), for copper particles, can be found in the property tables of Incropera *et al.* (2006) [11,25]:

$$\rho = 1.4386\times10^{3} - 1.8711T + 2.737\times10^{-3}T^{2} - \\ -2.3793\times10^{-6}T^{3}\,(\mathrm{kg/m^3}) \tag{8}$$

$$k = 0.14644 + 2.0353\times10^{-5}T - 1.9367\times10^{-7}T^{2} + \\ +1.0614\times10^{-11}T^{3}\,(\mathrm{W/m\,K}) \tag{9}$$

$$C_p = 2.125\times10^{3} - 11.017T + 0.0499T^{2} - \\ -7.766\times10^{-5}T^{3} + 4.394\times10^{-8}T^{4}\,(\mathrm{J/kg\,K}) \tag{10}$$

$$\mu = 366.1 - 3.0154T + 8.3409\times10^{-3}T^{2} - \\ -7.723\times10^{-6}T^{3}\,(\mathrm{mPa\,s}) \\ (285.15\ \mathrm{K} \le T \le 373.15\ \mathrm{K}) \tag{11}$$

$$\mu = 23.165 - 0.1476T + 3.617\times10^{-4}T^{2} - \\ -3.984\times10^{-7}T^{3} + 1.654\times10^{-10}T^{4}\,(\mathrm{mPa.\,s}) \\ (373.15\ \mathrm{K} \le T \le 698.15\ \mathrm{K}) \tag{12}$$

$$\rho_{Cu} = 8993.0 \text{ kg/m}^3$$

$$k_{Cu} = 441.6 - 0.17119T + 1.5446\times10^{-4}T^2 - \\ -7.2917\times10^{-8}T^3\,(\text{W/m K}) \quad (14)$$

$$C_{pCu} = 258.8 + 0.44631T - 5.2054\times10^{-4}T^2 - \\ -2.3958\times10^{-7}T^3\,(\text{J/kg K}) \quad (15)$$

The calculation of nanofluid properties (nf index) considers the base fluid (bf index), nanoparticles (np index), and volume concentration of particles (φ) in Eqs. (16)-(20) [11]:

$$\rho_{nf} = (1-\varphi)\rho_{bf} + \varphi\rho_{np} \quad (16)$$

$$k_{bf} = 0.25\left[(3\varphi-1)k_{np} + (2-3\varphi)k_{bf} + \sqrt{\Delta}\right] \quad (17)$$

$$\Delta = \left[(3\varphi-1)k_{np} + (2-3\varphi)k_{bf}\right]^2 + 8k_{bf}k_{np} \quad (18)$$

$$C_{pnf} = \frac{(1-\varphi)C_{pbf}\rho_{bf} + \varphi C_{pnp}\rho_{np}}{(1-\varphi)\rho_{bf} + \varphi\rho_{np}} \quad (19)$$

$$\mu_{nf} = \mu_{bf}\left(123\varphi^2 + 7.3\varphi + 1\right) \quad (20)$$

Bellos and Tzivanidis [12] characterized the thermophysical properties of a polydimethylsiloxane nanofluid containing copper oxide particles. Base fluid parameters are temperature dependent and were obtained from data provided by the manufacturer's catalog. The properties of the nanofluids are calculated through Eqs. (16) and (21)-(23) [12]:

$$k_{nf} = k_{bf}\frac{k_{np} + 2k_{bf} + 2(k_{np} - k_{bf})(1-\beta)^3\varphi}{k_{np} + 2k_{bf} - (k_{np} - k_{bf})(1-\beta)^3\varphi} \\ (\beta = 0.1) \quad (21)$$

$$C_{pnf} = \frac{\rho_{bf}(1-\varphi)}{\rho_{nf}}C_{pbf} + \frac{\rho_{np}\varphi}{\rho_{nf}}C_{pnp} \quad (22)$$

$$\mu_{nf} = \mu_{bf}\left(1 + 2.5\varphi + 6.5\varphi^2\right) \quad (23)$$

Copper oxide nanoparticles are present in the nanofluid at a concentration (φ) of 6.0% by volume and were characterized with a density (ρ_{np}) of 6320.0 kg/m³, thermal conductivity (k_{np}) of 77.0 W/(m K) and specific heat ($C_{\text{p np}}$) of 532.0 J/(kg K) [12].

With all the mathematical framework presented, data was regressed in Petro-SIM® in the temperature range from 303.15 to 653.15 K. Thus, each of the configured hypothetical compounds well represented the thermophysical properties of the respective nanofluids in the elaborated steady-state simulations.

RESULTS AND DISCUSSION

Representation of design conditions

The representation of the design parameters in the simulation was validated based on two main criteria: the heat duty associated with each heat exchanger and the comparison between the temperature at the beginning of the cycle (suction of pump P-01) and at the end of the cycle (liquid stream from the expansion vessel V-01).

Table 10 presents the percentage difference between the simulated heat duty values and those reported in the datasheets of each one of the exchangers that make up the hot oil system.

Table 10. Percentage Error, comparing heat exchanger duty simulated and from the equipment datasheet

Heat exchanger	Error, %
HT-01	0.00
HT-02	+3.58
HT-03	+8.00
HT-04	-1.48

All the heat exchangers showed satisfactory adherence, with the largest deviation being 8.0% for reboiler HT-03. This result can be justified by the lack of data on the composition of the *n*-paraffin streams used as a cold fluid for HT-03 and HT-04, and therefore it was necessary to obtain them from previous simulations of the fractionation towers T-01 and T-02, illustrated in Figure 3.

The T-01 feed stream was considered to be an average mass composition based on various results of routine laboratory analysis. The greater number of uncertainties associated with these exchangers may have caused a higher percentage error for HT-03, although it was still possible to obtain good adjustment for HT-04.

The temperature found for the liquid stream of the expansion vessel was exactly 2.0% higher than the suction temperature of pump P-01. Since these streams are actually only one and as the present study deals with a closed-loop system, this result indicates a good representation of the cycle, and the deviation can be explained by heat losses to the environment that were not represented in the simulation.

The heat duty supplied by furnace F-01 to the hot oil was 10.57 Gcal/h and served as a parameter for comparison with the other fluids evaluated in this paper because this energy demand is directly linked to the heat that is transferred from the heat exchangers to the process streams, considering Eq. (24) when losses to the environment are negligible:

$$Q_{F-01} = Q_{HT-01} + Q_{HT-02} + Q_{HT-03} + Q_{HT-04} \tag{24}$$

Since the simulation of design basis in Petro-SIM® presented satisfactory representativeness, it was possible to develop, with good reliability, the following topic in which possible substitutes for the eutectic mixture of biphenyl and diphenyl oxide are analyzed.

Performance evaluation of proposed heat transfer fluids

In this section, the term "paraffin fluid" refers to the *n*-C_{13}^{+} stream. The eutectic mixture of biphenyl and diphenyl oxide with 6 vol.% copper nanoparticles was labeled "Nanofluid 1", and the mixture composed of polydimethylsiloxane and 6 vol.% copper oxide nanoparticles was labeled "Nanofluid 2" in the tables presented.

According to the methodology used for the elaboration of the simulations of this study, the initial and final temperatures of the cycle for each of the proposed fluids were analyzed first.

It was observed that all substances had a lower end-cycle temperature compared to the eutectic mixture of biphenyl and diphenyl oxide. To adjust the simulation, the beginning of the cycle was equalized with the lowest temperature conditions so that there was a new convergence of the equipment blocks.

This change in temperature represents an increase in heat duty transferred to the hot oil in furnace F-01; however, as they are substances with different thermophysical properties, it does not necessarily mean that the absorbed heat will be greater than it would be with the eutectic mixture of biphenyl and diphenyl oxide.

The percentage difference between the pump P-01's suction temperature of each simulated heat transfer fluid and the design condition with the eutectic mixture of biphenyl and diphenyl oxide was calculated through Eq. (25):

$$\Delta T_{suctionP-01} = 100\frac{T_{V-01simulated} - T_{P-01design}}{T_{P-01design}} \tag{25}$$

To be a suitable replacement, the fluid under evaluation must be able to meet or exceed the design's heat duty value for each of the system's heat exchangers. Based on this criterion, the percentage gain in heat duty was defined by Eq. (26):

$$GainQ\% = 100\frac{Q_{FTsubstitute} - Q_{design}}{Q_{design}} \tag{26}$$

It was considered that the heat duty of the exchanger was met without operating clearance for percentage gains between -5 and +5%, attributing this margin of error to the approximations and assumptions made during the whole process of elaboration and convergence of the simulation calculations.

The summary of the compared criteria for the *n*-C_{13}^{+}, the proposed nanofluids, and the simulation of design conditions are represented in Table 11.

As previously shown, paraffin oil has demonstrated to be a promising substitute candidate for the eutectic mixture of biphenyl and diphenyl oxide, even providing a higher heat duty than that of the design for reboilers HT-03 and HT-04.

In this case, the heat duty transferred to the fluid by the furnace, in order to reach the same outlet temperature, was higher than for the thermal oil currently used, which justifies the higher heat availability for the heat exchangers and operating clearance.

Nanofluid 1 presented 1.37% lower temperature at the beginning of the cycle, and the heat duty supplied by F-01 is 21.4% lower than in the design condition.

The results presented showed that the same behavior observed by the Cu nanofluid + the eutectic mixture of biphenyl and diphenyl oxide occurred for Nanofluid 2; the suction temperature of the pump P-01 is 8.14% lower, and the heat duty provided by the furnace is 20.88% below expected.

The simulations have demonstrated that the nanofluids under study are not suitable for use under the design conditions as they could not provide the proper heat duty for three of the four exchangers that make up the hot oil system. More severe conditions would be required to obtain satisfactory performance,

Table 11. Performance evaluation for the proposed heat transfer fluids

Parameter	Equipment	Current fluid	Paraffinic fluid	Nanofluid 1	Nanofluid 2
$\Delta T_{\text{suction P-01}}$, %	P-01	-	-1.71	-1.37	-8.14
Heat duty, Gcal/h	F-01	10.57	13.79	8.31	8.51
Gain $Q_{\%}$, %	HT-01	0.00	-3.13	+1.84	-3.74
	HT-02	+3.58	0.00	-35.81	-43.65
	HT-03	+8.00	+9.33	-23.10	-26.64
	HT-04	-1.48	+40.05	-25.83	-20.79

but this, in turn, would require an assessment of system equipment and components to determine whether it would be possible to operate under more severe operating conditions without damage.

CONCLUSION

Thermal performance evaluation by static simulation of the studied hot oil system demonstrated that paraffin oil stood out when compared to the nanofluids evaluated and the eutectic mixture of biphenyl and diphenyl oxide, because the oil reached a heat duty of 13.79 Gcal/h, surpassing by 30.46% the thermal energy absorbed by the synthetic oil currently used (10.57 Gcal/h). The *n*-C13+ presented a satisfactory performance for all heat exchangers, providing higher heat duty than expected for HT-03 and HT-04.

Both nanofluids did not perform satisfactorily at the same operating conditions as the system. The Cu/eutectic of biphenyl and diphenyl oxide nanofluid only enhanced thermal energy in 8.31 Gcal/h and the CuO/polydimethylsiloxane nanofluid in 8.51 Gcal/h. The operating conditions might have to be modified to reach a higher temperature at the furnace outlet so that satisfactory thermal performance of these fluids could be obtained, but it should be preceded by a study on whether the devices and components of the system could endure such conditions.

REFERENCES

[1] D.C. Álvarez, PhD Thesis, University of Vigo, 2015

[2] A. Bahadori, Essentials of Oil and Gas Utilities - Process, Design Equipment and Operation. 1st ed., Elsevier Inc., Oxford, 2016, pp. 193-199

[3] E. Bellos, C. Tzivanidis, D. Tsimpoukis, Energy Convers. Manage. 156 (2017) 388-402

[4] A. Yasinskiy, J. Navas, T. Aguilar, R. Alcántara, J.J. Gallardo, A. Sanchez-Coronilla, E.I. Martin, D. de los Santos, C. Fernandez-Lorenzo, Renewable Energy 119 (2018) 809-819

[5] D. Cabaleiro, J.J. Segovia, M.C. Martin, L. Lugo, J. Chem. Thermodyn. 93 (2015) 86-94

[6] M.M. Sarafraz, M.R. Safaei, M. Goodarzi, B. Yang, M. Arjomandi. Int. J. Heat Mass Transfer 139 (2019) 675-684

[7] N. Kumar, S.S. Sonawane, S. H. Sonawane, Int. Commun. Heat Mass Transfer 90 (2018) 1-10

[8] S.U.S. Choi, J.A. Eastman. Office of Scientific and Technical Information, U.S. Department of Energy, 1995, pp. 1-8

[9] A.H. Aref, A.A. Entesami, H. Erfan-Niya, E. Zaminpaima, J. Mater. Sci. 52 (2016) 2642-2660

[10] J. Navas, A. Sanchez-Coronilla, E. I. Martin, L. Teruel, J. J. Gallardo, T. Aguilar, R. Gómez-Vilarejo, R. Alcántara, C. Fernandez-Lorenzo, J. C. Piñero, J. Martín-Calleja, Nano Energy 27 (2016) 213-224

[11] A. Mwesigye, Z. Huan, J.P. Meyer, Energy Convers. Manage. 120 (2016) 449-465

[12] E. Bellos, C. Tzivanidis, Energies (Basel, Switz.) 10 (2017) 848-880

[13] M.M. Sarafraz, H. Arya, M. Saeedi, D. Ahmadi, Appl. Therm. Eng. 138 (2018) 552-562

[14] M.M. Sarafraz, M. Arjomandi, Int. Commun. Heat Mass Transfer 94 (2018) 39-46

[15] M.M. Sarafraz, H. Arya, M. Arjomandi, J. Mol. Liq. 263 (2018) 382-389

[16] M.M. Sarafraz, M. Arjomandi, Appl. Therm. Eng. 137 (2018) 700-709

[17] E. Jalali, O.A. Akbari, M.M. Sarafraz, T. Abbas, M.R. Safaei, Symmetry 11 (2019) 757 1-20

[18] Petro-SIM® Process Simulation, https://www.kbc.global//software/process-simulation-software/ (accessed in 03 May 2019)

[19] Dowtherm® A Heat Transfer Fluid, Product Technical Data. http://msdssearch.dow.com/PublishedLiteratureDOWCOM/dh_0030/0901b803800303cd.pdf (accessed in 20 April 2018)

[20] Therminol® VP-1 heat transfer fluid, Ultrahigh-temperature vapor/liquid phase fluid. https://www.eastman.com//Literature_Center/T/TF9141.pdf (Accessed in 20 April 2018)

[21] Syltherm® 800 Heat Transfer Fluid, Product Technical Data. http://msdssearch.dow.com/PublishedLiteratureDOWCOM/dh_0880/0901b80380880bfe.pdf?filepath=/heattrans/pdfs/noreg/176-01435.pdf&fromPage=GetDoc (accessed in 07 March 2019)

[22] B.R.G. Couto, Dimensionamento de uma Caldeira a Termofluido. Master Dissertation, University of Porto, 2009 (in Portuguese)

[23] J.P. Wauquier, El refino del Petróleo - Petróleo Crudo; Productos Petrolíferos; Esquemas de Fabricación. 1st ed., Repsol Foundation YPF, Madrid, 2004, pp. 109-112 (in Spanish)

[24] Petro-SIM User Manual Version 6.2. KBC Advanced Technologies Ltd. KBC-Yokogawa Company, Surrey, 2017, pp. 248-276, 522, 535, 546-549

[25] P.F. Incropera PF, D. P. DeWitt, T. L. Bergman, A. S. Lavine, Fundamentals of heat and mass transfer. 6th ed., John Wiley & Sons, New York, 2006, pp. 929-932.

LIS DA SILVA OSTIGARD
SILVANA MATTEDI

Federal University of Bahia, Polytechnic School, Chemical Engineering Department, Graduate Program in Chemical Engineering, Salvador, BA, Brazil

NAUČNI RAD

EVALUACIJA TERMIČKIH PERFORMANSI TOPLIH ULJA I NANOFLUIDA SIMULIRANJEM INDIREKTNOG TOPLOTNOG POSTROJENJA

Ovaj rad analizira termičke performanse četiri različite tečnosti za prenos toplote u sistemu sa vrelim uljem postrojenju za hidrotretman i frakcionisanje u rafineriji nafte. Softver Petro-SIM® (KBC-Iokogava) je korišćen za izradu simulacija stacionarnih stanja namenjenih poređenju tečnosti za prenos toplote koje se trenutno koriste (eutektik bifenil- i difenil-oksida) i tri tečnosti predložene kao zamene: parafinsko ulje (n-C_{13+}) proizvedeno industrijski, nanotečnost eutektik bifenil i difenil oksida/bakar (zapreminski udeo 6%) i nanotečnost CuO/polidimetilsiloksan (zapreminski udeo 6%). Rezultati su pokazali da je n-C_{13+} jedina tečnost za prenos toplote koja može da zameni eutektik difenil oksid/ /bifenil u analiziranom sistemu, jer je apsorbovala toplotu od 13,79 Gcal/h, što je premašilo toplotnu energiju od 10,57 Gcal/h koju je apsorbovala tečnost koja se trenutno koristi pri istim radnim uslovima. Nanotečnosti Cu/eutektika bifenil- i difenil-oksida i CuO/polidimetilsiloksan pokazale su slabije performance u odnosu na vrelo ulje (8,31 i 8,51 Gcal/h, redom).

Ključne reči: prenos toplote, tečnost za prenos toplote, vrelo ulje, nanotečnosti, simulacija.

CI&CEQ
Chemical Industry & Chemical Engineering Quarterly

Available on line at
Association of the Chemical Engineers of Serbia *AChE*
www.ache.org.rs/CICEQ

Chem. Ind. Chem. Eng. Q. 27 (1) 57–68 (2021) CI&CEQ

HUIBO MENG[1]
ZHONGGEN LI[1]
YANFANG YU[1]
MENGQI HAN[1]
SHUNING SONG[2]
XIUHUI JIANG[1]
ZONGYONG WANG[1]
JIANHUA WU[1]

[1]Engineering and Technology Research Center of Liaoning Province for Chemical Static-Mixing Reaction, School of Mechanical and Power Engineering, Shenyang University of Chemical Technology, Shenyang, P.R. China
[2]School of Chemistry and Molecular Bioscience, the University of Queensland, Brisbane, Australia

SCIENTIFIC PAPER

UDC 66.023.3:66.063.8:66.07:004

THE FLOW AND MASS TRANSFER CHARACTERISTICS OF CONCENTRIC GAS-LIQUID FLOW IN AN ADVANCED STATIC MIXER

Article Highlights

- The dynamic characteristics of concentric gas-liquid bubbly flow in the FKSM were studied
- The mass transfer and enhancement characteristics in the FKSM were evaluated
- The secondary vortexes were distinguished based on the radial holdup and axial velocity profiles

Abstract

The fluid dynamic and mass transfer characteristics of concentric upward gas--liquid flow were studied in an industrial static mixer with four equally spaced helical inserts (FKSM). The numerical simulations of the gas volume fraction in a Kenics mixer was in good agreement with the numerical and experimental results provided by Rabha et al. The characteristics of radial gas void fraction and local mass transfer coefficients in the FKSM were evaluated under different operating conditions. The velocity profiles of the concentric air phase accelerated by the bubble forces first became sharp and narrow until z/l = = -3.27 and then slowly decreased and stabilized at z/l = -1.5 before entering the first mixing element. Some extra unimodal profile of radial gas holdup gradually generated near the rectangle cross-sections of the mixing elements. The α_G *gradually enlarged from r/R = 0.2 to r/R = 0.55 and then weakened from r/R = 0.65 to r/R = 0.874. The air void fractions in the bulk flow region decreased with the increasing initial uniform bubble diameter. The inlet effect of the first leading edge enhanced the air phase dispersion and local mass transfer coefficients sharply increased from 2.04 to 3.69 times of that in the inlet. The local mass transfer coefficients in each mixing group had unimodal profiles.*

Keywords: static mixer, multi-helical inserts, upward gas-liquid flow, gas void fraction, local mass transfer coefficients.

Multiphase flows occur in a great variety of natural phenomena and technical processes [1,2]. Distribution and dispersion mixing of fluids as important unit operations of fine chemical, polymerization processes, pharmaceutical industry, bio-chemical and other chemical production processes play a very important role in the success or failure of industrial processes [3-6]. It is well known that the bubble column, mechanically stirred vessels and static mixers are usually employed in multi-phase mixing unit operations. The dynamic mixing device is typically used in an intermittent production process and the static mixer is used in a continuous production process. The static mixer can complete the mixing task only by much lower energy consumption for pressure drop. They have a number of advantages over dynamic mixers, such as having no moving parts, low cost of installation and operation, easy installation, increasing the mass transfer coefficient for gas-liquid mixing. It is widely known that a static mixer could be used in broad operation conditions including laminar flow, creeping flow and turbulent flow [1,6]. Increasing

---

Correspondence: Y. Yu, Engineering and Technology Research Center of Liaoning Province for Chemical Static-Mixing Reaction, School of Mechanical and Power Engineering, Shenyang University of Chemical Technology, Shenyang, P. R. China.
E-mail: taroyy@163.com
Paper received: 13 December, 2019
Paper revised: 1 June, 2020
Paper accepted: 13 July, 2020

https://doi.org/10.2298/CICEQ191213024M

interest in chemical process intensification during the past years improves online static mixers as an attractive choice compared to the bubble column and mechanically stirred tanks [7].

Woven wire meshes have been employed in a multitude of flow operations and more sophisticated operations as static mixers in multiphase reactors/ /contactors [8,9]. In chemical reactors/contactors, screens have been successfully employed to promote multiphase contacting between phases to enhance mass transfer and/or reaction operations [10-13]. Volumetric mass transfer coefficient and oxygen transfer rate in a static mixer with screen-type elements could be as high as 0.44 s^{-1} and 4.2 kg/kWh when liquid superficial velocity was up to 2.0 m/s and gas holdups as high as 0.15 [10]. Azizi and Al Taweel [11] used population balance model to predict gas-liquid contacting in the screen-type static mixers for the case of industrial streams where the presence of amphiphilic constituents was found to retard coalescence and result in average interfacial areas as high as 2100 being achieved. Azizi and Al Taweel [12] used the screen static mixers to promote gas-liquid interphase mass transfer in order to improve the selectivity and yield of multiphase reactions. The results showed that the $k_L a$ values that surpassed those of most conventional reactors/contactors by an order of magnitude. The ability to reach 98% equilibrium within residence times of less than 800 ms also allowed for the use of static mixing units that were several orders of magnitude smaller than conventional mechanically agitated tanks and bubble columns. Azizi and Hweij [13] found that the liquid-phase axial dispersion coefficient was consistently lower in all cases than that of gas-liquid pipe flows without STSMs under the same conditions.

The single-phase flow and liquid-liquid swirl flow in the static mixers have been quite extensively investigated by different researchers [1,6,14-19]. They offer many advantages over conventional reactors (such as packed bed reactors, fluidized bed reactors) especially when used for gas/liquid systems. Some examples of the application of static mixers for dispersive mixing of the gaseous phase into the liquid phase are ozonation processes in wastewater treatment process, and scrubbing ammonia or cyanides with water and hydrogenation of vegetable oils [1,6,7,20]. Tajima and his colleagues [21-23] analytically and experimentally elucidated the effects of flow division, flow reversal and secondary flow induced by the Kenics static mixer on the formation of CO_2 hydrate. The liquefied CO_2 was transported through a pipeline and mixed with seawater in a KSM at a depth of 500-1000 m then released into the ocean. More experimental results about the interfacial mass transfer between liquid CO_2 and water had been obtained in the horizontal KSM. Rabha *et al.* used ultrafast electron beam X-ray tomography to measure the dispersive mixing of upward co-current gas-liquid flow and quantitatively analyzed the bubble size distribution and gas holdup in a KSM [7]. During the past years, the physical scale resolved in a CFD simulation has become smaller and smaller because of ever-increasing computer power [24]. The development of suitable closure models for gaining a full understanding of multiphase flows is still an active research field owing to the complex physics involved and broad range of relevant length scales [2]. Taking into account of the mono-disperse bubble sizes assumption and the dependency of non-drag forces, Zidouni *et al.* [25] performed an Euler-Euler gas-liquid bubbly flow simulation validated by the literature data of Rabha *et al.* to predict the gas phase characteristics. Kanizawa and Ribatski [26,27] employed a capacitive probe to measure the gas holdup of air-water upward external flow across a triangular tube bundle and presented a review on predictive methods for gas holdup and pressure drop.

In the past years, many experimental studies about turbulent bubbly flows inside the KSM have been carried out to enrich the comprehensive databases. The static mixer with four equally spaced helical inserts (FKSM) as a novel gas-liquid mixing equipment has been successfully applied in the industrialized production of dichloroethane by direct chlorination of ethylene and propylene oxide by chlorohydrination in tubular reactor dichloride [4,28]. Adequate further understanding of intensification mechanism of gas-liquid flow in the complex static mixer is indispensable. However, there are not adequate literatures on the gas-liquid flow in the FKSM. In this study, the characteristics of velocity field, radial gas void fraction and local mass transfer coefficients of concentric upward gas-liquid flow characteristics in the FKSM were investigated, respectively.

MATHEMATICAL MODEL

Governing equations

Computational fluid dynamics (CFD) is considered the one indispensable tool in resolving problems that involve mass and heat transfer. A widely used approach to model two-phase flows with significant volume fractions of both phases is the Eulerian two-fluid framework of interpenetrating continua [2,25]. The numerical cases of the concentric upward gas-liquid bubble flows in the FKSM was implemented in the ANSYS Fluent V16.1 with multi-fluid Euler-Euler approach. The continuity equation for phase *q* is [29]:

$$\frac{\partial}{\partial t}\left(\alpha_q \rho_q\right)+\nabla\cdot\left(\alpha_q \rho_q \boldsymbol{u}_q\right)=\sum_{p=1}^{n}\left(m_{pq}-m_{qp}\right)+S_q \tag{1}$$

where α_q is the volume fraction of phase *q*, ρ_q denotes the density of phase *q*, u_q is the velocity of phase *q* and m_{pq} characterizes the mass transfer from the p^{th} to the q^{th} phase, and m_{qp} characterizes the mass transfer from phase *q* to phase *p* [30].

The momentum conservation for phase *q* yields:

$$\begin{aligned}&\frac{\partial}{\partial t}\left(\alpha_q \rho_q \boldsymbol{u}_q\right)+\nabla\cdot\left(\alpha_q \rho_q \boldsymbol{u}_q \boldsymbol{u}_q\right)=-\alpha_q \nabla p+\nabla\cdot\overline{\overline{\tau}}_q+\\&+\alpha_q \rho_g+\sum_{p=1}^{n}\left(\boldsymbol{R}_{pq}+m_{pq}\boldsymbol{u}_{pq}-m_{qp}\boldsymbol{u}_{qp}\right)+\\&+\left(\boldsymbol{F}_q+\boldsymbol{F}_{lift,q}+\boldsymbol{F}_{wl,q}+\boldsymbol{F}_{vm,q}+\boldsymbol{F}_{td,q}\right)\end{aligned} \tag{2}$$

where $\overline{\overline{\tau}}_q$ is the *q* phase stress-strain tensor, μ_q and λ_q denote the shear and bulk viscosity of phase *q*, F_q is an external body force, $F_{lift,q}$ is a lift force, $F_{wl,q}$ is a wall lubrication force, $F_{vm,q}$ is a virtual mass force, and $F_{td,q}$ is a turbulent dispersion force (in the case of turbulent flows only) [31,32].

It is well known that the *k-ω* turbulence model attempts to predict turbulence by two partial differential equations for the turbulence kinetic energy (*k*) and specific rate of dissipation (*ω*) [33]. As a result, SST *k-ω* model is employed as a closure for the RANS equations of Eulerian mode in multiphase turbulent flows. Furthermore, the relative Reynolds number for the primary phase *q* and secondary phase *p* is obtained from [34]:

$$Re=\frac{\rho_q\left|u_p-u_q\right|d_p}{\mu_q} \tag{3}$$

Bubble forces

The suitable closure model for adiabatic bubbly flow is achieved once the bubble forces have been expressed in terms of the average flow parameters by means of analytical or empirical correlations [35]. The drag forces also describe the momentum exchange in flow direction and the non-drag forces including a lift-force, a wall-force and a turbulent dispersion-force play an important role for the development of the flow structure in a two fluid approach [36].

Drag force

A drag force as the resistance force derives from the motion of the bubbles through the surrounding water and has the opposite direction of the incoming flow. The interfacial drag force acted on a micro-body traveling through a fluid is given by [25]:

$$\boldsymbol{F}_{drag}=-\frac{3}{4d_B}C_D \rho_L \alpha_G\left|\boldsymbol{u}_G-\boldsymbol{u}_L\right|\left(\boldsymbol{u}_G-\boldsymbol{u}_L\right) \tag{4}$$

The drag coefficient (C_D) is evaluated as suggested by Ishii and Zuber in the following format [37]:

$$C_D=\max\left(C_{D,sphere},\min\left(C_{D,ellipse},C_{D,cap}\right)\right) \tag{5}$$

where

$$C_{D,sphere}=\frac{24\left(1+0.1Re^{0.75}\right)}{Re} \tag{6}$$

$$C_{D,ellipse}=\frac{2}{3}\sqrt{Eo} \tag{7}$$

$$C_{D,cap}=8/3 \tag{8}$$

The drag coefficient C_D depends strongly on the *Re* and for deformable bubbles also on the Eötvös number *Eo* but turns out to be independent of the Morton number *Mo* [25,38]:

$$Eo=\frac{\left(\rho_L-\rho_G\right)gd_B^2}{\sigma} \tag{9}$$

$$Mo=\frac{\left(\rho_L-\rho_G\right)g\mu_L^4}{\rho_L^2\sigma^3} \tag{10}$$

where σ denotes the surface tension, *g* represents gravity, and d_B is the diameter of uniform bubbles.

Lift forces

The bubbles in a shear flow are subjected to a lift force which is due to velocity gradients and acts perpendicular to the direction of bubble motion. From Drew and Lahey [39], the lift force acting on a dispersed phase in a continuous phase could be calculated as:

$$\boldsymbol{F}_{lift}=-C_L \rho_L \alpha_G\left(\boldsymbol{u}_G-\boldsymbol{u}_L\right)\times\left(\nabla\times\boldsymbol{u}_L\right) \tag{11}$$

For in co-current pipe flow, the lift coefficient C_L of spherical bubbles is positive which indicates that the lift force acts in the opposite direction of the velocity gradient of liquid phase. The original Tomiyama lift model was lightly modified by Frank *et al.* as follows [40,41]:

$$C_L = \begin{cases} \min[0.288\tanh(0.12Re), f(Eo_\perp)] & Eo_\perp \le 4 \\ f(Eo_\perp) & 4 < Eo_\perp \le 10 \\ -0.27 & Eo_\perp > 10 \end{cases} \tag{12}$$

where

$$f(Eo_\perp) = 0.00105Eo_\perp^3 - 0.0159Eo_\perp^2 - \\ -0.0204Eo_\perp + 0.474$$

$Eo_\perp$ is a modified Eötvös number based on the long axis of the deformable bubble, $d_\perp$ [42]:

$$Eo_\perp = \frac{(\rho_L - \rho_G) g d_\perp^2}{\sigma} \tag{13}$$

$$d_\perp = d_B(1 + 0.163Eo^{0.757})^{1/3} \tag{14}$$

Wall lubrication force

In the bubbly upward flow of a vertical pipe, the wall lubrication force tends to push the gas phases away from walls and results in the dispersed bubbles concentrating in a region near, but not immediately adjacent to, the wall [43]. Complete neglect of the wall force does not give a satisfactory prediction of the void fraction profiles. Therefore, the influence of wall lubrication forces on the bubbles is necessarily included in the gas-liquid bubbly flows in FKSM. The wall lubrication force has the general form [25]:

$$\boldsymbol{F}_{wall} = \frac{2}{d_B} C_W \rho_L \alpha_G \left| \boldsymbol{u}_G - \boldsymbol{u}_L \right|^2 \hat{y} \tag{15}$$

The empirical relationship was concluded by Tomiyama *et al.* [44] and Hosokawa *et al.* [45].

Numerical aspects

Physical model and fluid properties

It is well known that the classical KSM is usually composed of a number of Kenics blades with a twist angle of 180° and a staggered angle of 90° relative to the previous one [1,7]. The advanced FKSM as presented in Figure 1 contained four Kenics blades which were symmetrically uniformly distributed in the mixer cross-section. The FKSM contained 12 element groups in the axial direction. The adjacent axial mixing groups have an opposite twist direction and are placed at an angle of 45°. As illustrated in Figure 1, the geometry models of a multi-swirling static mixer with smooth tube entrance and exit sections employed in the numerical cases could be obtained by Solidworks. The computational flow domain was comprised of a vertical static mixer with 40 mm internal diameter and 505 mm length. The other detailed information has been given in Table 1.

Table 1. The geometrical parameters of FKSM

Parameter	Value
Tube diameter, *D* (m)	0.04
Twisted plate width, *W* (m)	0.02
Aspect ratio, *Ar*	1.5
Twisted plate thickness, δ (m)	0.002
Twisted angle, Θ (°)	180
Inlet length, l_i (m)	0.12
Mixing length, l_m (m)	0.36
Outlet length, l_o (m)	0.025

For the concentric upward gas-liquid flow in the FKSM, water was employed as the continuous phase and air as the discrete phase. The volume flow of water, Q_L, had a range of 1–4 m^3/h and the corresponding *Re* was in the range from 7547 to 30190. The gas was treated as the incompressible fluid according to the ideal gas law [25]. All simulations were performed using water as the primary phase (μ_L = = 8.899×10^{-4} kg/(m·s), ρ_L = 997.0 kg/m^3), gas as the secondary phase (μ_G = 1.831×10^{-5} kg/(m·s), ρ_G = = 1.185 kg/m^3). The surface tension between the two phases was set as 0.072 N/m.

Boundary condition and solution method

The numerical cases were implemented in parallel with 4 processors using an academic version

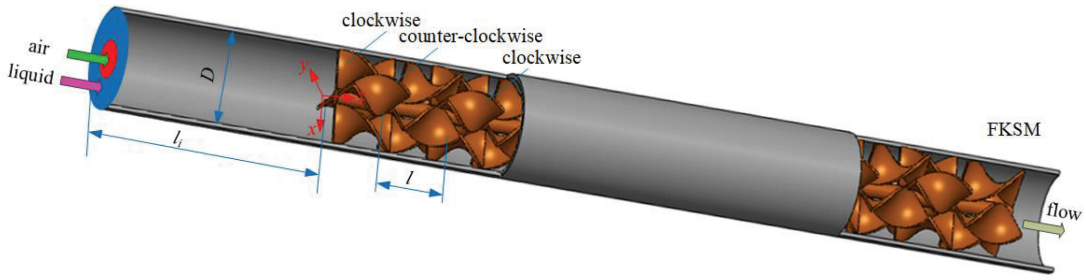

Figure 1. The schematic diagram for FKSM.

of ANSYS Fluent V16.1. A smaller time step size of 1×10^{-3} s was used in the numerical solutions in a Dell workstation T3600 with Intel Xeon Processor E5-1650 and 32.0 GB RAM. A pressure-based solver was chosen with implicit scheme for transient formulations in the static mixers [46]. The pressure-velocity Coupling was achieved based on Phase Coupled SIMPLE which had been proven to be robust [47]. The gradients were discretized on the basis of the Green-Gauss cell-based method. The second-order upwind scheme was employed to discretize the momentum, volume fraction, turbulent kinetic energy and specific dissipation rate, respectively.

The ordinate origin of the Cartesian system was set at the cross-section center of the first mixing element's leading edge [5]. The reference pressure location was at the outlet center of the mixer [4]. The liquid and gas phase inlets were assigned as the velocity inlet, and the outflow outlet was specified. The average axial velocity of the liquid phase ranged from 0.245 to 0.98 m/s in the positive z-direction. The gas was injected through a concentric inlet with 12.5 mm internal diameter. The user-defined functions were adopted to obtain the fully-developed profiles for each phase. The wake region behind the bubbles with a size smaller than the critical bubble diameter d_c = = 10 mm is not obvious and its effect on collision and coalescence could be ignored [37]. In view of the comparison with the available experimental data and the simplified treatment, mono-disperse approximation was employed and imposed in all simulations as described by Zidouni *et al.* [25]. The gas phase had the initial uniformly dispersed bubbles with a diameter d_B of 1.0, 3.0, 5.8 and 8 mm, respectively. The volume fraction of the gas phase satisfied for $\alpha_G \le 0.3$ so that the resulting flow pattern was in the bubbly flow topology [32].

In order to obtain an initial solution for the primary phase, the Eulerian multiphase calculation was first set up as usual. Secondary, the volume fraction in the Equations list in the Equations Dialog Box was deselected to compute the flow for the primary phase only. At last, the volume fraction equation was turned back on and the calculation for all phases continued. The residual rules for the mass equation and other conservation equation components satisfied with the absolute criteria of 10^{-4} and 10^{-6}, respectively.

Model validation

In order to compare the gas volume fraction with literature data provided by Rabha *et al.* [7], the same model of KSM was employed: a vertical pipe with an inner diameter of 80 mm and 3450 mm length consisted of the only three elements with the aspect ratio fixed at 1; the gas inlet injected through a 12.5 mm inner diameter was located at 615 mm upward of the cross-section of the first mixing element. As experimental working fluid, the de-mineralized water as the liquid and air as the gas phase were employed in the numerical simulations and the effect of gravity took place in the negative z-direction; a typical cross-section at z = 75 mm was monitored. The time-averaged distribution of cross-sectional gas holdup were evaluated at u_G = 0.11 m/s and u_L = 0.6 m/s. The numerical prediction of two large-scale zones with higher gas holdup symmetrically separated by the mixing inserts as shown in Figure 2a had a good agreement with the numerical result in Figure 2b and experimental result in Figure 2c provided by Rabha *et al.* [7,25]. It is well known that the velocity field and flow pattern in the KSM is induced by the helical Kenics inserts [6,8,23]. The FKSM derived from the basic KSM is identically composed of three mixing functions, flow division, flow reversal, and radial mixing. As a result, the used computation model as described above is considered to be capable of predicting gas-liquid flow in the FKSM.

Grid independence test

Because of the complex mixing elements, the computational domain was meshed with unstructured grids. A 2D face mesh with quadrilateral cells with a 1

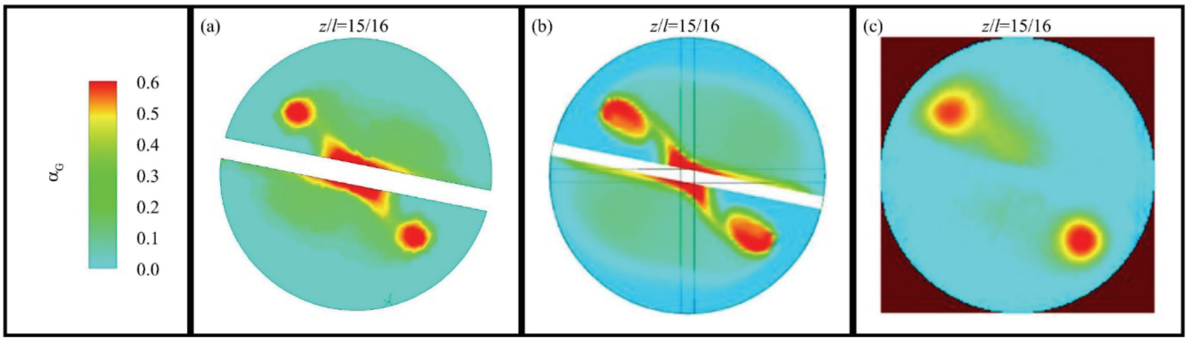

Figure 2. Comparison of gas holdup counter among: a) the numerical result, b) the literature numerical and c) the experimental data.

mm interval was generated at the cross-sections of inlet and outlet, and then a 3D volume mesh with tetrahedral cells was generated [46]. The mesh cells near the boundary zones included the inlet, outlet, tube and tapes walls were refined based on boundary adaption [32]. To ensure the accurate prediction of the multiphase flow filed which was independent of the grid system, five grid systems with about 1182872, 623954, 491576, 379049, and 346496 cells were adopted in the numerical simulations of gas-liquid flow in the FKSM.

From Figure 3 under Q_L = 1 m^3/h and α_{ave} = = 0.15, it is obviously seen that the average *z*-directional velocity of the liquid phase decreased first and then increased with the increasing cell numbers. It was noted that the minimum of average axial velocity of water approached 0.260 m/s with about 623954 cells. As far as the variable cross-sections is concerned, the theoretical average axial velocity with a value 0.258 m/s could be obtained from the continuity equations at the cross-section of *z*/*l* = 0 and 11/2. To our knowledge, the deviation between the theoretical and minimum of numerical average axial velocity was only 0.775%.

From the average mesh quality as presented in Figure 3, both Equiangle Skew (Q_{EAS}) and Equivolume Skew of mesh first increased and then decreased with the increasing cell numbers. The mesh quality would be much worse when the Q_{EAS} was higher than 0.75. Furthermore, the average Q_{EAS} of higher mesh quality system had a value of 0.4 [48]. The average Q_{EAS} of the grid system with 623954 cells was closer to 0.4 than that of the other three-dimensional models. In view of the computational accuracy and efficiency, the mesh with a cell number of 623954 was chosen for the following numerical computation process.

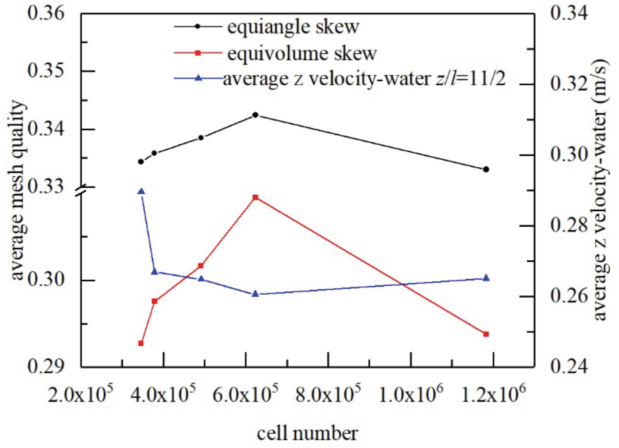

Figure 3. Grid quality test and grid independence test for numerical simulation in FKSM.

RESULTS AND DISCUSSION

Flow field of water and air phase

For further evaluation of the water-air two-phase flow in the FKSM, it was necessary to investigate the velocity profiles of the water and air phases. The profiles of area-weighted average air and water velocities versus normalized axial position at different cross-sections are shown in Figure 4a. It could be obviously seen that the average air phase velocity profiles gradually became much larger before *z*/*l* = 0, because of the mass transfer from the local high velocity air phase with bigger uniform bubble diameter to the surrounding low velocity liquid. Furthermore, the inlet length for average air velocity in excess of the primary phase was getting shorter from *z*/*l* = -0.333 to *z*/*l* = = -0.733 with the increasing uniform bubble diameter. With the increasing axial length, the average air velocity was improved from 0.467 to 0.825 m/s and the liquid phase reduced slightly from 0.361 to 0.338 m/s.

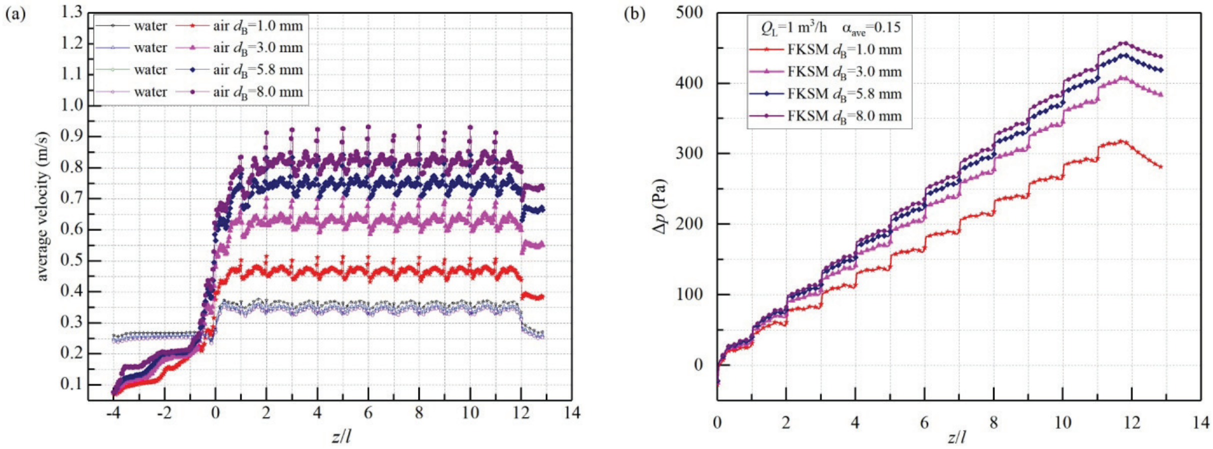

Figure 4. The profiles of: a) area-weighted average air and water velocities at Q_L = 1 m^3/h and α_{ave} = 0.20, and b) pressure drop versus normalized axial position at different cross-sections at Q_L = 1 m^3/h and α_{ave} = 0.15.

The periodic effects of static mixing functions induced the average axial air and water velocity had "W" profiles in each segment. Furthermore, the local maximum of air phase velocity in each mixing element was obtained earlier than that of the water phase. The average liquid velocity decreased down to the minimum and the average air velocity increased up to the maximum at the transition regions of adjacent mixing elements at the same time. In the mixing sections, the relative velocities between air and water increased from 0.106 to 0.486 m/s with the increasing initial uniform bubble diameter. At the last ending edge of the mixing group, the average velocities of air and water phases first suddenly decreased, and then the primary phase gradually reduced to the inlet velocity because of the larger cross-section and reduced turbulent intensity.

The profiles of pressure drop of gas-liquid flow between the first and end leading edges in the FKSM *versus* dimensional axial position are illustrated in Figure 4b. It could be seen that the pressure drops for d_B 3.0, 5.8 and 8.0 mm had an obvious increasement larger by 18.41−30.53%, 29.86−40.83% and 35.61−46.04% than that in the FKSM with d_B = 1.0 mm, respectively. As a result, a much smaller bubble diameter is necessary and expected for larger interface areas and lower energy consumption.

Radial gas fraction distribution

The cross-sectional contour and secondary flow vector of air velocity in the inlet, mixing and outlet wake flow sections are shown in Figure 5. It was noted that the air phase injected in the tube center was gradually dispersed and transferred to the plate wall and tube wall. The secondary flow vectors in Figure 5 show that the bubbles flow first transferred to the tube wall induced by flow division of the leading edge, and then migrated to the tube center with the help of radial mixing function and finally moved to the surrounding fluid derived from the flow reverse function of the downstream mixing elements. The longitudinal vortices of the air phase began to generate from $\Delta z/l$ = 0.25 which was derived from the swirling flow of the primary phase in each mixing segment. In other words, four pairs of longitudinal vortices generated at the eight helical passages and a much larger in scale longitudinal vortex with a diameter of 8 mm swirled with the central axis in the cross-sections. The number of leading edges in a cross-section at the transition was up to 4 times of that in the KSM, which may play a much more important role in the gas fraction distributions, as shown in Figure 5. As a result, much more uniform distributions of the air phase were obtained in the downstream mixing region compared with the smooth inlet tube. The homogeneity of the gas phase was reduced and the longitudinal vortices gradually weakened in the outlet wake region, as shown in the flow map at z/l = 38/3.

It could be clearly seen from Figure 6 that the effect of cross-section geometry of mixing groups on the radial profiles of the air void fraction was obviously intensified. The distributions of gas fraction α_G in the smooth inlet were classical symmetrical unimodal profiles, as shown in Figure 6a. The only difference was that the tails of profiles expanded from r/R = 0.2 to r/R = 0.6 because of local mass transfer induced by the bubble forces. In the mixing regions, the radial distributions of α_G began to shift from the tube center to the tube wall by the coupled effect between the lift force and secondary flow induced by the helical element. The maximum value of α_G at z/l = -4.0 began to shift to the central axis at r/R = 0.2, as shown in Figures 5 and 6a. The maximum values of α_G first increased from 0.689 to 0.827 and then decreased down to 0.55. Furthermore, a new unimodal profile gradually generated around the rectangle cross-sections of mixing elements at z/l in range 0.25-0.75 with d_B = 3.0 mm. The air void fractions in the bulk flow region decreased with the increasing bubble

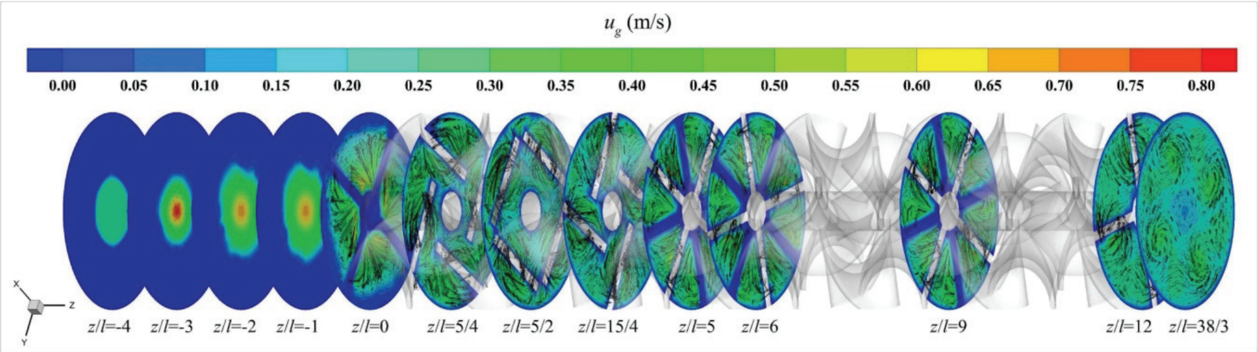

Figure 5. The cross-section velocity contour and second flow vector of air phase at Q_L = 1 m^3/h and α_{ave} = 0.20.

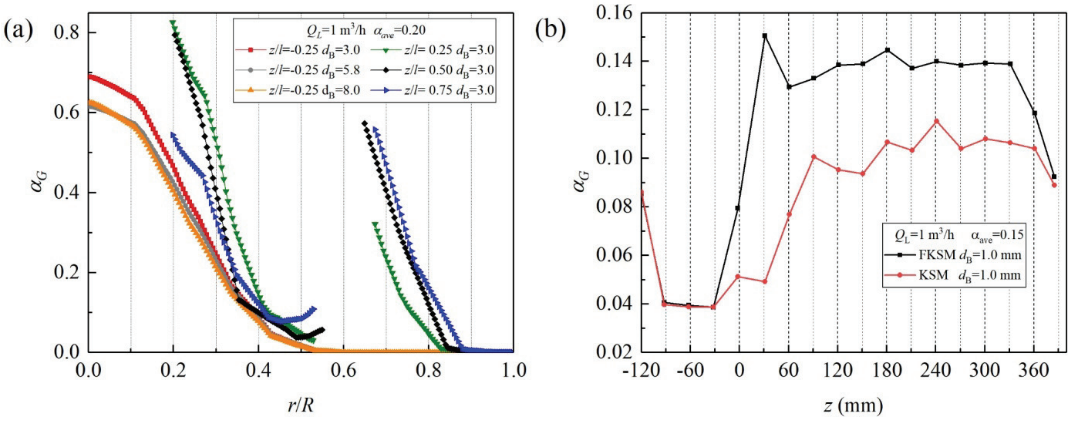

Figure 6. The radial gas fraction distributions: a) the radial profiles of α_G at different cross-sections in the first mixing element and b) area weighted average profiles versus axial dimensional mixing length.

diameter and radius from *r/R* = 0.2 to *r/R* = 0.5. The air void fraction α_G at the inner side of helical blades was gradually enlarged and α_G at the tube-wall side was gradually weakened with the increasing radial positions from *r/R* = 0.5 to *r/R* = 0.874. Furthermore, a comparison about the gas holdup dispersion distribution could be obtained in the FKSM and KSM, as shown in Figure 6b. It is noted that the area weighted average air void fractions in the FKSM dramatically increased up to 206% by the first four leading edges and then the relative enhancement became smaller and smaller, from 68.22 to 30.64%, compared to that in the KSM with d_B = 1.0 mm.

Figure 7 illustrates the radial and axial velocity distributions of the air phase before and after the twelve mixing segments. From the radial and axial comparison of velocity distributions of the air phase in the initial developing inlet sections, as shown in Figure 7a and b, a relative jet flow of the air phase was fully developed with higher velocity. Before entering the first mixing element, the velocity profiles of the concentric air phase accelerated by bubble forces first became sharp and narrow until *z/l* = -3.27 and then slowly decreased and started to stabilize at *z/l* = -1.5, because of the new local mass transfer equilibrium. That is to say, some higher turbulent energy of the air phase may be used for radial mass transfer. With the increasing of dimensionless axial length, the axial u_G in the near-wall region of *r/R* > 0.7 gradually decreased and the axial u_G in the tube center region of *r/R* ≤ 0.25 increased, as illustrated in Figure 7c. In the wake flow regions, as shown in Figure 7c and d, multiple secondary vortices were induced by static mixing segments with four equally spaced helical inserts. The existence of two pairs of coupled free vortexes after the ending edge of mixing element at *z/l* = 38/3 in Figure 5 was proved by the radial profiles of the air phase, as presented in Figure 7d. On the one hand, the vortex core gradually moved closer to the center of the outlet with the increasing weak flow passage. On the other hand, the maximum velocity started to decrease and the velocity of the center bulk zone increased. Therefore, two pairs of free vortexes gradually weakened.

Axial local mass transfer

The mass transfer process between air and liquid was enhanced by the multi-helical segment as shown in Figure 8. On the basis of Higbie's classical permeability theory and Kolmogorov's isotropic turbulence theory [49], the local mass transfer coefficients, k_La, could be defined as:

$$k_La = \frac{12\alpha_G(1-\alpha_G)}{d_B}\left(\frac{D_f}{\pi}\right)^{1/2}\left(\frac{u_{GL}\rho_L g\alpha_G}{\mu_L}\right)^{1/4} \tag{16}$$

where D_f is diffusivity, m^2 s^{-1}.

As shown in Figure 8a, the values of k_La in the mixing region became much larger than those in the smooth inlet tube with the increasing dimensionless axial mixing length. The intensification ability of the smooth tube at α_{ave} = 0.2 could be easily obtained at *z/l* = -3.5 with the approximate value of k_La = 20.5 s^{-1} which indicated that the mass transfer process was no longer sensitive to the axial positions. The inlet effect induced by the first leading edge of the mixing segment played an important role on the distribution mixing process, and the intensification of local mass transfer coefficient increased sharply, which was 2.04–3.69 times of that in the inlet tube. In the flow passage generated by the first mixing element, the local transfer coefficient first declined and then increased, and finally decreased, which indicated that a new equilibrium between air and water may be gradually obtained.

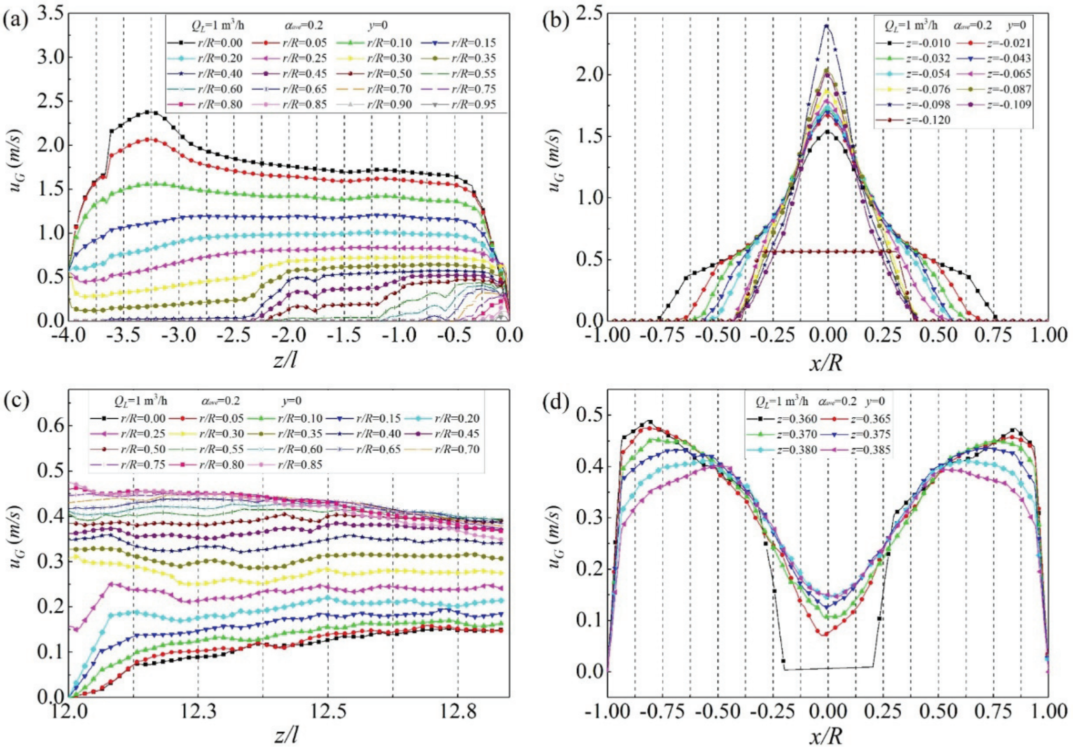

Figure 7. The radial and axial velocity distribution of air phase before and after the twelve mixing segments.

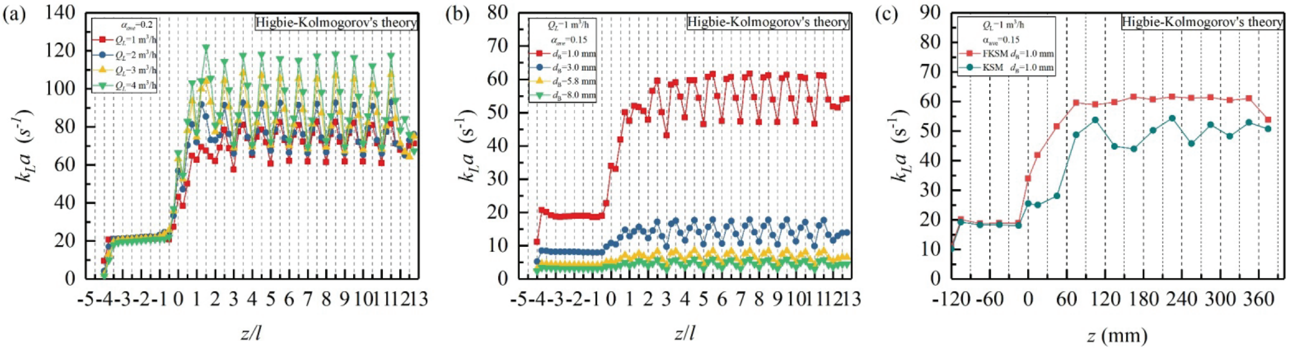

Figure 8. The axial profiles of local mass transfer coefficient at different: a) liquid inlet velocity, b) initial uniform bubble diameter and c) comparison between FKSM and KSM.

Periodic varying cross-sections of downstream mixing elements, as shown in Figure 5, induced stronger coupling among bubble forces, flow division, flow reverse and secondary flow functions, and made the local mass transfer profile approach one-humped distribution in Figure 8. The minimum of average k_La were 2.99–3.51 times of that in the inlet tube, which indicated that the temporary equilibrium may be broken at the transition of adjacent mixing segments induced by the mixing function between flow division and flow reverse. Furthermore, the maximum values of average k_La in the cross-section of the middle mixing element were 3.96–5.67 times of that in the smooth tube which indicated that the radial mixing function and lift force made the interface updated frequently. On the one hand, the local mass transfer may be improved by the increasing primary phase velocity for a given α_G, as presented in Figure 8a. On the other hand, it was noted in Figure 8b that the effect of intensification on mass transfer between air and water largely weakened with the increase of initial uniform bubble diameter from 1.0 mm to 8.0 mm. The excellent enhancement ability of local mass transfer coefficients could be evaluated between FKSM and KSM as shown in Figure 8c. It is clearly seen that the local mass transfer coefficients in the FKSM are enhanced by 18.41%−30.53% than that in the KSM for Q_L = 1 m³/h with α_{ave}=0.2 and d_B=1.0 mm.

CONCLUSION

The performances of radial gas void fraction and local mass transfer coefficients in the industrial FKSM were predicted. There is a free vortex near the central shaft and five pairs of free vortices nearby the helical blades. The local maximum of air phase velocity in each mixing element could be attained earlier than that of that water phase. The average liquid velocity decreased down to the minimum and the average air velocity increased up to the maximum at the transition regions of adjacent mixing elements. Some extra unimodal profile of radial gas holdup gradually generated near the rectangle cross-sections of mixing elements. The α_G at the inner side gradually enlarged and α_G at the tube-wall side gradually decreased from r/R = 0.2 to r/R = 0.874. The first leading edge enhanced the air phase dispersion from 2.04 to 3.69 times of that in the inlet tube. The local mass transfer coefficients in each mixing group had unimodal profiles. The maximum values generated in the middle cross-section and the minimum values in the adjacent transition regions were 3.96-5.67 times and 2.99-3.51 times of that in the smooth inlet tube. Two pairs of vortexes gradually moved closer to the outlet center and slowly weakened in the wake region. A population balance model considering the initial bubble size distributions would be employed in the further investigations to accurately predict the dispersion of the gas phase within FKSM.

Nomenclature

A_r	Aspect ratio
C_D	Drag coefficient
C_L	Lift coefficient
C_W	Wall lubrication force coefficient
d_B	Diameter of uniform bubbles, m
d_c	Critical bubble diameter, mm
$d_\perp$	Long axis of the deformable bubble
D	Tube diameter, m
D_f	Diffusivity, $m^2\ s^{-1}$
Eo	Eötvös number
$Eo_\perp$	Modified Eötvös number
F	External body force
F_{lift}	Lift force
F_{td}	Turbulent dispersion force
F_{vm}	Virtual mass force
F_{wl}	Wall lubrication force
g	Gravity, m/s^2
k_La	Local mass transfer coefficients, s^{-1}
l	Twisted plate length, m
l_i	Inlet length, m
l_m	Mixing length, m
l_o	Outlet length, m
Mo	Morton number
Q	Flow rate, m^3/h
Q_{EAS}	Equiangle skew
r	Radial position
R	Radius of the tube
Re	Reynolds number
S	Source item
t	Time, s
u	Velocity in the x direction, m/s
W	Twisted plate width
z	Section position in z direction, m

Greek

α	Volume fraction
δ	Twisted plate thickness, m
Θ	Twisted angle, °
κ	Turbulence kinetic energy, m^2/s^2
ρ	Density, kg/m^3
μ	Dynamic viscosity, kg/(m·s)
σ	Surface tension, N
$\bar{\bar{\tau}}$	Stress-strain tensor
ω	Specific rate of dissipation, m^2/s^3

Subscript

p	Primary phase
q	Secondary phase
L	Liquid
G	Gas

Abbreviations

CFD	Computational Fluid Dynamics
FKSM	Static mixer with four equally spaced helical inserts
ID	Inner Diameter
KSM	Kenics Static Mixer
SIMPLE	Semi-Implicit Method for Pressure Linked Equations
URANS	Unsteady Reynolds-Averaged Navier-Stokes equations

Acknowledgements

The authors would like to express their sincere thanks to the National Natural Science Foundation of China (Project nos. 21476142 and 21306115), Liaoning Distinguished Professor Program (Project no. [2018]35), Liaoning BaiQianWan Talents Program (Project no. 201892151), Liaoning Natural Science Foundation (Project no. 2019-ZD-0082), the Higher Education Program Funds for the Key Laboratory Research of Liaoning Province (Project no. LQ2019003), the Planning Program of Shenyang Science and Technology Bureau (Project nos. RC180011 and RC200032) for financially supporting this study. We thank the referees for their enlight-

ening remarks which helped us improve the manuscript.

REFERENCES

[1] A. Ghanem, T. Lemenand, D.D. Valle, H. Peerhossaini, Chem. Eng. Res. Des. 92 (2014) 205-228

[2] R. Rzehak, E. Krepper, Nucl. Eng. Des. 287 (2015) 108--118

[3] K. Somnuk, N. Soysuwan, G. Prateepchaikul, Renewable Energy 131 (2019) 100-110

[4] H.B. Meng, F. Wang, Y.F. Yu, M.Y. Song, J.H. Wu, Ind. Eng. Chem. Eng. 53 (2014) 4084-4095

[5] H.B. Meng, X.H. Jiang, Y.F. Yu, Z.Y. Wang, J.H. Wu, Korean J. Chem. Eng. 34 (2017) 1328-1336

[6] R.K. Thaku, Ch. Vial, K.D.P. Nigam, E.B. Nauman, G. Djelveh, Chem. Eng. Res. Des. 81 (2003) 787-826

[7] S. Rabha, M. Schubert, F. Grugel, M. Banowski, U. Hampel, Chem. Eng. J. 262 (2015) 527-540

[8] A. Kołodziej, J. Łojewska, M. Jaroszyński, A. Gancarczyk, P. Jodłowski, Int. J. Heat Fluid Flow 33 (2012) 101-108

[9] A.M. Al Taweel, F. Azizi, G. Sirijeerachai, Chem. Eng. Process 72 (2013) 51-62

[10] A.M. Al Taweel, J. Yan, F. Azizi, D. Odedra, H.G. Gomaa, Chem. Eng. Sci. 60 (2005) 6378-6390

[11] F. Azizia, A.M. Al Taweel, Chem. Eng. Sci. 62 (2007) 7436-7445

[12] F. Azizi, A.M. Al Taweel, Ind. Eng. Chem. Res. 54 (2015) 11635-11652

[13] F. Azizi, K.A. Hweij, AIChE J. 63 (2017) 1390-1403

[14] D.M. Hobbs, P.D. Swanson, F.J. Muzzio, Chem. Eng. Sci. 53 (1998) 1565-1584

[15] Z. Jaworski, P. Pianko-Oprych, Chem. Eng. Res. Des. 80 (2002) 910-916

[16] Z. Jaworski, H. Murasiewicz, Chem. Pap. 64 (2010) 182--192

[17] H.B. Meng, Z.Q. Liu, Y.F. Yu, Q. Xiong, J.H. Wu, Int. J. Chem. React. Eng. 9 (2011) 1-19

[18] E. Lobry, F. Therona, C. Gourdona, N.L. Sauzea, C. Xuereba, T. Lasuyeb, Chem. Eng. Sci. 66 (2011) 5762--5774

[19] H.B. Meng, Z.Q. Liu, Y.F. Yu, J.H. Wu, Braz. J. Chem. Eng. 29 (2012) 167-182

[20] A. Couvert, C. Sanchez, I. Charron, A. Laplanche, C. Renner, Chem. Eng. Sci. 61 (2006) 3429-3434

[21] H. Tajima, A. Akihiro Yamasaki, F. Kiyono, Energy Fuels 18 (2004) 1451-1456

[22] H. Tajima, A. Yamasaki, F. Kiyono, H. Teng, AIChE J. 50 (2004) 871-878

[23] H. Tajima, A. Yamasaki, F. Kiyono, Energy Fuels 19 (2005) 2364-2370

[24] Y.X. Liao, R. Rzehak, D. Lucas, E. Krepper, Chem. Eng. Sci. 122 (2015) 336-349

[25] F. Zidouni, E. Krepper, R. Rzehak, S. Rabha, M. Schubert, U. Hampel, Chem. Eng. Sci. 137 (2015) 476-486

[26] F.T. Kanizawa, G. Ribatski, Int. J. Heat Fluid Flow 65 (2017) 200-209

[27] F.T. Kanizawa, G. Ribatski, Int. J. Heat Fluid Flow 65 (2017) 210-219

[28] J.H. Wu, Chinese Patent CN 200510045606.8 (2007)

[29] A. Sakin, I. Karagoz, Chem. Ind. Chem. Eng. Q., 23 (2017) 483-493

[30] B.K. Dhar, S.K. Mahapatra, S.K. Maharana, A. Sarkar, S.S. Sahoo, J. Comput. Multiphase Flows 8 (2016) 201--212

[31] M.E. Garmakova, V.V. Degtyarev, N.N. Fedorova and V.A. Shlychkov, AIP Conf. Proc. 1939 (2018) 020037-1--020037-12

[32] ANSYS, ANSYS Fluent Theory Guide Release 16.0, ANSYS Inc., Canonsburg, 2015, p. 570

[33] R. Taghavi-Zenouz, M.H.A. Behbahani, Aerosp. Sci. Technol. 72 (2018) 409-417

[34] V. Abdolkarimi, H. Ganji, Braz. J. Chem. Eng. 31 (2014) 949-957

[35] R. Rzehak, E. Krepper, C. Lifante, Nucl. Eng. Des. 253 (2012) 41-49

[36] E. Krepper, D. Lucas, H.M. Prasser, Nucl. Eng. Des. 235 (2005) 597-611

[37] M. Ishii, N. Zuber, AIChE J. 25 (1979) 843-855

[38] R. Rzehak, M. Krauß, P. Kováts, K. Zähringer, Int. J. Multiphase Flow 89 (2017) 299-312

[39] D.A. Drew, R.T. Lahey, In particulate two-phase flow, Butterworth-Heinemann, Oxford, 1993, pp. 509-506

[40] A. Tomiyama, Multiphase Sci. Technol. 10 (1998) 369--405

[41] T. Frank, J. Shi, A.D. Burns, Validation of Eulerian multiphase flow models for nuclear safety applications, in Proceeding of the 3rd International Symposium on Two--Phase Flow Modelling and Experimentation, Pisa, Italy, 2004, pp. 1-9

[42] B. Vadlakonda, N. Mangadoddy, Sep. Purif. Technol. 184 (2017) 168-187

[43] D. Lucas, E. Krepper, H. M. Prasser, Int. J. Therm. Sci. 40 (2001) 217-225

[44] A. Tomiyama, A. Sou, I. Zun, N. Kanami, T. Sakaguchi, Adv. Multiphase Flow (1995) 3-15

[45] S. Hosokawa, A. Tomiyama, S. Misaki, T. Hamada, Lateral migration of single bubbles due to the presence of wall, in Proceedings of ASME FEDSM'02, Montreal, Canada, 2002, pp. 855-860

[46] Y.F. Yu, H.Y. Wang, M.Y. Song, H.B. Meng, Z.Y. Wang, J.H. Wu, Appl. Therm. Eng. 94 (2016) 282-295

[47] ANSYS, ANSYS Fluent User's Guide Release 16.0, ANSYS Inc., Canonsburg, 2015, p. 1429

[48] FLUENT, Gambit 2.4 User's Guide, FLUENT Inc., Canonsburg, 2007, p. 3-91

[49] M. Tobajas, E. Garcia-Calvo, M.H. Siegel, S.E. Apitz, Chem. Eng. Sci. 54 (1999) 5347-5354.

HUIBO MENG[1]
ZHONGGEN LI[1]
YANFANG YU[1]
MENGQI HAN[1]
SHUNING SONG[2]
XIUHUI JIANG[1]
ZONGYONG WANG[1]
JIANHUA WU[1]

[1]Engineering and Technology Research Center of Liaoning Province for Chemical Static-Mixing Reaction, School of Mechanical and Power Engineering, Shenyang University of Chemical Technology, Shenyang, P. R. China
[2]School of Chemistry and Molecular Bioscience, the University of Queensland, Brisbane, Australia

NAUČNI RAD

STRUJNE I MASENO-PRENOSNE KARAKTERISTIKE KONCENTRNOG STRUJANJA GASNO-TEČNO U NAPREDNOM STATIČKOM MEŠAČU

Fluido-dinamičke fluida i maseno-prenosne karakteristike koncentričnog strujanja gasno-tečno nagore proučavane su u industrijskom statičkom mešaču sa četiri jednako raspoređena spiralna umetka (FKSM). Numeričke simulacije sadržaja gasa u Keniksovom mešaču dobro su se slagale sa numeričkim i eksperimentalnim rezultatima Rabhe i sar. Karakteristike radijalne frakcije sadržaja gasa i lokalni koeficijenti prenosa mase u FKSM procenjeni su pod različitim radnim uslovima. Profili brzine koncentrične gasne faze ubrzane silama mehura prvo su bili oštri i uski sve do z/l = -3,27, a zatim su polako opadali i stabilizovali se na z/l = -1,5 pre ulaska u prvi element za mešanje. Neki ekstra unimodalni profil radijalnog zadržavanja gasa postepeno se stvara u blizini pravougaonih poprečnih preseka elemenata za mešanje. AG se postepeno povećavao sa r/R = = 0,2 na r/R = 0,55, a zatim je oslabio sa r/R = 0,65 na r/R = 0,874. Udeo vazduhu u regionu glavnog toka smanjuju se sa povećanjem početnog uniformnog prečnika mehurića. Ulazni efekat prve vodeće ivice pojačao je disperziju gasne faze i lokalni koeficijenti prenosa mase naglo su porasli sa 2,04 na 3,69 puta u odnosu na one na ulazu. Lokalni koeficijenti prenosa mase u svakoj grupi mešanja imali su unimodalne profile.

Ključne reči: statički mešač, multihelikalni umetci, protok gas-tečnost nagore, sadržaj gasa, lokalni koeficijenti prenosa mase.

CI&CEQ
Chemical Industry & Chemical Engineering Quarterly

Available on line at
Association of the Chemical Engineers of Serbia *AChE*
www.ache.org.rs/CICEQ

Chem. Ind. Chem. Eng. Q. 27 (1) 69–78 (2021) CI&CEQ

RURU FU[1]
ZHUANGZHANG HE[1]
SHIKAI QIN[1]
QINGZE JIAO[1,2]
CAIHONG FENG[1]
HANSHENG LI[1]
YUN ZHAO[1]

[1]School of Chemistry and Chemical Engineering, Beijing Institute of Technology, Beijing, PR China
[2]School of Materials and Environment, Beijing Institute of Technology, Zhuhai, Guangdong, PR China

SCIENTIFIC PAPER

UDC 66.092-097.3:678.065:628

LIGHT OLEFIN PRODUCTION USING THE MIXTURE OF HZSM-5/MCM-41 AND γ-Al_2O_3 AS CATALYSTS FOR CATALYTIC PYROLYSIS OF WASTE TIRES

Article Highlights

- The mixtures of γ-Al_2O_3 and HZSM-5/MCM-41 were used as catalysts
- The mixed catalysts have micro-, meso- and macropores
- The catalysts were used to catalyze the pyrolysis of waste tires
- The selectivity to light olefins was enhanced by the introduction of γ-Al_2O_3

Abstract

In this paper, micro-mesoporous HZSM-5/MCM-41 zeolites were prepared by a two-step hydrothermal method using commercial HZSM-5 with two different silica/alumina ratios (38 and 50) as starting materials. The structures, morphologies and acidity of as-prepared zeolites were analyzed using XRD, FT-IR, SEM, N_2-adsorption/desorption and NH_3-TPD. The HZSM-5/MCM-41 zeolites combined the acidity of microporous HZSM-5 with the pore advantages of mesoporous MCM-41. Mesopores and microspores of 3.34 and 0.95 nm in diameter were found to be present in HZSM-5/MCM-41 zeolites. When they were used to catalyze the pyrolysis of waste tires, the selectivity of light olefins for HZSM-5/MCM-41 prepared using HZSM-5 with the silica/alumina ratio of 50 as starting materials was 21.42%, higher than 18.43% of HZSM-5/MCM-41 synthesized using HZSM-5 with the silica/alumina ratio of 38. In order to further overcome the pore size constraints and mass transfer limitations of HZSM-5/MCM-41 zeolites for catalyzing pyrolysis of waste tires, macroporous γ-Al_2O_3 were mixed with HZSM-5/MCM-41 and used as catalysts. The selectivity to light olefins for the mixture of γ-Al_2O_3 and HZSM-5/MCM-41 prepared using HZSM-5 with the silica/alumina ratio of 50 as starting materials was 33.65%, which was obviously enhanced by the introduction of γ-Al_2O_3.

Keywords: catalytic pyrolysis, HZSM-5, light olefins, MCM-41, waste tires, γ-Al_2O_3.

Light olefins (C_2-C_4 olefins) are important basic chemical materials for producing polyolefins, which are widely applied in various fields. In recent years, the demand for light olefins has been rising and the contradiction between supply and demand will also become increasingly prominent [1]. At present, the source of light olefins is mainly petroleum as well as coal. The gradual depletion of oil and coal reserves has aroused people's interest in finding alternative sources of energy. At the same time, the number of waste tires is growing more and more with the rapid development of the automotive industry. It is very important to effectively recycle and reuse the waste tires [2]. In addition to fuel oil and aromatic compounds, light olefins can also be obtained by catalytic cracking of waste tires. In other words, waste tires could be a potential resource for the production of light olefins. However, most researchers have focused on obtaining oils rather than valuable light olefins by waste tire pyrolysis due to the low selectivity and yields of olefins [3-5]. Therefore, it is a key factor to find an effective catalyst for pyrolysis of waste tires

---

Correspondence: Y. Zhao, Shengtailou 330, School of Chemistry and Chemical Engineering, Beijing Institute of Technology, Liangxiang, Fangshan District, Beijing 102488, P. R. China.
E-mail: zhaoyun@bit.edu.cn
Paper received: 2 March, 2020
Paper revised: 5 July, 2020
Paper accepted: 14 July, 2020

https://doi.org/10.2298/CICEQ200302025F

to produce light olefins with high selectivity and yields [6-8].

Zeolites are the most commonly used catalysts for cracking waste tires. Salmasi *et al.* [9] studied the effect of HZSM-5 zeolites on the pyrolysis of polybutadiene rubber, and the yield of olefins was about 16.8%. Shen *et al.* [10,11] used USY and ZSM-5 catalysts for catalytic pyrolysis of waste tires, respectively. The concentrations of straight chain and cyclic olefins obtained by USY were 3.49 and 0.76%, lower than 5.80 and 21.46% of HZSM-5 in the light fractions. Some zeolites such as standard ZSM-5, nanocrystalline n-ZSM-5 and beta zeolites were proved to increase the selectivity towards monocyclic aromatics including toluene (up to 19.82%), *m*/*p*-xylene (up to 16.91%) and benzene (up to 10.28%) [12].

Commercial HZSM-5 molecular sieves and other microporous zeolites have relatively low olefin selectivity and relatively high aromatic selectivity due to the following reasons. Firsty, long and narrow micropores are not suitable for the diffusion of light olefins, as obtained light olefins continue to react to produce aromatics or even carbon deposits [13,14]. Secondly, the local acid density is so high that the resulting light olefins continue to react at strong acid sites to produce aromatics or even carbon deposits [15,16].

In order to overcome the pore size constraint of microporous zeolites, mesoporous zeolites and hierarchical zeolites with micro- and mesopores are used to catalyze the pyrolysis of waste tires.

Anh *et al.* [1,17] studied the effect of Ru/MCM-41 and Ru/MCM-48 composite catalysts on tire pyrolysis. The yield of light olefins of non-catalyst, Ru/MCM-41 and Ru/MCM-48 catalysts were approximately 2.5, 4.6 and 7.6%, respectively. The light olefins obtained using Ru/MCM-41 and Ru/MCM-48 were 2 and 4 times as much as non-catalyst-obtained. Additionally, the mesoporous MCM-48 gave higher selectivity of propylene than ethylene.

Witsarut *et al.* [18] studied the effect of HY/MCM-41 core-shell composites on waste tire pyrolysis. The HY/MCM-41 composite contains micro- and mesopores. The yields of olefins of non-catalyst, HY, MCM-41 and the HY/MCM-41 core-shell composite were 9.0, 8.1, 10.0 and 12.0%, respectively. Compared to microporous HY and mesoporous MCM-41, the HY/MCM-41 composite with both micro- and mesopores showed an increased yield of olefins. HZSM-5/MCM-41 is the most common kind of hierarchical zeolites with micro- and mesopores. Although few investigations of HZSM-5/MCM-41 have been reported for catalyzing waste tire pyrolysis, they are used as catalysts for pyrolysis of other materials. Zhao *et al.* [19] used hierarchical HZSM-5/MCM-41 for catalytic pyrolysis of rice husk. The relative abundance of olefins for HZSM-5/MCM-41 was 14.5%, higher than 10.1% of HZSM-5. Sang *et al.* [20] prepared HZSM-5/MCM-41 composite molecular sieves for catalytic cracking of *n*-decane, and the maximum selectivity of light olefins was about 21%.

Herein, hierarchical HZSM-5/MCM-41 catalysts with micro- and mesopores were synthesized by a two-step hydrothermal method using a commercial HZSM-5 zeolite as a starting material and CTAB as a template. Considering some characteristics of macroporous γ-Al_2O_3, such as large specific surface area, larger pore diameter (pore size distribution of 5-70 nm), and a certain amount of acid sites, γ-Al_2O_3 were added into HZSM-5/MCM-41 to obtain the mixed catalysts with micro-, meso- and macropores to catalyze the pyrolysis of waste tires. The effects of catalyst composition on the selectivity of light olefins for the catalytic pyrolysis of waste rubber tires were investigated.

EXPERIMENTAL

Materials

HZSM-5 zeolites (SiO_2/Al_2O_3 ratios of 38 and 50) were obtained from Nankai University Catalyst Plant. Cetyltrimethylammonium bromide (CTAB), hydrochloric acid (HCl, 2 M in water) and quartz sand (10-20 mesh and 100-200 mesh) were purchased from Sinopharm Chemical Reagent Co., Ltd. Sodium hydroxide (NaOH), ammonia chloride (NH_4Cl) and potassium bromide (KBr) were obtained from Shanghai McLean Biochemical Technology Co., Ltd. γ-Al_2O_3 was obtained from Tianjin Kevin Technology Co. Ltd. The waste rubber tires used in the experiment are black solid powders obtained by pulverizing the waste rubber tires of automobiles after removing the fiber and the iron wire.

Preparation of HZSM-5/MCM-41

A certain amount of commercial HZSM-5 zeolites (SiO_2/Al_2O_3 ratios of 38 and 50, respectively) was added into a 1.5 M NaOH solution and treated at 40 °C for 1 h. The quantitative CTAB templates (the mole ratio of SiO_2/CTAB is 4.16) were dissolved in deionized water. The fully dissolved CTAB solution was added into above alkali-treated HZSM-5 solution and stirred at 60 °C for 1 h. Thereafter, the solution was transferred into a Teflon®-lined stainless-steel autoclave, followed by the first crystallization at 110 °C for 4 h. The pH value of the obtained suspension was then adjusted to be about 8.5 using 2.0 M hydrochloric acid solution. The second crystallization was continued at 110 °C for 24 h. During this process, part of the dissolved silicon and aluminum sources formed MCM-41 structure, which was introduced around the undissolved ZSM-5 grains. The precipitates were then separated, washed with distilled water and ethanol, dried, and calcined at 550 °C for 6 h to obtain Na-ZSM-5/MCM-41. Finally, HZSM-5/MCM-41 was then prepared by ion exchange of Na-ZSM-5/MCM-41 using a 1.0 M ammonium chloride solution. The commercial HZSM-5 with SiO_2/Al_2O_3 ratios of 38 and 50 were denoted as HZ-38 and HZ-50, respectively. The real SiO_2/Al_2O_3 ratios of HZSM-5/MCM-41 synthesized using HZ-38 and HZ-50 as starting materials were 36.4 and 39.6, respectively, which were denoted as HZM-38 and HZM-50 based on their starting materials. The decrease of the real SiO_2/Al_2O_3 ratios for HZSM-5/MCM-41 was due to the removal of some silicon species from HZSM-5 molecular sieves by alkali treatment [21,22]. A diagram of the preparation process for HZSM-5/MCM-41 is shown in Figure 1.

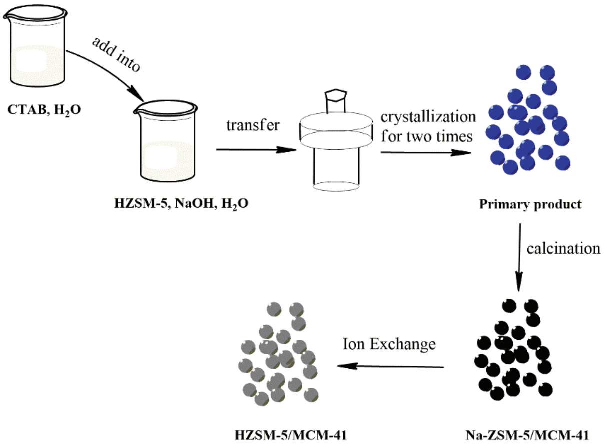

Figure 1. A schematic diagram of the preparation process for HZSM-5/MCM-41.

Characterization

Powder X-ray diffraction (XRD) patterns were recorded on an Ultima IV X-ray diffractometer (40 kV, 40 mA) with a CuK_α radiation source at a scanning rate of 20° min^{-1} from 5 to 80°. Fourier infrared spectroscopy (FTIR) was carried out on a Shimadzu IRAffinity-1s infrared spectrometer in the range of 4000-400 cm^{-1}; the resolution was 4 cm^{-1} and the number of scans was 10 times. The morphology and size of the samples were observed using a JSM-7500F scanning electron microscope (SEM). The N_2-adsorption/desorption analysis was carried out on a BELSORP-MAX specific surface area and pore structure analyzer to characterize the pore structure of the sample. The DFT pore-size distribution of different samples were obtained from the desorption branch. NH_3 temperature-programmed desorption test of the samples was performed on a TP-5076 TPD/TPR dynamic adsorption instrument to characterize the acidity and acid strength of the samples.

Catalytic performance evaluation

1.00 g waste tire and 0.25 g zeolites were mixed evenly and loaded into stainless steel tube, which was then put into the batch reactor. After they were pretreated at 120 °C for 1 h under N_2 atmosphere (30 mL/min), they were heated at a rate of 10 °C min^{-1} to the final temperature of 500 °C, and kept at 500 °C for 1 h. When the temperature reached 400 °C for 1 min, the product stream was injected into two on-line gas chromatographs through two six-port valves and connected by means of a line thermostat at 180 °C to avoid the condensation of heavy products. The total hydrocarbon distribution in terms of the carbon number and the content of monocyclic aromatics and limonene were detected using GC-2014 gas chromatograph equipped with a DB-5MS column (30 m×0.25 mm). However, the C_1-C_4 components could not be effectively separated on the DB-5MS capillary column, so C_1-C_4 hydrocarbons were detected using GC7900 gas chromatograph equipped with a CP7518 column (50 m×0.53 mm). By integrating the above two chromatographic data, a whole component analysis of the pyrolysis product could be obtained.

For all the products injected into gas chromatography, they were artificially divided into C_1-C_4, C_5, C_6, C_7, C_8, C_9-C_{10} and $C_{>10}$ components. The carbon-containing gas phase components (C_1-C_4) in the pyrolysis products would peak in a certain order on the CP7518 capillary chromatographic column. The retention time of each product was obtained using standard substances, so that the corresponding products were qualitatively determined. On the other hand, C_5-$C_{>10}$ components such as monocyclic aromatics and limonene were qualitatively analyzed by obtaining the retention time using the standard substances on the DB-5MS capillary chromatographic column.

The specific calculation process was as follows. First of all, the relative content (Ca(i)) of each component of C_1-C_4 was calculated using the peak area of each component in the chromatograph obtained by GC7900, as shown in Eq. (1) (where f_i is the correction factor, Aa (i) and Ab (i) are the peak areas of substances in i on the GC7900 and GC-2014 chromatographs, respectively):

$$\mathrm{Ca}\ (i) = \left[fiAa(i)\right] / [\sum_{i=1}^{4} fiAa(i)] \tag{1}$$

Then the relative component content calculated by Eq. (1) was used to distribute the peak area of the peaks (superimposed peaks) of C_1-C_4 components in the GC-2014 chromatograph, as shown in Eq. (2):

$$n_b\,(i) = f\,A_{b(1\text{-}4)} \frac{f\,iAa(\,i)}{\sum_{i=1}^{4} f\,iAa(\,i)} \tag{2}$$

Finally, combined with the peak area of C ($n > 4$) components in GC-2014 chromatograph, the content of each component was calculated by area normalization method, as shown in Eq. (3):

$$C_{b\,(i)} = 100\ \frac{\sum_{i=1}^{4} nbi}{\sum_{i=1}^{4} nbi + \sum_{i=5}^{n} f\,iAbi} =$$

$$= \frac{\sum_{i=1}^{4} Ab(\,i)}{\sum_{i=1}^{4} nbi + \sum_{i=5}^{n} f\,iAb(\,i)} \tag{3}$$

For the products in the system, only the hydrocarbons were analyzed. Because their properties were similar, the correction factor (fi) of each component was specified as 1 in the content calculation.

The industrial analysis of waste tire powders proceeded with reference to the industrial analysis method of coal [23]. The elemental analysis of waste tires was carried out on the elemental analyzer of the Elementar Vario MACRO cube. Elemental analysis and industrial analysis results of the waste rubber tires are shown in Table 1.

RESULTS AND DISCUSSION

Structures and morphologies of HZSM-5/MCM-41

The XRD patterns of HZ-38, HZ-50, HZM-38 and HZM-50 zeolites are shown in Figure 2. The peaks between 7 and 10° and between 22.5 and 25° are the characteristic peaks for HZSM-5 molecular sieve, corresponding to the (101), (020), (501), (151) and (303) crystal planes, respectively. It can be seen from Figure 2 that all four samples have five characteristic diffraction peaks of HZSM-5 zeolites. In addition, the XRD patterns in the 2θ of 1-6° for HZM-38 and HZM-50 show the typical MCM-41 structure, with (100), (110) and (200) diffraction peaks appearing at 2θ of about 2.2, 4.1 and 4.6°, respectively. It indicates that HZM-38 and HZM-50 are all HZSM-5/MCM-41 composites. The results show that HZSM-5 is partially dissolved after alkali treatment, while some silicon and aluminum sources dissolved by alkali treatment form MCM-41 structure, which is introduced around the undissolved HZSM-5 grains [24].

SEM images of HZ-38, HZ-50, HZM-38, HZM-50 and γ-Al_2O_3 are shown in Figure 3. The two kinds of

Table 1. Elemental analysis and industrial analysis results of waste rubber tires

Analysis	Elemental analysis					Industrial analysis			
Component	C	H	N	O	S	Moisture	Ash	Volatile	Fixed carbon
Content, wt.%	83.0	5.9	0.6	2.4	1.8	0.84	6.17	56.10	36.89

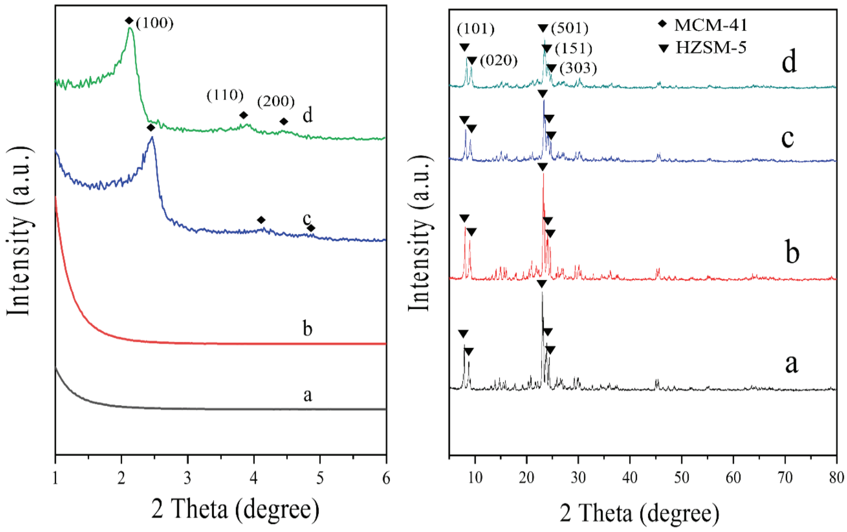

Figure 2. XRD patterns of different zeolites: a) HZ-38; b) HZ-50; c) HZM-38; d) HZM-50.

commercial HZSM-5 catalysts exhibit a hexagonal-like morphology with the size of several micrometers. Similar sizes and more irregular particles are observed for two kinds of HZSM-5/MCM-41 catalysts prepared by alkali treatment of HZSM-5. It can also be seen that the γ-Al_2O_3 have a nonuniform particle size and an unsmooth surface.

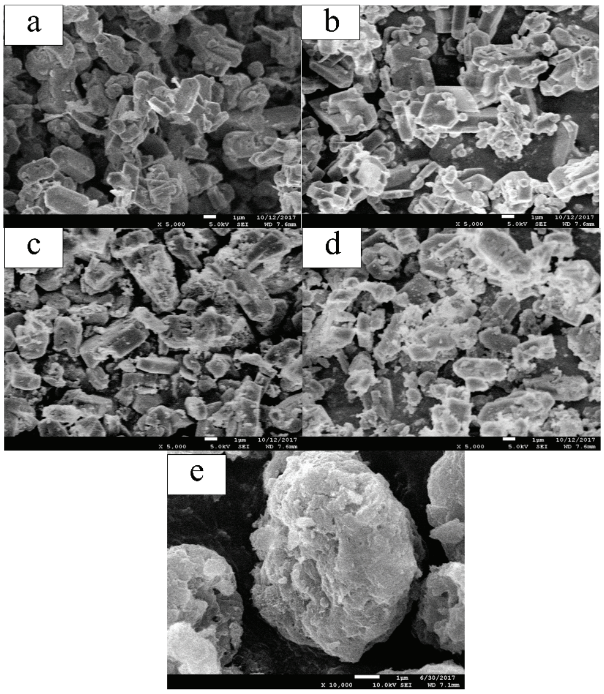

Figure 3. SEM images of different catalysts: a) HZ-38; b) HZ-50; c) HZM-38; d) HZM-50; e) γ-Al_2O_3.

The FTIR spectra of HZ-38, HZ-50, HZM-38 and HZM-50 catalysts are shown in Figure 4. The absorption peak of 1228 cm^{-1} belongs to the in-plane antisymmetric stretching vibration of the five-membered rings. The peaks of 1061 and 793 cm^{-1} are assigned to the out-of-plane antisymmetric stretching vibration and the out-of-plane symmetric stretching vibration of the tetrahedral Si-O-T (T=Si or Al) bond, respectively. The band at 454 cm^{-1} is representing the internal SiO_4 and AlO_4 tetrahedron units [25]. The characteristic peak at 544 cm^{-1} attributed to the vibration peak of five-membered ring structure is a typical peak of MFI catalysts, indicating that all the four samples have the structural units of HZSM-5 catalyst. This is consistent with the results of XRD patterns.

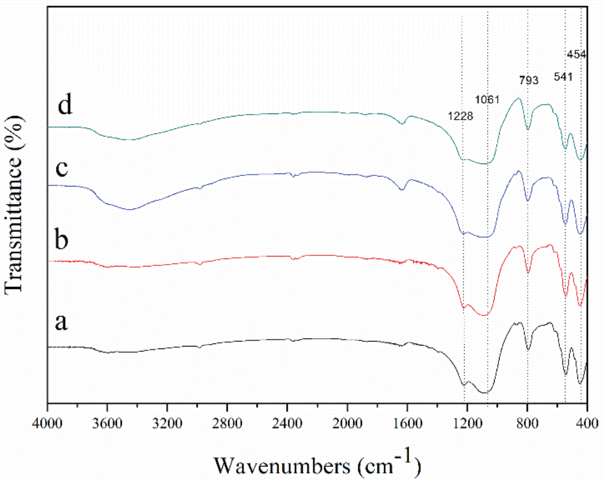

Figure 4. FTIR spectra of different catalysts: a) HZ-38; b) HZ-50; c) HZM-38; d) HZM-50.

Pore structure and acidity of HZSM-5/MCM-41

Figure 5 shows the N_2 adsorption-desorption isotherms of HZ-38, HZ-50, HZM-38 and HZM-50 catalysts. N_2 adsorption-desorption isotherms are related to pore structures of the catalysts. The isotherms of HZ-38 and HZ-50 are type I of typical microporous zeolite catalysts [26], while the isotherms of HZM-38 and HZM-50 show combined characteristics of type I and IV isotherms. The type IV isotherm is the most common adsorption behavior of mesoporous molecular sieves [27], indicating the coexistence of micropores and mesopores. A broad hysteresis loop at the relative pressure of 0.40-0.95 indicates the presence of mesopores in HZM-38 and HZM-50. When the relative pressure is low, the monolayer adsorption of N_2 molecules occurs on the wall of micropores, which makes the isotherm rise linearly. With the increase of relative pressure, the adsorption of N_2 molecules occurs in single-layer and multi-layer adsorption in mesoporous channels. When the relative pressure is increased to 0.40-0.95, the adsorption capacity increases suddenly and an obvious lag loop appears. This is caused by the capillary condensation of N_2 molecules in the mesoporous channels.

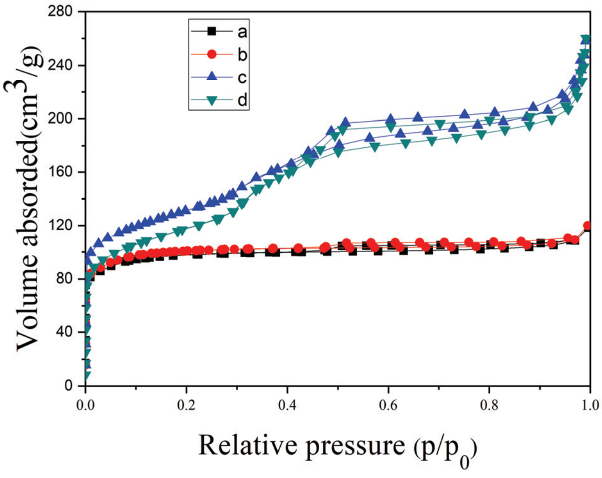

Figure 5. N_2 adsorption-desorption isotherms of different catalysts: a) HZ-38; b) HZ-50; c) HZM-38; d) HZM-50.

Figure 6 shows the pore size distribution of HZ-38, HZ-50, HZM-38, HZM-50 and γ-Al$_2$O$_3$ catalysts, and Table 2 shows the structural parameters of the corresponding samples. Compared to HZ-38 and HZ-50, the pore-size distributions of HZM-38 and HZM-50 indicate the coexistence of mesopores and micropores, confirming the presence of mesopores. It can also be seen from Table 2 that the two kinds of HZSM-5/MCM-41 catalysts have larger specific surface areas (418.7 and 468.5 m^2/g) than the two HZSM-5 catalysts (373.2 and 386.6 m^2/g) due to the introduction of mesoporous MCM-41. In addition to the specific surface area, the total pore volume also obviously increases for HZM-38 and HZM-50. As shown in Figure 6e, both mesopores and macropores are found to be present in γ-Al$_2$O$_3$.

The NH$_3$-TPD profiles of HZ-38, HZ-50, HZM-38, HZM-50 and γ-Al$_2$O$_3$ catalysts are shown in Figure 7. The peak shape of HZ-38 and HZ-50 is consistent with that of HZSM-5 catalyst reported in the literature [28], the peak at 100-310 °C is assigned to weak acid site, and the peak at 310-600 °C is assigned to strong acid site [29]. γ-Al$_2$O$_3$ is recognized as a solid acid catalyst without strong acid sites, therefore there is a broad and low desorption peak for the NH$_3$-TPD curve of γ-Al$_2$O$_3$. Compared to HZ-38 and HZ-50, the peaks of strong acid site for HZM-38 and HZM-50 decrease obviously. This indicates that the strong acid sites of HZM-38 and HZM-50 are less than those of HZ-38 and HZ-50. During the process of alkali treatment of HZSM-5 molecular sieve, part of Al is dissolved from the skeleton structure of HZSM-5 molecules and participates in the formation of MCM-41, resulting in the conversion of some B acid sites to L acid sites [20].

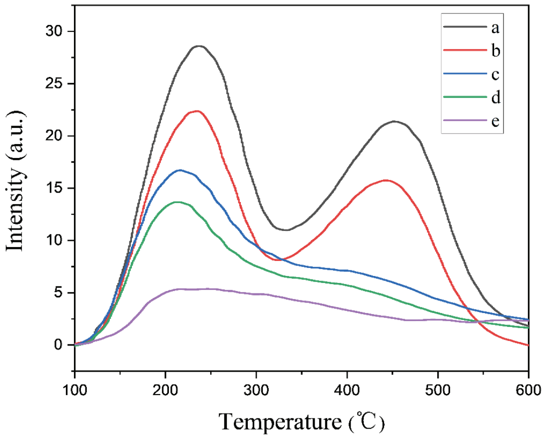

Figure 7. NH$_3$-TPD profiles of different catalysts: a) HZ-38; b) HZ-50; c) HZM-38; d) HZM-50; e) γ-Al$_2$O$_3$.

For zeolites, the total acid content decreases with the increase of SiO$_2$/Al$_2$O$_3$ ratio. As shown in

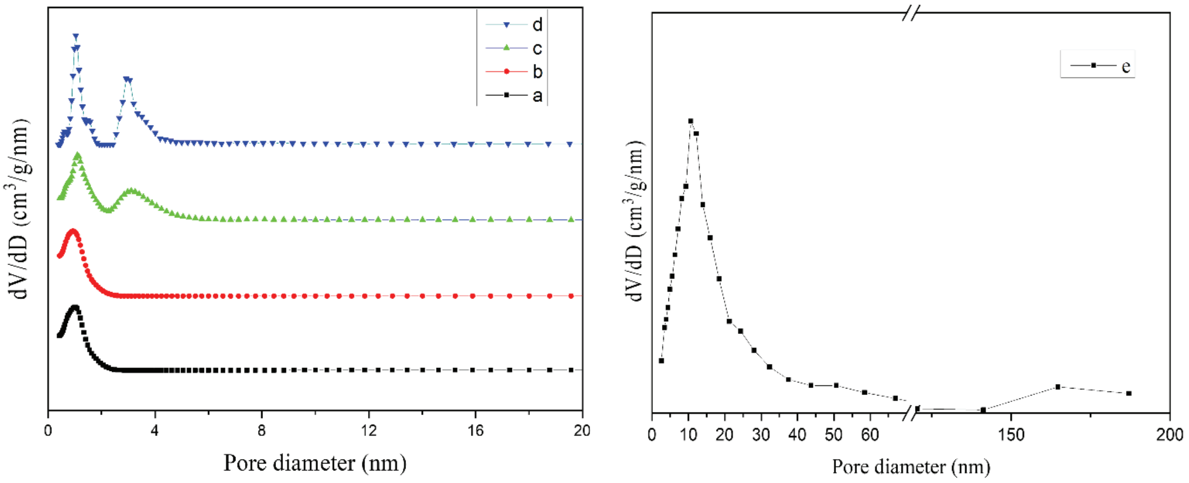

Figure 6. Pore size distribution of different catalysts: a) HZ-38; b) HZ-50; c) HZM-38; d) HZM-50; e) γ-Al$_2$O$_3$.

Table 2. Structure parameters of different catalysts

Sample	S_{BET}[a] (m^2/g)	V_{total}[b] (cm^3/g)	Dp_{micro}[c] (nm)	Dp_{meso}[d] (nm)	Dp_{macro}[e] (nm)
HZ-38	373.2	0.180	0.94	-	-
HZ-50	386.6	0.182	0.96	-	-
HZM-38	418.7	0.388	1.05	3.32	-
HZM-50	468.5	0.292	1.06	3.35	-
γ-Al$_2$O$_3$	263	1.28	-	11.81	166.20

[a]BET surface area; [b]total pore volume; [c]average micropore diameter; [d]average mesopore diameter; [e]average macropore diameter

Table 3, HZ-50 and HZM-50 exhibit the less total acid contents than HZ-38 and HZM-38, respectively, due to the higher SiO_2/Al_2O_3 ratios [30,31]. However, for HZSM-5/MCM-41catalysts, their total acid content is much lower than that of HZSM-5 catalyst with the same SiO_2/Al_2O_3 ratio. Because of alkali treatment, part of the HZSM-5 structure is destroyed, therefore the total acid content especially the amount of strong acid sites obviously decreases.

Catalytic performances of different catalysts

Considering some characteristics of macroporous γ-Al_2O_3, such as large specific surface area (Table 2, 263 m^2/g), larger pore diameter (Figure 6, pore size distribution of 5-70 nm), and a certain amount of acid sites (Figure 7 and Table 2, 131.18 μmol/g), 0.5 g of γ-Al_2O_3 were added into 0.25 g of HZSM-5/MCM-41 to obtain the mixed catalysts with micro-, meso- and macropores to catalyze the pyrolysis of waste tires. The mixture of γ-Al_2O_3 and HZM-38 (or HZM-50) were named as HZM+A-38 (or HZM+A-50). In order to confirm the role of γ-Al_2O_3, 0.5 g of inert SiO_2 was mixed with 0.25 g HZM-50 to catalyze the pyrolysis of waste tires. The mixture of SiO_2 and HZM-50 was named as HZM+S-50.

The catalytic performances of γ-Al_2O_3, HZM-38, HZM-50, HZM+A-38, HZM+A-50 and HZM+S-50 for the pyrolysis of waste tires are shown in Figure 8. The product selectivities for thermal pyrolysis of waste tires is also displayed in Figure 8. As shown in Figure 8A, the pyrolysis products include different hydrocarbons from C_1 to $C_{>10}$. In Figure 8B, the selectivity of

Table 3. Acid content distribution of different catalysts

Sample	Total acid content, μmol/g	Weak acid amount, μmol/g	Strong acid amount, μmol/g
HZ-38	569.10	265.77	303.33
HZ-50	441.17	204.75	236.42
HZM-38	286.55	142.10	144.45
HZM-50	229.26	115.07	114.19
γ-Al_2O_3	131.18	72.07	59.11

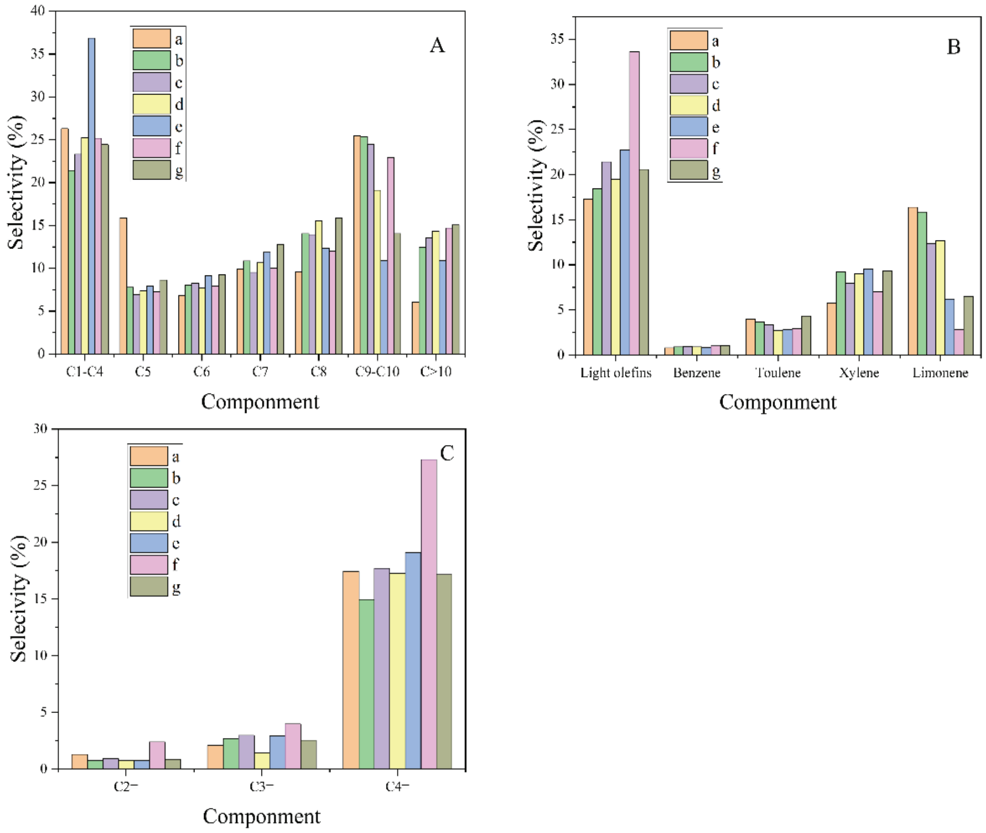

Figure 8. Effect of different catalysts on the catalytic performances for the pyrolysis of waste tires: a) non-catalysts; b) HZM-38; c) HZM-50; d) γ-Al_2O_3; e) HZM+A-38; f) HZM+A-50; g) HZM+S-50.

light olefins without catalysts is the lowest, which is 17.27%. The selectivities of light olefins for γ-Al_2O_3, HZM-38 and HZM-50 are 19.50, 18.43 and 21.42%, respectively. The selectivities of light olefins for HZM+A-38 and HZM+A-50 are 22.74 and 33.65%, respectively, higher than corresponding HZM-38 and HZM-50. HZM+A-50, the mixture of γ-Al_2O_3 and higher SiO_2/Al_2O_3 HZSM-5/MCM-41, shows the highest light olefin selectivity. This indicates that the selectivity of light olefins is significantly improved due to the introduction of macroporous γ-Al_2O_3 into hierarchical HZSM-5/MCM-41 with micro- and mesopores. As shown in Figure 8C, the selectivities of ethylene are almost the same. The source of ethylene may be due to olefin cracking in the range of gasoline. Ethylene as the primary product of waste tire cracking in the presence of zeolite catalysts is kinetically unfavorable because the formation of ethylene involves relatively unstable primary carbene ion intermediates, and changes of C_2-gases are not always be observed by lower levels of catalysts. The selectivity of propylene is improved to some extent. The addition of catalysts increases the effective cracking/hydrogen transfer ratio because it mainly acts on the cracking of higher olefins to C_3-C_5 olefins [32]. In addition, C_4 olefins are dominant in the light olefins; this may be attributed to the fact that the main component of the tire is styrene-butadiene rubber (SBR) [33].

As can be seen from Figure 8B, the selectivities of "BTX" (benzene, toluene, xylene) for γ-Al_2O_3, HZM-38, HZM+A-38, HZM-50 and HZM+A-50 are 12.65, 13.77, 13.16, 12.26 and 10.96%, respectively. While the selectivity of "BTX" is 10.56% in the case of waste tire thermal pyrolysis. HZM-50 shows lower "BTX" selectivity than HZM-38, and HZM+A-50 exhibits lower "BTX" selectivity than HZM+A-38. This indicates that the catalysts with higher SiO_2/Al_2O_3 ratios do not benefit the production of aromatic hydrocarbons due to their lower acid density. In addition, the introduction of γ-Al_2O_3 can also decrease the selectivity for "BTX". Compared with the selectivity of light olefins for waste tire pyrolysis using different catalysts, higher SiO_2/Al_2O_3 ratio of HZSM-5/MCM-41 and their mixtures with γ-Al_2O_3 show higher light olefin selectivity and lower "BTX" selectivity. During the process of waste tire pyrolysis, as-produced ethylene and propylene are further converted to aromatics at acid sites by aromatization and Diels-Alder reaction [34] due to the pore size constraint and higher acid density. Because the diffusion of light olefins is not easy in the long and narrow micropores, as-obtained light olefins continue to react at acid sites in the pores to produce aromatics [13,14]. Furthermore, the higher acid density also makes the resulting light olefins continue to react at strong acid sites to produce aromatics [15,16]. After macroporous γ-Al_2O_3 is mixed with HZSM-5/MCM-41, the acidity and the pore size constraint decrease to some extent. Therefore, the light olefin selectivity increases and the "BTX" selectivity decreases. In addition, lower SiO_2/Al_2O_3 ratio of HZSM-5/MCM-41 has higher acid density, as-obtained light olefins can also react at close acid sites to form aromatics. That is why HZM-38 (SiO_2/Al_2O_3: 36.4) show lower light olefin selectivity and higher "BTX" selectivity than HZM-50 (SiO_2/Al_2O_3: 39.6). Therefore the mixture of higher SiO_2/Al_2O_3 ratio of HZSM-5/MCM-41 and γ-Al_2O_3 show the highest light olefin selectivity and the lowest "BTX" selectivity due to the lower acid density as well as improved pore size constraint.

As can be seen from Table 4, there are some reports on HZSM-5/MCM-41 composites used as catalysts for pyrolysis of rice husk and n-decane. Other molecular sieves such as HZSM-5, HY and HY/MCM-41 are reported as catalysts for pyrolysis of tire

Table 4. Light olefin selectivity/yield/concentration/relative abundance of waste tire cracking using different catalysts; S/Y/C/RA: S - selectivity; Y - yield; C - concentration; RA - relative abundance

No.	Catalysts	Raw material	S/Y/C/RA	Ref.
1	HZSM-5/MCM-41 HZSM-5/MCM-41+γ-Al_2O_3	Waste tire	Light olefins 21.42%(S) Light olefins 33.65%(S)	This work
2	HZSM-5	Polybutadiene rubber	Olefins 16.8%(Y)	[9]
3	USY HZSM-5	Waste tire	Olefins 4.25%(C) Olefins 27.26%(C)	[10,11]
4	Ru/MCM-41 Ru/MCM-48	Tire	Light olefins 7.6%(Y)	[1,17]
5	HY/MCM-41	Waste tire	Olefins 12.0%(Y)	[18]
6	HZSM-5/MCM-41	Rice husk	Olefins 14.5%(RA)	[19]
7	HZSM-5/MCM-41	n-decane	Light olefins 21%(S)	[20]
8	nano-HZSM-5/γ-Al_2O_3	Waste tires	Light olefins 29.9%(S)	[37]
9	Used catalyst	Waste tire	Propene and 1-butene 18.25%(Y)	[38]

wastes. In the catalytic cracking of waste tires or other polymers, the mixture of γ-Al_2O_3 and HZSM-5/MCM-41 in this work shows the highest selectivity of light olefins compared with other studies. This may be due to the unique composition and micro-, meso- and macroporous structure of the catalysts.

Limonene is the main component of C_9-C_{10}. The selectivities of limonene for HZM-38, HZM-50, HZM+A-38 and HZM+A-50 are 15.87, 12.37, 6.22 and 2.85%, respectively. The lowest limonene selectivity is obtained using HZM+A-50 catalysts. Unlike other reports on pyrolysis and catalytic reforming of volatile components [10,11,35], with the presence of HZSM-5 catalyst, limonene is mainly converted to aromatic compounds [36]. The yield of limonene depends on the strength and density of acid sites and the pore structure of acid catalysts [39]. Compared with HZSM-5/MCM-41 composite catalysts, the selectivity of light olefins can be improved by adding γ-Al_2O_3. The increase of selectivity of gas products is at the cost of reducing the selectivity of liquid products. Therefore, it can also be seen from the figure that the selectivity of liquid products has been reduced to a certain extent, especially the selectivity of limonene, which has decreased by about 10%.

As shown in Figure 8B, the selectivity of light olefins for the pyrolysis of waste tires using HZM+A-38 as catalysts can be partially improved with the introduction of γ-Al_2O_3 compared with HZM-38 molecular sieves. However, it is much lower than that of HZM+A-50 catalysts. This further illustrates the importance of appropriate acid strength and acid content for catalytic cracking waste rubber tires to obtain higher selectivity of light olefins. Compared with HZM-50 zeolites, the selectivity of light olefins obtained using HZM+S-50 nearly does not change, except for limonene. In addition, compared with HZM+S-50, the selectivity of light olefins for HZM+A-50 is obviously higher, indicating that the large pore size, high specific surface area and suitable acid content of γ-Al_2O_3 play an important role in obtaining higher selectivity of light olefins.

CONCLUSIONS

Compared with HZSM-5 catalyst, the micro-mesoporous HZSM-5/MCM-41 catalyst has larger pore diameter, larger specific surface area and lower total acid content. When HZSM-5/MCM-41 is used as the catalyst, the selectivity of light olefins for HZM-50 (21.4%) is higher than that of HZM-38, while the HZM-38 can obtain higher selectivity of "BTX". The selectivity of light olefins can be improved by adding γ-Al_2O_3. When HZM+A-50 is used as catalyst, the selectivity of light olefins is 33.6%, which is much higher than that of 21.4% without γ-Al_2O_3. It is of great practical significance to use waste tires as the production resource of light olefins.

Acknowledgments

The authors of this paper would like to thank the Analysis & Testing Center, Beijing Institute of Technology for sponsoring this research. This research was also supported by Beijing Key Laboratory for Chemical Power Source and Green Catalysis, Beijing Institute of Technology.

REFERENCES

[1] D.N. Anh, K. Raweewan, W. Sujitra, J. Sirirat, J. Anal. Appl. Pyrolysis 86 (2009) 281-286

[2] J.M. Lee, J.S. Lee, Energy 20 (1996) 969-976

[3] G. Lopez, M. Olazar, M. Amutio, R. Aguado, J. Bilbao, Energy Fuels 23 (2009) 5423-5431

[4] P.T. Williams, Waste Manage. 33 (2013) 1714-1728

[5] A.M. Fernández, C. Barriocanal, R. Alvarez, J. Hazard. Mater. 203-204 (2012) 236-243

[6] J.P. Falkenhagen, L. Maisonneuve, P.P. Paalanen, N. Coste, N. Malicki, B.M. Weckhuysen, Chem.Eur.J. 24 (2018) 4597-4606

[7] S. Abbasizadeh, R. Karimzadeh, Ind. Eng. Chem. Res. 57 (2018) 7783-7794

[8] K. Sana, P. Maria, T. Mohand, K. Besma, Z. Fethi, J Energy Resour. Technol. 139 (2016) 032203

[9] S.S.Z. Salmasi, M.S. Abbas-Abadi, M.N. Haghighi, H. Abedini, Fuel 160 (2015) 544-548

[10] B. Shen, C. Wu, C. Liang, B. Guo, R. Wang, J. Anal. Appl. Pyrolysis 78 (2007) 243-249

[11] B. Shen, C. Wu, B. Guo, R. Wang, C. Liang, Appl. Catal., B 73 (2007) 150-157

[12] G.S. Miguel, J. Aguado, D.P. Serrano, J.M. Escola, Appl. Catal., B 64 (2006) 209-219

[13] J. Zheng, Q. Zeng, Y. Yi, Y. Wang, J. Ma, B. Qin, X. Zhang, W. Sun, R. Li, Catal. Today 168 (2011) 124-132

[14] J. Shah, M.R. Jan, F. Mabood, Energy Convers. Manage. 50 (2009) 991-994

[15] S. Kotrel, H.G.C. Knozinger Microporous Mesoporous Mater. 35-36 (2000) 11-20

[16] X. Li, B. Shen, C. Xu, Appl. Catal., A 375 (2010) 222-229

[17] C. Witpathomwong, R. Longloilert, S. Wongkasemjit, S. Jitkarnka, Energy Procedia 9 (2011) 245-251

[18] W. Namchot, S. Jitkarnka, J. Anal. Appl. Pyrolysis 121 (2016) 297-306

[19] Z. Li, Z. Zhong, B. Zhang, W. Wang, W. Wu, J. Anal. Appl. Pyrolysis 138 (2019) 103-113

[20] Y. Sang, Q. Jiao, H. Li, Q. Wu, Y. Zhao, K. Sun, J. Nanopart. Res. 16 (2014) 2755

[21] T. Fu, R. Qi, W. Wan, J. Shao, J.Z. Wen, Z. Li, ChemCatChem 9 (2017) 4212-4224

[22] Z. Ma, T. Fu, Y. Wang, J. Shao, Q. Ma, C. Zhang, L. Cui, Z. Li, Ind. Eng. Chem. Res. 58 (2019) 2146-2158

[23] R.A. Nadkarni, Anal. Chem. 52 (1980) 929-935

[24] H. Li, S. He, K. Ma, Q. Wu, Q. Jiao, K. Sun, Appl. Catal., A 450 (2013) 152-159

[25] F.G. Denardin, O.W. Perez-Lopez, Microporous Mesoporous Mater. 295 (2020) 109961

[26] Y.F. Yeong, A.Z. Abdullah, S.B.A. Latif Ahmad, Microporous Mesoporous Mater. 123 (2009) 129-139

[27] Y. Luo, P. Yang, J. Lin, Microporous Mesoporous Mater. 111 (2008) 194-199

[28] K. Ding, Z. Zhong, B. Zhang, J. Wang, A. Min, R. Ruan, J. Anal. Appl. Pyrolysis 122 (2016) 55-63

[29] Y. Gu, N. Cui, Q. Yu, C. Li, Q. Cui, Appl. Catal., A 429-430 (2012) 9-16

[30] A.S. Al-Dughaither, H. de Lasa, Ind. Eng. Chem. Res. 53 (2014) 15303-15316

[31] D. Ma, W. Zhang, Y. Shu, X. Liu, Y. Xu, X. Bao, Catal. Lett. 66 (2000) 155-160

[32] Y.G.A.J. Scott Buchanan, Appl. Catal., A 134 (1996) 247-262

[33] C. Berrueco, E. Esperanza, F.J. Mastral, J. Ceamanos, P. García-Bacaicoa, J. Anal. Appl. Pyrolysis 74 (2005) 245-253

[34] S. Muenpol, R. Yuwapornpanit, S. Jitkarnka, Clean Technol. Environ. Policy 17 (2016) 1149-1159

[35] M. Olazar, M. Arabiourrutia, G. López, R. Aguado, J. Bilbao, J. Anal. Appl. Pyrolysis 82 (2008) 199-204

[36] M. Arabiourrutia, M. Olazar, R. Aguado, G.L. Pez, A. Barona, J. Bilbao, Ind. Eng. Chem. Res. 47 (2008) 7600-7609

[37] Z. He, Q. Jiao, Z. Fang, T. Li, C. Feng, H. Li, Y. Zhao, J. Anal. Appl. Pyrolysis 129 (2018) 66-71

[38] C. Wang, X. Tian, B. Zhao, L. Zhu, S. Li, Processes 7 (2019) 335.

RURU FU[1]
ZHUANGZHANG HE[1]
SHIKAI QIN[1]
QINGZE JIAO[1,2]
CAIHONG FENG[1]
HANSHENG LI[1]
YUN ZHAO[1]

[1] School of Chemistry and Chemical Engineering, Beijing Institute of Technology, Beijing, PR China
[2] School of Materials and Environment, Beijing Institute of Technology, Zhuhai, Guangdong, PR China

NAUČNI RAD

PROIZVODNJA LAKIH OLEFINA KORIŠĆENJEM SMEŠE HZSM-5/MCM-41 I γ-Al_2O_3 KAO KATALIZATORA ZA KATALITIČKU PIROLIZU OTPADNIH GUMA

U ovom radu, mikro-mezoporozni HZSM-5/MCM-41 zeoliti pripremljeni su dvostepenom hidrotermičkom metodom koristeći komercijalni HZSM-5 sa dva različita odnosa silika/ /glinica (38 i 50) kao polaznim materijalima. Strukture, morfologije i kiselost pripremljenih zeolita analizirani su korišćenjem KSRD, FT-IR, SEM, N_2*-adsorpcija/desorpcija i* NH_3*-TPD. Zeoliti HZSM-5/MCM-41 kombinovali su kiselost mikroporoznog HZSM-5 sa prednostima pora mezoporoznog MCM-41. Utvrđeno je da su mezopore i mikrospore sa prečnikom od 3,34 i 0,95 nm prisutne u zeolitima HZSM-5/MCM-41. Kada su korišćeni za katalizu pirolize otpadnih guma, selektivnost lakih olefina za HZSM-5/MCM-41 pripremljenih korišćenjem HZSM-5 sa odnosom silika /glinice 50 kao početnih materijala iznosila je 21,42%, što je više od 18,43% ostvarenog sa HZSM-5 / MCM-41 koji je sintetizovan pomoću HZSM-5 sa odnosom silika/glinica od 38. Da bi se dalje prevazišla ograničenja veličine pora i ograničenja prenosa mase zeolita HZSM-5/MCM-41 za katalizu pirolizu otpadnih guma, makroporozni g-*Al_2O_3 *je pomešan sa HZSM-5/MCM-41 i korišćen kao katalizator. Selektivnost prema lakim olefinima za smešu* γ-Al_2O_3 *i HZSM-5/MCM-41, koji je pripremljen upotrebom HZSM-5 sa odnosom silika/glinice od 50 kao polaznih materijala, iznosila je 33,65%, što je očigledno poboljšannje.*

Ključne reči: katalitička piroliza; HZSM-5; laki olefini; MCM-41; Otpadne gume. γ-Al_2O_3.

CI&CEQ
Chemical Industry & Chemical Engineering Quarterly

Available on line at
Association of the Chemical Engineers of Serbia *AChE*
www.ache.org.rs/CICEQ

Chem. Ind. Chem. Eng. Q. 27 (1) 79–84 (2021) CI&CEQ

MARJANA SIMONIČ[1]
LIDIJA FRAS ZEMLJIČ[2]

[1]Faculty of Chemistry and Chemical Engineering, University of Maribor, Maribor, Slovenia
[2]Faculty of Mechanical Engineering, Institute for Engineering Materials and Design, University of Maribor, Maribor, Slovenia

SCIENTIFIC PAPER

UDC 58:66:67/68

PRODUCTION OF BIOPLASTIC MATERIAL FROM ALGAL BIOMASS

Article Highlights

- Algae-based bioplastic possesses very good mechanical features
- Biodegradability is comparable to that of the cellulose-based thermoplastic
- Application of algae biomass for sustainable bioplastic is viable

Abstract

Bioplastic composite material was developed from polylactic acid used as basic polymer and microalgae. Two types of biomaterials were prepared based on the proportion of microalgae and polylactic acid. The mass ratios were set to 5:95 and 10:90. First, spirulina was chosen as initial material and then a mixed culture of microalgae community from the biogas digestate treatment. The aim of the research was to study the characteristics of materials in order to determine whether the algal biomass community could be used in the production of bioplastics. It was found out that microalgae do not significantly impact the properties of the polylactic acid material. The degree of material crystallinity increased, the melting temperature reduced, and the modules of losses increased.

Keywords: PLA, spirulina, calorimetry, biodegradability.

Currently, 80% of polymer material is produced from fossil fuels and the need for plastic increases. Consequently, waste quantity is increasing and the environmental impact increases [1]. The main concern is due to their non-biodegradability. Reduction in plastic use is an option but has proven difficult to regulate internationally [2].

Plastics are the major components in municipal waste [3]. Particularly concerning is the growing quantity of microplastics. One of the alternatives is production of bioplastic from natural biodegradable materials, made from renewable sources [4]. Potentially promising material could be algea [5]. Spirulina and chlorella have been incorporated into thermoplastic blends with high density polyethylene (HDPE). Spirulina gave better results in final thermoplastic blends' properties. Unlike fossil-based plastics, microalgae-based bioplastics can be designed for biodegradability in natural as well as industrial composting settings. Main classes of currently developed bio-based plastics include plastics based on starch, polyhydroxyalkanoates (PHAs), polylactic acid (PLA) and celulose [4]. PLA is one of the most studied bioplastics regarding recyclability [6]. Polylactic acid (PLA) is a thermoplast which results by condensation of lactic acid or ring opening polymerization of lactide [4]. PLA provides high mechanical strength and very good thermal properties in comparison to other fossil-based polymers. The properties of the amorphous PLA glass transition, and the mechanisms involved during the aging process were investigated [7,8]. The high cooling rates enable reaching the thermodynamic equilibrium after a few minutes. Assimilation occurs where microorganisms are supplied by necessary carbon, energy and nutrient sources from the fragmentation of polymers and convert carbon of plastic to CO_2, water and biomass [9]. Parameters, such as pH, temperature, moisture and the oxygen content are among the most significant environmental factors that must be considered in the biodegradation of polymers [10]. The aim of this paper was to use the algal biomass community form the biogas digestate treatment for the production of novel composite biodegradable material. For this purpose, PLA was used and blended

---

Correspondence: M. Simonič, Faculty of Chemistry and Chemical Engineering, University of Maribor, Smetanova 17, SI-2000 Maribor, Slovenia.
E-mail: marjana.simonic@um.si
Paper received: 24 October, 2019
Paper revised: 14 July, 2020
Paper accepted: 16 July, 2020

https://doi.org/10.2298/CICEQ191024026S

with algal biomass community from the biogas digestate treatment plant for the first time. The mechanical, thermal and rheological properties of the obtained materials were characterized by the static tensile test, TGA, DSC and DMA analysis. Finally, the biodegradability of the prepared samples was tested.

EXPERIMENTAL

Materials

The biomass was taken from anaerobic biogas digestate treatment (BDT). It was air-dried for 24 h at 29 °C. Dry biomass was grinded. Spirulina was purchased from Algen Company, Slovenia. It was powdered in a glass mortar. The resulting fine blue powder was stored at room temperature until analysis.

The blends were prepared first from spirulina with polylactic acid (PLA) and then from biomass with PLA. Polylactic acid type 2003D in pellet form was supplied by Nature Works LCC (Minnetonka, MN, USA). The density was determined at 1.24 g/cm^3.

5 different granulated samples were prepared:

- Sample PLA: 100% PLA
- Sample PLA-A-5: 95% PLA and 5% of algal biomass community
- Sample PLA-A-10: 90% PLA and 10% algal biomass community
- Sample PLA-S-5: 95% PLA and 5% of spirulina
- Sample PLA-S-10: 90% PLA and 10% of spirulina.

The dried material blends were placed into a co-rotating twin-screw extruder (Laboratory extruder LTE20-44, LabTech, USA). The temperature was set to 175 °C. The screw speed was between 20 and 50 rpm.

Blends were granulated in Krauss Maffei CX 50-180 Blue Power machine and stored at room temperature. Dark blends with algal biomass community and samples with pure PLA are seen in Figure 1.

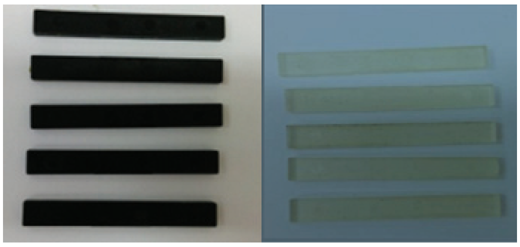

Figure 1. Final spirulina blend samples (left) and 100% PLA samples (right).

Methods

The thermogravimetric analysis (TGA) was performed to record the weight loss as function of temperature. Samples were heated from 40 to 600 °C at the heating rate of 10 °C/min under flow of O_2 (20 ml/min) and then heated from 600 to 990 °C at the heating rate of 10 °C/min under flow of N_2 (20 ml/min).

The tensile test was performed on a Shimadzu Ag-X testing machine according to EN-ISO 527:2004.

Dynamic mechanical analysis (DMA) was performed on a dynamic mechanical analyzer, DMA 8000 (Perkin Elmer).

The thermal properties were characterised by Differential Scanning Calorimetry (DSC) using TGA/ /DSC 3+ Instrument (Mettler Toledo, USA). First, the samples were conditioned at 20 °C for 2 min. Then, measurements were carried out from 20 to 190 °C, at a heating rate of 10 °C/min, under a nitrogen atmosphere.

Biodegradability of composted material samples was studied using a respirometer (ECHO, RESEP 2). The biological activity of organisms was determined by measuring the concentration of carbon dioxide in the exhausted air under controled conditions. Chambers were filled with compost and samples. The time of composting was set to 45 days. Biodegradability was determined for the following samples:

- Sample PLA: 100% PLA
- Sample PLA-A-5: 95% PLA and 5% of algal biomass community
- Sample PLA-A-10: 90% PLA and 10% of algal biomass community
- Sample PLA-S-5: 95% PLA and 5% of spirulina
- Sample PLA-S-10: 90% PLA and 10% of spirulina
- Sample compost
- Sample control.

RESULTS AND DISCUSSION

Thermogravimetric analyses

Thermogravimetric analyses for the samples with algal biomass community and for the spirulina blend are presented in Figure 2.

The one-stage degradation of microalgae is seen from Figure 2a. The degradation peak is seen at 295 °C. The weight loss due to water loss is at 115 °C. From 295 to 590 °C degradation took place with formation of volatile reaction compounds. The total weight loss of 86.9 and 13.1% loss of inorganic remains were determined.

Figure 2b represents the two-stage decomposition of spirulina blends. The weight loss due to water loss was determined at 91 °C. The material degradation peak is seen at 317 °C. From 317 to 590 °C degradation took place with formation of volatile

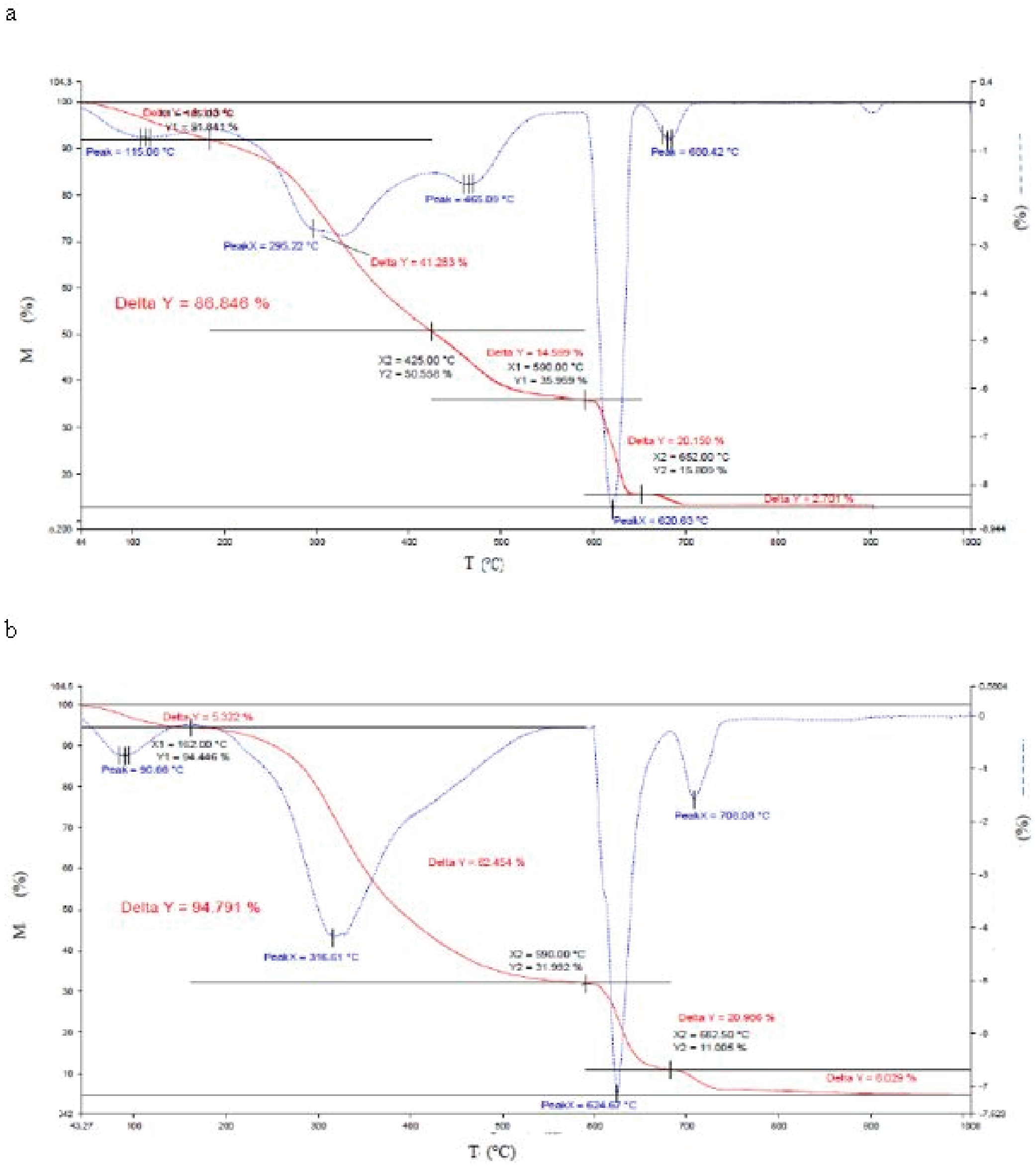

Figure 2. TGA curves: a) for algal biomass community + PLA; b) spirulina.

reaction compounds. The total weight loss of 94.8 and 5.2% loss of inorganic remains were determined.

The spirulina blends showed higher degradation rates and temperature resistance than algal biomass community, and the degradation started at higher temperature. The difference in inorganic residue quantity probably represents the heavy metals which are likely absorbed by algal biomass community [5].

The results of tensile tests are given in Table 1. Tensile strength, elongation and module of elasticity (E module) were determined.

The results showed higher tensile strength than the reported 63.4 MPa [13]. Tensile strength decreases with increasing the share of algal biomass

Table 1. Results of mechanical tests

Composition	Tensile strength, MPa	Elongation at break, %	*E*-module, GPa
PLA	95.52 ± 1.93	4.47 ± 0.05	3.31 ± 0.62
PLA-A-5	81.16 ± 0.48	3.88 ± 0.15	3.28 ± 0.63
PLA-A-10	69.46 ± 0.98	2.91 ± 0.51	3.31 ± 0.75
PLA-S-5	62.67 ± 7.26	2.32 ± 0.56	3.32 ± 0.65
PLA-S-10	77.23 ± 2.78	3.55 ± 0.56	3.37 ± 0.44

community. It seemed that algal biomass community was not compatible with PLA and the adhesion between the polymer matrix and algae seemed to be poor. On the other hand, an elongation increment was observed in contrast with spirulina blends.

Modification of bioplastic by adding a plasticizer such as epoxidized soybean oil (ESO) could improve the tensile strength and elongation properties [11]. Condensation reaction between the oxirane rings in ESO and the hydroxyl groups (starch) improved mechanical properties as well as increase hydrophobicity of biocomposite material.

The *E*-module does not change much if different samples are compared, as seen from Table 1. The sample rigidity did not change by adding more algal biomass community (see samples PLA-A-10 and PLA-S-10) to the blends.

DMA and DSC analyses

Dynamic mechanical analysis (DMA) results are presented in Table 2.

The higher the dynamic elastic module the higher the degree of crystallinity. With both spirulina samples the dynamic module of elasticity (E_{dm}) increases with the spirulina share at 30 and 80 °C, and *vice versa* with DTP algal biomass community. Therefore, the degree of crystallinity has a decreasing tendency with algal biomass community, and the amorphosity of the material increases.

In Table 3, the thermal properties of blends are summarized. The value of glass transition temperature Tg of PLA was measured at 76.8 °C, which is a little higher in comparison with the reported data, Tg = = 66.2 °C [12] and Tg = 56.1 °C [13]. Tg of blends did not change significantly regardless of the algae share. All Tg remained in range of 72.2-74.3 °C. PLA melting temperature was determined at Tm = 153.3 °C, which coincide with the earlier reported value of Tm = 151.6 °C [13]. The share of spirulina (5 and 10 mass%) did not affect the Tm, while Tm of PLA-A-5 decreased for 4 °C in comparison with pure PLA. The reason could be due to the immense increase in the degree of crystallinity. It increased from 50% for PLA up to 86% in PLA-A-5. Algae act as a nucleation core which influences the increase in crystallisation.

Table 3. The thermal properties of blends

Sample	Tg / °C	ΔCp / Jg^{-1} K^{-1}	Degree of crystallinity, %	Tm / °C
PLA	76.8	0.228	50.32	153.5
PLA-A-5	72.2	0.306	86.64	149.5
PLA-A-10	73.3	0.211	39.61	152.3
PLA-S-5	74.3	0.106	41.35	153.4
PLA-S-10	74.3	0.075	55.20	153.3

Heat capacity step ΔCp is in accordance with literature [7], where the value 0.25 J/(g K) was reported. High cooling rate in PLA/algae samples leads to higher enthalpy, and more free volume in the blend, and consequently Tg is lower. Thus, the diffusion related to the structural recovery is higher. In blends with spirulina, a lower cooling rate was observed.

As already mentioned, some results of material properties could be the consequence of heavy metal content in the algal biomass community. Therefore, analysis on metals which are most likely present in real algal biomass community was performed. The results of metal measurements in algal biomass community (w_{A}), in spirulina (w_{S}) and maximum allowed values of first-class compost (w_{c}) are presented in Table 4. As seen from Table 4, the concentration of metal in algal biomass community is higher compared with spirulina. We can accept the suspicion that algae absorb metals from water streams. However, for composting, only the concentration of Zn is problematic in blended algal biomass community. Zhao [15] found out that Zn does not cause any changes in the germination index. In samples with spirulina, the measured concentrations are very low. Zhang proposed the mixing ratios which were safe for land application [14]. In our case, the mixing ratio should be 1:5 between algal biomass community (w_{A}) and spirulina (w_{S}).

A biodegradable material is converted to CO_2, water, inorganic compounds and biomass [17]. During 45 days of incubation, most samples reached the plateau in producing CO_2. Figure 3 represents the CO_2 production in time dependence.

Table 2. Results of dynamical mechanical analyses

Sample	E_{dm} at 30 °C, GPa	E_{dm} at 80 °C, GPa	Module losses at 30 °C, MPa	Module losses at 80 °C, MPa
PLA	3.86	18.33	37.4	11.9
PLA-A-5	3.06	53.20	75.1	26.3
PLA-A-10	2.26	36.76	57.2	17.4
PLA-S-5	2.86	32.61	50.4	18.2
PLA-S-10	3.55	42.36	61.1	20.3

Table 4. Determination of metal ions concentrations in real algal biomass community and in spirulina, in comparison with compost

Metal	w_A / mg kg^{-1}	w_S / mg kg^{-1}	w_C / mg kg^{-1}
Cu	56.5	<2	100
Zn	2110	14.1	400
Cd	<1	<1	1.5
Cr	67.6	<2	100
Ni	43.0	<2	50
Pb	8.6	<2	120

The most CO_2 was produced by the spirulina blend sample PLA-S-10, which contained the highest share of spirulina (10%), followed by the sample with a little lower share of spirulina (5%). Samples with 100% PLA also produced a lot of CO_2. PLA is susceptible to biodegradation by compost, and isolated soil microorganisms were capable of degrading PLA as well, such as *Amycolatopsis* sp. The strain represented the highest enzyme activity toward the PLA and PCL bioplastics [15]. As seen from Figure 3, the production of CO_2 is fastened by algae addition: the higher the share of algal biomass community, the faster the digestion. Spirulina speeded up the process of CO_2 conversion more than algal biomass community due to certain microorganism strains [16]. The CO_2 production of samples with WWTP sludge (PLA-A-5 and PLA-A-10) was slower. The result could be attributed to the fact that algal biomass community contained some metals (see Table 4) which inhibit the CO_2 production.

CONCLUSIONS

Bioplastic composite material was developed from polylactic acid (PLA), which represent a basic polymer and microalgae. After extraction, the solid matrix was dried.

Algae-based bioplastic possesses very good mechanical features, with tensile strength and elongation at break over 81 MPa and over 4% elongation, respectively, for 95% PLA and 5% algae sample. Based on presented results of the mass loss test, the new bioplastic is demonstrated to be totally decomposed within 45 days. In terms of the biodegradability of this material, data showed that CO_2 production was comparable to that of cellulose-based thermoplastic. These results highlight the possibility to obtain a new sustainable bioplastic. Algal biomass community can also be easily managed because it does not require any separation from other waste. Therefore, the application of algal biomass community for bioplastic production appears to be realistic.

Acknowledgements

The authors would like to acknowledge the Slovenian Research Agency for the financial support (Project No. P2-0032, P2-0118). Authors acknowledge Silvester Bolka and Ana Podgoršek for technical support and laboratory assistance.

REFERENCES

[1] N.D. Duranay, Chem. Ind. Chem. Eng. Q. 25 (2019) 239-246

[2] H. Karan, C. Hunk, M. Grabert, M. Oey, B. Hankamer, Trends Plant Sci. 24 (2019) 237-249

[3] F. Bilo, S. Pandini, L Sartore, L.E. Depero, G. Gargiulo, A. Bonassi, S. Federici, E. Boonetempi, J. Clean. Prod. 200 (2018) 357-368

[4] M-A. Zeller, R. Hunt, A. Jones, S Sharma, J. Appl. Polym. Sci. 130 (2013) 3262-3275

[5] T. Cai, S.Y. Park, Y. Li, Renewable Sustainable Energy

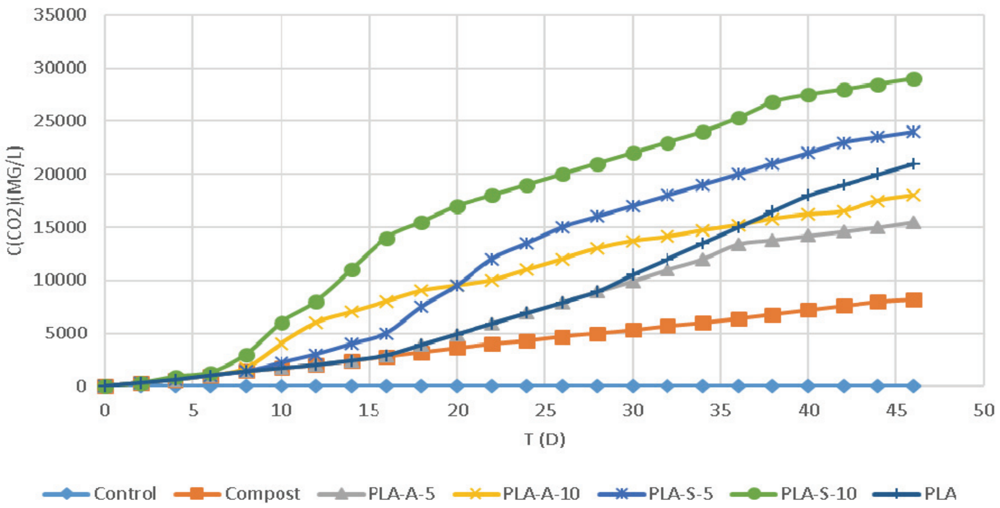

Figure 3. Dependence of CO_2 production on time.

Rev. 19 (2012) 360-369
[6] A. Soroudim, I. Jakubowicz, Eur. Polym. J. 49 (2013) 2839-2858
[7] X. Monnier, A. Saiter, E. Dargent, Thermochim. Acta 648 (2017) 13-22
[8] I. Spiridon, K. Leluk, A.M. Rosmerita, R.N. Darie, Composites, B 69 (2015) 342-349
[9] N. Lucas, C. Bienaime, C. Belloy, M. Queneudec, F. Silvestre, J.-E. Nava-Saucedo, Chemosphere 73 (2008) 429-442
[10] S.M. Emadian, T.T. Onay, B. Demirel, J. Waste Manage. 59 (2017) 526-536
[11] A. Przybytek, M. Sienkiewicz, J. Kucinska-Lipka, H. Janik, Ind. Crops Prod. 122 (2018) 375-383
[12] I. Pillin, N. Montrelay, A. Bourmaud, Y. Grohens, Polym. Degrad. Stab. 93 (2008) 321-328
[13] M. Kodal, A.A. Wis, G. Ozcok, Radiat. Phys. Chem. 153 (2018) 214-225
[14] D. Zhang, W. Luo, Y. Li, G. Wang, G. Li, Bioresour. Technol. 250 (2018) 853-859
[15] J. Zhao, X. Sun, M. K. Awasthi, Q. Wang, X. Ren, R. Li, H. Chen, M. Wang, T. Liu, Z. Zhang, Bioresour. Technol. 267 (2018) 688-695
[16] W. Penkhrue, C. Khanongnuch, K. Masaki, W. Pathom-aree, W. Punyodom, S. Lumyong, World J. Microbiol. Biotechnol. 31 (2015) 1431-1442
[17] S. Thakur, J. Chaudhary, B. Sharma, A. Verma, S. Tamulevicius, V.K. Thakur, Curr. Opin. Green Sustain. Chem. 13 (2018) 68-75.

MARJANA SIMONIČ[1]
LIDIJA FRAS ZEMLJIČ[2]

[1]Faculty of Chemistry and Chemical Engineering, University of Maribor, Maribor, Slovenia
[2]Faculty of Mecanical Engineering, Institute for Engineering Materials and Design, University of Maribor, Maribor, Slovenia

NAUČNI RAD

PROIZVODNJA BIOPLASTIČNOG MATERIJALA IZ ALGALNE BIOMASE

Bioplastični kompozitni materijal je razvijen od poli(mlečne kiseline) (PLA), koja se koristi kao osnovni polimer, i mikroalgalne biomase. Dve vrste biomaterijala su pripremljene na osnovu udela mikroalgi i PLA. Korišćeni su maseni odnosi 5:95 i 10:90. Najpre je korišćenabiomasa spiruline, a zatim mešana kultura mikroalgi iz proizvodnje biogasa. Cilj istraživanja bio je proučavanje karakteristika materijala, kako bi se utvrdilo da li se biomasa zajednica algi može koristiti u proizvodnji bioplastike. Otkriveno je da mikroalge ne utiču značajnije na svojstva materijala PLA. Stepen kristalnosti materijala i moduli gubitaka su se povećali, a temperatura topljenja smanjila.

Ključne reči: PLA, spirulina, kalorimetrija, biorazgradivost.

CI&CEQ
Chemical Industry & Chemical Engineering Quarterly

Available on line at
Association of the Chemical Engineers of Serbia *AChE*
www.ache.org.rs/CICEQ

Chem. Ind. Chem. Eng. Q. 27 (1) 85–97 (2021) CI&CEQ

A. AZMI
S.A. SATA
F.S. ROHMAN
N. AZIZ

School of Chemical Engineering, Engineering Campus, Universiti Sains Malaysia, Seri Ampangan 14300 Nibong Tebal, Seberang Perai Selatan, Penang, Malaysia

SCIENTIFIC PAPER

UDC 678.742:66

DYNAMIC OPTIMIZATION OF LOW-DENSITY POLYETHYLENE PRODUCTION IN TUBULAR REACTOR UNDER THERMAL SAFETY CONSTRAINT

Article Highlights

- The dynamic optimization of low density polyethylene (LDPE) industry is carried out
- Mass and energy balances of LDPE are validated using industrial data
- The expression of reactor temperature under critical condition is developed for thermal safety
- The safety component can be inserted in problem optimization as an inequality path constraint
- The maximization of monomer under thermal safety is solved using orthogonal collocation method

Abstract

A commercial low-density polyethylene (LDPE) which is produced by the polymerization process of ethylene in the presence of initiators in a long tubular reactor is the most widely used in polymer industry. The highly exothermic nature of the LDPE polymerization process and the heating-cooling prerequisite in the tubular reactor can lead to various problems, particularly safety in terms of thermal runaway and productivity, i.e., decreasing monomer conversion. Therefore, model-based optimization of an industrial LDPE tubular reactor under thermal safety consideration is required to be implemented. A first principle model for this process is developed and validated using industrial data. Mass and energy balances have been derived from kinetics of LDPE polymerization. Thereafter, an expression of reactor temperature under critical condition is developed and incorporated in the reference model for the thermal safety study. In order to ensure the process is thermally safe and meets the desired product grade, the constrained dynamic optimization is proposed to maximize the conversion of the monomer using orthogonal collocation (OC). The dynamic optimization result shows that the maximum reaction temperature under critical condition constraint can be satisfied by optimizing the reactor jacket. Moreover, it is achieved without jeopardizing the monomer conversion and the product grade.

Keywords: low-density polyethylene, tubular reactor, dynamic optimization, thermal safety.

Low density polyethylene (LDPE) is a major polymer that is vastly used as feedstock in the production of packaging, adhesives, coatings, and films. The robustness quality of LDPE's properties leads to various usages of such a polymer which is considered as an exclusive and high demand commodity [1,2]. The production and consumption rates of LDPE are reported to be 20.31 million tons in 2015 [3]. Market study reveals that the projection of LDPE consumption and production rates would continue to increase steadily, which justifies its continuous improvement for the past 40 years [4,5].

LDPE is produced by the polymerization process of ethylene in the presence of initiators either in

---

Correspondence: N. Aziz, School of Chemical Engineering, Engineering Campus, Universiti Sains Malaysia, Seri Ampangan 14300 Nibong Tebal, Seberang Perai Selatan, Penang, Malaysia.
E-mail: chnaziz@usm.my
Paper received: 8 January, 2019
Paper revised: 26 June, 2020
Paper accepted: 16 July, 2020

https://doi.org/10.2298/CICEQ190108027A

a long tubular reactor, as shown in Figure 1, or in a well-stirred autoclave reactor. On an industrial scale, most LDPEs are produced in tubular reactors [6]. The advantages of using LDPE tubular technology over autoclave reactors include better heat removal and cheaper organic peroxides that can be used as initiators. Moreover, there is no need to use α-olefins which can cause the formation of side branches in the polymer chain that is generated by the radical polymerization process itself [7].

The monomer conversion (X_M) in the tubular reactor is reported to be very low, which is in the range of 20-30% per pass [8]. Considering the requirement for high compression power and the expensive cost of raw materials, the utility cost of LDPE production in the tubular reactor is quite high. The X_M, which is proportional to profits has always been the focus for researchers and engineers in this field. However, there are several issues that complicate the improvement task.

Ethylene, along with initiators and chain transfer agents (CTA), are used to produce LDPE *via* free radical polymerization in extreme conditions, typically at pressures of 1,500-3,000 atm and temperatures of 50-350 °C [9]. Ethylene polymerization is a highly exothermic reaction and a rapid process. Once the polymerization process occurs, the reaction temperature would rise rapidly until all the injected initiator is exhausted [10]. A sharp increase in temperature and of conversion will occur in a short reaction zone signalling to the development of the ethylene polymerisation process. This process occurs rapidly and can lead to a thermal runaway if the temperature rise is not controlled. Under normal operating conditions, the use of maximum temperature limit (T_{max}) alone is probably adequate to ensure the free radical polymerization process runs safely, however, for a reactor behaving in an abnormal condition, the use of the T_{max} value will be an inappropriate indicator of a safety process [11]. Thus, maximum temperature under a critical condition (Tc_{max}) constraint must be imposed as a constraint to ensure the process is thermally safe.

Heat exchange failure or cooling system breakdown at any spot in this reactor may lead to a runaway condition and fatal failure. Therefore, it is essential to conduct a study to determine the optimal condition of operating parameters that can guarantee safe operation in the critical condition. However, this kind of study presents various challenges, particularly when it can lead to a reduction in production output. Monomer conversion, which is proportional to profit calculation, will most probably be reduced to facilitate the optimal condition of this study.

Numerous optimization studies that consider maximum X_M have been reported by previous researchers [8,12]. However, none of the studies consider thermal safety constraints. To bridge the gap, the dynamic optimization with thermal safety constraint must be carried out. The main objective of this work is to carry out dynamic optimization using two optimization problems. The first problem is to maximize the X_M under maximum temperature (T_{max}) constraint whereas the second problem is to maximize the X_M under maximum critical temperature (Tc_{max}). For both optimization problems, the reactor jacket (T_J) is considered as a control variable. Since the dynamic optimization method applied required a reliable model of the process, in this work, a mathematical model of LDPE polymerization in a tubular reactor that is validated with industrial data is developed.

Process modeling of LDPE tubular reactor

The first principle model which provides the kinetic and fundamental theory [13], is selected to describe the process in detail. The first principle model of the LDPE tubular reactor incorporates the conser-

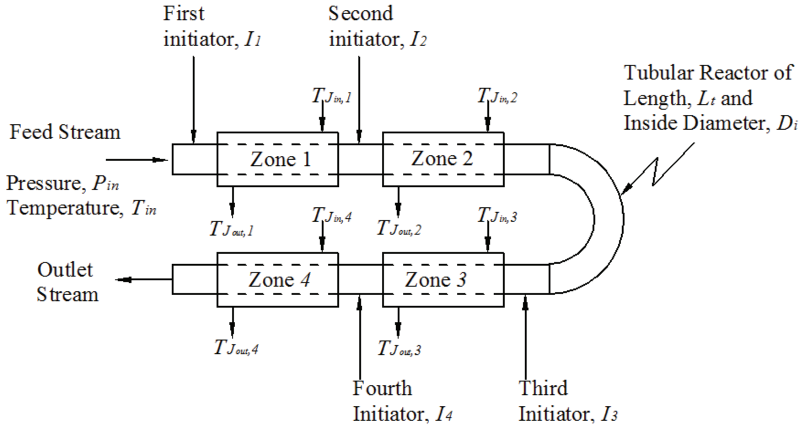

Figure 1. Schematic diagram of an industrial LDPE tubular reactor.

vation of mass, energy, and momentum balance in the reactor.

Reaction mechanism and kinetic model

LDPE is produced through a free radical polymerization of ethylene at high pressure and temperature. The main reactions involved in LDPE polymerization are chain initiation by initiator decomposition, followed by propagation and termination. Additional reaction mechanisms involved are chain transfer to monomer, chain transfer to polymer, chain transfer to solvent, and backbiting. The main reactions which are peroxide initiation, monomer thermal initiation, chain propagation, termination by combination, termination by disproportionation and thermal degradation are all common to free radical polymerization [14]. The main reactions of free radical polymerization are summarized in Eqs. (1)-(6) [6]:

Peroxide initiation: $I_{m,i} \xrightarrow{k_{d,i}} 2R(0)$ (1)

Monomer thermal initiation: $3M \xrightarrow{k_{th}} 2R(0)$ (2)

Propagation: $R(m) + M \xrightarrow{k_p} R(m+1)$ (3)

Termination by combination:

$$R(n) + R(m) \xrightarrow{k_{tc}} P(n+m) \tag{4}$$

Disproportionation: $R(x) + R(y) \xrightarrow{k_{td}} P(x) + P(y)$ (5)

Thermal degradation: $R(m+1) \xrightarrow{k_{thd}} P(m) + R(0)$ (6)

In addition to the main reactions which occur in all free radical polymerization processes, several side reactions are also present. The inter-molecular chain transfer, produces long chain branches (LCB) in LDPE. The back-biting or intramolecular chain transfer reaction is the major source of short chain branches (SCB) in LDPE. Both SCB and LCB are important characteristics of LDPE [8]. The content of SCB in a typical LDPE is 30 per 1000 CH_2, whereas the content of LCB is 10-30 per molecule. Meanwhile, the formation of vinyl (V_i) and vinylidene (V_{id}) unsaturated groups are closely associated with the scission of secondary and tertiary radicals [8]. The reaction schemes for the side reactions are summarized in Eqs. (7)-(12) [7]. A detailed explanation on the polymerization reaction mechanisms and molecular structure of each component involved in Eqs. (1)-(12) can be found in Agrawal's [8] work:

Chain transfer to monomer:

$$R(m) + M \xrightarrow{k_{tm}} P(m) + R(0) \tag{7}$$

Chain transfer to transfer agent:

$$R(m) + S \xrightarrow{k_{ts}} P(m) + R(0) \tag{8}$$

Chain transfer to polymer:

$$R(n) + P(m) \xrightarrow{k_{tp}} P(n) + R(m) \tag{9}$$

Backbiting: $R(m) \xrightarrow{k_{bb}} R(m)$ (10)

β-Scission of secondary radical:

$$R(m) \xrightarrow{k_\beta} P(m) + R(0) \tag{11}$$

β1-Scission of tertiary radical:

$$R(m) \xrightarrow{k_{\beta 1}} P(m) + R(0) \tag{12}$$

Reactor model equations

The first principle model is expressed as the mass balances of initiator, solvent, monomer, free radicals, and dead polymer in conjunction with the energy balances at the reaction and jacket sides along the reactor. The reactor scheme for this study is shown in Figure 1. The model takes into account four initiator injection points, variable density, viscosity, and velocity of the reaction stream. The derivative of axial velocity with respect to axial length in materials balance is ignored in the present study as it is considered negligible [15,16]. The developed model uses data from reported industrial production. The mass balances with regards to each respective component in the LDPE tubular reactor polymerization process are given by Eqs. (13)-(18) [7]:

Peroxide initiator mass balance:

$$v\frac{dC_{I_i}}{dz} + 2f_{d,x}K_{d_i}C_{I_i} = 0 \tag{13}$$

Monomer mass balance:

$$v\frac{dC_M}{dz} + K_pC_M\lambda_0 + 2K_{th}C_M^3 + K_{tm}C_M\lambda_0 = 0 \tag{14}$$

Solvent mass balance:

$$v\frac{dC_S}{dz} + K_{ts}C_S\lambda_0 = 0 \tag{15}$$

Methyl group/1000 CH_2 mass balance:

$$v\frac{dC_{Me}}{dz} + K_{bb}\lambda_0 = 0 \tag{16}$$

Vinyl group/1000 CH_2 mass balance:

$$v\frac{dC_{Vi}}{dz}+K_{\beta 1}\lambda_0=0 \tag{17}$$

Vinylidene group/1000 CH_2 mass balance:

$$v\frac{dC_{Vid}}{dz}+K_{\beta}\lambda_0=0 \tag{18}$$

The energy balance for the reaction and cooling zones are represented by Eqs. (19) and (20), respectively [7]:

$$\frac{dT}{dz}=\frac{1}{\rho C_P v}\left[-\Delta H K_p C_M \lambda_0-\frac{4U\left(T-T_J\right)}{D_i}\right] \tag{19}$$

$$\frac{dT}{dz}=\frac{1}{\rho C_P v}\left[-\frac{4U\left(T-T_J\right)}{D_i}\right] \tag{20}$$

Meanwhile, the pressure profile in the reaction mixture is expressed in Eq. (21):

$$\frac{dP}{dz}=-\frac{2f_r v^2}{D_{in}} \tag{21}$$

The expressions for the moments of live radical (λ_j) distribution are defined by Eqs. (22)-(24) [7,15]:

$$v\frac{d\lambda_0}{dz}=2fK_{d_i}C_{I_i}+2K_{th}C_M{}^3-\left(K_{tc}+K_{td}\right)\lambda_0^2 \tag{22}$$

$$\begin{aligned} v\frac{d\lambda_1}{dz}&=2fK_{d_i}C_{I_i}+2K_{th}C_M{}^3-\left(K_{tc}+K_{td}\right)\lambda_0\lambda_1-\\ &-\left(K_{tm}C_M+K_{ts}C_S+K_{thd}+K_{bb}+K_{\beta}+K_{\beta 1}\right)\times\\ &\times\left(\lambda_1-\lambda_0\right)+K_pC_M\lambda_0+K_{tp}\left(\lambda_0\mu_2-\lambda_1\mu_1\right)\end{aligned} \tag{23}$$

$$\begin{aligned} v\frac{d\lambda_2}{dz}&=2fK_{d_i}C_{I_i}+2K_{th}C_M{}^3-\left(K_{tc}+K_{td}\right)\lambda_0\lambda_2-\\ &-\left(K_{tm}C_M+K_{ts}C_S+K_{thd}+K_{bb}+K_{\beta}+K_{\beta 1}\right)\times\\ &\times\left(\lambda_2-\lambda_0\right)+K_pC_M\lambda_0+2K_pC_M\lambda_1+K_{trp}\left(\lambda_0\mu_3-\lambda_2\mu_1\right)\end{aligned} \tag{24}$$

The concentration of the radical moments is considered to be pseudo-stationary as inferred from previous studies [7,15], therefore Eqs. (22)-(24) are converted into Eqs (25)-(27):

$$\lambda_0=\sqrt{\frac{2fK_{d_i}C_{I_i}+2K_{th}C_M{}^3}{\left(K_{tc}+K_{td}\right)}} \tag{25}$$

$$\lambda_1=\frac{2fK_{d_i}C_{I_i}+2K_{th}C_M{}^3+K_pC_M\lambda_0+K_{tp}\lambda_0\mu_2+\left(K_{tm}C_M+K_{ts}C_S+K_{thd}+K_{bb}+K_{\beta}+K_{\beta 1}\right)\lambda_0}{\left(K_{tc}+K_{td}\right)\lambda_0-\left(K_{tm}C_M+K_{ts}C_S+K_{thd}+K_{bb}+K_{\beta}+K_{\beta 1}\right)+K_{tp}\mu_1} \tag{26}$$

$$\lambda_2=\frac{2fK_{d_i}C_{I_i}+2K_{th}C_M{}^3+K_pC_M\lambda_0+2K_pC_M\lambda_1+K_{tp}\lambda_0\mu_3+\left(K_{tm}C_M+K_{ts}C_S+K_{thd}+K_{bb}+K_{\beta}+K_{\beta 1}\right)\lambda_0}{\left(K_{tc}+K_{td}\right)\lambda_0-\left(K_{tm}C_M+K_{ts}C_S+K_{thd}+K_{bb}+K_{\beta}+K_{\beta 1}\right)+K_{tp}\mu_1} \tag{27}$$

The expression of live radical moments, as shown in Eqs. (25)-(27) is also implemented as a solution to molecular weight distribution [15,16].

The mass balance on a polymer model based on the reaction mechanism is given in the Eqs. (28)-(30):

$$\begin{aligned} v\frac{d\mu_0}{dz}&=K_{td}\lambda_0^2+\frac{1}{2}K_{tc}\lambda_0^2+\\ &+\left(K_{tm}C_M+K_{ts}C_S+K_{thd}+K_{bb}+K_{\beta}+K_{\beta 1}\right)\lambda_0\end{aligned} \tag{28}$$

$$\begin{aligned} v\frac{d\mu_1}{dz}&=K_{td}\lambda_0\ \lambda_1+K_{tc}\lambda_0\ \lambda_1+\\ &+\left(K_{tm}C_M+K_{ts}C_S+K_{thd}+K_{bb}+K_{\beta}+K_{\beta 1}\right)\lambda_1+\\ &+K_{tp}\left(\lambda_1\mu_1-\lambda_0\mu_2\right)\end{aligned} \tag{29}$$

$$\begin{aligned} v\frac{d\mu_2}{dz}&=K_{td}\lambda_0\ \lambda_2+K_{tc}\left(\lambda_0\ \lambda_2+\lambda_1^2\right)+\\ &+\left(K_{tm}C_M+K_{ts}C_S+K_{thd}+K_{bb}+K_{\beta}+K_{\beta 1}\right)\lambda_2+\\ &+K_{tp}\left(\lambda_2\mu_1-\lambda_0\mu_3\right)\end{aligned} \tag{30}$$

The closure method of the polymer moment (μ_3) is represented by Eq. (31) [17]:

$$\mu_3=\frac{\mu_2}{\mu_0\mu_1}\left(2\mu_0\mu_2-\mu_1^2\right) \tag{31}$$

The equations of live radical moments which are shown in Eqs. (25)-(27) and the differential equations of polymer moments which are shown in Eqs. (28)-(30) are crucial in mass balance as they enable the determination of polymer properties which includes molecular weight (*MW*) and melt flow index (*MFI*). The kinetic parameter K_x values are estimated via the parameter estimation study. The values of K_x are not exposed due to proprietary reasons. The simulated data is then validated by using data from an industrial company which operates in Malaysia.

Properties of the mixture

The density and the specific heat capacity of the reaction mixture considered in this study are denoted as the composition of pure ethylene. The equations are in the function of pressure and temperature as prescribed by Buchelli *et al.* [18]. The density and the specific heat capacity of the reaction mixture are approximated by Eqs. (32) and (33), respectively:

$$\rho_m = \left(\left(X_e / \rho_e \right) + \left(\left(1 - X_e \right) / \rho_{pe} \right) \right)^{-1} \tag{32}$$

$$Cp_m = X_e Cp_e + \left(1 - X_e \right) Cp_{pe} \tag{33}$$

Heat properties

The overall heat transfer coefficient (U) is calculated directly from the temperature differences and heat transferred in the reactor using Eq. (34) [19]:

$$U = \left((Q / A) \Delta T_{lm} \right) \tag{34}$$

The value of heat transfer (Q) is calculated from the heat rise of the water coolant stream as in Eq. (35):

$$Q = \left(\dot{m}_J Cp_J \left(T_{J,out} - T_{J,in} \right) \right) \tag{35}$$

and the log mean temperature (ΔT_{lm})is given as in Eq. (36):

$$\Delta T_{lm} = \frac{\left(\left(T_{P,in} - T_{J,out} \right) - \left(T_{P,out} - T_{J,in} \right) \right)}{\ln \left(\left(T_{P,in} - T_{J,out} \right) / \left(T_{P,out} - T_{J,in} \right) \right)} \tag{36}$$

Production output

Eqs. (37)-(39) represent the calculations for monomer conversion (X_M), weight-average molecular weight (MW) [8] and melt flow index (MFI) [20]:

$$X_M = 100 \left[1 - \left(\frac{C_M}{C_{M_0}} \right) \right] \tag{37}$$

$$MW = 28.05 \left(\frac{\mu_2 + \lambda_2}{\mu_1 + \lambda_1} \right) \tag{38}$$

$$MFI(\text{g/10min}) = (2.75e33)(gMW \times 10^{-4})^{-7.61} \tag{39}$$

Assessment criteria for the severity of a runaway condition

The assessment criteria for the severity of a runaway condition is based on ΔT_{ad} value. This value is chosen since it shows the amount of reactor temperature rise for LDPE polymerization in the tubular reactor. A severity criterion of potential for runaway condition which is listed in Table 1, is assessed according to the Zurich Insurance Company and is commonly used in the chemical industry [11]. If the assessment occurs on a three-level scale, the upper levels for "critical" and "catastrophic" may be considered one level, "high".

Table 1. Assessment criteria for the severity of a runaway condition [11]

Simplified	Extended	ΔT_{ad} / °C	Order of magnitude of Q, kJ kg^{-1}
High	Catastrophic	>400	>800
	Critical	200-400	400-800
Medium	Medium	50-100	100-400
Low	Negligible	<50 and no pressure	<100

Based on the literature [4,12,21] the temperature rise due to introduction of the initiator under normal operating conditions is observed to be in the range of 100-200 °C. The temperature rise has a higher possibility to increase even higher from this range, especially in the event of a heat exchange failure. According to the Zurich hazard analysis (ZHA), an adiabatic rise of temperature of more than 200 °C can be classified as high severity for a runaway reaction and requires safety technical measures [11]. For this reason, the present study considers a temperature increase of 200 °C and above to be critical. The rise in temperature can be considered as the reaction temperature under critical condition.

Reaction temperature under critical condition (T_c) and maximum temperature under critical condition ($T_{c,\max}$)

When the heat transfer failure occurs, the energy balance in Eq. (19) zones become Eq. (40):

$$\frac{dT_c}{dz} = \frac{1}{\rho C_P V} \left[-\Delta H K_p C_M \lambda_0 \right] \tag{40}$$

Thus, the profile of T_c represents the reaction temperature under critical conditions while T in Eq. (19) represents the reaction temperature running under normal conditions. Both T and T_c have different profiles with different maximum temperatures. In the reaction temperature running under normal conditions (T), its maximum value is directly taken from the plant operating manual, while in the case of the reaction temperature under critical conditions (T_c), its maximum value is decided by the sum of T_{in} and ΔT_{ad}.

The critical condition scenario is designed at the reaction zone only since this is the area where the highly exothermic polymerization reaction occurs. Therefore, failure or breakdown is most likely to occur in this zone rather than in the cooling zone [11].

Dynamic optimization study

The dynamic optimization technique applied which is based on the direct-discretization method is orthogonal collocation (OC). The OC method is executed by using the dynopt code package within

Matlab R2015a that has been developed by Cizniar [22] which utilizes an algorithm developed by Cuthrell and Biegler [23]. In this approach, state and control variables are parameterized simultaneously by using OC on finite elements. The iteration step for differential equation solver and the optimizer are computed simultaneously [24].

In this study, the orthogonal collocation (OC) on finite elements is used to convert the original optimization problems into nonlinear programming (NLP) problems [25,26]. The resulting NLP problems are solved by sequential quadratic programming (SQP). The gradients of the objective function, states and the constraints required in the SQP are differentiated by using Matlab symbolic function. The basic procedure followed is: 1) discretize both inputs and states using a Lagrange polynomial; 2) discretize the state equation with their initial conditions for selected interval time, *i.e.*, the differential equations are satisfied only at a finite number of interval length (*via* orthogonal collocation). These two steps modify the discretized optimization problem into a standard nonlinear program; 3) specify an initial guess for the decision variables, number of collocation and interval length; 4) calculate for the optimal solution of the specified objective function and generate the optimal trajectories by using the SQP method. The basic algorithm of OC can be described in Figure 2.

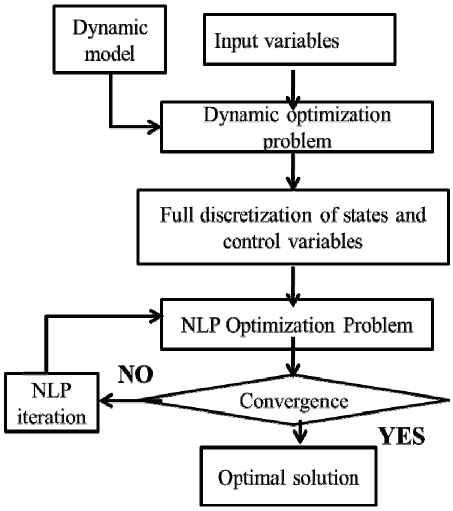

Figure 2. Basic procedure of orthogonal collocation method.

The Optimization Toolbox with *fmincon* (find minimum of constrained nonlinear multivariable function) command was used to solve SQP problems within the MATLAB® environment. In the search iteration, the convergence criterions which must be predetermined are TolX and TolFun. TolX is a minimum allowable size of a step. If the SQP acquires a searching step that is smaller than TolX, the iterations finalized. TolFun is a minimum allowable on the change in the value of the objective function during a searching step. For those algorithms, if $|F(x_n) - F(x_{n+1})|$ < TolFun, the iterations end. TolX and TolFun can be specified as 10^{-6}, in order to obtain an accurate solution.

Problem optimization formulation

Two problem optimization formulations are considered in this study. The first problem is to maximize the X_M under maximum temperature (T_{max}) constraint whereas the second problem is to maximize the X_M under maximum critical temperature (Tc_{max}). The only different between Problem 1 and Problem 2 is the path constraint imposed on each optimization formulation. In Problem 1, the reactor is considered to behave normally, whereas in the reactor in Problem 2 is assumed to run under critical condition. The terminal inequality constraint applied for both problems is *MFI*. The reactor jacket (T_J) is considered as a control variable. The dynamic optimization formulations for the two problems which consist of the objective function, decision variables, process, bounds and constraints are shown as follows:

Problem 1 - Maximum conversion with maximum reactor temperature (T_{max}).

The problem can be described as:

Given	The fixed final length and the allowable range of LDPE's *MFI*
Optimize	The reactor jacket temperature profile
Searching parameter	Monomer, solvent, initiators feed flow rate and reactor inlet pressure
So as to maximize	The conversion of the monomer
Subject to constraints	Model equation, bounds on the feed flow rate, bounds on the reactor jacket temperature
Subject to path constraints	Maximum reactor temperature (T_{max})

Mathematically the optimization problem can be written as in Eq. (41):

Problem 1: $$\max_{T_{J,i}(z),F_{M0},F_{S0},F_{I,i0},P_{in}} X_M \tag{41}$$

Subject to:

$M\dot{x}(z) = f(x(z),u(z),p,z)$	(Eqs. (13)-(31))
$0.69 \le \dfrac{T_{J,i}}{T_{J,i(ref)}} \le 1.69$	(Lower and upper control variable bound)

$0.96 \le \frac{F_{M0}}{F_{M0\,(ref)}} \le 1.02$;	(Lower and upper parameter bound)
$0.95 \le \frac{F_{S0}}{F_{S0\,(ref)}} \le 1.22$	
$0.23 \le \frac{F_{I,i0}}{F_{I,i0\,(ref)}} \le 1.27$;	
$0.93 \le \frac{P_{in}}{P_{in\,(ref)}} \le 1.03$	
$0.93 \le \frac{MFI}{MFI_{ref}} 1.03$	(Lower and upper MFI bound)
$\frac{z_f}{z_{f\,ref}} = 1.00$	(Terminal equality constraint)
$T_{max} / T_{max\,ref} \le 1.03$	(Inequality path constraint)

Problem 2 - Maximum conversion with maximum critical reactor temperature (Tc_{max}).

The problem can be described as:

Given	The fixed final length and the allowable range of LDPE's MFI
Optimize	The reactor jacket temperature profile
Searching parameter	Monomer, solvent, initiators feed flow rate and reactor inlet pressure
So as to maximize	The conversion of the monomer
Subject to constraints	Model equation, bounds on the feed flow rate, bounds on the reactor jacket temperature
Subject to path constraints	Maximum critical reactor temperature (Tc_{max})

Mathematically the optimization problem can be written as in Eq. (42):

$$\text{Problem 2:} \quad \max_{T_{J,i}(z), F_{M0}, F_{S0}, F_{I,i0}, P_{in}} X_M \tag{42}$$

Subject to:

$M\dot{x}(z) = f(x(z), u(z), p, z)$	(Eqs. (13)-(31))
$0.69 \le \frac{T_J}{T_{J\,(ref)}} \le 1.69$	(Lower and upper control variable bound)
$0.96 \le \frac{F_{M0}}{F_{M0\,(ref)}} \le 1.02$;	(Lower and upper parameter bound)
$0.95 \le \frac{F_{S0}}{F_{S0\,(ref)}} \le 1.22$	
$0.23 \le \frac{F_{I,i0}}{F_{I,i0\,(ref)}} \le 1.27$;	
$0.93 \le \frac{P_{in}}{P_{in\,(ref)}} \le 1.03$	
$0.93 \le \frac{MFI}{MFI_{ref}} 1.03$	(Lower and upper *MFI* bound)
$\frac{z_f}{z_{f\,ref}} = 1.00$	(Terminal equality constraint)
$T_{c\,max} / T_{max\,ref} \le 1.24$	(Inequality path constraint)

The bounds for the variable and parameters in Problem 1 and Problem 2 have been chosen based on the industrial data.

RESULTS AND DISCUSSION

The results of the modeling and optimization are presented and discussed in this section. In order to quantify the accuracy of the model, the comparison between the developed model and industrial data is carried out [27]. Then, the *R*-squared (R^2) obtained is used to assess the model accuracy and validity. The validated model is then used for the safety study. In the safety study, the T_c profile obtained is analyzed. In the optimization part, the results of the control variable trajectory, optimum parameter values, reactor temperature, and monomer conversion are analyzed with respect to thermal safety constraint consideration. For clarification, only relative values are displayed due to confidentiality reasons.

Model validation

Figures 3 and 4 show the model predictions for the temperature and the monomer conversion profiles versus the industrial data. The end product melt flow index (*MFI*) property obtained from the developed model also shows a satisfactory prediction with small error, 0.39%. It is observed that the model can predict the profiles very well with *R*-squared (R^2) values of 0.991 and 0.989 obtained for the reactor temperature and the monomer conversion (X_M) profiles are very close to 1.

The temperature profile in Figure 3 shows there are eight zones, which consist of four reactions and four cooling zones that exist in the LDPE tubular reactor. In the reaction zones, a sharp temperature peak is observed due to the highly exothermic rise of the polymerization reaction which generates a free radicals reaction between the feed in the initiator and the monomer. Monomer conversion (X_M) also indicates a fast escalation, and according to this temperature peak almost all of the initiator is consumed at this point. Due to no reaction occuring, X_M stays constant until another initiator is injected in the next react-

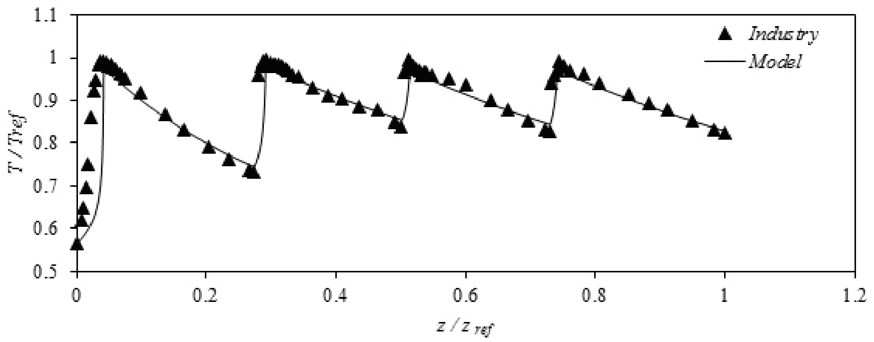

Figure 3. Reactor temperature, T profile of industrial case and model prediction.

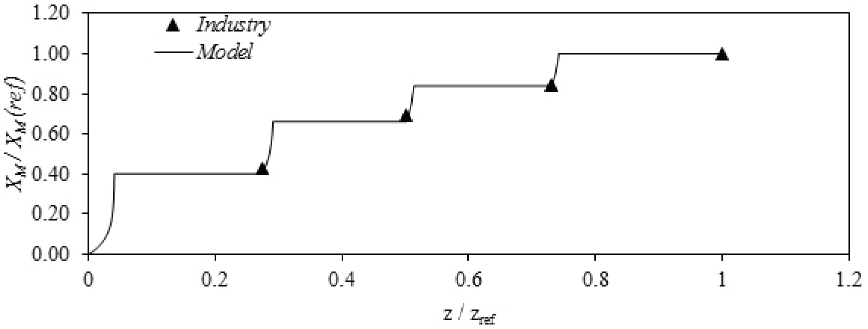

Figure 4. Monomer conversion, X_M profile of industrial case and model prediction.

ion zone. In the second zone, the reaction mixture is cooled down to the optimal temperature level for the half-life decomposition of the second initiator. Initiator disassociation is highly dependent on temperature and will be inefficient if the temperature exceeds its half-life temperature [16]. This inefficiency will reduce the initiation reaction and propagation rate thus reducing the monomer conversion value.

In the cooling zone, the temperature of the reaction mixture is cooled down steadily using a counter-current heat exchanger. This steady cooling process is to decrease the formation rate of a polymer-rich layer on the inner wall of the tubular reactor. The second initiator is injected in the third zone to aggravate the monomer conversion, as shown in Figure 4. This initiator is also exhausted soon after its injection into the reactor. The reaction mixture is again cooled in the fourth zone to the suitable level for the half-life of the third initiator, which generates the high efficiency of the initiator. These processes are repeated in the subsequent zone until the eighth zone where the product will undergo further separation and treatment processes.

Reaction temperature under critical condition (T_c) for reference model

The reaction temperature profiles in normal and critical operating conditions are shown in Figure 5.

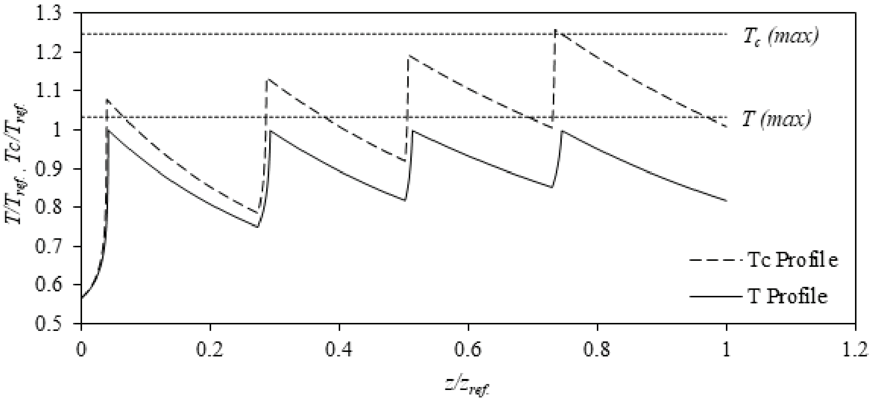

Figure 5. Reactor temperature (T) and critical reactor temperature (T_c) profiles of Base Case (reference model) across the tubular reactor.

The maximum reaction temperature (T_{max}) is used as an upper bound for normal conditions whereas the maximum critical reaction temperature (Tc_{max}) is used as an upper bound for the process in the event a reactive system cannot exchange energy with its surroundings (critical condition).

Here, it is clearly seen that the reactor peak temperature under critical condition (T_c) significantly rises beyond the operational T_{max} limit of 1.03. Therefore, the use of the T_{max} is impractical since the reaction temperature already exceeded the limit. In order to ensure that the LDPE tubular reactor polymerization is thermally safe, a new value for maximum reaction temperature under critical condition ($T_{c,max}$) must be introduced. As shown in Table 1, a process can be classified as critical when the adiabatic temperature rise (ΔT_{ad}) is more than 200 °C, therefore $T_{c,max}$ value is determined by adding up ΔT_{ad} of 200 °C with reactor inlet temperature (T_{in}).

With regards to the reaction process running under critical conditions, it can be observed from Figure 5 that the reaction critical temperature profile (T_c) already exceeds $T_{c,max}$ thus indicating that the present industrial LDPE tubular reactor produces an adiabatic temperature rise ΔT_{ad} of more than 200 °C which is considered as high severity for a runaway condition according to the Zurich hazard analysis (ZHA) [18]. This approach is a pre-assessment method to predict how far the temperature will rise adiabatically during the critical condition.

From Figure 5, it can be observed that the T_c profile has a significant trend change from the original T profile, as shown in Figure 5. At $z/z_{ref.} = 0 - 0.042$, where the first reaction occurs, the T/T_{ref} peak is 0.995 while the T_c/T_{ref} peak rises to 1.079, as shown in Figure 5. The T_c peak rises even higher in the next three reaction zones, located at $z/z_{ref.} = 0.2738 - - 0.2928$, $z/z_{ref.} = 0.5019 - 0.5133$ and $z/z_{ref.} = 0.7300 - - 0.7452$. The highest T_c/T_{ref} peak observed is 1.2592 that is obtained at the fourth reaction zone ($z/z_{ref.} = = 0.7300 - 0.7452$). This is largely due to the high inlet temperature for each of the reaction zones as a result of heat exchange absence, thus causing the sharp increment in the T_c profile as shown in Figure 5. The obvious way to ensure the T_c profile satisfies the $T_{c,max}$ is by reducing the peak T profile in Figure 5, however, it will reduce the X_M as well since the peak T profile and X_M are proportionally related. Consequently, the dynamic optimization study has to be carried out so that the X_M can be either increased or maintained while ensuring the T_c profile satisfies the $T_{c,max}$.

Optimization

These studies aim to maximize the monomer conversion for the LDPE tubular reactor running under maximum reaction temperature (T_{max}) and critical temperature constraints ($T_{c,max}$). For Problem 1, T_{max} constraints with bounds on the decision variables are imposed in the optimization problem, while in Problem 2, $T_{c,max}$ constraints with bounds on the decision variables are imposed.

The optimum results consist of the objective function (X_M), T_{max}, $T_{c,max}$ and *MFI* values of both Problems 1 and 2 are tabulated in Table 2. The melt flow index (*MFI*) is the parameter which is commonly practiced in the global LDPE manufacturing industry. It acts as an indicator of the molecular weight (*Mw*) and is favoured over other parameters because of its rapid and simple determination [20]. The results shown in Table 2 are the optimum reactor output achieved with optimal parameter values and trajectory of T_J as shown in Table 3 and Figure 6, respectively. The resulting optimization profiles of X_M, T, and T_c are shown in Figures 7-9, respectively. From Table 2, it can be observed that the $X_M/X_{M(ref)}$ in Problem 1 increases to 1.14. In Problem 1, temperature, T/T_{ref} peak is allowed to increase up to the maximum limit of 1.03 and this allows for extra monomer conversion to occur in the reaction zones.

From Table 2, it can be seen that the final $X_M/X_{M(ref)}$ obtained for Problem 2 is 1.10, which is higher than the Base Case. Compared to Problem 1, the final $X_M/X_{M(ref)}$ of Problem 2 is slightly lower than the former. In Problem 2, the maximum T/T_{ref} peak

Table 2. Results for maximize conversion of using different constraints

Problem	Constraint	$X_M/X_{M(ref)}$	$T_{max}/T_{max(ref)}$	$T_{c,max}/T_{max(ref)}$	$MFI/MFI_{(ref)}$
1	Max. reaction temperature, T_{max}	1.14	1.03	1.29	1.00
2	Max. critical temperature, $T_{c,max}$	1.10	1.03	1.25	1.00

Table 3. Optimal values of parameter variables (p_x) for maximize conversion with different constraints study

Problem	$F_{M0}/F_{M0(ref)}$	$F_{S0}/F_{S0(ref)}$	$F_{I,10}/F_{I,10(ref)}$	$F_{I,20}/F_{I,20(ref)}$	$F_{I,30}/F_{I,30(ref)}$	$F_{I,40}/F_{I,40(ref)}$	$P_{in}/P_{in(ref)}$
1	0.98	1.00	1.05	1.00	0.92	0.90	1.00
2	0.98	1.00	1.05	0.99	0.91	0.70	1.00

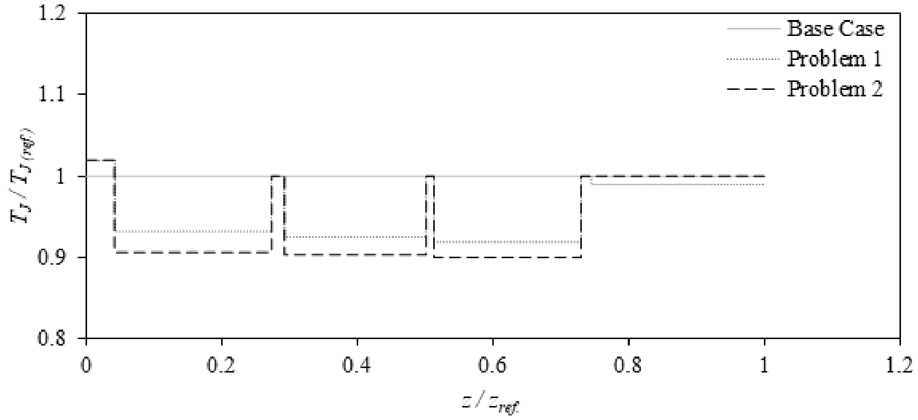

Figure 6. Reactor jacket temperature profiles across the tubular reactor.

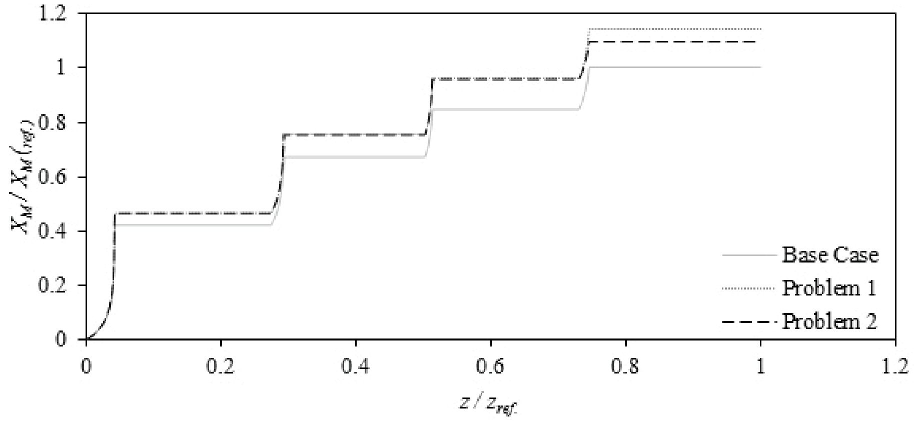

Figure 7. Monomer conversion profiles of Base Case, Problem 1 and Problem 2.

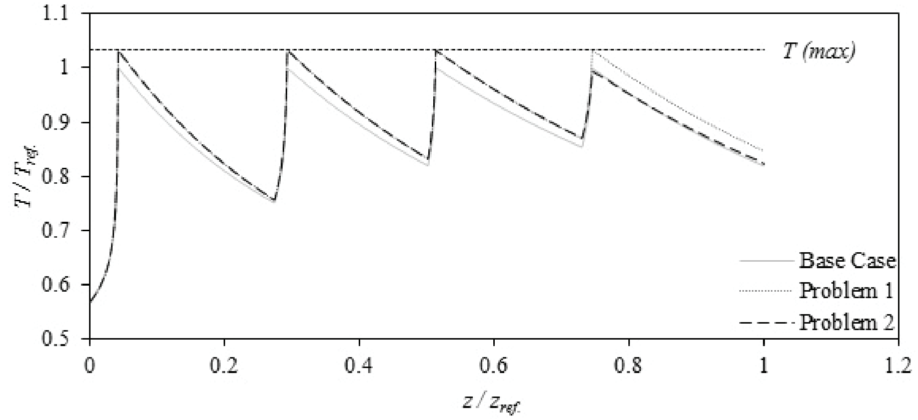

Figure 8. Comparison of reactor temperature profiles of Base Case, Problem 1 and Problem 2.

obtained is 1.0260, which is lower than the maximum T/T_{ref} peak obtained in Problem 1. This is because, in Problem 2, the maximum reaction critical temperature constraint ($T_{c,max}$) is imposed, therefore the reduction in Problem 2 peak temperature occurs to ensure that the trajectory of the reaction critical temperature (T_c) satisfies the $T_{c,max}$ constraint. It is also observed in Table 2 that both problems satisfy the *MFI* grade ranges. This is due to the presence of terminal inequality constraints at both problem optimization formulations. Maintaining polymer product within the specified grade is a primary performance indicator in LDPE production.

Figure 9 shows that the maximum peak temperature of T_c of Problem 1 is 1.29, which is obtained at the end of the fourth reaction zone 4R (at $z/z_{ref.}$ =

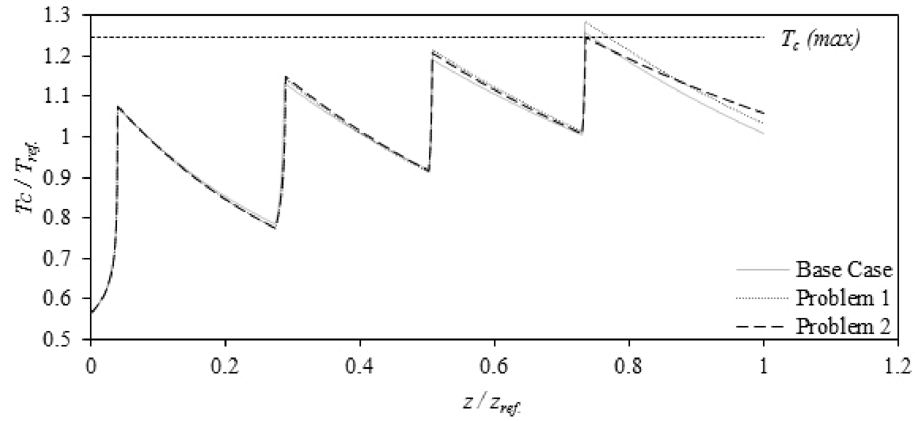

Figure 9. Comparison of reactor critical temperature profiles of Base Case, Problem 1 and Problem 2.

= 0.7452). This T_c/T_{ref} value exceeds $T_{c,max}$, indicating that the process does not compel thermal safety constraints. Therefore, adding reaction temperature constraint (T_{max}) alone would not be sufficient to ensure a thermal safety process. Figure 9 shows that the reaction temperature under critical condition T_c for Problem 2 successfully satisfies the maximum critical temperature ($T_{c,max}$) imposed on the optimization problem. However, it comes at the cost of a slightly lower conversion percentage. In a different optimization study carried out by Srinivasan, Palanki and Bonvin [28] using the batch reactor, they reported a similar reduction trend in conversion as a result of thermal safety constraint. This reduction is obtained in order to bring down the peak temperature. For the thermal safety constraint study, usually, the maximum peak temperature is lowered to facilitate the safety tolerance value [19]. For this reason, the monomer conversion is reduced as well since it is proportionally related to reaction temperature [29]. By tracking the optimal T_J trajectory obtained in Problem 2, the on-spec of LDPE grade can be produced within thermal safety precautions.

CONCLUSION

In the present paper, three main studies have been carried out to optimize LDPE production in a tubular reactor under thermal safety constraint which are process modelling, thermal safety risk assessment and optimization of tubular reactor process under thermal safety constraint. For the process modelling, it has been observed that the model can accurately predict the profiles of the reactor temperature and the monomer conversion with values of R^2 close to 1. The comparison of the product properties at the reactor end also showed a satisfactory agreement where a low percentage of error was observed between the model and industrial data.

On the thermal safety risk assessment aspect, the present industrial LDPE tubular reactor has produced an adiabatic temperature rise (ΔT_{ad}) of more than 200 °C, which is considered as high severity for a runaway condition. For this reason, an optimal set of parameters need to be determined to ensure that ΔT_{ad} should not exceed 200 °C in the event of a cooling failure.

The dynamic optimization result has shown that an increase in monomer conversion has been achieved by both problem optimization formulations. The increment was obtained by optimal parameter values and trajectory of jacket temperature. Although Problem 1 has higher conversion than Problem 2, nevertheless the Problem 2 result has satisfied the thermal safety constraint $T_{c,max}$. These results demonstrate that $T_{c,max}$ constraint must be incorporated for a thermal safety operation since the T_{max} constraint is insufficient to protect the reactor, particularly in the event of cooling failure.

List of symbols

A_i	Inside pipe area, cm^2
A_o	Outside pipe area, cm^2
$A_{x,i}$	Frequency factor of x process with i-th number, l/(s cm^3/mol·s)
bb	Backbiting, -
$C_{x,i}$	Concentration *x* component with *i*-th number, mol/cm^3
D_{in}	Inside diameter of reactor, cm
D_e	Equivalent diameter, cm
D_{Ji}	Inner diameter of jacket wall,cm
$E_{x,i}$	Activation energy of *x* process with *i*-th number, cal/mol
e	Ethylene, -
F_x	Mass flow rate of *x* component, kg/h

f_x	Initiation efficiency of *x*-th peroxide, -
f_r	Fanning friction factor, -
G_c	Jacket volumetric flux rate, cm^3/s
ΔH_p	Heat of polymerization, cal/mol
h_i	Reactor side heat transfer coefficient, cal/(cm^2·K)
h_o	Outside film heat transfer coefficient, cal/(cm^2·K)
h_w	Heat transfer coefficient of reactor wall, cal/(cm^2·K)
$K_{d,i}$	Rate constant of peroxide initiation with *i*-th number, l/s
K_{th}	Rate constant of monomer thermal initiation, l/s
K_p	Rate constant of propagation, l/(mol·s)
K_{td}	Rate constant of termination by thermal degradation, l/(mol·s)
K_{thd}	Rate constant of termination by disproportionation, l/(mol·s)
K_{trm}	Rate constant of chain transfer to monomer, l/(mol·s)
K_{trp}	Rate constant of chain transfer to polymer, l/mol·s
K_{trs}	Rate constant of chain transfer to solvent, l/s
K_β	Rate constant of *β*-scission to secondary radical, l/s
$K_{\beta 1}$	Rate constant of *β*-scission to tertiary radical, l/s
K_m	Thermal conductivity of reaction mixture, cal/(cm·s·K)
K_w	Thermal conductivity of reactor wall, cal/(cm·s·K)
K_J	Thermal conductivity of jacket water, cal/(cm·s·K)
L	Length of reactor, m
I	Initiator, -
M	Monomer, -
m	Reaction mixture, -
$\dot{m}_x$	Mass flow rate of *x*-th component, g/s
Nu	Nusselt number, -
P	Reaction pressure, bar
pe	Polyethylene, -
P_{in}	Reactor inlet pressure, Bar
Pr	Prandtl number, -
p_x	Input variable of *x* component
$P(x)$	Dead polymer with chain length *x*, -
Q	Heat transfer, J
r_o	Outside radius of tubular reactor area, cm
r_i	Inside radius tubular reactor area, cm
R	Ideal gas constant, cal/(mol·K)
$R(x)$	Live radical with chain length *x*, -
Re	Reynolds number, -
R_f	Fouling resistance, cm^2·s·K/cal
R_{fmax}	Maximum fouling resistance, cm^2·s·K/cal
S	Solvent, -
ΔT_{ad}	Adiabatic temperature rise, °C
ΔT_{lm}	Log mean temperature, -
T_{in}	Reactor inlet temperature, °C
T_J	Reactor jacket temperature, °C
T_{max}	Maximum reaction temperature, °C
$T_{c,max}$	Maximum reaction critical temperature
T_{cpeak}	Peak critical temperature, °C
U	Overall heat transfer coefficient, cal/(cm^2·s·K)
u_x	Control variable of x component,
v	Linear velocity of the reaction mixture in reactor, cm/s
V_i	Vinyl group
V_{id}	Vinylidene group
V_m	Specific volume of monomer, cm^3/g
V_p	Specific volume of polymer, cm^3/g
$\Delta V_{x,i}$	Activation volume of *x* component with *i*-th number, l/mol
X_M	Monomer conversion, %
z	Axial distance from reactor inlet, cm

Greek symbols

λ_x	*x*-th moment of the live polymer radical, -
μ_x	*x*-th moment of dead polymer radical, -
β	Beta scission of secondary radical, -
$\beta 1$	Beta scission of tertiary radical, -
$\varnothing$	Diameter
ρ	Reaction mixture density, g/cm^3
η_s	Viscosity of reactant mixture, P
η_r	Relative viscosity of monomer, P
η_o	Viscosity of monomer, P
η_s	Viscosity of reaction,P
w_m	Weight fraction of monomer, -
w_p	Weight fraction of polymer, -

Acknowledgment

The financial support from Kementerian Pengajian Tinggi (KPT) through Grant No. 203/PJKIMIA/ /6071368 and MyBrain15's Fund to the first author are greatly acknowledged.

REFERENCES

[1] M.K. Chang, J. Ind. Eng. Chem. 27 (2015) 96-101

[2] V.P. Haribal, Y. Chen, L. Neal, F. Li, Eng. J. 4 (2018) 714-721

[3] LDPE EVA Market Outlook, Nexant, Inc., Asia Petrochemical Industry Conference, Japan, 2017, pp. 121-125

[4] C.H. Chen, J.G Vermeychuk, J.A. Howell, P. Ehrlich, AIChE J. 22 (1976) 463-471

[5] D. Muhammad, Z. Ahmad, N Aziz, IOP Conf. Ser.: Mater. Sci. Eng. 736 (2020) 042014

[6] A. Azmi, N. Aziz, International J. Appl. Eng. Res. 11 (2016) 9906-9913

[7] F.Z Yao, Master Thesis, Nanchang University, 2004

[8] N. Agrawal, PhD Thesis, National University of Singapore, 2008

[9] M. Asteasuain, A. Brandolin. Comput. Chem. Eng. 32 (2008) 396-408

[10] A. Azmi, Sudibyo, S.A. Sata, N. Aziz, AIP Conference Proceedings, 2018

[11] F. Stoessel, Thermal Safety of Chemical Processes: Risk Assessment and Process Design, Wiley-VCH, New York, 2008

[12] M. Asteasuain, S. Pereda, M.H. Lacunza, P.E. Ugrin, A. Brandolin. Polym. Eng. Sci. 41 (2001) 711-726

[13] J.S. Tse, Eng. J. 5 (2019) 421-433

[14] A. Azmi, N. Aziz, Procedia Eng. 148 (2016) 1170-1176

[15] C. Kiparissides, A. Baltsas, S. Papadopoulos, J.P. Congalidis, J.R. Richards, M.B. Kelly, Y. Ye, Ind. Eng. Chem. Res. 44 (2005) 2592-2605

[16] D. Kim, P.D. Iedema, Chem. Eng. Sci. 59 (2004) 2039--2052

[17] R.C.M. Zabisky, W.M. Chan, P.E. Gloor, A.E. Hamielec, Polymer 33 (1992) 2243-2262

[18] A. Buchelli, M.L. Call, A.L. Brown, A. Bird, S. Hearn, J. Hannon, Ind. Eng. Chem. Res. 44 (2005) 1474-1479

[19] J.M. Coulson, J.F Richardson, J.R. Backhurst, J.H. Harker, Chemical Engineering: Fluid Flow, Heat Transfer and Mass Transfer, Vol. I, 5th ed., Butterworth-Heinemann, Oxford, 1996

[20] A. Azmi, S. A. Sata, F.S. Rohman, N. Aziz, J. Phys.: Conf. Ser. 1349 (2019) 012094

[21] H. Mavridis, C. Kiparissides, Polym. Proc. Eng. 3 (1985) 263-290

[22] M Cizniar, Diploma Work, Slovak Technical University in Bratislava, 2005

[23] J.E. Cuthrell, L.T. Biegler, AIChE J. 33 (1987) 1257-1270

[24] E.S. Lopez-Saucedo, I.E. Grossmann, J.G. Segovia-Hernandez, S. Hernández, Chem. Eng. Res. Des 111 (2016) 83-99

[25] D. Rodrigues, D. Bonvin, Optim. Control Appl. Methods (2019) 1-20

[26] B.Houska, H. J. Ferreau, M. Diehl, Optim. Control Appl. Methods 32 (2011) 298-312

[27] W. Yan, Y. Qian, W. Ma, B. Zhou, Y. Shen, F. Lin, Eng. J. (2017) 701-707

[28] B. Srinivasan, S. Palanki, D. Bonvin, Comput. Chem. Eng. 27 (2003) 1-26

[29] M. Vallerio, F. Logist, P.V. Erdeghem, C. Dittrich, J.V. Impe, Ind. Eng. Chem. Res. 52 (2013) 1656−1666

[30] H.A. Zogg, “Zurich” Hazard Analysis: A Brief Introduction to the “Zurich” Method of Hazard Analysis Zurich Insurance Group, Risk engineering, 1987.

A. AZMI
S.A. SATA
F.S. ROHMAN
N. AZIZ

School of Chemical Engineering, Engineering Campus, Universiti Sains Malaysia, Seri Ampangan 14300 Nibong Tebal, Seberang Perai Selatan, Penang, Malaysia

NAUČNI RAD

DINAMIČKA OPTIMIZACIJA PROIZVODNJE POLIETILENA NISKE GUSTINE U CEVNOM REAKTORU POD OGRANIČENJEM TERMIČKE SIGURNOSTI

Komercijalni polietilen niske gustine (LDPE), koji se proizvodi postupkom polimerizacije etilena u prisustvu inicijatora u dugačkom cevnom reaktoru, najčešće se koristi u industriji polimera. Veoma egzotermna priroda procesa polimerizacije LDPE i preduslov grejanja i hlađenja u cevnom reaktoru mogu dovesti do različitih problema, posebno sigurnosti u pogledu nekontrolisane promene temperature i produktivnosti, tj. smanjenja konverzije monomera. Zbog toga je potrebno primeniti optimizaciju zasnovanu na modelu industrijskog cevnog reaktora za proizvodnju LDPE uz razmatranje termičke sigurnosti. Prvi osnovni model za ovaj proces je razvijen i potvrđen korišćenjem industrijskih podataka. Bilansi mase i energije izvedeni su iz kinetike polimerizacije LDPE. Nakon toga, razvijen je izraz za temperature u reaktoru pod kritičnim uslovima i uključen u referentni model za proučavanje toplotne sigurnosti. Da bi se osiguralo da je postupak termički bezbedan i da zadovoljava željeni kvalitet proizvoda, pretpostavljena je ograničena dinamička optimizacija, kako bi se maksimalno povećala konverzija monomera, pomoću ortogonalne kolokacije. Rezultati dinamičke optimizacije pokazuju da se maksimalna reakciona temperatura pod kritičnim uslovima može zadovoljiti optimizacijom omotača reaktora. Štaviše, postiže se bez ugrožavanja konverzije monomera i kvaliteta proizvoda.

Ključne reči: Polietilen niske gustine, cevni reaktor, dinamička optimizacija, toplotna sigurnost.

CI&CEQ
Chemical Industry & Chemical Engineering Quarterly

Available on line at
Association of the Chemical Engineers of Serbia *AChE*
www.ache.org.rs/CICEQ

Chem. Ind. Chem. Eng. Q. 27 (1) 99–106 (2021) CI&CEQ

ALI ABDUL RAHMAN-AL EZZI

Department of Chemical Engineering, University of Technology, Baghdad, Iraq

SCIENTIFIC PAPER

UDC 547.56:628.3:502:66.081.3

PHENOL REMOVAL USING PULSATION BUBBLE COLUMN WITH INVERSE FLUIDIZATION AIRLIFT LOOP REACTOR

Article Highlights

- The study is an integrated system of a pulsation bubble column with an inverse fluidization reactor
- The effectiveness of the present design was tested with one of the chemical contaminants, namely phenol
- The method works for a variety of airflow rates, residence time, and molar ratio of phenol to H_2O_2
- Results showed that the phenol removal efficiencies are ~90%

Abstract

Phenol and phenolic compounds are omnipresent organic contaminants which are sent out to water bodies and wastewater systems produced from industrial processes, and they require specific attention due to their extraordinary features such as high toxicity, carcinogenic characteristics, and ability to accumulate, which affects the health of humans and the environment. In this practical study, the integrated system of a pulsation bubble column with an inverse fluidization air loop reactor was tested to remove phenol. The test platform was made and operated with a bubble column containing at its upper end an electrical solenoid valve engaged via at least two timers, and connected to the air loop reactor consisting of an outer rectangular tube and an internal draft tube by one-way valve, where the granular activated carbon is put as an adsorbent material in the annulus region between the inner and outer tube. The effects of various parameters [molar ratio of Phenol to H_2O_2 *(1/10, 1/15 and 1/20), airflow rate (5-20 L/min), remediation time (5-60 min), initial phenol concentration (10-150 mg* L^{-1}*) have been studied. Removing 90% of the contaminated phenol as a result of this study may represent a partial solution to the ecological problem.*

Keywords: phenol, pulsation bubble column, inverse fluidization, stripping, oxidation, adsorption.

Wastewater remediation *via* the removal of organic contaminants stills an earnest environmental and general problem. Moreover, in the face of tougher laws, polluted water has become a major concern and a priority for most industrial sectors. Phenolic compounds and its derivatives are usually found in the environment as a result of their vast industrial uses [1]. Several remediation techniques applied for removing the chemical, oil, and petrochemical wastes, can be categorized as three types: physical, chemical and biological. The choice of the best technology is based on many factors, like the chemical nature of the waste, the impact of the effective cost, space occupied by equipment, discharge and reusing policy, permanent operation and side products. The main wastes produced from these categories are composed of hydrocarbon compounds, phenolic compounds, dyes, heavy metals, etc. [2-6]. Most of these compounds have pernicious ecological effects and may be labeled as serious waste; also, they are carcinogenic and have a malignant impact on human health. They are the largest contributors to the pollution of surface and groundwaters [7,8]. Centrifugal separation, adsorption, membrane separation, reverse osmosis, nanofiltration, ultrafiltration and micro-

---

Correspondence: A.A. Rahman-Al Ezzi, Department of Chemical Engineering, University of Technology, Baghdad, Iraq.
E-mail: ali.a.nsaif@uotechnology.edu.iq
Paper received: 12 March, 2020
Paper revised: 11 July, 2020
Paper accepted: 21 July, 2020

https://doi.org/10.2298/CICEQ200312028A

filtration are particularly physical treatment methods; however, these methods have multiple restrictions, like producing great volumes of muds, expensive cost of equipment, in addition to installation and operation costs [9-12]. Air stripping is a technology that uses air flow jet for volatile organic contaminate removal from wastewater by increasing the contact surface area of the polluted water that is exposed to air; an organic pollutant which having low Henry's constant will require a much higher air/liquid ratio or steam stripping for efficient removal [13]. In the literature of wastewater remedy by adsorption, activated carbon adsorbents interact with adsorbates, keeping the adsorbate on the adsorbent surface and thus eliminating it from the aqueous phase. Adsorption *via* activated carbon is a prevalent wastewater treatment style because of its vigourous ability to remove organic materials even at low concentrations [14]. Powdered activated carbons may be directly used in the wastewater resource tanks, while granular activated carbons can be packed into a bed inside columns through which wastewater flows continuously [14]. The cheap carbon materials created from a residue material - which can noticeably minimize the cost of water remedy and supply an evaluation way for varied waste streams - have been studied through recent decades as another wastewater remedy choice [15--17]. The large consumption of chemicals and the costs of operation and maintenance in addition to skilled labor make the chemical processes such as oxidation, electrochemical deposition and advanced oxidation processes less economically feasible [18-25]. The advanced oxidation processes are characterized by the creation of reactive sorts, such as hydroxyl radicals ($HO^\bullet$), which are strong oxidation agents [26]. AOPs based on the production of $HO^\bullet$ have a higher oxidation potential than those of ozone and hydrogen peroxide, and are responsible for the complete oxidation for organic pollutants [27,28]. Although biological treatment processes use multiple types of algae, fungi, yeast, genetically modified organisms, and biologically active substances, some problems however, such as the difficulty of introducing the above materials into the reactor containing a filling in addition to the bypass phenomenon as a result of channeling, have led to limited use of biological treatment. Therefore, the need to find a new, efficient, inexpensive and environmentally friendly design is necessary to reduce the negative impact of hazardous pollutants on water and to preserve the natural water cycle in the environment. The main objective of the current research is to test the effectiveness of the new design that integrates the performance of two devices and two techniques, the bubble column having a solenoid valve controlling to the pulsation-time of treated water and the inverse fluidization loop reactor under the effect of three processes of oxidation, stripping and adsorption, with various scenarios and operating conditions.

EXPERIMENTAL

Materials and methods

The application of the proposed system required a synthetic wastewater model containing phenol as a polluting source. The chemical specifications of commercial formula phenol C_6H_5OH that was imported from Sigma-Aldrich which was employed in this study: the pureness is more than 99%, molecular weight (g/mol) 94.144, molar volume (cm^3/mol) 90, solubility in water (mg/L) 50-100 at 19 °C. Five synthetic solutions with varied successive concentrations (10, 20, 50, 100, 150 mg/L) were prepared from the prepared stock solution of phenol (1000 mg/L with acidic pH 3.5-4).

The experiments were carried out using a commercial granular activated carbon (GAC) (8-20 mesh, 3-4 mm particle size, specific surface area 1050 m^2/g, solid density 1.153 (g/ml)) obtained from Sigma-Aldrich. The GAC was washed many times by deionized water to eliminate the undesired particles, then drying in a furnace until reaching 105 °C. The oxidizing agent hydrogen peroxide with 35 vol.% concentration was obtained from HiMedia Laboratories Pvt. Ltd., Sigma Chemical Co.

Experimental setup

The proposed design model consists of two units (Figure 1). The first is the pulsation bubble column (PBC) with an effective volume of 4 L that was made from diaphanous acrylic that allows us to see what's going on inside. The outside diameter and height of the reactor were 5 and 210 cm, respectively. At the upper end of the PBC, a solenoid valve was placed and worked under the control of two timers which control the residence time for the contaminated solution, and created a pulsation flow during the period of opened and closed valve to transfer the treated water to the inverse fluidization air loop reactor (IFALR). The aqueous solution of phenol and hydrogen peroxide solution was premixed before entering the PBC via the two dosing pumps (P1 and P2 called SECO, chemical dosing type, country of origin: China). The compressed air was continuously fed through the compressor (C1) to the column with various flow rates of 2 and 20 L/min by an air sparger placed at 50 cm above the base of the column to vigorously mix the phenol and hydrogen peroxide solution for giving sufficient time for the stripping and oxidation process to occur. During the opening and closing of the solenoid valve, a difference in pressure was created between the water in the PBC, and IFALR makes the water passes through a one-way valve into the loop reactor. The solenoid valve is reopened and closed at different times, up to stability condition in the water flow, and samples of treated water are taken at intervals through the valve model No. 1.

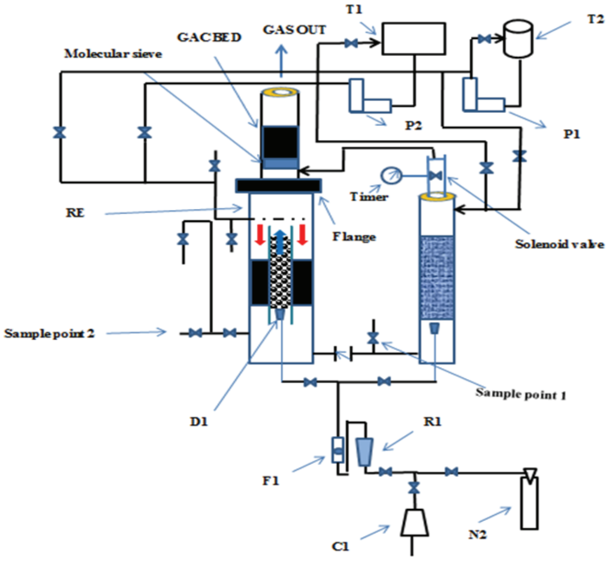

Figure 1. The design of the proposed treatment system; ⧓ *- valves, P1, P2 - dosing pumps, T1 - waste water tank, F1 - flow meter, R1 - regulator, RE - reactor, C1 - compressor, T2 - hydrogen peroxide tank, N2 - nitrogen cylinder, D1 - distributor.*

The inner tube for IFALR reactor is fixed in a manner that allows for creating empty space under the column to allow the water to circulate, in addition to its centering in the outer box for any distance extended above the base of the outer box, by three supports fixed *via* screws for each region: top, middle, and bottom of the reactor. Each support is comprised of 16 punctures, and every hole has a 1 mm diameter; these holes permit water to pass and do not allow the passage of activated carbon due to their small size (1 mm) compared to the size of the granulated carbon (3-4 mm). Screws participate in the installation of the draft tube from one side and loading the granulated carbon on the prop on the other. The direction of movement of the circulation of dispersed water will be from the top of the inner (draft) tube passing through the annulars to penetrate the activated carbon layer to complete the adsorption process for the remainder of the phenol, with the occurrence of synchronization of both stripping and oxidation processes.

Experimental procedure

The integrated system operates in the following sequence.

The first step is a preparation of a synthetic solution contaminated with phenol at a concentration of 150 ppm, in the feed tank T1 with acidity ranging from 3.5-4. One liter of hydrogen peroxide is added to 8 L of deionized water in tank T2 to prepare a solution of hydrogen peroxide, depending on the molar proportion, as operational condition required 20 mol of hydrogen peroxide per 1 mol of phenol. 4.4 cm^3 from the assigned bed size for the adsorption process is filled with 5 kg of granular activated carbon. Installation of the flow rates for each pump: 0.3 L/min for contaminated synthetic wastewater for pump P2, and 0.2 L/min for hydrogen peroxide solution for pump P1. The two pumps operate at a pressure of 2 bar. For reaching stability, the system must be operating for an hour before conducting the experiments.

After installing the timer control for operating the solenoid valve (at 30 s to open the valve + 5 s to close), a sample is taken to test the water treated for the first experiment at the sample-taking point No. 1.

Five samples are taken within thirty minutes from the sample-taking point of the treated water No. 1, at the rate of one sample for every five minutes, to check the concentration of phenol *via* the UV spectrophotometer (Chrome Tech UV-VV-1100, UEBO9025, Japan) at a wavelength of 254 nm.

As a result of the difference in density of oxidized water due to the dispersion via the flowing air between the draft tube and the outer box, the treated water passes from PBC to IFALR at the same time the water forced to pass and recirculate through (GAC) padding at the inverse direction from top to bottom, to give full chance for efficient conjunction for stripping, oxidation and adsorption processes.

One sample every six minutes was taken from the sample checking point No. 2, to compute the concentration of phenol in the treated water.

The same steps were repeated by changing the following parameters.

A: The residence time ranged for all processes from 5 to 60 min;

B: various timers set the range for opening the solenoid valve (40, 50, 60, 120, 180 s), while the closed valve period remained 5 s during all experiments;

C: the rate of airflow ranged from 2 to 20 L/min;

D: three mole ratios were used in all experiments: 1/10, 1/15, 1/20 phenol to hydrogen peroxide.

The efficiency of the integrated system was calculated *via* the percentage of phenol removal through the following equation:

$$\eta = 100\frac{C_{ph,in} - C_{ph,out}}{C_{ph,in}} \tag{1}$$

where η is the phenol abstraction efficiency (%), $C_{ph,in}$ and $C_{ph,out}$ are the initial and final concentrations of phenol in ppm, respectively.

RESULTS AND DISCUSSION

The results can be discussed in two stages: the results obtained from the pulse bubble column during the occurrence of two processes (stripping and oxidation) and the effect of four variables.

A: The curing time is associated with the opening and closing times of the solenoid valve located above the bubble column;

B: the mole ratio of the pollutant to the oxidizing agent;

C: the rates of airflow;

D: the pollutant concentration in the feeding input;

The results are based on the models taken from the Model No. 1 pull point.

From Figure 2 it is clear that by increasing the shutdown time of the solenoid valve, the contact period increases, thus increasing the processing time, this giving sufficient time to the $^{\bullet}$OH free radicals resulting from the decomposition of hydrogen peroxide to attack the phenol ring with increased capability for completely mineralizing the phenol pollutant to H_2O and CO_2 [29]. This is consistent with findings (Haroun and Idris, 2009) in that the increase in the residence time leads to an increase in the reactor performance [30]. At the same time, the process of mass transfer of phenol from the liquid phase (water) to the gas phase (air) occurs in the stripping process. The increase in the removal percentage *via* increasing the concentration of the pollutant in the feed stream is due to the increase in the driving force of the mass transfer process generated by partial pressure reduction on the permeate side, in the stripping process [31,32]. The percentages of removal of phenol for thirty minutes for 10, 50, 100 and 150 ppm were 22.7, 43.2, 60.8 and 63.3%, respectively.

Figure 3 shows that the mole ratio of hydrogen peroxide to phenol is the key to controlling the dissociation rate of phenol in the oxidation reaction, based on the literature for oxidation processes in the presence of a single oxidizing agent (hydrogen perox-

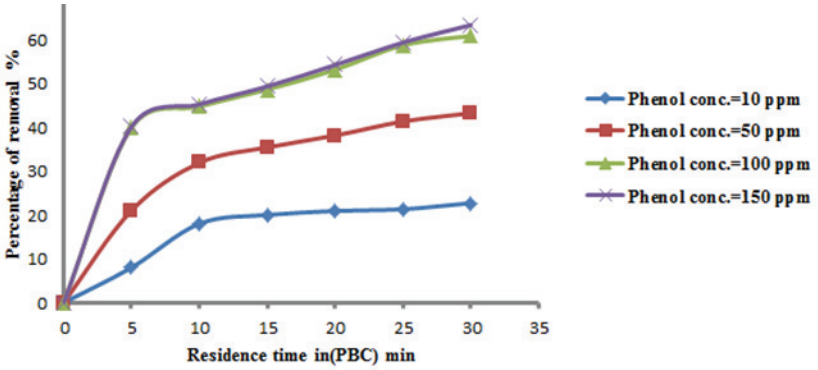

Figure 2. Impact of time curing on the percentage of elimination of phenol, for different concentrations of phenol inputs.

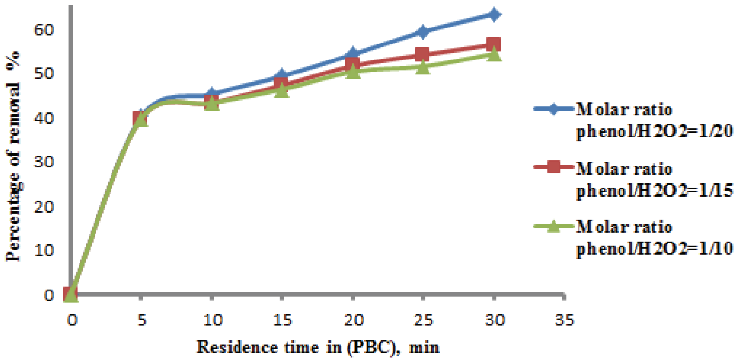

Figure 3. Influence of the remediation period on the percentage of removal, for a different range of molar ratios of phenol to hydrogen peroxide in PBC.

ide) [33]. Redoubling the molar number of hydrogen peroxide approximately twenty times twice the number of moles of phenol, with a 30 min remediation period, showed that the removal rate did not exceed 63.3%. The increase or decrease in this molar ratio caused in both cases a decrease in the dissociation rate of phenol, as the increase leads to what is known as the sweeping or scavenging the free radicals of hydrogen peroxide, where the decrease causes the numerical diminution of the free radicals that attack phenol and, consequently, the rate of dissociation in the oxidation reaction. The increase or decrease beyond the optimal concentration leads to decreasing the process efficiency due to the scavenging effect of the $HO^{\bullet}$ [29]. The ascending order of percentages of phenol removal for a treatment period of approximately 30 min, according to molar ratios 1:10, 1:15 and 1:20, are 56.4, 54.3 and 63.3%, respectively.

Figure 4 shows the limited effect of the change in the rate of airflow on the percentage of phenol removal for a 30-min treatment period, where at the flow rate of 5 L/min, the percentage of removal was approximately 52%, while at 18 L/min the percentage for removal was approximately 63%, at the same treatment period of 30 min. The difference in removal efficiency does not exceed 16%. This confirms the limited effect of a relative change in flow rate on the percentage of elimination efficiency. The percentage of removal for phenol with airflow rates 5, 10 and 18 L/min within 30 min remediation time was 52.8, 59.7 and 63.3%, respectively.

The second stage of the results appears in the IFALR reactor that are represented via the samples taken from checking point No 2*.* These results are illustrated by the continuous effect of both stripping and oxidation processes, in addition to the new important factor represented by the adsorption process, with continuous changing in operating conditions (treatment period, concentration, airflow rates and the molar ratio of the pollutant to the oxidizing agent) [34].

From Figure 5 the effect of adsorption on the phenol removal rate for different phenol concentrations in the entering feeding stream appears evident. Furthermore, when concentration was 150 ppm, the removal rate was 89% for a 30-min treatment period in the second stage remedy, occurring in a reverse fluidization reactor (IFALR), *i.e.*, with a total period of stay in the treatment system of 60 min, with the synergy of oxidation and stripping processes, in addition to the adsorption process which has the main effect in the work of the IFALR reactor. The dispersed water in the inner column of the reactor (draft) creates a differ-

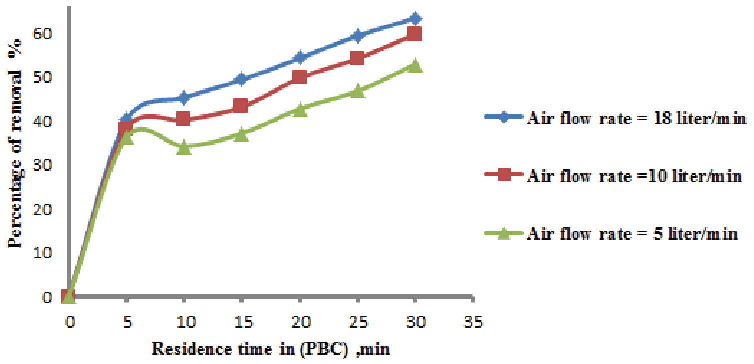

Figure 4. Impact of residence time on the percentage of phenol elimination with various airflow rates in PBC.

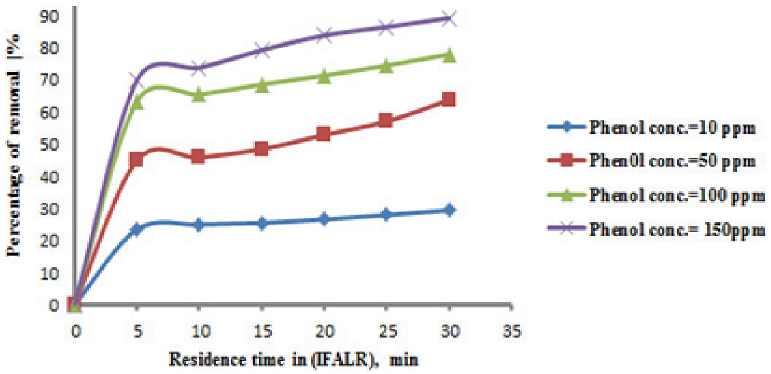

Figure 5. Influence of remediation time on the percentage of elimination of phenol with several initial concentrations of phenol, during stripping, oxidation, and adsorption processes in IFALR.

ence in density between the water treated in the draft tube and the water present in the annulars, forcing the water to circulate in the direction from the top, passing through the packed bed padding with activated carbon (inverse fluidization), where the adsorption of phenol takes place depending on the principle of the mass transfer *via* the concentration difference of phenol between water and carbon, which gives the opportunity to increase the efficiency of the process of elimination of phenol in the contaminated water. Many researchers confirmed that the adsorption process is affected by the gas and liquid velocities, particle size, and initial static bed height, and the initial phenol concentration, flow rate, and bed particle size as well [34,35]. The removal rates of phenol in 30 minu for 10, 50, 100 and 150 ppm were 29.29, 63.6, 77.8 and 89.09%, respectively.

The rate of the oxidation reaction depends on the optimum ratio between the pollutant and the oxidizing agent (hydrogen peroxide). Figure 6 shows that the highest removal efficiency of 89.1% was obtained in the second stage of the water treatment, which occurred in the reverse liquefaction reactor (IFALR) when the ratio of hydrogen peroxide to phenol was twenty, and this is due to the appropriate number of free radicals generated by the dissociation of the oxidizing agent, which was not too many that it caused the sweep of free radicals and not too few to lead to a decrease in the oxidation rate, so as to ensure the best and highest efficiency of phenol removal [29]. It is noticed that the removal percentage of phenol at 30 min in the second remedy stage in IFALR with a serial molar ratio of 1:10, 1:15 and 1:20, and total residence period in the treatment system of 1 h, was 74.2, 80.1 and 89.09%, respectively.

Reverse liquefaction reactor (IFALR) used in the design of the second stage of the proposed treatment system, uses air to disperse and recirculate the contaminated water between the two parts of the reactor, the riser and downcomer, which leads to control of design factors, such as surface area of contact, mixing intensity, and residence time. Figure 7 shows that the airflow rate of 18 L/min and the use of 5 kg of activated carbon in building the optimum dimensions of the filling bed for getting the highest rate for phenol mass transfer from the liquid state (polluted water) to the solid (activated carbon) [36], has achieved an approximate removal rate of 90% in a treatment period of 30 min in a reverse liquefaction reactor, and the total remedy time was 1 h in the treated system. The removal rates of phenol in 30 min for 5 , 10 and 18 L were 80.1, 86.09 and 89.09%,

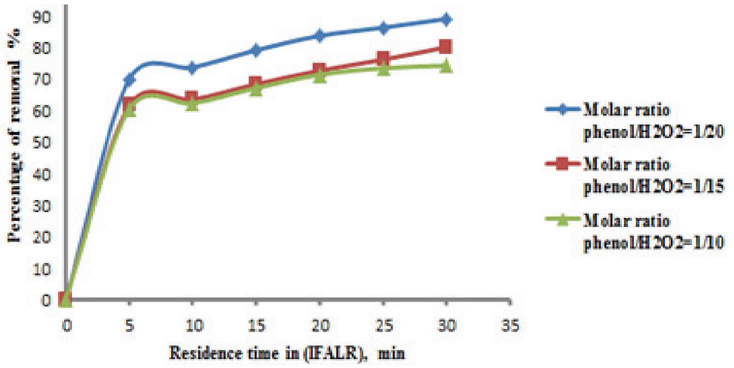

Figure 6. Impact of the remediation period on the proportion of phenol elimination for different molar ratios of phenol to hydrogen peroxide in IFALR.

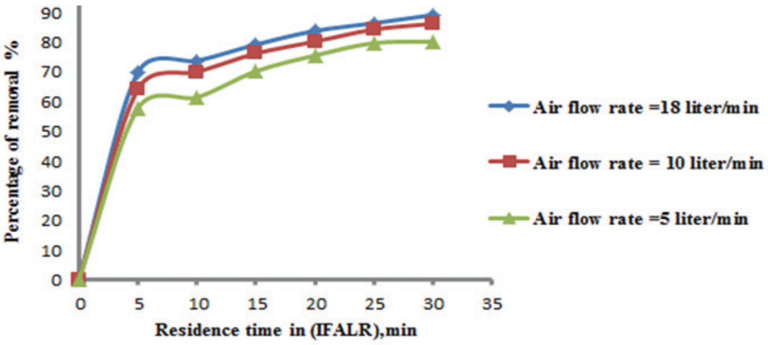

Figure 7. Effects of treatment time on the proportion of phenol removal for various airflow rates in IFALR.

respectively. The difference in efficiency percentage does not exceed 0.1%. This confirms the limited effect of flow rate on the elimination percentage.

CONCLUSIONS

From the results of the research, it is possible to conclude the following.

The success of the design idea based on the use of a solenoid valve with a bubble column to determine the residence time and transport of polluted water without the need to use a pump in what is known as PBC.

The success of the idea of combining PBC with the inverse fluidization reactor IFALR was achieved in one treatment system.

Three processes were achieved: stripping, oxidation, and adsorption.

Three techniques were implemented: pulsation propulsion, inverse fluidization, and use of a single oxidizing agent.

The best operating conditions for the removal system were checked.

The clearance rate of 89% was obtained in the following operational conditions:

A: one hour of total processing time;

B: 18 L/min airflow rate;

C: mole ratio of 1/20 of phenol to hydrogen peroxide.

With the successful removal of phenol, the present treatment system can be used to remove various types of organic pollutants in water.

The system can be used to reduce the risks of organic compounds that have a negative impact on the environment.

REFERENCES

[1] M. Hairuddin, N. Mubarak, M. Khalid, E. Abdullah, R. Walvekar, R. Karri, Environ. Sci. Pollut. Res. Int. 26 (2019) 35183-35197

[2] A. Mathur, C. Balomajumder, Bioresour. Technol. 142 (2013) 9-17

[3] P. Xin, B. Wu, C. Wu, C. Lin, J. Hazard. Mater. 244-245 (2013) 765-772

[4] L. Zhang, C. Zhang, Z. Cheng, Y. Yao, J. Chen, Chemosphere 90 (2013) 1340- 1347

[5] H. El-Naas, A. Acio, E. El Telib, J. Environ. Chem. Eng., A 2 (2014) 1104-1122

[6] Y. Huang, L. Li, Water Environ. Res. 86 (2014) 277-284

[7] S. Kim, R .Krajmalnik-Brown, O. Kim, J. Chung, Sci. Total Environ. 497-498 (2014) 250-259

[8] S.Stasik, Y.Wick, K. Wendt-Potthoff, Chemosphere 138 (2015) 133-139

[9] H. Diya'uddeen, A. Daud, R. Abdul Aziz, Process Saf. Environ. Prot. 89 (2011) 95-105

[10] P. Shariati, B. Bonakdarpour, Z. Ashtiani, Bioresour. Technol. 102 (2011) 7692-7699

[11] E. Santo, P. Vilar, S. Botelho, A. Bhatnagar, E. Kumar, A. Boaventura, Chem.Eng. J. 183 (2012) 117-123

[12] S. Zhao, P. Wang, C. Wang, L. Langer, G. Abulikemu, X. Sun, Chem. Eng. J. 219 (2013) 419- 428

[13] N. Lu, J. Li, X. Wang, T. Wang, Y. Wu, Plasma Chem. Plasma Process. 32 (2011) 109-121

[14] F.Shahrezaei, Y. Mansouri, L. Zinatizadeh, A. Akhbari, Powder Technol. 221 (2012) 203- 212

[15] O. Cooney, David, Adsorption for Wastewater Treatment, in: Adsorption. Design for. Wastewater Treatment, Lewis Publishers, Boca Raton, FL, 1999, pp. 1-8

[16] D. Mohan, A. Sarswat, Y.S. Ok, C.U. Pittman, Bioresour. Technol. 160 (2014) 191-202

[17] R. RaoKarri, N. Jayakumar, J. Sahu, J. Molecular Liq. 231 (2017) 249-262

[18] R. Karri, J. Sahu, N. Jayakumar, J. Taiwan Inst. Chem. Eng. 80 (2017) 472-487

[19] I. Ben Hariz, A. Halleb, N. Adhoum, L. Monser, Sep. Purif. Technol. 107 (2013) 150-157

[20] S. Mizzouri, G. Shaaban, J. Hazard. Mater. 250-251 (2013) 333-344

[21] H. Panjeshahi, in Handbook of process integration, J.J. Klemes (Ed.), Woodhead Publishing, Sawston, 2013, pp. 633-704

[22] H. El-Naas, A. Acio, E. El Telib, J. Environ. Chem. Eng., B 2 (2014) 56-62

[23] S. Sharma, P. Rangaiah, in Proceedings of the 24th European Symposium on Computer Aided Process Engineering, Budapest, Hungary, 2014, pp. 1531-1536

[24] Y. Zhou, F.Gao, Y.Zhao, J. Lu, J. Saudi Chem. Soc. 18 (2014) 589-592

[25] G. Hu, J. Li, H. Hou, J. Hazard. Mater. 283 (2015) 832--840

[26] H. Srichandan, S. Singh, K. Blight, A. Pathak, J. Kim, S. Lee, W. Lee, Int. J. Miner. Process. 134 (2015) 66-73

[27] A. Zazo, A. Casas, B. Molina, A.Quintanilla, J. Rodriguez, Environ. Sci. Technol. 41 (2007) 7164-7170

[28] C. Villegas, N. Mashhadi, M. Chen, D. Mukherjee, E. Taylor, A. Biswas, Curr. Pollut. Rep. (2016) 1-11

[29] E. Neyens, A. Baeyens, J.Hazard. Mater. 98 (2003) 33-50

[30] M. Ahmadi, B. Ramavandi, S. Sahebi, Chem. Eng. Commun. 2029 (2015) 1118-1129

[31] M. Haroun, A. Idris, Desalination 237(2009) 357-366

[32] F. Zareei, A. Ghoreyshi, World Appl. Sci. J. 13 (2011) 2067-2074

[33] I. Muangthai, C. Ratanatamsakul, M. Lu, Sustain. Environ. Res. 20 (2010) 325-331

[34] A. Al-ezzi, Sci. Int. (Lahore) 30 (2018) 673-680

[35] M. Jovanovic, Z. Grbavcic, N. Rajic, B.Obradovic, Chem. Eng. Sci. 117 (2014) 85-92

[36] J. Kulkarni, W. Tapre, V. Patil, B. Sawarkar, Procedia Eng. 51 (2013) 300-307

[37] K. Balaji, S. Poongothai, Int. J. Eng. Sci. Technol. 4 (2012) 3134-3139.

ALI ABDUL RAHMAN-AL EZZI

Department of Chemical Engineering,
University of Technology, Baghdad,
Iraq

NAUČNI RAD

UKLANJANJE FENOLA POMOĆU PULZACIONE BARBOTAŽNE KOLONE SA INVERZNIM FLUIDIZACIJSKIM AIT-LIFT REAKTOROM SA UNUTRAŠNJOM CEVI

Fenol i fenolna jedinjenja su sveprisutni organski zagađivači, koji se ispuštaju u vodotokove i sisteme otpadnih voda proizvedenih u industrijskim procesima. Ovaj problem privlači pažnju zbog karakteristika, kao što su visoka toksičnost, kancerogena svojstva i sposobnost sakupljanja koje utiče zdravlje ljudi i životnu sredinu. U ovoj praktičnoj studiji, integrisani sistem pulzacione barbotažne kolone i inverznim fluidizacionim air-lift reaktorom sa sa unutrašnjom cevi testiran je za uklanjanje fenola. Probna platforma napravljena je tako da je barbotažna kolona sa solenoidnim elektro-ventilom na gornjem kraju, koji je uključen preko najmanje dva tajmera, povezana sa air-lift reaktorom parvougaonog poptrčnog preseka sa unutrašnjom cevi dok je anularni proctor ispunjen zrnastim aktivnim ugljem. Efekat različitih parametara (molski odnos fenola prema H_2O_2 *1/10, 1/15 i 1/20, protok vazduha 5-20 L/min, vreme tretmana 5-60 min, početna koncentracija fenola 10-150 mg/L). Uklanjanje 90% fenola kao rezultat ove studije može predstavljati delimično rešenje ovog ekološkog problema.*

Ključne reči: fenol, pulsni stupac mehurića, inverzna fluidizacija, skidanje, oksidacija, adsorpcija.